

# **INSTRUMENTATION DEVELOPMENT FOR WALL SHEAR-STRESS APPLICATIONS IN 3D COMPLEX FLOWS**

THÈSE N° 3772 (2007)

PRÉSENTÉE LE 20 AVRIL 2007

À LA FACULTÉ DES SCIENCES ET TECHNIQUES DE L'INGÉNIEUR

Institut des sciences de l'énergie

SECTION DE GÉNIE MÉCANIQUE

ÉCOLE POLYTECHNIQUE FÉDÉRALE DE LAUSANNE

POUR L'OBTENTION DU GRADE DE DOCTEUR ÈS SCIENCES

PAR

**Elena-Lavinia BERCA**

Ingénieur en Energétique, Université Polytechnique de Bucarest, Roumanie  
et de nationalité roumaine

acceptée sur proposition du jury:

Prof. J. R. Thome, président du jury

Prof. F. Avellan, directeur de thèse

Dr Ph. Dupont, corapporteur

Dr Ph. Flückiger, corapporteur

Dr G. D. Ciocan, corapporteur



ÉCOLE POLYTECHNIQUE  
FÉDÉRALE DE LAUSANNE

Lausanne, EPFL

2007



*To my dear daddy,  
I hope you're proud of me,  
to my lovely family and  
to the man of my life, JD*





# Acknowledges

The work in this thesis has been carried out, mainly in the Laboratory for Hydraulic Machines, Mechanical Department, at Ecole Fédérale Polytechnique de Lausanne, Switzerland. Many people have been involved in the work and I am very grateful for their help, but there are some persons I want to thank especially.

In the first place, I would like to express my gratitude to my supervisor, Dr. Gabriel Ciocan for his intellectual and moral support over the past four years. It has been a great pleasure to work under its professional guidance in the field of mechanics and turbulence, for clarifying discussions on the analysis of the boundary layer, and to be inspired by his positive attitude through the best and the worst of times. I would also like to thank Gabriel for his interest and contribution in my professional and personal growth.

Meanwhile, I would like to thank my thesis director, Prof. François Avellan for giving me the opportunity to work in these projects and for his insightful comments during various stages of this work. In the same time, I would like to thank all the jury, Dr. Philippe Fluckiger and Dr. Philippe Dupont for their constructive remarks, as well as to Prof. John Richard Thome for agreeing to serve as the chairman of my thesis committee.

Nevertheless, I would like to thank from all my heart to Prof. Isbasoiu and all his team in Hydraulic Machinery Department, "Politehnica" University of Bucharest, Romania, for guiding my first steps in hydraulic scientific field and also for all the knowledge they thought me during my university years.

I would like to bring a special thanks to the mechanical staff in the Laboratory for Hydraulic Machines for all the technical support furnished during all these years: to Louis Bezençon and Maxime Raton for their support in accomplishment of the new hot-film probe encapsulation, which required a rigourously work, as well as in the connectors welding. Another special thanks goes to all the mechanical staff in EPFL, which contributed to the accomplishment of the all necessary instruments used in this thesis, namely Freddy, Jean-Pierre and Marc.

I wish to thank Pierre Barmaverain for his help with designing many of the mechanical components used in experiments. Moreover special thanks to Mr. Claude Amendola for his help in the wafers dicing, as well as to Mr. George Vaucher for his availability in welding the wires for the new sensors.

The new multidirectional micromachined hot-film sensor was developed together with the CMI staff in EPFL, to whom I wish to thank for their kindness in assisting me within the new developments, for their involvement and technical support to my project. A first approach was performed together with Christophe Beguin, to whom I thank for introducing me the microtechnology field. Several aspects of the work presented in this thesis, related to the intermediary steps regarding the new device manufacturing are a direct follow-up of his original work.

My collaboration with the other students and doctors has been thoroughly enjoyable and helped me in acquiring a great learning experience. I have made some really good friends, during my stage in the Laboratory for Hydraulic Machines. I am thankful to all of them (especially to Shadija Avdulah) for a pleasant, stimulating and inspiring atmosphere, as well as for their friendship and support. I would also like to thank my present and former colleagues with whom I have spent many fun and interesting times both at work and off-work hours.

All the other past and present members of our research group have assisted me in some way or the other over the years. I would like to thank: Prof. Jean-Louis Kueny, Sebastiano Mauri, Yousef Ait Bouziad, Georges Crittin, Daniel Rouiller, Maria Anitua.

I would like to thank to DANTEC Measurements for their collaboration in the final new electronical device development, and meanwhile to Flavien Baumgartner and Daniel Bommottet, in Wavemind, for their trials in building the electronical circuit.

I would like to thank to all FLINDT Project - Eureka n° 1625 - partners: Electricité de France, Alstom Hydro, GE Hydro, VA Tech Escher Wyss Hydro, Voith Hydro, PSEL (Funds for Projects and Studies of the Swiss Electric Utilities), Hydrodyna Project - Eureka no. 3246 - partners: Electricité de France, Alstom Hydro, GE Hydro, VA Tech Escher Wyss Hydro, Voith Hydro, UPC and the CTI (Commission for Technology and Innovation), for their financial support.

I would like to thank, from all my heart, to my family (parents, brother, sister and grand-mothers) for their moral support and encouragement through out my educational career. My parents have made innumerable sacrifices for my education and I find it difficult to express my gratitude in just a few words. As a tribute, I dedicate this thesis to them.

Last but not the least, I would like to thank to the man of my life, Jean-Daniel Niederhäuser, for his encouragement, understanding and mechanical support since the beginning of my thesis. I am specially grateful to him, because without his friendship and advice, this thesis would not have been possible, due to several personal losses suffered during last 3 years.

# Version abrégée

Dans le domaine des turbomachines, les pertes par frottement pariétal sont intensivement étudiées dû à leur influence sur le rendement global de la machine. Son rôle est essentiel pour l'évaluation de la tendance de détachement de la couche limite et la prédiction des pertes. Ainsi, le premier objectif de cette thèse a été la caractérisation du développement de la couche limite dans le cône d'une turbine Francis. Ensuite, dans la deuxième partie de ce travail, un nouveau capteur de frottement pariétal multidirectionnel est conçu, fabriqué et testé pour applications dans les turbomachines.

Ce développement fait partie d'un projet de recherche concernant la prédiction de l'écoulement dans l'aspirateur pour lequel, l'EPFL a rejoint plusieurs partenaires industriels dans le contexte de l'initiative européenne EUREKA no. 1625.

Dans la première partie de cette thèse, une campagne expérimentale a été menée dans une turbine Francis de vitesse spécifique  $nq$  92. En utilisant la technique de film chaud, deux sections - l'entrée et la sortie - du cône de l'aspirateur ont été explorées. 6 points de fonctionnement sont investigués, en couvrant une plage de fonctionnement - de 70% à 110% par rapport au débit du point de fonctionnement de meilleur rendement de la turbine. Pour cet aspirateur spécifique, la caractéristique du rendement présente une chute sévère, près du point de meilleur rendement, et la distribution du frottement pariétal dans cette région est particulièrement analysée.

Les procédures d'étalonnage et de mesure sont présentées, ainsi que l'étude de la précision de mesure. L'évolution des valeurs stationnaires de frottement pariétal avec la position spatiale du capteur dans le cône - 16 positions ont été explorées - et avec le point de fonctionnement correspondant est analysée. Une tendance de séparation de la couche limite pour les points de fonctionnement à charge partielle, a été mise en évidence, ainsi que l'influence du coude sur l'évolution spatiale du frottement pariétal. Ces résultats ont été utilisés pour la validation des calculs numériques dans l'aspirateur de cette turbine.

Des mesures LDV additionnelles, combinées avec celles du frottement pariétal ont permis la reconstruction de la couche limite. La meilleure approximation de la couche limite a été obtenue avec une loi puissance composé. Toutefois, la couche limite tridimensionnelle est un sujet complexe et des investigations supplémentaires sont nécessaires.

Du point de vue non-stationnaire, l'amplitude prédominante des fluctuations de frottement pariétal, est synchrone avec la fréquence de rotation de la roue. Pour les points de fonctionnement à charge partielle, la valeur de fluctuations principales correspond à la fréquence du passage de la torche et son amplitude dépend de 2 paramètres : la valeur du  $\sigma$  et la proximité de la torche par rapport à la paroi.

Pour une meilleure compréhension du comportement de la couche limite dans les turbomachines, est nécessaire l'exploration complète des couches limites 3D turbulentes, autant dans les parties fixes de la machine - cône et directrices - mais aussi dans les parties tour-

nantes - la roue, foyer des principales pertes par frottement dans une turbomachine. Des exigences spécifiques pour l'application dans les turbomachines doivent être remplies pour le développement d'un nouveau capteur:

- La miniaturisation, pour pouvoir l'instrumenter dans les géométries complexes des turbomachines,
- La sensibilité directionnelle, pour pouvoir reproduire le caractère complexe de l'écoulement, en principal le caractère 3D de l'écoulement,
- La sensibilité et la dynamique, permettant d'obtenir les principales caractéristiques non-stationnaires de l'écoulement: le sillage des directrices, le sillage des aubes de la roue, la fréquence de tourbillon, la fréquence de l'interaction turbine-circuit, etc.,
- Une bonne isolation électrique entre la surface du capteur, qui est en contact avec l'eau, et l'élément du film chaud.

Ainsi, le deuxième objectif de ce travail a été la conception et le développement d'un nouveau capteur de frottement pariétal, multidirectionnel, pour l'étude de la couche limite turbulent dans les turbomachines.

Le développement d'un nouveau capteur multidirectionnel a profité des opportunités offertes par les technologies MEMS. Ces technologies permettent d'obtenir un produit qui répond aux impératives de miniaturisation et précision demandés pour ce type de capteur, à un cout réduit. Le nouveau capteur représente un pont entre 2 différents domaines, la micro-mécanique et la mécanique des fluides. Le capteur est constitué de trois films chauds disposées en triangle, ayant chacun une surface globale de  $1.12 \times 0.1$  mm et une épaisseur de 110nm. Le film, en platine, est maintenu à une température constante de  $65^{\circ}\text{C}$ , par un feed-back électronique.

Les principaux processus utilisés dans la procédure de fabrication de ce nouveau capteur sont : la lithographie, le micro-usinage volumique, la déposition des films fins, le micro-usinage des surfaces, le décolage et le polissage chimique-mécanique. La fabrication du nouveau capteur de frottement pariétal miniaturisé est basée sur l'association de toutes ces techniques.

Un développement spécifique est réalisé pour la réalisation d'une surface isolant-thermique, ayant comme objectif la réduction de transfert de chaleur par conduction dans le substrat, surface sur laquelle le film chaud est déposé. Cette surface isolante est obtenue par la fabrication des couches de dioxyde en silicium, très fins, de  $4\mu\text{m}$ , en utilisant la technique DRIE. Le substrat est réalisé sous la forme de piliers en silicium, qui sont ensuite oxydés et/ou remplis avec oxyde ou nitrure de LPCVD. Un critère majeur pour le remplissage des tranchées est l'uniformité de la surface après le remplissage. 2 paramètres ont été optimisés: les dimensions et la disposition des piliers en silicium, pour obtenir une isolation continue et uniforme. La modélisation numérique, en utilisant Ansys, a permis l'évaluation de l'épaisseur optimale pour une bonne isolation thermique entre la structure chauffée et les structure environnantes.

Les principales étapes de développement ont été: le design d'un nouveau capteur de frottement pariétal, le développement de chaque étape de fabrication, la validation de ces étapes et leurs optimisations, la modélisation numérique pour l'étude du comportement thermique des films chauds, la fabrication de ce capteur et son encapsulation.

Le nouveau capteur a été caractérisé en termes de constante de temps, isolation électrique, fiabilité et robustesse. L'étalonnage du capteur a montré qu'il assure une précision et une sensibilité suffisante pour les mesures en turbines hydrauliques. Les principales

innovations, qui font l'originalité de ce capteur, sont: son design qui assure une réponse directionnelle nécessaire pour l'étude des couches limite 3D turbulents et la surface isolante utilisée pour réduire substantiellement les pertes par chaleur dans le substrat.

**MOTS CLEFS:** hydraulique, frottement pariétal, capteur à film chaud, turbomachine, microtechnique



# Abstract

In the turbomachines field, friction losses are intensively studied due to their important influence in the overall efficiency of the machine. The parameter helping in quantifying these friction losses is the wall shear-stress. Its role is essential for the qualification of the boundary layer separation tendency and the losses prediction. Thus, the first aim of this PhD is to characterize the boundary layer development, in the cone of the Francis turbine. Afterwards, in the second part of this study, a new multidirectional wall shear-stress sensor is designed, manufactured and tested for the turbomachines applications.

To develop this knowledge and the tools for flows prediction in the draft tube, EPFL joined major manufacturers in the context of the European initiative EUREKA project n° 1625.

In the first part of the thesis, an experimental campaign is leaded in the cone of the nq 92 Francis turbine, to characterize the wall stress, using the hot-film technique. 6 operating points were investigated, covering a large operating range - from 70% to 110% from best efficiency point flow rate. For this specific draft tube, the efficiency characteristic has a sever drop, close to the best efficiency point, and the wall shear stress evolution in this region is pointed out.

The calibration and measurement procedures are exposed and the accuracy study is performed. The evolution of the wall shear-stress steady values related to the spatial position of sensor -16 positions were explored - and to the corresponding operating point is analyzed. A boundary layer separation tendency for the part load operating points is pointed out, as well as the bend influence on the spatial evolution of the wall shear-stress. These results were used to validate numerical calculation in the draft tube.

Additional LDV measurements combined with the wall shear-stress results allowed to reconstruct the boundary layer. The best fit for representing the boundary layer is obtained with a composite power law. However the 3D boundary layer is complex and a profound knowledge is needed.

From the unsteady point of view, in the runner outlet section, the amplitude of the wall shear-stress fluctuations obtained synchronous with the runner's rotating frequency is predominant. For the partial load operating points, the main fluctuations magnitude is obtained for the rope passage frequency and its amplitude depends on 2 parameters: the  $\sigma$  value and the proximity of the rope to the wall.

To increase the knowledge for the boundary layers in turbomachines, it is necessary to explore fully 3D unsteady boundary layers, both in the fixed and rotating parts of the machine. Thus a multidirectional sensor with specific requirements is needed for the turbomachines application:

- a miniature hot film probe, which can be implemented in the complex geometry of the turbines,

- a multidirectional one, to take into account the complex character of the flow, mainly the strongly 3D flow,
- a sensor with a sensitivity and dynamic, allowing to obtain the main flow unsteady characteristics (guide vanes wake, runner blades wake, rope frequency, turbine-circuit interaction frequency, etc.),
- a good electrical isolation between the surface of the probe, which comes in contact with the water, and with the hot-film support.

In this way, the second aim of this PhD becomes the design and development of a new multidirectional wall shear-stress sensor for turbulent boundary layer research for turbomachines applications.

The development of the new multidirectional sensor implies technological developments using microtechnology, as MEMS offers opportunities for developing and manufacturing sensors with regard to complex applications, allowing, in the same time, a high accuracy at low cost. The new sensor represents a bridge between 2 different disciplines: micro-mechanical technology and fluid mechanics. Its concept is based on the heat transfer generated by a hot film with a general top-area of  $1.12 \times 0.1$  mm and a thickness of 110 nm. The film, in platinum, is maintained at a constant temperature, of  $65^{\circ}\text{C}$ , by a feed-back electronic.

Key process steps in fabrication of the new device are lithography, bulk micromachining, thin film deposition, surface micromachining, lift-off and chemical mechanical polishing. The manufacturing of new miniature wall shear-stress sensor is based on a combination of these techniques.

A specific development is performed for the achievement of an insulating surface to reduce the heat conduction between the hot film and the sensor body, on which the hot film is deposited. This surface is obtained by manufacturing silicon dioxide layers, of  $4\text{ }\mu\text{m}$ , by DRIE technique, in order to create high-aspect-ratio silicon pillars, which are then oxidized and/or refilled with LPCVD oxide or nitride. One of the major criteria for the trenches filling was the surface planarity at the end of the refill. 2 parameters are optimized: the thickness and the silicon pillars arrangement. Thermal numerical computations were carried out using Ansys and they allowed the achievement of the optimum thermal isolation thickness between the heated structures and the surrounding structures.

During the development of the new wall shear-stress probe, the main topics, achievements and contributions can be categorized into: design of a new wall shear-stress sensor, fabrication steps development, validation and optimization of the design, numerical simulations of the thermal behavior of the heated-films, manufacturing of the new device.

The new sensor is characterized in terms of time response, electrical insulation between the surface of the probe, which comes in contact with the water, and the hot-film, and reliability. The sensor is robust, with a good sensitivity for water measurements.

The main improvements, which make the current device distinct, are its design for a directional response for 3D turbulent boundary layer study and the insulating surface for substantially reduction of the heat losses by conduction between the film and the surrounding substrate.

**KEYWORDS:** hydraulic, wall shear-stress, hot-film probe, turbomachine, microtechnology



# Contents

<b>1</b>	<b>INTRODUCTION</b>	<b>1</b>
<b>2</b>	<b>OBJECTIVES</b>	<b>5</b>
<b>3</b>	<b>GENERAL ASPECTS</b>	<b>7</b>
3.1	TURBULENCE AND BOUNDARY LAYER . . . . .	7
3.1.1	Turbulent flow . . . . .	7
3.1.2	Boundary layer definition . . . . .	8
3.1.3	Boundary layer on a flat plate . . . . .	8
3.2	HEAT TRANSFER IN THE BOUNDARY LAYER . . . . .	15
3.2.1	Laminar boundary layer . . . . .	15
3.2.2	Turbulent boundary layer . . . . .	17
3.3	TECHNIQUES USED FOR WALL SHEAR-STRESS MEASUREMENTS	19
3.3.1	Direct techniques . . . . .	20
3.3.2	Indirect techniques . . . . .	22
<b>4</b>	<b>WALL SHEAR-STRESS PROBE CALIBRATION</b>	<b>27</b>
4.1	DEFINITION AND PRINCIPLE . . . . .	27
4.2	EXPERIMENTAL SET-UP . . . . .	27
4.2.1	Hydrodynamic water tunnel . . . . .	27
4.2.2	Procedure for velocity measurements . . . . .	31
4.3	HOT-FILM PROBE CALIBRATION PROCEDURE . . . . .	32
4.3.1	Operation theory for the hot-film probe . . . . .	32
4.3.2	Flow velocity evolution in the boundary layer . . . . .	36
4.3.3	Calibration parameters for hot-film probe measurements . . . . .	39
4.3.4	Hot-film probe calibration procedure . . . . .	40
<b>5</b>	<b>WALL SHEAR-STRESS MEASUREMENTS IN THE CONE</b>	<b>43</b>
5.1	BACKGROUND . . . . .	43
5.2	HOT-FILM PROBE CHARACTERIZATION . . . . .	45
5.2.1	Calibration curve . . . . .	47
5.2.2	Sensitivity parameters . . . . .	50
5.3	MEASUREMENT OF THE WALL SHEAR-STRESS IN A FRANCIS TURBINE'S CONE . . . . .	55
5.3.1	Experimental set-up . . . . .	55
5.3.2	Wall shear stress measurements procedure . . . . .	57
5.4	THE ANALYSIS OF THE RESULTS AT THE RUNNER OUTLET . .	62

5.4.1	Near BEP operating points . . . . .	62
5.4.2	Partial load operating points . . . . .	71
5.5	THE ANALYSIS OF THE RESULTS AT THE CONE OUTLET . . . . .	82
5.5.1	Near BEP operating points . . . . .	82
5.5.2	Partial load operating points . . . . .	88
<b>6</b>	<b>BOUNDARY LAYER CHARACTERIZATION IN THE CONE</b>	<b>97</b>
6.1	NEAR WALL 2D LDV MEASUREMENTS AND RESULTS . . . . .	98
6.2	BOUNDARY LAYER ANALYSIS . . . . .	99
6.2.1	Boundary layer representation . . . . .	99
6.2.2	Scaling laws for turbulent flows . . . . .	101
6.2.3	Comparison with the classical model of boundary layer . . . . .	103
6.2.4	Comparison with the power model of the boundary layer . . . . .	106
<b>7</b>	<b>DESIGN AND DEVELOPMENT OF THE NEW HOT-FILM PROBE</b>	<b>111</b>
7.1	BACKGROUND . . . . .	111
7.1.1	MEMS wall shear-stress sensors - historical survey . . . . .	112
7.1.2	MEMS wall shear-stress sensors - examples . . . . .	116
7.1.3	Motivation . . . . .	117
7.2	CONCEPTION OF THE NEW HOT-FILM PROBE FOR WALL SHEAR-STRESS MEASUREMENTS . . . . .	118
7.3	HOT-FILM DEPOSING TECHNOLOGY AND FABRICATION STEPS	120
7.3.1	The center of MicroNanoTechnology - overview . . . . .	120
7.3.2	First new hot-film probes generation . . . . .	120
7.4	SECOND GENERATION . . . . .	138
7.4.1	Improvements . . . . .	138
7.4.2	Thick silicon dioxide fabrication . . . . .	145
7.4.3	Sensors second generation fabrication . . . . .	151
7.5	EXPERIMENTAL SET-UP . . . . .	152
7.5.1	Probe encapsulation . . . . .	152
7.5.2	Design and manufacturing of the rotating support . . . . .	155
<b>8</b>	<b>MEASURES AND EVALUATION OF THE NEW PROBE</b>	<b>157</b>
8.1	PROBE CHARACTERIZATION . . . . .	157
8.2	TESTS IN THE WATER TUNNEL . . . . .	158
8.2.1	Instrumentation . . . . .	158
8.2.2	Calibration procedure . . . . .	159
8.3	NEW PROBE CALIBRATION . . . . .	159
8.3.1	Time response calculation . . . . .	160
8.3.2	Time response measurement . . . . .	164
8.3.3	New wall shear-stress sensor calibration and sensitivity parameters study using miniCTA . . . . .	170
8.3.4	Sensitivity parameters . . . . .	170
<b>9</b>	<b>CONCLUSIONS</b>	<b>181</b>
<b>10</b>	<b>PERSPECTIVES</b>	<b>185</b>

---

<b>A</b>	<b>Measurement systems for wall hot-film probe calibration</b>	<b>189</b>
A.1	Measurement system for the velocity acquisition . . . . .	189
A.1.1	The Pitot tube . . . . .	189
A.1.2	The Preston tube . . . . .	190
A.1.3	Instrumentation for flow pressure probe sensors . . . . .	193
A.1.4	Oscilloscope . . . . .	193
A.1.5	SC-2040 . . . . .	193
A.1.6	Workstation . . . . .	195
A.2	Measurement system for the hot-film probe . . . . .	195
A.2.1	The hot-film probes . . . . .	195
A.2.2	The Constant-Temperature Anemometer (CTA) . . . . .	195
<b>B</b>	<b>Constant Temperature Anemometer calibration</b>	<b>197</b>
<b>C</b>	<b>Fabrication technologies</b>	<b>199</b>
C.1	Photolithography . . . . .	199
C.2	Film deposition technique . . . . .	201
C.3	Etching . . . . .	204
C.4	Surface micromachining . . . . .	207
C.5	Chemical Mechanical Polishing . . . . .	208
C.6	Lift-off . . . . .	209
C.7	Electroplating . . . . .	210
C.8	Wafer dicing . . . . .	210



# Notations

## BOUNDARY LAYER, HEAT TRANSFER THEORY AND HOT-FILM CALIBRATION

$u$	General variable for characterizing the turbulent flow	
$u'$	Fluctuating part of a variable in turbulent flow	
$\bar{u}$	Time independent part of a variable in turbulent flow	
$\delta$	Boundary layer thickness	[m]
$\tau_p$	Wall shear-stress	[Pa]
$C_\infty$	Mean flow velocity	[m/s]
$c_0$	Flow velocity outside boundary layer	[m/s]
$\rho$	Water density	[kg/m <sup>3</sup> ]
$p_0$	Static pressure	[N/m <sup>2</sup> ]
$\frac{dp}{dx}$	Pressure gradient	[N/m <sup>3</sup> ]
$\mu$	Water dynamic viscosity	[kg/(s·m)]
$L$	Heated element's length of the heat transfer	[m]
$c'_x, c'_y$	Turbulent velocity fluctuations in x and y directions	[m/s]
$\bar{c}_x, \bar{c}_y$	Mean flow velocity components in x and y directions	[m/s]
$c^+$	Dimensionless velocity	[-]
$y^+$	Dimensionless distance from the wall	[-]
$c_\tau$	Friction velocity	[m/s]
$\tau$	Total shear stress	[Pa]
$\tau_t$	Turbulent shear stress	[Pa]
$\tau_l$	Laminar shear stress	[Pa]
$\chi$	Von Karman constant	[-]
$C$	Integration constant	[-]
$\bar{T}$	Averaged temperature	[°C or K]
$T'$	Fluctuating temperature	[°C or K]
$\dot{q}$	Heat flux	[J/m <sup>2</sup> ]
$\lambda$	Thermal conductivity	[W/(m · K)]
$\frac{dT}{dy}$	Temperature gradient	[K/m]

$c_p$	Specific heat at constant pressure	[J/(kg · K)]
$\Lambda$	Thermal diffusion coefficient	[-]
$\delta_{th}$	Thermal boundary layer thickness	[m]
$T^*$	Dimensionless temperature	[-]
$T_s$	Temperature on the wall surface	[°C or K]
$T_\infty$	Mean free-stream temperature	[°C or K]
Pr	Prandtl number	[-]
$Pr_t$	Turbulent Prandtl number	[-]
$\dot{q}_l$	Laminar heat flux	[J/m <sup>2</sup> ]
$\dot{q}_t$	Turbulent heat flux	[J/m <sup>2</sup> ]
$\varepsilon_h$	Turbulent thermal diffusion coefficient	[-]
$\varepsilon$	Turbulent viscosity	[m <sup>2</sup> /s]

## WALL SHEAR-STRESS MEASUREMENTS

$n_p$	Rotation speed of the pump	[rot/min]
$Q$	Flow discharge	[m <sup>3</sup> /s]
$P_h$	Pump's hydraulic power	[kW]
$A$	Area of the test vein	[m <sup>2</sup> ]
$\Delta p$	Pressure difference	[Pa]
$\theta$	Water temperature	[°C or K]
$V_{pitot}$	Voltage output from the Pitot tube	[V]
$V_{c=0}$	Reference voltage	[V]
$R_1, R_{int}$	Top resistances	[Ω]
$R$	Comparison resistance	[Ω]
$R_{var}$	Probe resistance in the Wheatstone bridge	[Ω]
$R_c$	Cables resistance	[Ω]
$\dot{Q}_J$	Heat transfer by Joule effect	[J]
$\Sigma \dot{Q}$	Heat transferred to surroundings	[J]
$dQ_{film}$	Thermal energy stored in the film	[J]
$\dot{Q}_{conv}$	Heat transferred by convection	[J]
$\dot{Q}_{cond}$	Heat transferred by conduction	[J]
$\dot{Q}_{rad}$	Heat transferred by radiation	[J]
$V$	Voltage across the hot-film probe	[V]
$R_f$	Hot-film probe resistance at the operating temperature	[Ω]
$T_f$	Operating temperature of the hot-film probe	[°C]
$\alpha_R$	Temperature coefficient of resistivity	[%/°C]

$\alpha$	Thermal diffusivity	[m <sup>2</sup> /s]
$\tilde{T}$	Dimensionless temperature	[-]
$\eta$	Similarity parameter	[-]
$M$	Constant	[-]
$a, b$	Constants used for obtaining the relationship between dimensionless parameters $y^+$ and $c^+$	[-]
$\sigma$	Thoma number	[-]
$\chi$	Pressure recovery factor	[-]
$\phi_{runner}$	Runner diameter	[m]
$\varphi$	Flow rate coefficient for different operating points	[-]
$V$	Output voltage from the hot-film probe	[V]
$a_i$	Polynomial coefficients	[-]
$A_e$	Hot film's surface	[m <sup>2</sup> ]
$\Delta T$	Temperature difference between the sensor and fluid	[°C or K]
$H$	Overheating rate	[-]
$I$	Anemometer's current	[A]
$A, B$	Calibration curve coefficients	[-]
$V_{mes}$	Measured voltage value at the hot-film output	[V]
$\theta_{mes}$	Measured temperature value	[°C or K]
$V_{cor,T}$	Voltage value adjusted to a reference temperature, T	[V]
$\varphi$	Discharge coefficient	[-]
$n_q$	Specific speed	[-]
$\psi$	Specific energy coefficient	[-]
$\tau(t)$	Instantaneous value of the wall shear-stress	[Pa]
$\tilde{\tau}(t_1)$	Synchronous average for an instant $t_1$ of the period	[Pa]
$\tau'(t)$	Random turbulent fluctuations of the wall shear-stress	[Pa]
$t_1$	An instant of a period	[s]

## BOUNDARY LAYER

$c_x$	Tangential component of the velocity	[m/s]
$c_z$	Axial component of the velocity	[m/s]
$y$	Distance from the wall	[m]
$R$	Radius corresponding to the measurement cross sectional area	[m]
$Re$	Reynolds number	[-]
$\Phi$	Dimensionless function	[-]
$\kappa$	Universal constant	[-]

---

$C$	Universal constant	[-]
$c_{x'}$	Tangential velocity component related to the local system attached to the hot-film probe	[m/s]
$c_{z'}$	Axial velocity component related to the local system attached to the hot-film probe	[m/s]
$Re_\theta$	Reynolds number based on the momentum displacement thickness	[-]

## NEW MINIATURE HOT-FILM PROBE

$\Phi$	Hot-film probe diameter	[m]
$L$	Hot-film impedance	[ $\Omega$ ]
$\alpha$	Temperature coefficient of resistance	[% / °C]
$T(y)$	Temperature distribution in the probe's substrate	[°C or K]
$T _{y=0}$	Hot-film temperature	[°C or K]
$T_0$	Water temperature at the film's upper surface and at the lower substrate's surface	[°C or K]
$k_{su}$	Heat conductivity of the substrate	[W/(m · K)]
$H(c)$	Heat transfer function	[-]
$c$	Flow velocity	[m/s]
$h_1$	Insulating surface's thickness	[m]
$k_{su1}$	Heat conductivity of the insulating surface	[W/(m · K)]
$k_{su2}$	Heat conductivity of the silicon substrate	[W/(m · K)]
$h$	Substrate's thickness	[m]
$\hat{h}$	Local heat transfer coefficient	[-]
$T_h$	Temperature of the lower substrate surface for static conditions	[°C or K]
$x$	Biot number	[-]
$A, B, n$	Constants	[-]
$R_0$	Hot-film's resistance at the reference temperature $T_0$	[ $\Omega$ ]
$T_0$	Reference temperature	[°C or K]
$M$	Time constant	[-]



# Chapter 1

## INTRODUCTION

Flow understanding in a hydraulic turbomachine is essential for increasing its efficiency and, thus, the associated output power. An impediment in studying the flow is its complex character and, thus, many different factors must be taken into account and evaluated.

An important process occurring in most fluid flows, influencing the transport of momentum, heat and mass is turbulence. In this way, it plays a role in the generation of fluid friction losses. For understanding the fluid flow behavior and for designing and evaluating engines, pumps, the turbulence study is essential.

Nevertheless, rapid fluctuations in velocity occur in most flows of practical interest: boundary layer above wings and fuselage surfaces, wakes behind obstacles in flows, jets from the nozzles of rockets and gas-turbine engines and flows inside engine components. These fluctuations have effects on drag, surface shear stress, boundary layer separation, mixing between fuel and air in engines, turbomachines vibrations and control surfaces. To understand such phenomena, the velocity fluctuations must be measured accurately.

In a hydraulic turbine, the main part, where an important amount of kinetic energy is recovered, due to the increasing of the flow section, is the cone of the draft tube.

Moreover, the amount of energy recovered in the cone increases as the opening angle of the cone increases when no unsteady separations occur. Meanwhile, the flow in the cone is strongly unsteady and it takes place with an adverse pressure gradient. These 2 factors are favorable for the unsteady separations, which decrease the flow velocity and, thus, the amount of the energy that has to be recovered.

The unsteady separations limit the efficiency of the turbine and studies must be carried out, for characterizing the non-stationary phenomena.

One interesting parameter of the flow, in this part of the turbine, important to comprehend the performance of various systems, is the wall shear-stress, the friction force applied by a fluid to a solid wall.

From scientific and engineering perspectives, the wall shear stress is an essential quantity to compute, measure or infer in a wall-bounded turbulent flow. One of the most important results of boundary layer theory has been the determination of the wall shear stress, a quantity which largely determines the energy necessary for moving the flow of liquids and gases over solid walls. Most wall shear stress studies are based on the assumption that the mean flow velocity gradient and the heat transfer rate near/or at the wall are both proportional to the wall shear stress.

Knowledge of the wall shear stress is very important for many technical applications

and for the understanding of all wall-bounded shear flows. Time-averaged values of this quantity are indicative of the global state of the flow along a surface and can be used to determine body-averaged properties. The time resolved part of the wall shear stress is a measure of the unsteady structures in the flow, which are responsible for the individual momentum transfer events and is an indicator of the turbulence activities. Therefore one would like to know the magnitude, mean and fluctuating value, and the direction of the wall shear-stress vector, as well as, its distribution over a surface. The flow may be compressible or incompressible, laminar or turbulent and can even reverse its direction in the vicinity of the wall in an adverse pressure gradient.

Spatially distributed values of the instantaneous wall shear stress can be used in a feedforward or feedback control loop to effect beneficial changes in the boundary layer.

Over the last few decades, a lot of experiments were performed for wall shear stress measurements. The complexity of the flow, the geometry of the boundaries and the limitations in the measuring device used are studied. Some accomplishments were achieved, like the wall shear stress distribution along flat plates and on simple bodies of revolution, but generally, due to difficulties, wall shear stress knowledge and its fluctuating component are limited.

Wall shear stress is, also, an interesting parameter for some other several, different technical fields. In aeronautics is intensively studied by NASA, for improving the aircraft performances, by studying the boundary layer on the wings and developing different wings profiles. The figure 1.1, evidences the wall shear stress magnitude on the suction side of a wingtip model, both from the computational and experimental point of view.

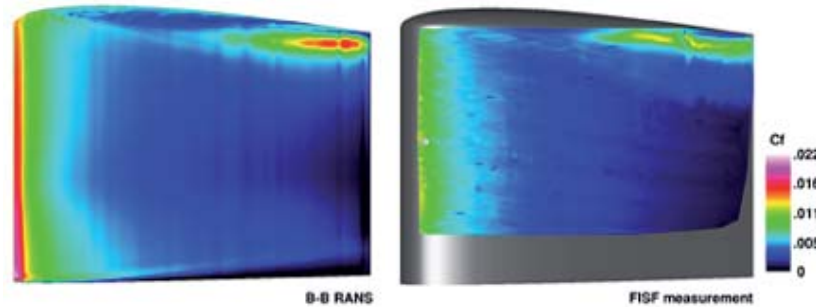


Figure 1.1: Comparison of computed (left) and measured (right) wall shear stress on a wingtip, Chow et al. [1997]

This comparison shows reasonable agreement on the inboard part of the wing, where the flow is nearly 2D. In the vicinity of the wingtip vortex, where the flow is highly 3D, substantial differences in wall shear stress magnitude are seen and they are explained by the turbulence modelling deficiencies in the computed Navier-Stokes solution. Another example is shown in the wall shear stress distribution on a typical propeller driven fighter, see figure 1.2.

Nevertheless, the wall shear stress estimation can be also applied to optimize drag reduction in pipe flow or skin friction in aerodynamics.

Moreover, the measurement of fluid velocity becomes very interesting in many other industrial and laboratory applications extending to air flows for monitoring and controlling living and working environments in a building.

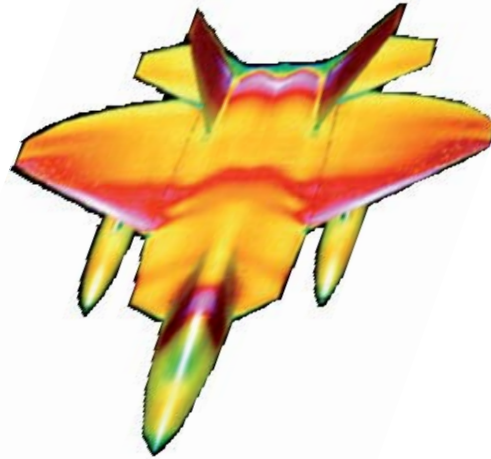


Figure 1.2: Wall shear stress distribution on a typical propeller driven fighter

Another interesting field for the wall shear stress is navy, where there was developed a technique for reducing frictional drag using a super-water-repellent surface and air injection. The results are quite impressive, the frictional resistance on the SWR surface was reduced by 80% for a flow velocity of  $4m/s$  and by 55% for a flow velocity of  $8m/s$ .

In turbomachines field, boundary layer is of interest for CFD codes validation and for its influences on the flow, for flow prediction by frictional losses and separation studies.

Generally, wall shear-stress is a small magnitude parameter. Some typical values are worth bearing in mind for the following discussion. A submarine cruising at  $30\ km/h$  has an estimated value of the shear stress of about  $40\ Pa$ ; an aircraft flying at  $420km/h$ ,  $2\ Pa$ ; and a car moving at  $100\ km/h$ ,  $1\ Pa$ . Such small forces per unit area require very sensitive measuring devices.

From the calculation point of view, the wall shear-stress allows the validation of the wall laws used for the turbulence modelling near the wall.

These are the main determinant reasons to study the flow in the cone, for evaluating the tendency of the unsteady separations, in this part of the turbine, and to validate the CFD codes.

Using conventional flow measurement techniques, a great part of the turbulence and wall shear stress characteristics have been investigated and understood. Thermal anemometry is one of the most widely used method for turbulent flows study and for estimating the wall shear-stress. Meanwhile, due to the limitations in the spatial and temporal resolution of existing experimental techniques for wall boundary layers, wall shear stress fluctuations have not yet been accurately measured. New developments in the microtechnology field allow new perspectives in a lot of research technical fields. By miniaturization, sensors can be fabricated with increased performances.

The size of a typical MEMS sensor is less than  $100\ \mu m$  in size, meaning at least one order of magnitude smaller than traditional sensors used for velocity, pressure or temperature measurements. Moreover, due to their size, the inertial mass and thermal capacity are reduced, making MEMS sensors suitable for dynamic measurements in turbulent flows where a high-frequency response and a fine spatial resolution are required. Meanwhile, MEMS sensors are not hand-made, but several in the same time, each unit is fabricated within extremely small tolerance and at very low cost.

The sensors performances improvement, resulting in sensitive elements miniaturization, is a decisive factor for the progress of the research in many fields, like aerodynamics, turbomachines, offering new possibilities for profound understanding of the physics of turbulent wall boundary layers.

# Chapter 2

## OBJECTIVES

A first aim of this thesis is represented by wall shear-stress measurements performance in a Francis turbine's cone, using a classical hot-film probe together with a constant temperature anemometer and the fluid behavior analysis in this part of the turbine, by developing and studying the boundary layer.

The thesis begins with the study and the development of the calibration procedure for the hot-film probe in the hydrodynamic tunnel in Laboratory for Hydraulic Machines in E.P.F.L. It is described the whole acquisition system used to get through all the stages needed by the calibration procedure.

Moreover, it is studied the influence of several sensitivity parameters over the measurements, namely water temperature, orientation of the hot-film probe in the flow, contamination of the probe. There are explained all the corrections needed related to those parameters.

Further, following the calibration of the hot-film probe, measurements in a Francis turbine's cone have been performed and they were analyzed. It was studied the tendency of the unsteady separations using the wall shear-stress, as a reference.

Moreover, the procedure applied for eliminating the influence of the additional parameters, like water temperature, probe contamination, over the measurements in turbine, is presented.

Meanwhile, the experiments showed that main frictional losses of a turbomachine take place in the runner. Generally, the availability and performance of the commercial hot film sensors, for boundary layer investigation in this region of a turbomachine, have been limited by different specific constraints.

The accelerated development of silicon micromachined sensors and actuators has meant that many new and competitive application areas have arisen, one of these being the use of silicon sensors in complex flows. Using silicon micromachined sensors, sufficient spatial and temporal resolution for the measurements of turbulent fluctuating pressure and wall shear stress for finding the correlation coefficients can be obtained.

A second aim of this thesis reports on the design, analysis and fabrication of a new multidirectional and miniature sensor specially designed for experiments in 3D complex turbulent flows. Its operating principle is based on the hot-film anemometry and the sensor is fabricated on silicon substrate using MEMS technology. The sensor is qualified in a turbulent flat plate boundary layer. Thus, a detailed analysis of the working mechanism, and simulation is carried out using finite element analysis method. Finally, the calibration results and comparisons with the classical hot-film probe are presented.



# Chapter 3

## GENERAL ASPECTS

### 3.1 TURBULENCE AND BOUNDARY LAYER

#### 3.1.1 Turbulent flow

All flows occurring in engineering practice are turbulent, explained by a 3D, time-dependent, eddying motion with many scales, causing continuous mixing of fluid elements and often superposed on a simpler mean flow. There is no definition of turbulence, but one could be "a state of continuous instability".

Turbulence is generated by the friction forces in the flow that takes place over fixed walls or in the flow, which takes place in layers with different velocities.

A typical feature of turbulent motion is that the velocity and pressure at a fixed point in space do not remain constant with time.

In turbulent flow, the variables are usually divided in one time-averaged part,  $\bar{u}$ , time independent part and one fluctuating part,  $u'$ , see equation 3.1.

$$u = \bar{u} + u' \quad (3.1)$$

The variables are decomposed, mainly, from 2 reasons:

- One reason is that when measuring flow quantities, the main interest is reported to the mean values rather than the time histories;
- Another reason is that when solving the Navier-Stokes equations it would be required a fine grid to resolve all turbulent scales and a fine resolution in time.

Turbulent flow has a number of characteristics:

1. **Irregularity.** Turbulent flow is irregular, random as well as chaotic. Even though turbulence is chaotic it is deterministic and is described by the Navier-Stokes equations. Probabilistic laws may describe turbulence and they allow the evaluation of mean values for different parameters like velocity, pressure, and temperature.
2. **Diffusivity.** In turbulent flow the diffusivity increases. The increased diffusivity increases also the wall shear stress in internal flows.
3. **Large Reynolds numbers.** Turbulent flow occurs at high Reynolds number.

4. **Three-dimensional.** Turbulent flow is always three-dimensional. Meanwhile, when the equations are time averaged, the flow will be considered as two-dimensional.
5. **Dissipation.** In turbulent flow, the kinetic energy in the small eddies is transformed into internal energy.
6. **Continuous.** It is considered that the turbulent flow is continuous.

The interaction between vorticity and velocity gradients is an essential element for creating and maintaining turbulence. Disturbances are amplified and they are turned into three-dimensional, chaotic, random fluctuations, with another words, turbulent flow by interaction between the vorticity vector and the velocity gradients. There can be identified 2 phenomena in this interaction process: vortex stretching and vortex tilting. Once this process has started it continues, because vorticity generated by vortex stretching and vortex tilting interacts with the velocity field and creates further vorticity and so on. The vorticity and velocity field becomes chaotic and random, which means that the turbulence has been created.

### 3.1.2 Boundary layer definition

The layer moving next to a solid object placed in the water, in which the velocity of the flow modifies from zero value for the surface of the object to the value corresponding to the outside flow and in which it occurs the intense manifestations of the friction forces is called *the boundary layer*.

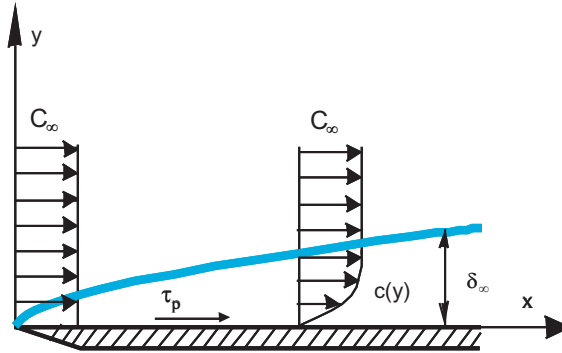


Figure 3.1: Boundary layer illustration

### 3.1.3 Boundary layer on a flat plate

Boundary layer begins as a laminar flow with zero thickness at the leading edge of flat plate or finite thickness on a blunt object. After some distance, downstream, the laminar flow undergoes transition to turbulent flow, see figure 3.2. The simplest case of boundary layer study is the boundary layer developed on a flat plate, illustrated in figure 3.1. By comparison, the flow in the pipes and drains with a given pressure gradient, the main differences are:



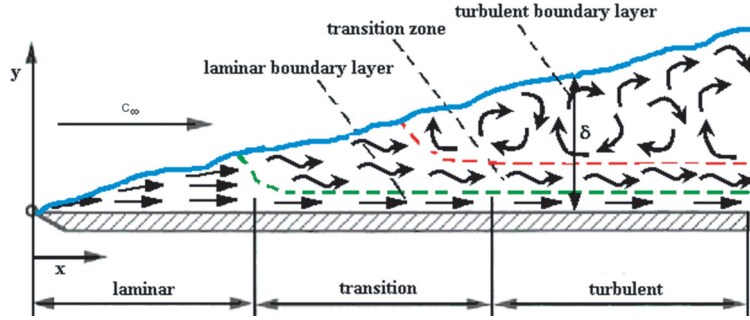


Figure 3.2: Boundary layer on a flat plate

- the boundary layer develops continuously in the flow direction; its thickness,  $\delta(x)$  increases with  $x$ ;
- the wall shear-stress variation,  $\tau_p(x)$ , is unknown;
- the exterior part of the flow is made by intermittent motions, turbulent or not;

In this layer, the suddenly increase of the tangential velocity determines great values for the velocity gradient and, as a consequence, the shear-stresses reach to considerable values, so the friction forces have great values, comparable with the inertial forces. Outside this boundary layer, the velocity gradient has a smaller value and the shear stress can be neglected, so the friction forces become negligible related to the inertial forces.

The main characteristic of the boundary layer is its thickness, which is defined, conventionally, as being the distance  $\delta$  from the body's surface, measured along the perpendicular to this surface, where the flow reaches around 99 % from the exterior potential flow velocity; it is estimated by relation 3.2.

$$\delta = y|_{c=0.99C_\infty} \quad (3.2)$$

The main direction of the flow is along the  $x$  axis, with the velocity outside of the boundary layer,  $c_0(x)$ . Statistics fluctuate with  $y$  and is independent of  $z$ , so that the velocity depends both on  $x$  and  $y$ .

Starting from Bernoulli's equation, see equation 3.3, and by projecting it on  $x$  direction it is obtained relation 3.4.

$$-p_0 + \frac{1}{2}\rho[c_0(x)]^2 = \text{cst} \quad (3.3)$$

$$-\frac{dp_0}{dx} = \rho c_0 \frac{dc_0}{dx} \quad (3.4)$$

This relation evidences 2 different cases of boundary layer:

- $\frac{dc_0}{dx} > 0 \implies \frac{dp_0}{dx} < 0$ , negative or favorable pressure gradient;
- $\frac{dc_0}{dx} < 0 \implies \frac{dp_0}{dx} > 0$ , adverse pressure gradient.

The adverse pressure gradient leads to the unsteady separations of the boundary layer from the surface; the 2 cases will be detailed further.

For the present study, as water is the fluid used, there are made some simplified assumptions:

- incompressible fluid;
- Newtonian fluid.

The boundary layer equation is obtain from the continuity equation and the Navier-Stokes equations system:

$$\begin{cases} \frac{\partial c_x}{\partial x} + \frac{\partial c_y}{\partial y} = 0 \\ \frac{\partial c_x}{\partial t} + c_x \cdot \frac{\partial c_x}{\partial x} + c_y \cdot \frac{\partial c_x}{\partial y} = -\frac{1}{\rho} \frac{\partial p}{\partial x} + \nu \left( \frac{\partial^2 c_x}{\partial y^2} + \frac{\partial^2 c_y}{\partial y^2} \right) \end{cases} \quad (3.5)$$

Considering the boundary layer thickness,  $\delta$ , very small and making the approximation of the size for the equations terms, the system of equations 3.5, which characterize the flow in the boundary layer becomes:

$$\begin{cases} \frac{\partial c_x}{\partial x} + \frac{\partial c_y}{\partial y} = 0 \\ c_x \cdot \frac{\partial c_x}{\partial x} + c_y \cdot \frac{\partial c_x}{\partial y} = -\frac{1}{\rho} \frac{\partial p}{\partial x} + \nu \frac{\partial^2 c_x}{\partial y^2} \end{cases} \quad (3.6)$$

Furthermore, as the purpose is to study the flow in the cone, both at the inlet and at the outlet, and knowing that the flow in this part of a hydraulic turbine is turbulent and three-dimensional, the system of equations 3.6 has to be transposed corresponding for the turbulent flow case.

In turbulent flow, every flow parameter is considered to be made up of a temporal part and a fluctuating part:

$$c = c' + \bar{c}, \quad (3.7)$$

where  $c'$  represents the fluctuating part of the parameter  $c$  and  $\bar{c}$  represents the mean value of  $c$ .

Taking into account the relation 3.7 in the system of equations describing the flow in the boundary layer, equation 3.6, it is obtained the system of equations which characterize the boundary layer in a stationary flow, see equations 3.8.

$$\begin{cases} \frac{\partial c_x}{\partial x} + \frac{\partial c_y}{\partial y} = 0 \\ \rho \frac{\partial c_x}{\partial t} + \rho c_x \cdot \frac{\partial c_x}{\partial x} + \rho c_y \cdot \frac{\partial c_x}{\partial y} = -\frac{\partial p}{\partial x} + \mu \nabla^2 c + \rho f_x \end{cases} \quad (3.8)$$

Assuming that:

- flow is steady:  $c(t) = 0$ ,
- fluid is incompressible:  $\rho = cst$ ,

there is obtained the momentum equation for the turbulent flow, see relation 3.9.

$$\rho \bar{c}_x \cdot \frac{\partial \bar{c}_x}{\partial x} + \rho \bar{c}_y \cdot \frac{\partial \bar{c}_x}{\partial y} = -\frac{\partial p}{\partial x} + \mu \frac{\partial^2 \bar{c}_x}{\partial y^2} - \rho \frac{\partial}{\partial y} (\overline{c'_x c'_y}) \quad (3.9)$$

As the fluid is considered a Newtonian one, Newton's relation regarding the wall shear stress is valid, see relation 3.10:

$$\tau = \mu \frac{c}{L} \quad (3.10)$$

where  $\mu$  represents the dynamic viscosity,  $c$  is the flow characteristic velocity and  $L$  is the characteristic length of the flow.

If the last two terms of the momentum equation 3.9 are written like  $\frac{\partial}{\partial y} [\mu \frac{\partial \bar{c}_x}{\partial y} - \rho (\overline{c'_x c'_y})]$ , it can be noticed that the fluctuations produce a shear stress evidenced by the term  $\mu \frac{\partial \bar{c}_x}{\partial y}$ .

It can be seen that, in accordance with the boundary layer theory, and by considering  $c$ , the local velocity and  $y$ , the distance from the wall in the perpendicular direction to this wall, the wall shear stress is described by the relation 3.11.

$$\tau_p = \mu \frac{\partial \bar{c}}{\partial y} \Big|_{y=0} \quad (3.11)$$

In the turbulent flows, the flow in the boundary layer is laminar for small distances and then it goes through a transition zone, for a specified critical velocity, reaching into a turbulent flow, see figure 3.3.

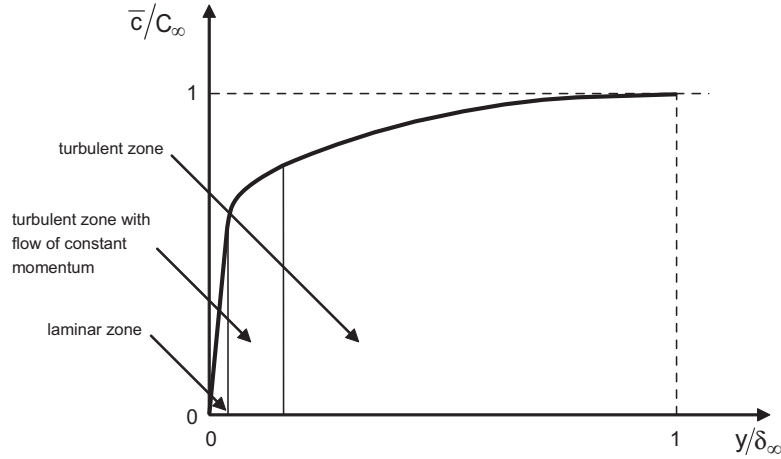


Figure 3.3: The three zones of the boundary layer on a flat plate

### 1. Inner layer

The length of the inner layer depends on the range of the turbulence in the exterior flow, on the roughness of the surface and on the place of the flat plane in a configuration of confuzor or diffuser.

*Observation.* For the present case, it is studied the flow at the runner outlet, which can be considered as a distributor, so that the flow velocity decreases downstream.

In this region, because the thickness of the layer is small enough, it can be assumed that the total friction is, approximate, equal with wall shear-stress, see relation 3.12.

$$\tau = \mu \frac{\partial \bar{c}_x}{\partial y} - \rho c'_x c'_y \equiv \tau_p \quad (3.12)$$

In the inner layer, the *law of the wall* is described by equation 3.13

$$\frac{c}{c_\tau} = f\left(\frac{c_\tau y}{\nu}\right), \quad (3.13)$$

where  $f$  represents an universal function.

It can be remarked that the behavior of the velocity near the wall is independent on the conditions of the flow far from the wall. The inner layer corresponds roughly to:

$$y/\delta < 0.1. \quad (3.14)$$

### Viscous sublayer

Meanwhile, very close to the wall, the turbulent fluctuations  $c'_x$ ,  $c'_y$  and the mean values  $\bar{c}_x$  and  $\bar{c}_y$  tend to zero, the wall shear stress being almost entirely viscous.

By noting  $c^+ = \frac{\bar{c}}{c_\tau}$  and  $y^+ = \frac{y c_\tau}{\nu}$ , in which  $c_\tau$  represents the friction velocity and it is defined as  $c_\tau = \sqrt{\frac{\tau_p}{\rho}}$  it is obtained the relation 3.15.

$$c^+ = f(y^+) \quad (3.15)$$

Considering  $y \rightarrow 0$ , the relation 3.12 becomes:

$$\tau_p = \mu \frac{\partial \bar{c}}{\partial y}, \quad (3.16)$$

so that  $c = \frac{\tau_p}{\mu} y$  and finally, the flow in this sublayer is characterize by the relation 3.17.

$$c^+ = y^+ \quad (3.17)$$

From experiences, see Ryhming [1985], this equation is available for:

$$y^+ < 5. \quad (3.18)$$

### 2. Overlap layer

In this region, takes place a suddenly increase of the boundary layer thickness,  $\delta$ , and a suddenly change of the velocity; the velocities increase very fast near the wall and they have the tendency to become uniform along the normal to the wall.

In this zone, the velocity profile is completely determined by:

$$c = c(y, \tau_p, \rho). \quad (3.19)$$

As this region is also situated close to the wall, it is considered that the equation 3.20 determines the velocity distribution.

$$c^+ = f(y^+) \quad (3.20)$$

The motion quantity transfer is produced, mainly, by turbulence, in this region.

$$\tau_t = -\rho \overline{c'_x c'_y} = \text{cst} \quad (3.21)$$

The total shear stress in this region, is defined by relation 3.22.

$$\tau = \mu \frac{\partial \overline{c_x}}{\partial y} - \rho \overline{c'_x c'_y} \quad (3.22)$$

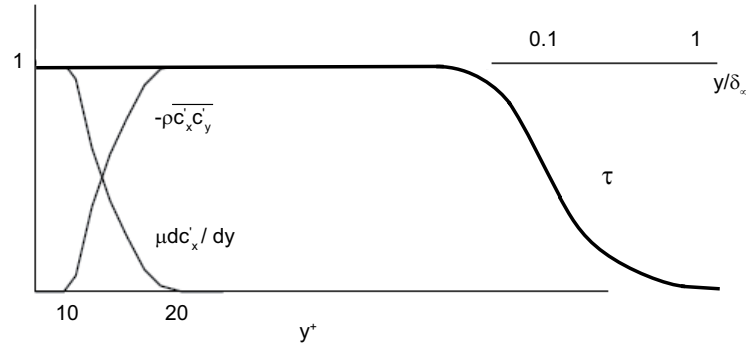


Figure 3.4: Shear stress distribution in turbulent boundary layer, with the wall distance: near the wall and total

As it is shown in figure 3.4, the two terms  $\mu \frac{\partial \overline{c_x}}{\partial y}$  and  $-\rho \overline{c'_x c'_y}$ , have a very fast variation near the wall, so that it can be considered that  $\tau$  is constant and equal with  $\tau_p$ , for  $0 < y/\delta_\infty < 0.05$ . In this way, far from the wall, the velocity increases very fast and then it flattened, see figure 3.5.

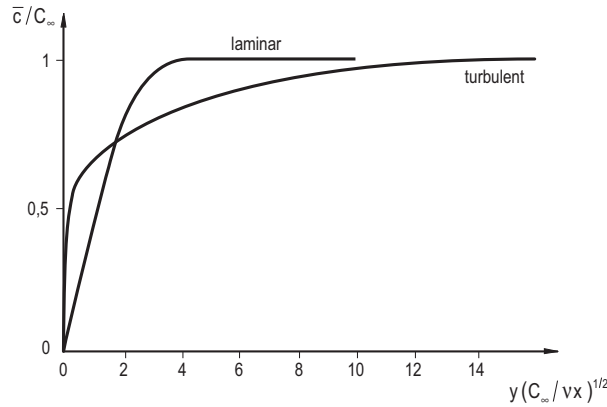


Figure 3.5: Comparison between a laminar and a turbulent velocity profile

In this region of the boundary layer, by replacing the velocity with the velocity gradient,  $c \rightarrow \frac{dc}{dy}$ , the velocity profile will be described by relation 3.23.

$$\frac{dc}{dy} = \frac{dc}{dy}(y, \tau_p, \rho) \quad (3.23)$$

There can be made the following assumptions: the fluctuating parts,  $c'_x$  and  $c'_y$ , must have the same order, so that the turbulent shear stress can be written as relation 3.24.

$$\tau_t = \rho l^2 \left( \frac{d\bar{c}}{dy} \right)^2, \quad (3.24)$$

where  $l$  represents the characteristic length and defined as  $l = \chi y$  when it is unknown, and  $\chi$  represents the Von Karman constant.

In this way, the wall shear stress becomes:

$$\tau_p = \rho \chi^2 y^2 \left( \frac{d\bar{c}}{dy} \right)^2, \quad (3.25)$$

finally, obtaining the differential equation 3.26.

$$\frac{d\bar{c}}{dy} y \tau_p^{1/2} \rho^{-1/2} = \frac{1}{\chi} = cst \quad (3.26)$$

Considering the dimensionless parameters,  $c^+$  and  $y^+$ , defined in the same way as for the laminar boundary layer, the relation 3.26 can be simplified, becoming the differential equation 3.27:

$$dc^+ = \frac{1}{\chi} \frac{dy^+}{y^+} \quad (3.27)$$

The velocity law in this region of the boundary layer is called *the log-law velocity profile* and it is described by relation 3.28.

$$c^+ = \frac{1}{\chi} \ln y^+ + C, \quad (3.28)$$

where  $C$  is the integration constant and it is determined by experiments, see Cousteix [1989]. This equation is available for

$$30 < y^+ < 500, \quad (3.29)$$

the value  $y^+ = 500$  corresponding to 5 – 15% of the turbulent boundary layer thickness.

### 3. Outer layer

In this region the velocity law is complex, see relation 3.30 and it is called *the over-drawn speed law*; it is difficult to provide, from the theoretical point of view, the velocity distribution. The turbulent zone concerns the other 85 to 95% from the boundary layer thickness. In this layer, one has *the velocity-defect law*:

$$\frac{C_\infty - c}{c_\tau} = \Phi\left(\frac{y}{\delta}\right) \quad (3.30)$$

$\Phi$  is a function depending on many factors like Reynolds number, pressure gradient.

The general velocity distribution for the turbulent boundary layer is illustrated in figure 3.6.

Due to its complexity and difficulty, this region can't be used for the experimental evaluation of the wall shear stress, for the studied case.

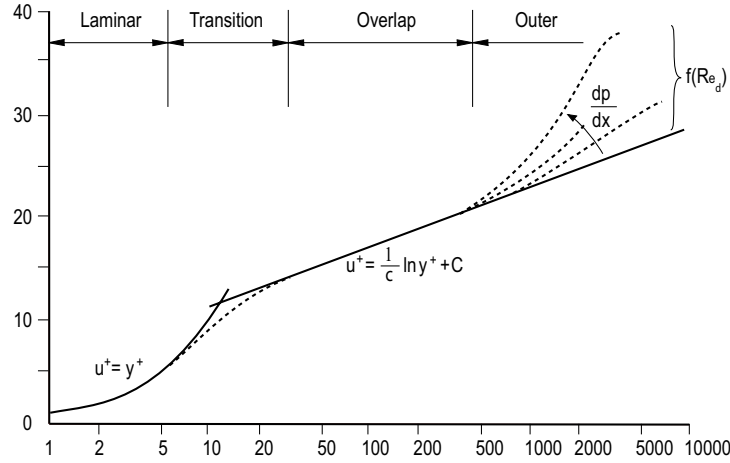


Figure 3.6: The distribution  $c^+(y^+)$  in the turbulent boundary layer

## 3.2 HEAT TRANSFER IN THE BOUNDARY LAYER

The presence of high velocity gradients in the boundary layer lead to very large temperature differences, so that, the temperature effect must be taken into account. In the same way, when a liquid of non-uniform temperature is caused to move turbulently, it is found that the turbulent mixing motion creates in it, turbulent fluctuations.

The fluctuating temperature may be represented in analogy with the equation for the fluctuating velocity, as a sum of a temporal average,  $\bar{T}$ , and a fluctuation,  $T'$ , see relation 3.31.

$$T = \bar{T} + T' \quad (3.31)$$

As shown in the part 3.1.3, the boundary layer may be divided, mainly, in 2 parts:

- Laminar boundary layer;
- Turbulent boundary layer.

There is studied the heat transfer in both parts, separately, because the temperature distribution is different in the laminar zone, than the one in the the turbulent zone, as the figure 3.7 shows.

### 3.2.1 Laminar boundary layer

In the laminar part of the boundary layer the molecules are moving in layers, following strictly the flow direction from the outside of the boundary layer. Here the heat transfer is realized through the friction of the molecules between the layers moving one next to each other.

The heat transfer is realized by *conduction* and it follows the Fourier law, meaning that the heat flux in the perpendicular direction to the flat plate through the surface unit is proportional with the temperature gradient, see relation 3.32:

$$\dot{q} = -\lambda \frac{dT}{dy} = -\rho c_p \Lambda \frac{dT}{dy}, \quad (3.32)$$

where:

- $\dot{q}$  - heat flux;
- $\lambda$  - thermal conductivity;
- $\frac{dT}{dy}$  - temperature gradient;
- $c_p$  - specific heat at constant pressure;
- $\Lambda$  - thermal diffusion coefficient.

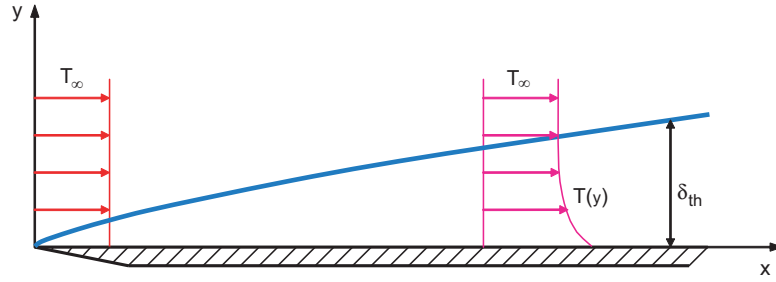


Figure 3.7: Temperature distribution in the boundary layer, on a heated flat plate

For the laminar boundary layer it is defined Prandtl number, which represents the ratio between the diffusion of the movement quantity and the thermal diffusion, see relation 3.33.

$$Pr = \frac{\nu}{\Lambda} \quad (3.33)$$

In the same time it expresses the ratio between the hydrodynamic thickness,  $\delta$ , and the thermal thickness,  $\delta_{th}$  of the boundary layer, see relation 3.34.

$$Pr^{1/3} = \frac{\delta}{\delta_{th}} \quad (3.34)$$

In this part of the boundary layer, the shear stress is given by the relation 3.35.

$$\tau_l = \mu \frac{dc}{dy} = \rho \nu \frac{dc}{dy} \quad (3.35)$$

The relationship between the heat transfer and the shear stress, for a flat plate, it is found by writing the Blasius solution for the boundary layer, see equation 3.36.

$$\frac{d^2(\frac{c}{C_\infty})}{d\eta^2} + 0.5f(\eta)\frac{d(\frac{c}{C_\infty})}{d\eta} = 0 \quad (3.36)$$

The boundary conditions are:

$$\frac{c(0)}{C_\infty} = 0; \quad (3.37)$$



$$\frac{c(\infty)}{C_\infty} = 1, \quad (3.38)$$

and  $\eta = y\sqrt{\frac{C_\infty}{\nu x}} = \frac{y}{x}Re^{1/2}$ .

By defining the dimensionless temperature, relation 3.39, where  $T_s$  is the temperature of the wall surface, the equation 3.36 can be rewritten as equation 3.40.

$$T^* = \frac{T - T_s}{T_\infty - T_s} \quad (3.39)$$

$$\frac{d^2 T^*}{d\eta^2} + 0.5f(\eta)Pr \frac{dT^*}{d\eta} = 0 \quad (3.40)$$

The boundary conditions can be rewritten with the new variable, see relations 3.41 and 3.43.

$$T^*(0) = 0 \quad (3.41)$$

$$T^*(\infty) = 1 \quad (3.42)$$

For water,  $Pr \approx 1$ , and for this value the relations 3.36 and 3.40 are similar. This implies:

$$T^* = \frac{c}{C_\infty} \quad (3.43)$$

By derivation with  $y$ , it is obtained the relation 3.44, and by taking into account the heat transfer definition,  $\dot{q}$ , relation 3.32 and the shear stress, for laminar flow,  $\tau$ , relation 3.35, it is obtained the relationship between those 2 parameters, see equation 3.45.

$$\frac{1}{T_\infty - T_s} \frac{\partial T}{\partial y} = \frac{1}{C_\infty \frac{\partial c}{\partial y}} \quad (3.44)$$

$$\frac{\dot{q}}{\tau} = -c_p \frac{T_\infty - T_s}{C_\infty} = \text{cst} \quad (3.45)$$

*Conclusion.* In the laminar boundary layer, for  $Pr = 1$ , the ratio between the heat transfer and the shear stress is constant.

### 3.2.2 Turbulent boundary layer

In the turbulent part of the boundary layer, the movement of the molecules takes no more place in the layers, but it leads to an exchange of movement quantity and an additional heat transfer. The turbulent heat transfer, due to the macroscopic fluctuations is illustrated by the relation 3.46:

$$\dot{q}_t = -\rho c_p \overline{c'_x T'} = -\rho c_p \varepsilon_h \frac{\partial \overline{T}}{\partial y}, \quad (3.46)$$

where  $\varepsilon_h$  is the turbulent thermal diffusion coefficient defined by relation 3.47.

$$\varepsilon_h = \frac{\overline{c'_x T'}}{\frac{\partial \overline{T}}{\partial y}} \quad (3.47)$$

It is defined, by similarity, with the laminar boundary layer, a turbulent shear stress proportional with the fluctuating velocities:

$$\tau_t = -\rho \overline{c'_x c'_y} = \rho \varepsilon \frac{\partial \overline{c_x}}{\partial y} \quad (3.48)$$

where  $\varepsilon$  is the turbulent viscosity defined by relation 3.51.

$$\varepsilon = \frac{\overline{c'_x c'_y}}{\frac{\partial \overline{c_x}}{\partial y}} \quad (3.49)$$

Furthermore, in the turbulent boundary layer it can be defined:

- the apparent shear stress:

$$\tau = \tau_l + \tau_t = \rho(\nu + \varepsilon) \frac{\partial \overline{c_x}}{\partial y} \quad (3.50)$$

- the apparent heat transfer:

$$\dot{q} = \dot{q}_l + \dot{q}_t = -\rho c_p (\Lambda + \varepsilon_h) \frac{\partial \overline{T}}{\partial y} \quad (3.51)$$

For the turbulent boundary layer, it is also defined, by analogy with the laminar boundary layer, a turbulent Prandtl number, which depends on the  $\varepsilon$  and  $\varepsilon_h$  distribution in the boundary layer, see relation 3.52.

$$Pr_t = \frac{\varepsilon}{\varepsilon_h} \quad (3.52)$$

#### Observations

1. The turbulent thermal diffusion coefficient and the turbulent viscosity depend on the temperature gradient,  $\frac{\partial \overline{T}}{\partial y}$ , respectively on the velocity gradient,  $\frac{\partial \overline{c_x}}{\partial y}$ ; they are independent on the physical properties of the fluid.
2. For the similitude reasons between the heat transfer and the movement quantity transfer it is considered  $Pr_t = 1$ .

In this part of the boundary layer, for finding the relationship between the heat transfer and the shear stress, for a flat plate, the Reynolds' analogy for the turbulent convection, which neglect the laminar and the transient zones of the turbulent boundary layer, has to be considered, obtaining the relationship 3.53.

$$\frac{\dot{q}}{\tau} = -c_p \frac{\varepsilon_h}{\varepsilon} \frac{\partial \overline{T}}{\partial y} = -\frac{c_p}{Pr_t} \frac{\partial \overline{T}}{\partial y} \quad (3.53)$$

Using Reynolds' similitude between the laminar and the turbulent boundary layers and considering  $Pr_t = 1$  it is found that the ratio between the heat transfer and the shear stress is also constant, see relation 3.54, for the turbulent case, in the same way as for the laminar boundary layer.

$$\frac{\dot{q}}{\tau} = -c_p \frac{T_\infty - T_s}{C_\infty} = \text{cst} \quad (3.54)$$

### 3.3 TECHNIQUES USED FOR WALL SHEAR-STRESS MEASUREMENTS

Several techniques for measuring wall shear stress have been developed and they are used for exploring the boundary layer, nowadays, in the world, depending on the application under consideration.

The required spatial and temporal resolutions are specific for each application and environment. For laminar flows, the sensors must be capable to evaluate the time-averaged shear stress, while in turbulent flows, both the mean and its fluctuating components are required.

An attempt to classify the techniques available for wall shear stress measurements was made by Haritonidis [1989], depending upon whether the wall shear stress is measured directly or is inferred from other measured properties: the small group of direct methods - floating element method and oil film interferometry - and the larger group of indirect methods which must be calibrated. All these techniques are summarized together with their applications, in table 3.1.

Author	Flow type	Direct techniques		Indirect techniques				
		Floating element balance	Oil-film interferometry	Preston tube	Surface fence	Wall pulsed wire	Hot-wire	Wall hot-film
Ruderich and Fernholz [1986]	Separation and recovery regions downstream of a normal plate with a splitter plate, adverse pressure gradient	-	-	✓	✓	✓	-	✓
Dengel et al. [1987]	Turbulent boundary layer, adverse pressure gradient	-	-	✓	✓	✓	-	✓
Dengel et al. [1987]	Separation and recovery regions downstream of a normal plate with a splitter plate, adverse pressure gradient	-	-	✓	✓	✓	-	✓
Dengel and Fernholz [1989, 1990]	Turbulent boundary layer with and without reverse flow, adverse pressure gradient	-	-	✓	✓	✓	-	-
Gasser [1992], Gasser et al. [1993]	Turbulent boundary layer with and without reverse flow, adverse pressure gradient	✓	-	✓	✓	✓	-	-
Janke [1993]	Separation and recovery regions downstream of a backwards-facing step, adverse pressure gradient	-	✓	-	✓	✓	✓	-
Warnack [1996]	Turbulent boundary layer, favorable pressure gradient	-	✓	✓	✓	-	✓	-

Table 3.1: Wall shear-stress technologies and their applications

A comparison between 4 wall shear-stress measuring techniques, namely wall hot-wire, wall pulsed-wire, oil-film interferometry and surface fence in turbulent wall-bounded shear flows was presented, see Fernholz et al. [1996]. They showed that oil-film interferometry and wall hot-wires may safely be applied in attached boundary layers and wall bounded shear layers with variable pressure gradients, while for wall hot-wires no reversal flow is required. Moreover, in highly accelerated boundary layers the surface-fence can not

be used and in flows where direction reverses Preston tubes must not be used. They concluded also that the wall-pulsed wire, the oil-film and the surface-fence techniques may be used in such flows with small deviations occurring for the surface-fence measurements close to separation and re-attachment due to probe small asymmetries.

The direct techniques are based on the mechanical evaluation of the force applied on an element with a floating wall. Meanwhile, the indirect techniques are based on the analogy between the wall shear-stress and other physical parameters.

Since there is a large number of different methods, it is beyond the scope of this work to review each technique. A trend common to all measurements and methods can, however, be highlighted. Since the mid 1950s, the evolution of the probes used has been directed towards utilizing smaller and smaller sensors to improve the accuracy, flexibility and resolution. There are several review papers that describe shear stress sensors and discuss in detail the merits and drawbacks of the methods used in a vast variety of flow situations. To cite a few, Winter [1977] gives a comprehensive review of available conventional methods and a good discussion of measurements in turbulent flows. Haritonidis [1989] summarizes conventional methods and introduces the first micromachined wall shear stress sensor. Hakkinen [1991] lists the merits and drawbacks of conventional techniques. Most recently, Hanratty and Campbell [1996] discuss the relevant experimental issues associated with the use of various wall shear stress sensors.

### 3.3.1 Direct techniques

Direct techniques for the wall shear-stress measurements rely on detection of the total amount of viscous drag experienced by a surface-mounted force balance. The force needed to maintain the floating element in equilibrium is a measure of the wall shearing stress. This technology implies a large area and a very sensitive technique to determine small forces. It allows a very accurate measurement of the steady wall shear-stress values, about  $\pm 2\%$ . The system frequency response is limited by the floating element size.

#### Floating element balance

The floating element balance, illustrated in figure 3.8, is one of the old device for wall shear-stress measurements implying a large area. It's a very sensitive technique for small forces determination.

Kempf [1929] used such a floating element balance for subsonic flow and, as the area of the balance could be reduced due to the high wall shear-stress, this technique could be applied in compressible boundary layers. An detailed survey on the design and applications of these balances was provided by Winter [1977], while a list of test cases in compressible boundary layers is presented by Fernholz and Finley [1977], Fernholz and Finley [1981].

For subsonic flows there are two more recent developments of floating element balances: so called "Bechert balances", designed mainly to compare the skin shear-stress of aerodynamically smooth and riblet (small-ribbed) surfaces, see Bechert et al. [1985] and Bechert et al. [1992], and balances developed by Dickinson [1965], which can be used only in flows with zero pressure gradient

The force measurement can be obtained by gauges or piezo-resistive elements. For improving the frequency response of the system, miniaturization of these types of sensors

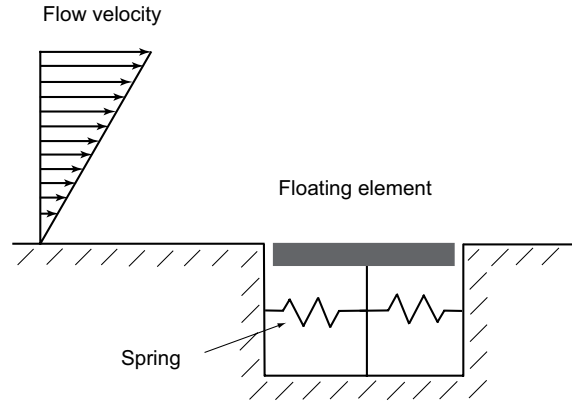


Figure 3.8: Floating element technique

are performed, see Huang et al. [2000], Jiang et al. [1996] and Löfdahl and Gad-el Hak [1999].

The main drawback of the floating-element sensors is that they have poor spatial and temporal resolution for low-magnitude shear stress measurement, offers a shear-stress value, integrated over a larger or a smaller area and fails in providing exact pointwise measurements. To obtain a measurable output signal in a low-shear environment, a large sensing element is required, leading to a loss of spatial resolution. Hence it is not possible to simultaneously achieve a high sensitivity and high bandwidth.

### Oil-film interferometry

This technique is based on the measurement of a oil drop's deformation, which is deposited on the test facility flow, see figure 3.9. The oil film is developed by drop's spreading due to the shearing. The thinning ratio of the oil film measured by interferometry is determined by interference fringes produced by a monochromatic light source.

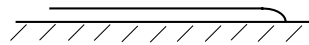


Figure 3.9: Oil-film interferometry technique

A first attempt of wall shear-stress evaluation from the movement of interference fringes of a thin oil film was realized by Tanner and Blows [1986]. A complete theory of the application of this technique have been described by Janke [1993].

As no calibration and no complex instrumentation for implementing it to the wall are needed - requiring only an optic access to the measurement zone-, this technique is attractive. Moreover, it does not require any assumptions concerning the flow field.

An accurate measurement of the mean wall shear-stress is acquired using this technique, being capable, in the same time, to measure reverse flow. The accuracy of the oil film method can be better, than within  $\pm 4\%$ . Meanwhile, it is easy to apply and needs little instrumentation. Thus, a precise knowledge of the oil's viscosity is required.

The main disadvantages of this method are:

- measuring time is relatively high, between 10 minutes and 3 hours are required, depending on the oil viscosity and wall shear-stress magnitude;
- oil's film speed should not be too high;
- a minimum wait time, 1-2 minutes, is necessary to obtain a steady state.

### 3.3.2 Indirect techniques

In indirect techniques, the wall shear stress is extracted from other measured physical parameters, like pressure, wall temperature, that are related to the shear stress.

#### Preston tube

For turbulent boundary layers, one of the most commonly used instrument for wall shear-stress measurements is the Preston tube illustrated in figure 3.10. The validity of this measuring technique depends on the validity of the logarithmic law of the wall.

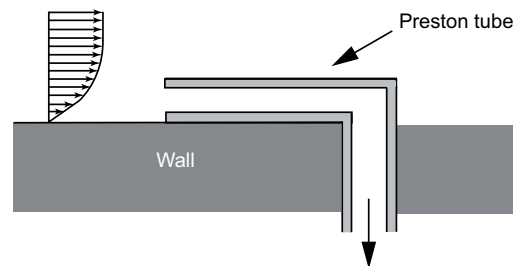


Figure 3.10: Preston tube technique

The dimensionless diameter must lie in the logarithmic region for calibration curves of Patel [1965], or Head and Vasanta Ram [1971] use, while user-friendly calibration curves were suggested by Bechert [1995] and Zurfluh [1984].

The accuracy of the Preston tube method is about  $\pm 3\%$  and less for adverse pressure gradients, see Patel [1965] and Hirt and Thomann [1986]. A complete presentation of Preston tube applications for compressible boundary layers is given by Finley and Gaudet [1995].

The main disadvantage of this technique, is that it allows only the mean wall shear stress value measurement.

#### Surface fence

Surface fence method has the advantage that it's easy to build and it needs only a precise manometer for pressure difference reading, between the upstream and downstream of the fence, see figure 3.11.

The surface fence or sublayer fence's first application for measuring the magnitude and direction of the wall shear-stress was carried out by Konstantinov and Dragnysh [1960].

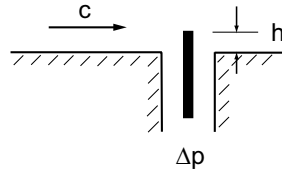


Figure 3.11: Surface fence technique

Head and Rechenberg [1962] and Vagt and Fernholz [1973] describe in detail the use of this technique.

Some constraints are required for its geometry, namely its height should not to exceed a value, corresponding to  $y^+ = 5$ , for measuring within the viscous sublayer and becoming in this way independent of the validity of the logarithmic law of the wall.

The accuracy of a surface fence, used together with the Preston tube as a calibration device, is about  $\pm 4\%$  and it may decrease if the turbulence structure of the studied flow differs strongly from the turbulence structure of the calibration flow.

Meanwhile one of its disadvantages is that it can be used only for the Reynolds numbers between 0.25 and 25. In the same time, due to the small size of the fence and the manufacturing tolerances, a calibration is needed for each fence. Moreover, this technique together with the oil interferometry method have poor resolution.

### Wall pulsed wire

Wall pulsed wire consists in 3 wires parallel mounted in a plane parallel to the wall, in the way illustrated in figure 3.12.

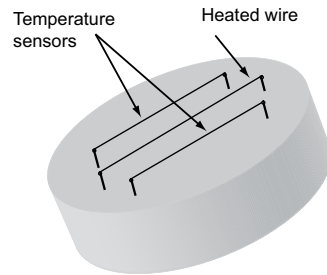


Figure 3.12: Wall pulsed wire technique

The central wire is heated by a very short electrical pulse, which generates a heat tracer. The 2 sensors are operated as temperature sensors and note the arrival of the heat tracer. The flight time of the heat tracer is a measure of the instantaneous wall shear-stress value.

The principle of the wall pulsed-wire was described in detail by Bradbury and Castro [1971], while its first application was made by Ginder and Bradbury [1973].

This technique is capable of measuring the instantaneous wall shear stress in highly turbulent flows with flow reversal, in the same way as oil-film interferometry or surface fences which, otherwise, have poor temporal resolution. The wall pulsed wire is usually calibrated against a Preston tube.

The wall pulsed-wire probe is not well suited to obtain spectra due to its low sampling rate, about 40 Hz. The combined errors of calibration and time of flight measurement, the resolution of the time of flight counter having an estimated error for high wall shear-stress values, typically 1% can lead to an overall error of about  $\pm 4\%$ .

Main disadvantage of this technique is that the range of the wall shear stress covered by the probe is limited by requirements that the probe should not extend the viscous sublayer. The range of wall shear-stress of such a probe lies within  $\pm 2Pa$ . Another disadvantage is that the thick pulsed wire gives a strong signal, producing, in the same time, larger wake.

### Hot-wire

This indirect technique consists in measuring the velocity gradient in a boundary layer very close to the wall. Shear stress is determined by applying Newton's law which links the flow deformation ratio and the shear stress. Wall shear-stress values obtained are instantaneous local values.

For the flow velocity it is used, generally, the hot-wire anemometry. The evaluation of the instantaneous wall shear-stress values by hot-wire measurements of the velocity gradient in the viscous sublayer is strongly affected by the proximity of the wall, while the distortion of the temperature field affects only the sensitivity of the probe, and not its frequency response.

For correct results, the velocity measurement must be performed in the viscous sublayer of the boundary layer. Several studies were carried out for investigating the wall distance dependence of hot-wire probes, see Janke [1987]. It found a single relationship for correcting the mean flow velocity both in laminar and turbulent boundary layers, showing in this way that the mean response of the wall hot-wire probe is independent on the turbulence structure of the flow.

Wall hot-wire probes, illustrated in figure 3.13, are mainly used for their capacity of retaining their dynamic sensitivity and of their facility of adaptation for heat transfer effects to the wall, see Wagner [1991].

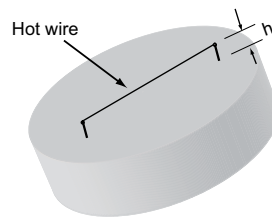


Figure 3.13: Wall hot-wire technique

Most common materials used for the wire are tungsten, platinum and their alloys. Tungsten wires, the most popular, are characterized by a high temperature coefficient of resistance, but their poor oxidation resistance makes them impossible of use at high temperatures in many gases. Platinum possesses a good temperature coefficient and a good oxidation resistance, but is very weak at high temperatures. The alloys have a good oxidation resistance, and they are more strength than platinum, but with a low



temperature coefficient of resistance. Usually, a thin platinum is coated for improving bond with the plated ends and the support needles.

The wall hot wire calibration must be performed in a fixed position, against another instrument measuring the local wall shear-stress. A first approach was carried out by Bradshaw and Gregory [1959], who determined only the mean wall shear-stress value, while Alfredsson et al. [1987] used this instrument in a turbulent zero-pressure-gradient boundary layer, evidencing that at high Reynolds numbers, acceptable results both for the mean and for the RMS value of the wall shear stress are obtained.

Meanwhile, the wall hot-wire probe sensitivity decreases with the Reynolds numbers decrease, leading to a limited maximum distance from the wall. This technique can be applied only for the cases where the viscous sublayers are thick enough, due to the difficulty of measuring the flow velocity by hot wire to a distance from the wall lower than 0.25mm.

The accuracy of the mean wall shear-stress value measured using this technique is about  $\pm 4\%$  for an accuracy of the calibration device of  $\pm 3\%$ .

Its main disadvantage is that it can't be mounted too close to the wall, for maintaining both its sensitivity and linearity.

### Wall hot-film

This technology is based on the analogy between the wall shear-stress and the heat transfer, see figure 3.14. It consists in measuring the convected heat flux induced by a heated film maintained at a constant temperature. Wall hot-film probes have been used to measure the instantaneous local wall shear stress.

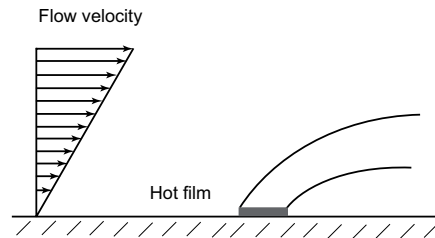


Figure 3.14: Wall hot-film technique

The wall-mounted hot films can be used for time-resolved measurements when the conductivity of the fluid is superior to the conductivity of the wall material. Its applications lay in water and oil, but they can't be used for air, as a reduced dynamic sensitivity of the hot film is recorded, see Tardu et al. [1991]. Although, this effect can be decreased by reducing the thermal conductivity of the substrate, Alfredsson et al. [1987] and Dengel et al. [1987] showed that RMS value of the wall shear stress recorded in turbulent boundary layers can be underestimated by up to 25%.

The analogy linking the heat transfer to the wall shear-stress is accepted only when the thermal boundary layer developed on the heated film is in the viscous sublayer,  $y^+ < 5$ . In this way, a restriction in the longitudinal dimension of the sensitive element is imposed.

Generally, the sensor is made up of a metallic film deposited on a substrate, which is heated by an electrical current and maintained at a constant temperature using an

electronic device containing a Wheatstone bridge, named hot-wire anemometry. Most films are made of platinum due to its good oxidation resistance and long-term stability.

By comparison with hot wires the wall hot-films offer, mainly, some advantages:

- *more design flexibility*, by availability of different surface shapes: wedge, conical, parabolic and flat,
- *reduced heat conduction* to the supports due to a low thermal conductivity of the substrate material,
- *better frequency response* because of the distribution on the surface of the sensor's sensitive part rather than including the wire's entire cross section,
- *easier to clean* due to the thin quartz coating on the surface,
- *more robust* for water applications.

Several difficulties are, although, encountered when using this technique:

- a considerable amount of the measured power is transformed in thermal conduction through the wall,
- flow temperature variation is influencing the measurements.

# Chapter 4

## WALL SHEAR-STRESS PROBE CALIBRATION

### 4.1 DEFINITION AND PRINCIPLE

Calibration means the act of checking or adjusting, by comparison with a standard, the accuracy of a measuring instrument. Hot-film probe calibration means the correlation of the output voltage induced by the hot-film resistance variation, with the wall shear stress.

The wall shear stress depends on the flow velocity, meaning that it also depends on the friction velocity directly connected to the boundary layer. The calibration is performed in a specific configuration, the simple case of a flat plate, where a zero-pressure gradient boundary layer is developed and well-known, presented in chapter 3.

### 4.2 EXPERIMENTAL SET-UP

#### 4.2.1 Hydrodynamic water tunnel

##### Main characteristics

The calibration of the hot-film probes is performed in the water tunnel of the Laboratory for Hydraulic Machines of Ecole Polytechnique Fédérale de Lausanne, see figure 4.1, having the main characteristics:

- the maximum rotation speed of the pump:  $n_p = 917 \text{ rot/min}$ ;
- the maximum discharge:  $Q_{max} = 0.452 \text{ m}^3/\text{s}$ ;
- the maximum velocity of the flow in the center section of the test section:  $c_{max} = 7.2 \text{ m/s}$ ;
- the maximum hydraulic power of the pump:  $P_h = 10.25 \text{ kW}$ ;
- the maximum power of the electrical machine:  $P = 32 \text{ kW}$ ;
- the area of the vein:  $A = 0.272^2 = 0.07398 \text{ m}^2$ ;

The LMH water tunnel is a single closed loop, closed test section, see figure 4.2. In this configuration, a maximum velocity of  $7.2 \text{ m/s}$  and a Reynolds number up to  $1.96 \cdot 10^6$  can be obtained in the center section of the test section.

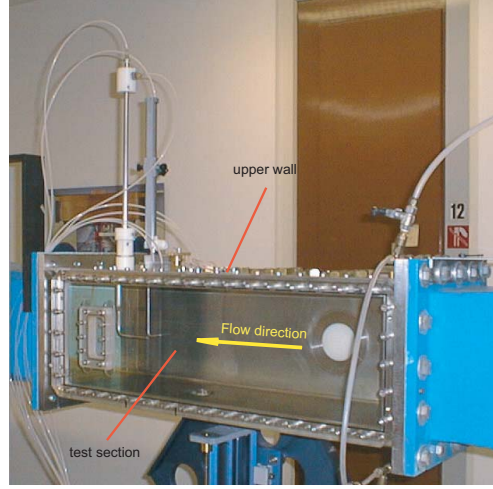


Figure 4.1: Test section area in the calibration tunnel

The calibration performance takes place in the test section, on the upper wall, by placing all the necessary instruments in the way shown in figure 4.3.

The measurement system, see figure 4.4 is made up by 2 different arms: one corresponding to the velocity acquisition and the second one corresponding to the hot-film probe output acquisition. The instrumentation used is detailed in annexe A.

### Experimental condition monitoring and control

The main parameters monitored and controlled during the calibration procedure, in the hydrodynamic water tunnel are:

1. flow velocity,
2. pressure,
3. water temperature.

The flow velocity is controlled in the calibration tunnel by controlling the pump speed, which is monitored on a tachometre, on the test stand. The pressure, in the tunnel, is controlled by keeping constant the level in the overflow, while the temperature water tunnel is surveyed with the thermometer placed next to the tachometre.

### Mean flow velocity variation with the pump speed

Before any hot-film probe calibration or measurement, there must be calibrated the water tunnel where the probe calibration will be performed, by obtaining the variation of the flow velocity in the tunnel with the pump speed. This relationship facilitates the way to obtain a desired flow velocity of the water in the tunnel. In this way it is established the pump speed, and using the relationship between those 2 parameters, it is evaluated the flow velocity, see equation 4.1.

$$C_{\infty} = 0.007927278 \cdot n_p - 0.016329334 \quad (4.1)$$

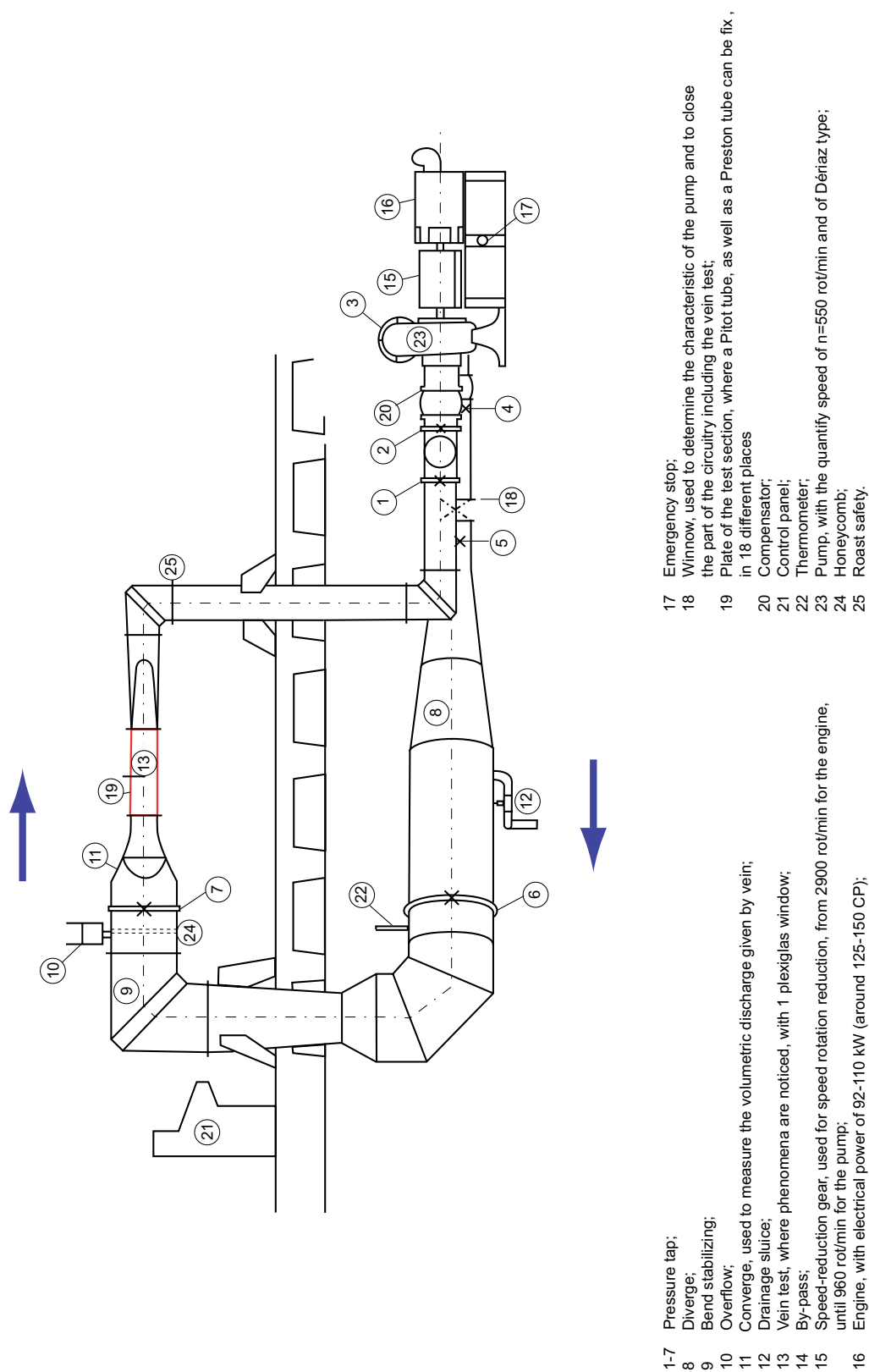


Figure 4.2: L.M.H. calibration tunnel

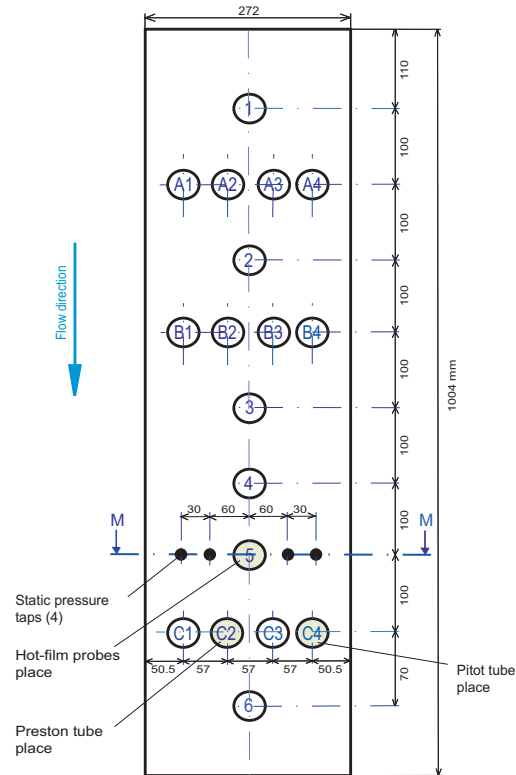


Figure 4.3: Tunnel upper wall design and the measurement instruments places

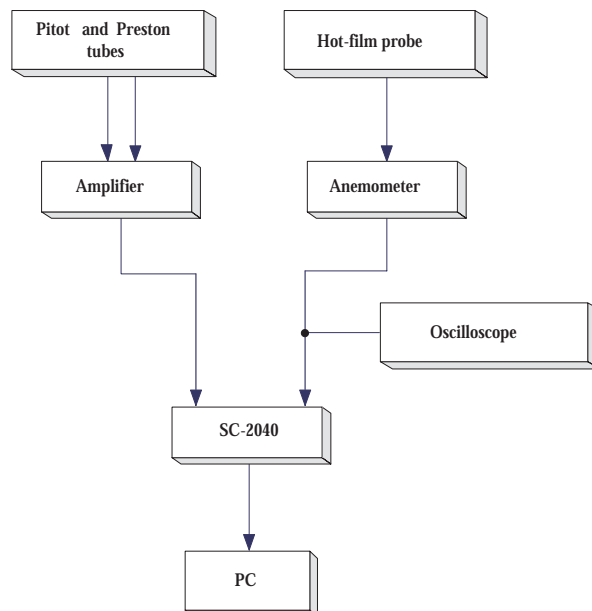


Figure 4.4: Measurement flow chart

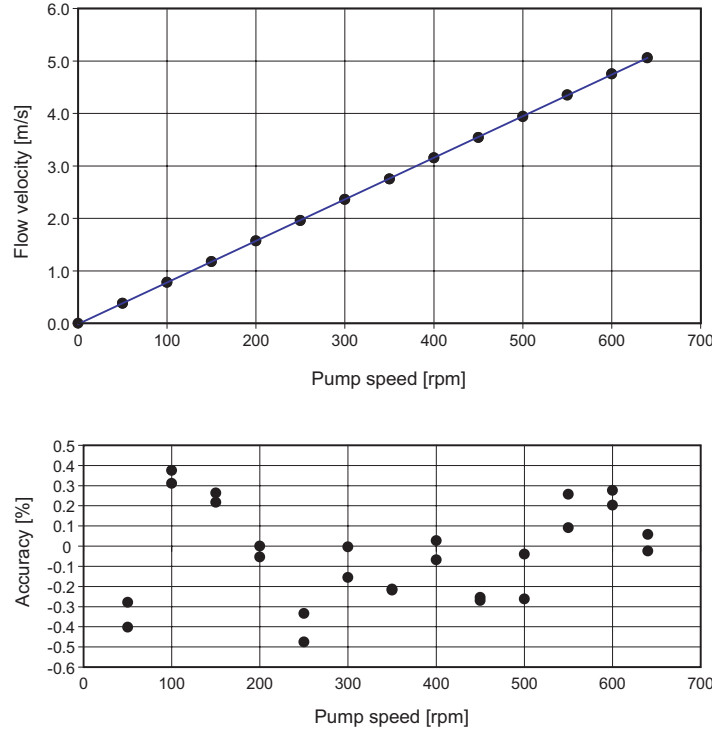


Figure 4.5: Flow velocity variation with the rotating speed of the tunnel's pump

#### 4.2.2 Procedure for velocity measurements

Measuring the mean flow velocity using the Pitot tube, implies the accomplishment of several stages:

1. The drain of the measurement circuitry

Before the beginning of the measurements, it is always necessary to drain the tubes. The main reason for doing this drain is that in the connection tubes there are a lot of air bubbles which can affect the measurements.

The drain is realized using the carriage of survey for the pressure sensors. After the accomplishment of all the necessary steps, it should be verified that in the connection tubes there are no more air bubbles. If the bubbles are still present this means that the drain was incomplete and it had to be done one more time or several times, until all the bubbles disappear.

2. The offset settlement

After the drain of the measurement circuitry, it must be established the offset for the flow velocity.

The signal coming from the sensor is acquired under the form of an electrical signal, a voltage, on the base of which it is calculated the pressure difference - dynamic pressure - with the calibration equation of the Pitot tube:

$$p_1 - p_2 = -0.0013 \cdot (V_{pitot}^2 - V_{c=0}^2) + 0.2056 \cdot (V_{pitot} - V_{c=0}) \quad (4.2)$$

where:  $V_{pitot}$  - the voltage acquired from the Pitot tube;

$V_{c=0}$  - the voltage acquired when the pump is stopped;

$p_1 - p_2$  - the difference between the total pressure and the static pressure,  
i.e. the dynamic pressure.

Knowing the pressure difference, it can be calculated the flow velocity using the relation 4.2 by taking also into account the influence of the temperature over the water density.

Therefore to establish the offset for the voltage, it will be measured the voltage coming from the Pitot when there is no flow,  $V_{c=0}$ .

This step is necessary to be repeated every time, before any measurement performance.

### 3. Measurements performance

Having done the drain of the measurement circuitry and the settlement of the offset for the velocity, the measurements can be performed.

## 4.3 HOT-FILM PROBE CALIBRATION PROCEDURE

### 4.3.1 Operation theory for the hot-film probe

The hot-film probe is working on the principle that the heat transfer from a sufficiently small heated surface depends only on the flow characteristics in the viscous region of the boundary layer. By similarity, between the heat and the gradient transport of momentum, the amount of the heat transfer into the fluid gives a measure of the wall shear-stress,  $\tau_p$ , see figure 4.6.

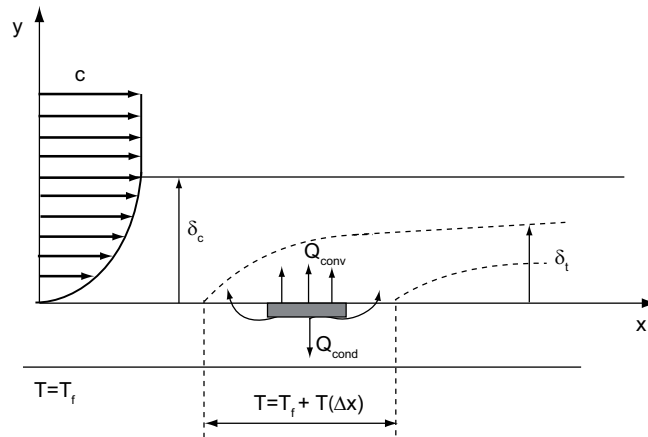


Figure 4.6: Main heat transfer components on a heated element



The energy balance at the upper surface, covered by the film, is:

$$\dot{Q}_J = \Sigma \dot{Q} + \frac{dQ_{film}}{dt}, \quad (4.3)$$

where:

- $\dot{Q}_J$  - heat power transferred by Joule effect;
- $\Sigma \dot{Q}$  - heat transferred to surroundings;
- $dQ_{film}$  - thermal energy stored in the film.

For equilibrium conditions, the heat storage is zero and the joule heating becomes equal with the heat transferred to surroundings.

$$dQ_{film} = 0 \implies \dot{Q}_J = \Sigma \dot{Q} \quad (4.4)$$

The heat transferred to the surroundings is made up of 3 components:

- convection from film to surrounding fluid;
- conduction to film support;
- radiation to surroundings.

$$\Sigma \dot{Q} = \dot{Q}_{conv} + \dot{Q}_{cond} + \dot{Q}_{rad} \quad (4.5)$$

There are made several assumptions:

- conduction to support is minimized by using insulating material, so it can be neglected;
- radiation losses are negligible.

Taking into account all the assumptions made above, the energy balance can be written as the equality between the joule heating and the average heat transferred to the fluid, directly, from the heating surface and, indirectly, through the heated portion of the substrate, see relation 4.6.

$$\dot{Q}_J = \dot{Q}_{conv} \quad (4.6)$$

The electrical power generated by Joule effect can be written, for a hot-film probe, as:

$$\dot{Q}_J = \frac{V^2}{R_f}, \quad (4.7)$$

where:  $V$  represents the voltage value across the hot-film probe, while  $R_f$  is the resistance value of the hot-film probe at the operating temperature,  $T_f$ , maintained constant by a constant temperature anemometer.

Knowing the resistance value of the hot-film,  $R_c$ , at a temperature  $T_c$ , the resistance value of the probe at the temperature  $T_f$  can be rewritten as:

$$R_f = R_c[1 + \alpha_R(T_f - T_c)] \quad (4.8)$$

where  $\alpha_R$  represents the temperature coefficient of resistivity.

To rely the heat transfer by convection to the wall shear-stress  $\tau_p$  it is assumed that the thermal boundary layer developed on the probe is within the viscous sublayer of a pre-existing momentum boundary layer.

The relationship between the  $\dot{Q}_{conv}$  and  $\tau_p$  is obtained by derivating the thermal energy transport equation near the wall, for 2D flow:

$$c \frac{\partial T}{\partial x} = \alpha \frac{\partial^2 T}{\partial y^2}, \quad (4.9)$$

where  $x$  represents the streamwise coordinate,  $y$  the normal-to-wall coordinate,  $T$  the temperature,  $c$  flow velocity in  $x$  direction and  $\alpha$  the thermal diffusivity. As at the sensor upstream, the flow is assumed unheated, the incoming flow temperature is the same as the free-stream temperature  $T_\infty$ .

In the viscous sublayer, the flow velocity can be approximate:

$$c = \left( \frac{\partial c}{\partial y} \right)_p y, \quad (4.10)$$

where  $\left( \frac{\partial c}{\partial y} \right)_p$  represents the mean velocity gradient at the wall and by considering  $\mu$  as the dynamic viscosity of the fluid, the wall shear-stress is:

$$\tau_p = \mu \left( \frac{\partial c}{\partial y} \right)_p \quad (4.11)$$

$$\tilde{T} = \frac{T - T_f}{T_\infty - T_f} \quad (4.12)$$

By introducing the non-dimensional temperature,  $\tilde{T}$ , defined by relation 4.12, the equation 4.9 becomes:

$$\left( \frac{\partial c}{\partial y} \right)_p y \frac{\partial \tilde{T}}{\partial x} = \alpha \frac{\partial^2 \tilde{T}}{\partial y^2} \quad (4.13)$$

The boundary conditions are:

$$\tilde{T} = 0 \quad \text{for} \quad y = 0 \quad (4.14)$$

$$\tilde{T} = 1 \quad \text{for} \quad y \rightarrow \infty \quad (4.15)$$

$$\tilde{T} = 1 \quad \text{for} \quad x = 0 \quad (4.16)$$

By introducing the similarity parameter,  $\eta$  defined by relation:

$$\eta = \frac{y \left( \frac{\partial c}{\partial y} \right)_p^{1/3}}{(3\alpha x)^{1/3}}, \quad (4.17)$$

the equation 4.13 can be rewritten as an ordinary differential equation, see relation 4.18:

$$\tilde{T}'' = \eta^2 \tilde{T}' \quad (4.18)$$

In this way, the boundary conditions in term of  $\eta$  becomes:

$$\tilde{T} = 0 \quad \text{for} \quad \eta = 0 \quad (4.19)$$

$$\tilde{T} = 1 \quad \text{for} \quad \eta \rightarrow \infty \quad (4.20)$$

By introducing, in the same time, the constant  $M$ , defined, by the relation 4.21, the solution of the ordinary differential equation is obtained and it is illustrated by the relation 4.22.

$$M^{-1} = \int_0^\infty e^{-\eta^3/3} d\eta = \frac{1}{3} \Gamma\left(\frac{1}{3}\right) = 0.893 \quad (4.21)$$

$$\tilde{T} = M \int_0^\eta e^{-\eta^3/3} d\eta \quad (4.22)$$

The heat flux at the surface is given by:

$$\dot{q} = -k \left( \frac{\partial T}{\partial y} \right)_f \quad (4.23)$$

Taking into account the equations 4.12, 4.22 and by considering:

$$\frac{\partial \tilde{T}}{\partial y} = \frac{\partial \tilde{T}}{\partial \eta} \frac{\partial \eta}{\partial y}, \quad (4.24)$$

the heat flux at the surface become:

$$\dot{q} = Mk(T_\infty - T_f) \frac{\left( \frac{\partial c}{\partial y} \right)_p^{1/3}}{(3\alpha)^{1/3}}. \quad (4.25)$$

Assuming that the hot-film is a rectangle surface having a constant length,  $l$ , in the streamwise direction and width  $w$  in the spanwise direction, the average heat transfer,  $\dot{Q}_{conv}$  integrated over  $l$  and  $w$  becomes:

$$\dot{Q}_{conv} = w \int_0^l q dx = \frac{3}{2} Mk(T_\infty - T_f) \frac{\left( \frac{\partial c}{\partial y} \right)_p^{1/3}}{(3\alpha)^{1/3}}, \quad (4.26)$$

By taking into account the relation 4.11, the average heat transfer,  $\dot{Q}_{conv}$ , is:

$$\dot{Q}_{conv} = \frac{3}{2} Mk(T_\infty - T_f) \frac{\left( \frac{\tau_p}{\mu} \right)^{1/3}}{(3\alpha)^{1/3}}, \quad (4.27)$$

By using in equation 4.6, the relations 4.7 and 4.27, and taking into account that the film temperature  $T_f$  and the free-stream temperature  $T_\infty$  are constants, it can be concluded that for a calibration it should be possible to determine the wall shear-stress value  $\tau_p$  by measuring the anemometer's output voltage  $E$ , see relation 4.28 and illustrated in figure 4.7.

$$\frac{E^2}{T_f - T_\infty} \propto \tau_p^{1/3} \quad (4.28)$$

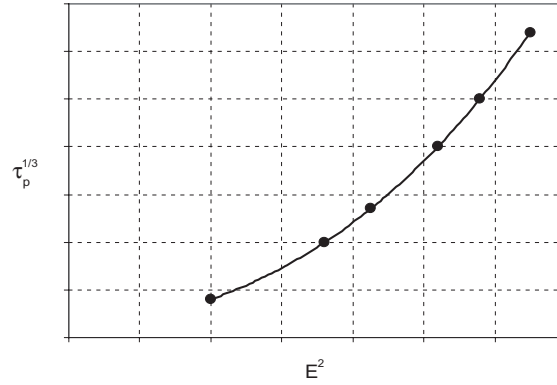


Figure 4.7: Wall shear stress evolution with the anemometer's output voltage

#### 4.3.2 Flow velocity evolution in the boundary layer

To calibrate the hot-film probe there must be determined the friction velocity using the Preston tube, in the constant flux part of the boundary layer - to verify the logarithmic shape, at less that 2 mm. It is accepted the hypothesis for the logarithmic boundary layer, at less that 0.06 mm, that means a linear variation of the flow velocity with the boundary layer's thickness.

For friction velocity evaluation, the variation of the flow velocity,  $c$ , with the wall distance,  $y$  must be known. This relationship is determined by considering the equation of the turbulent boundary layer at the flow of constant momentum, in the logarithmic region, see Schlichting [1979]:

$$c^+ = \frac{1}{\chi} \ln y^+ + C \quad (4.29)$$

By considering the dimensionless parameters, it is obtained:

$$\left. \begin{aligned} c^+ &= \frac{\bar{c}}{c_\tau} \\ y^+ &= \frac{y c_\tau}{\nu} \end{aligned} \right\} \Rightarrow \frac{c}{c_\tau} = \frac{1}{\chi} \ln\left(\frac{y c_\tau}{\nu}\right) + C \quad (4.30)$$

In the same time, the experiments show:

$$\frac{c}{c_\infty} = a \ln\left(\frac{y c_\infty}{\nu}\right) + b \quad (4.31)$$

For finding a relation similar as the experiments show, the equation 4.30 will be rewritten as it follows:

$$\frac{c}{c_\infty} \cdot \frac{c_\tau}{c_\infty} = \frac{1}{\chi} \ln\left(\frac{yC_\infty}{\nu} \cdot \frac{c_\tau}{C_\infty}\right) + C \quad (4.32)$$

$$\frac{c}{c_\infty} \cdot \frac{c_\tau}{c_\infty} = \frac{1}{\chi} \ln\left(\frac{yC_\infty}{\nu}\right) + \frac{1}{\chi} \ln\left(\frac{c_\tau}{C_\infty}\nu\right) + C \quad (4.33)$$

$$\frac{c}{c_\infty} = \frac{c_\tau}{C_\infty\chi} \ln\left(\frac{yC_\infty}{\nu}\right) + \frac{c_\tau}{C_\infty\chi} \ln\left(\frac{c_\tau}{C_\infty}\nu\right) + C \quad (4.34)$$

By comparing the experimental relationship, the relation 4.31 with the one obtained relation 4.34, it is found the value for the constant  $a$ , after which it is obtained the relationship between the flow velocity and the friction velocity:

$$a = \frac{c_\tau}{C_\infty\chi} \quad (4.35)$$

It is known that the relation between wall shear-stress and the friction velocity is

$$\tau_p = \rho c_\tau^2 \quad (4.36)$$

and, finally, it is showed that:

$$\tau_p = \rho(a\chi C_\infty)^2 \quad (4.37)$$

In this way it is found out the relationship between the wall shear stress and the flow velocity and so, for a given flow velocity it can be established the wall shear-stress value, see relation 4.37.

The wall shear-stress was determined for flow velocities between 1 and 5m/s, see Jandard [2000]. For a mean flow velocity of 1.95m/s the coefficients,  $a$  and  $b$ , are determined, equation 4.31, in figure 4.8. There was obtained a friction velocity using equation 4.35, of 0.0869m/s, as well as the wall shear-stress value using equation 4.37, of 7.5333 Pa.

Now the dimensionless parameters,  $c^+$  and  $y^+$  can be calculated and it can be represented the variation  $c^+(y^+)$ , see figure 4.9.

For the calibration curve one has to know the variation of the flow velocity, measured by the Pitot tube, with the velocity in the boundary layer, measured with the Preston tube. This relation is not changing because it depends strictly on the flow conditions and it is illustrated by the equation 4.38. The study of this variation was made by Jandard [2000] and is presented in figure 4.10.

$$c_\tau = 4.4195 \cdot 10^{-2} C_\infty \quad (4.38)$$

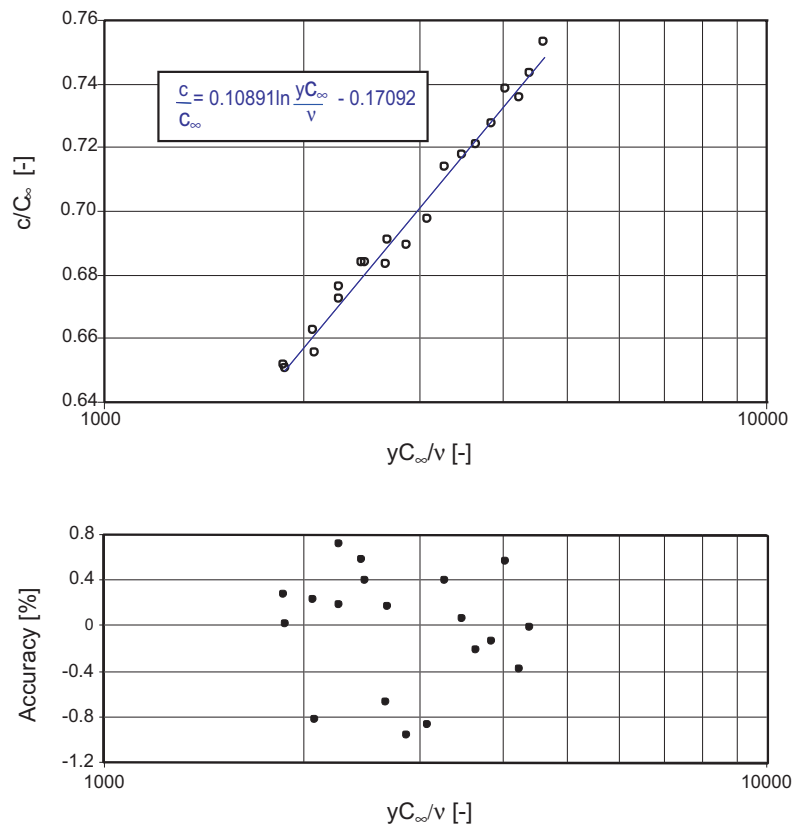


Figure 4.8: The adjustment of a logarithmic tendency in the turbulent boundary layer zone with flow of constant momentum

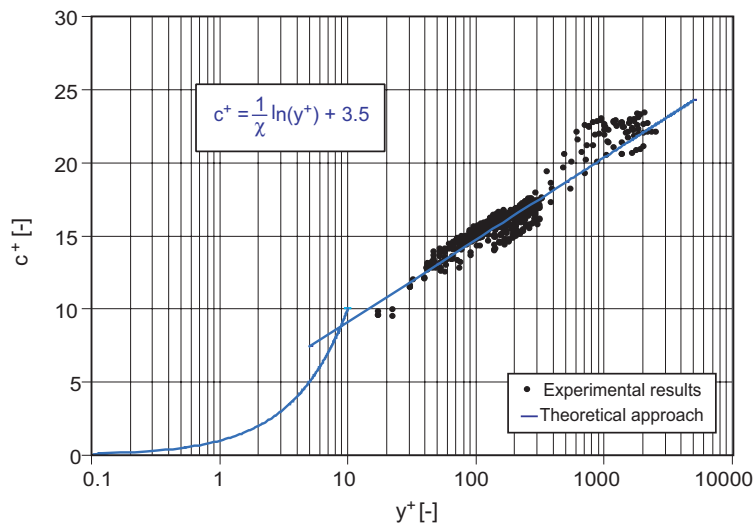


Figure 4.9: Velocity distribution in the boundary layer

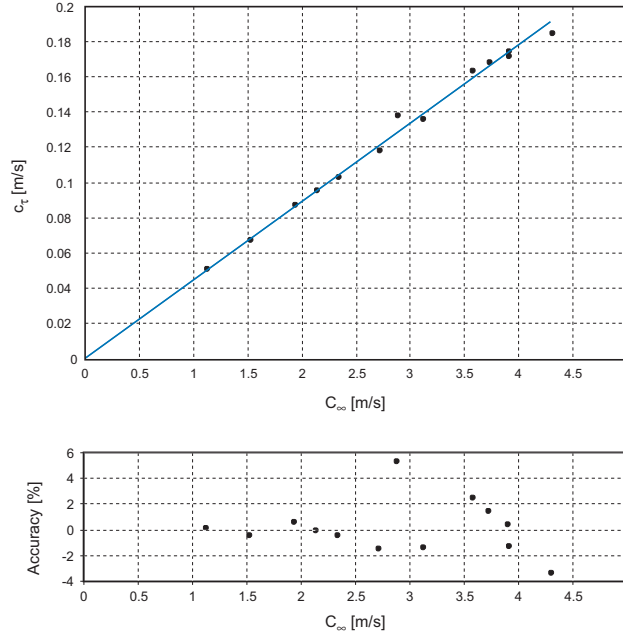


Figure 4.10: Flow velocity distribution with the velocity in the boundary layer and the measurements accuracy

### 4.3.3 Calibration parameters for hot-film probe measurements

The hot-film probe used is generally described in annexe A. The probe is located in the flow and that it is consequently cooled by it. In this time, between the probe and the flow takes place the heat transfer by convection. The magnitude of this convective loss depends on a number of parameters such as:

- the angle made by the hot-film probe with flow;
- the temperature difference between the water and the hot-film sensor;
- the aging of the hot-wire probe.

Therefore, for setting up the relation between the voltage given by the probe and the flow velocity, which is a non-linear relation, several steps must be accomplished by taking into account the influence of each one of the parameters reminded above over the measurements.

#### 1. Probe orientation influence

Preliminary step, before starting to find out the relation between the voltage coming from the hot-film probe and the flow velocity, is the sensor's localization in the flow. It is known that the maximum heat dissipation between the probe and the water takes place when the longitudinal direction of the film is perpendicular on the direction of the flow.

To find this position of the hot-film probe, the voltage for different angular positions is evaluated as it follows:

- it is chosen an initial position and measured the output voltage;
- the sensor position in the flow it is changed and measured the voltage corresponding to that angle, considering that turning on the right side of the initial position there are obtained positive angles and on the left one, negative angles;

- measurements validation by repeating them.

Observation For all measurements, the water temperature is recorded.

## 2. Probe-water temperature difference influence

One of the major influence over the measurements is given by the variation in the tunnel, of the water temperature. Due to the fact that the calibration tunnel is a closed loop, the water temperature tends to increase. In the same time, the hot-film's temperature is kept constant, so that its resistivity changes with the water temperature and it is needed to quantify this influence. Water temperature is measured with the thermometer placed next to the tachometer, which allows the pump speed reading, as well as with a temperature sensor mounted on the upper wall of the tunnel. For finding the way in which this parameter influences the measurements, one must do the followings:

- fix the flow velocity;
- measure the voltage given by the hot-wire probe while the temperature increases with  $0,1^{\circ}\text{C}$ ;

The relation obtained between the voltage and temperature will be used to correct all the measured data.

## 3. Calibration curve of the sensor

Having the sensor placed in the flow and knowing the influence of the temperature over the measurements one is able to start finding the relationship between the voltage given by the probe and the flow velocity.

The measurements are performed, by increasing the velocity, gradual, until the maximum is reached, by acquiring, simultaneously, the voltage and the velocity.

### 4.3.4 Hot-film probe calibration procedure

The calibration curve of the hot-film probes expresses the relationship between the wall shear-stress and the voltage given by the anemometer. To settle this curve, several stages have to be accomplished.

Three parameters are considered for the hot film probe measurements:

1. the orientation of the probe related to the flow direction;
2. the variation of the sensor voltage with the temperature difference between the water and the film;
3. the relationship between the voltage given by the sensor and the wall shear stress.

All the calibration stages can be summarized in a schematic representation, see figure 4.11.

Furthermore every block from the scheme is detailed, obtaining, finally, the calibration equation for the hot-film probe and it is evidenced the relationship between the wall shear stress and the flow velocity.

Meanwhile, the preliminary step for using a hot-film probe is its surface cleaning. Before mounting the hot-film probe in its support, on the test section upper wall, it must be cleaned as it follows:



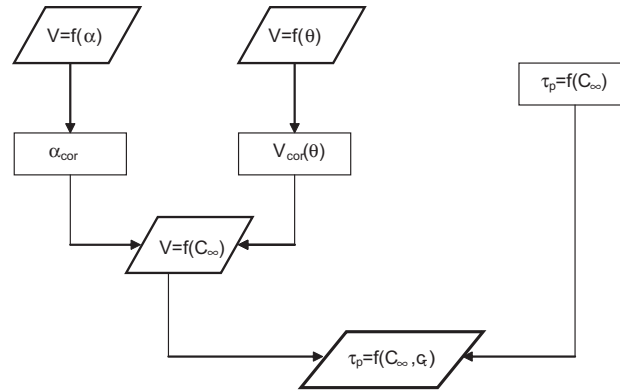


Figure 4.11: Calibration procedure systematized

1. Use a microscope to survey the probe's surface,
2. The surface cleaning, to remove the greases on the film, using a cotton rod covered by a *Kodak lens cleaning paper* impregnate with alcohol at  $90^\circ$ ,
3. Rinse with distill water, not to break the insulating layer on the surface of the probe
4. Control the surface of the probe on the microscope and redo the cleaning if needed.

One of the sources of error in using heated films is the positioning of the probe: it must be flush mounted relative to its support and to the wall. Therefore, the probe is flush mounted to the wall in the test section, the way illustrates in figure 4.12.

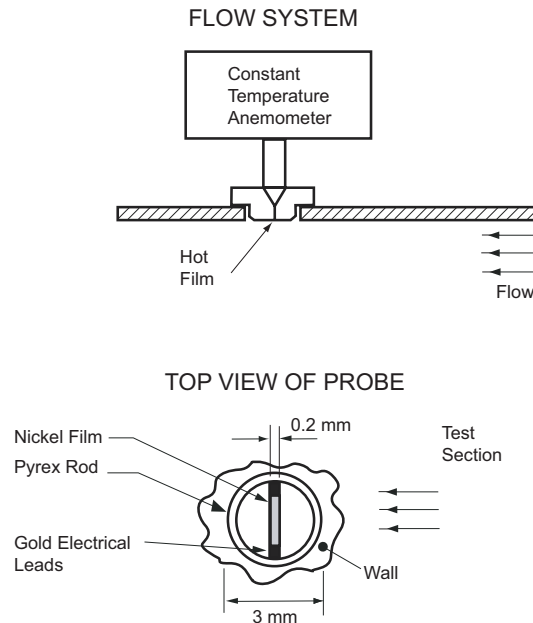


Figure 4.12: Uni-directional hot-film probe mounting in the calibration tunnel



# Chapter 5

## WALL SHEAR-STRESS MEASUREMENTS IN THE CONE

### 5.1 BACKGROUND

The draft tube of a Francis turbine converts the residual kinetic energy at runner outlet in pressure energy and, in this way, it increases the pressure difference between the inlet and the outlet of the turbine. This recovery of energy can represent a significant part of the total energy of the turbine, in particular, for the case of the low heads, and the correct operation of the draft tube is, from this point of view, an important quality factor for the turbine. The kinetic energy conversion into pressure energy in the draft tube is related to the increasing flow section, and the maximum opening angle of a conical diffuser is searched. The cone angle is limited by the onset of flow separation, because this separation decreases the flow section; the corresponding increasing of the flow velocity produces a decreasing of the pressure recovery.

In the presence of a rotating flow at the draft tube inlet, the fluid particles have a lengthened trajectory related to the flow without rotation. For this reason, the pressure gradient  $\frac{\partial p}{\partial s}$  experienced by the particle on its trajectory is reduced, and for relatively important opening angles of the draft tube, separation appears. The design responsibility becomes, in this way, the definition of the transversal areas evolution, assuring in the same time a flow without separation for the entire functioning domain of the machine, by reducing at maximum the dimensions - see figure 5.1.

In the same time, the flow in the cone is strongly unsteady and it takes place with an adverse pressure gradient. Depending on the operating point of the turbine, many unsteady phenomena can take place at this level of the draft tube: the swirl flow at the runner frequency, the wakes of the runner blades, the rope of the correspondent vortex for the low discharge operating points. All of these unsteady phenomena represent a supplementary difficulty for the optimal cone-opening angle design. The numerical simulations of the flow in this region are based, for the wall region, on the steady models of boundary layer and separations are not predicted. One of the most interesting parameter of the flow, in this part of the turbine, is the wall shear-stress, which is an indicator of the boundary layer's status and of the possible unsteady separations. From the calculation point of view, the wall shear-stress allows us to control the validation of the wall laws used for the turbulence modelling near the wall.

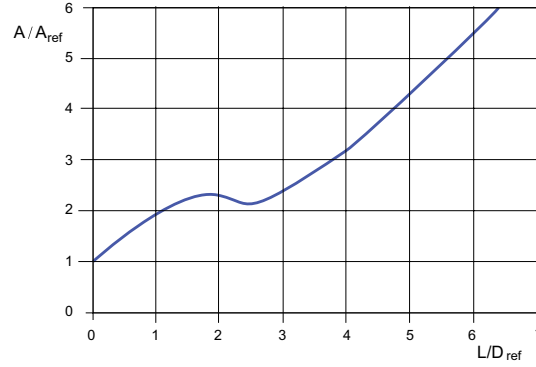


Figure 5.1: Area evolution in FLINDT draft tube

For these reasons, it is important to study the flow in the cone, to see the tendency of those unsteady separations and to validate the CFD codes.

There will be described the measurement procedure as well as the analysis of the results for wall shear-stress measurements performed at the runner outlet of the Francis turbine, to understand the behavior of the flow in this part of the turbine.

The wall shear-stress measurements are performed in 2 sections, at a distance of  $0.25\phi_{runner}$  from the runner outlet and  $0.7\phi_{runner}$  of the cone for each FLINDT II operating points. The global measurements of flow, head and efficiency are performed following IEC recommendations at LMH (Laboratory for Hydraulic Machines), \*\*\*\* [1993].

There are explored 4 "standard" and 1 off-design operating point, for 2  $\sigma$  values, to characterize the drop of the draft tube efficiency, see Arpe [2003]. The operating points are presented on the turbine efficiency hill chart in figure 5.2.

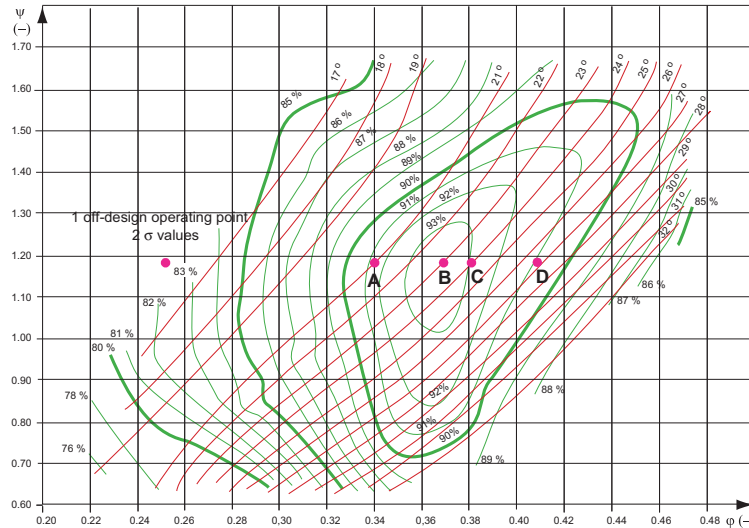


Figure 5.2: Operating points characterization for wall shear-stress measurements

## 5.2 HOT-FILM PROBE CHARACTERIZATION

For the wall shear-stress measurements it is used a flush mounted hot-film probe, 55R46, produced by DANTEC Measurement Technology, see figure 5.3.

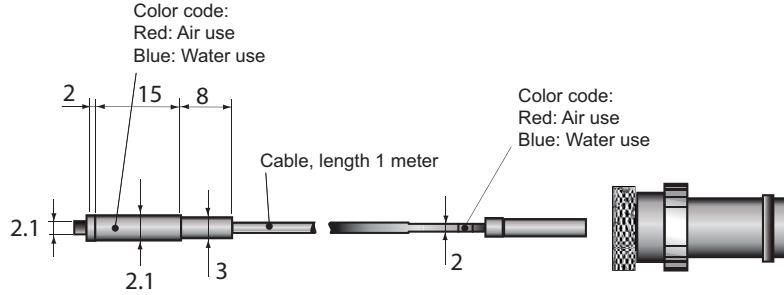


Figure 5.3: Flush mounted hot-film probe - detailed view

This probe is specially intended for measuring the wall shear-stress in both laminar and turbulent boundary layers.

They work on the principle of the similarity between temperature and velocity profiles in the viscous sublayer.

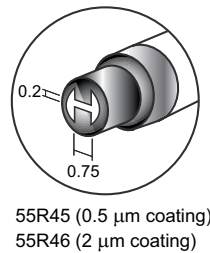


Figure 5.4: Flush mounted hot-film probe - front view

The sensor is embedded on a quartz cylinder, see figure 5.4. This quartz layer ensure an insulating protection of the probe and therefore, any voltage difference, between the water and the anemometer ground wire, can cause a breakdown in the insulating quartz coating destroying in this way the probe. That is why one have to pay attention and never forget to ground the water near the probe.

Thickness of quartz coating	Sensor material	Sensor dimensions	Sensor resistance $R_{20}$ (approx.)	Leads resistance	Temperature coefficient of resistance (TCR) $\alpha_{20}$ (approx.)	Max. sensor temperature	Max. ambient temperature	Max. ambient pressure	Frequency limit $f_{cpo}$
2 $\mu\text{m}$	nickel	0.75x0.2 mm	11.9 $\Omega$	1.4 $\Omega$	0.47%/C	150°C	100°C	70 bar	30 kHz

Table 5.1: Technical data for the 55R46 flush mounted hot-film probe

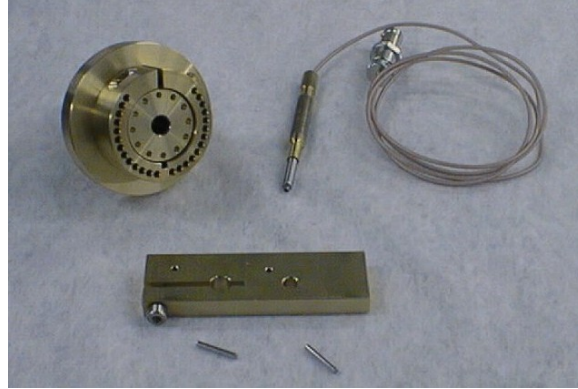


Figure 5.5: Rotating support and hot-film probe

Hot-film probe supports are designed so that they are adapted both to the test section, for the calibration and to the cone turbine section, see figures 5.5 and 5.6. They allow, in the same time, the angular rotation of the probe with about 260 degrees, every 10 degrees or 130 degrees, every 5 degrees.

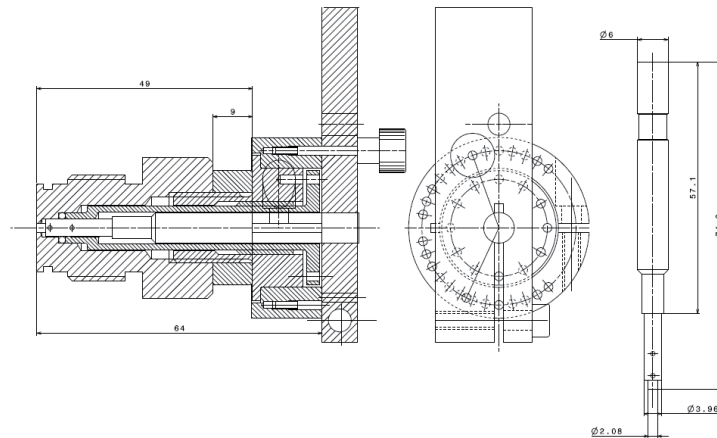


Figure 5.6: Rotating support for hot-film probe, mechanical design

Placing the hot-film probe in the flow requires the accomplishment of 2 steps:

1. A preliminary mechanical adjustment. The probe is mounted in its support and it is controlled on a microscope for placing it flush mounted related to the support. Once the probe is verified to be flush mounted in the support, the control of the angular position of the film related to its support is needed. It is parallel orientated with the direction of the support length, see figure 5.7, using a microscope.
2. Probe orientation in the water tunnel. Finally in the calibration tunnel, the hot-film probe in its support is perpendicularly orientated to the flow direction

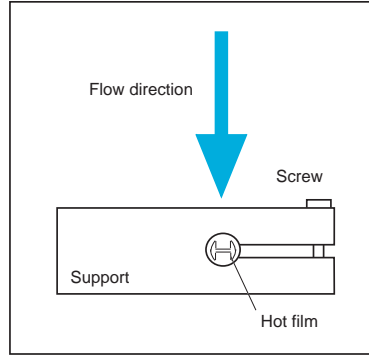


Figure 5.7: Hot-film probe orientation

### 5.2.1 Calibration curve

The voltage given by the hot-film probe is acquired simultaneously with the water temperature and the flow velocity, measured with the Pitot tube. The results are presented in figure 5.8.

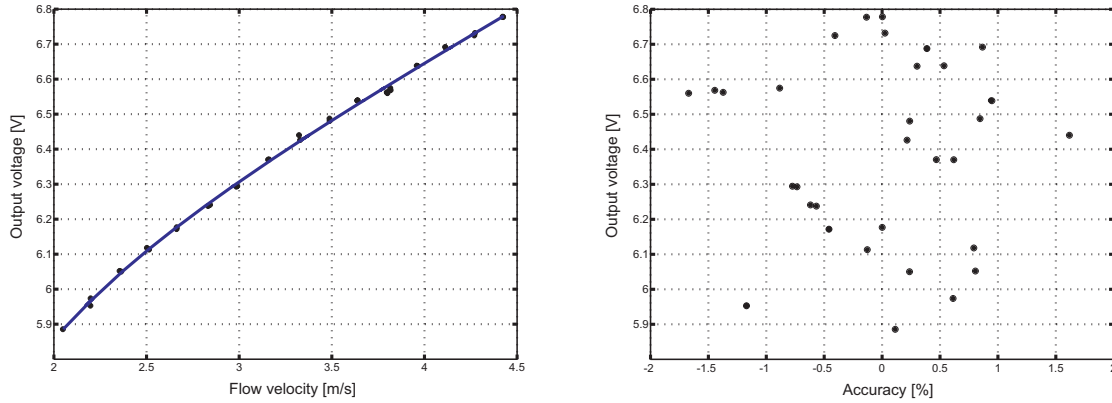


Figure 5.8: Output voltage variation with the mean flow velocity

The relation between the sensor voltage and the mean flow velocity is a polynomial one. The polynomial coefficients varies for each probe, depending on its characteristics:

$$C_{\infty} = a_3 \cdot V^3 + a_2 \cdot V^2 + a_1 \cdot V + a_0. \quad (5.1)$$

For this sensor:  $a_3 = -0.5378$ ,  $a_2 = 11.055$ ,  $a_1 = -72.55$ ,  $a_0 = 155.75$ .

The calibration relation is found by taking into account the equation 5.2 that describes the behavior of the hot-film probe, Goldstein et al. [1983].

$$\frac{q}{\Delta T} = 0.807 \frac{c_p^{1/3} \lambda^{2/3}}{L^{1/3} \mu^{1/3}} (\rho \tau_p)^{1/3} \quad (5.2)$$

It is known that the heat transfer is associated with the heated current and with its resistance by equation 5.3.

$$q = \frac{I^2 R}{A_e} \quad (5.3)$$

By replacing the relation 5.3 in the equation 5.2 and taking into account that the term  $0.807 A_e \frac{c_p^{1/3} \lambda^{2/3}}{L^{1/3} \mu^{1/3}}$  depends only on the temperature, so that it can be considered  $A(\theta) = 0.807 A_e \frac{c_p^{1/3} \lambda^{2/3}}{L^{1/3} \mu^{1/3}}$  it is obtained the relation 5.4.

$$\frac{I^2 R}{\Delta T} = A'(\rho \tau_p)^{1/3} \quad (5.4)$$

From the experiences, see Goldstein et al. [1983], the relation 5.4 becomes:

$$\frac{I^2 R}{\Delta T} = A'(\rho \tau_p)^{1/3} + B' \quad (5.5)$$

where B' is the term that characterize the heated losses, which do not arrive directly in the water.

$$\Delta T = \frac{H - 1}{\alpha} \quad (5.6)$$

For a very small temperature range,  $\Delta T \rightarrow 0$ , it is known that the relation 5.6 is valid, so that the relation 5.5 becomes:

$$\frac{I^2 R}{H - 1} = \frac{A'}{\alpha}(\rho \tau_p)^{1/3} + \frac{B'}{\alpha} \quad (5.7)$$

and by considering:

$$\begin{aligned} A &= \frac{A'}{\alpha} \\ B &= \frac{B'}{\alpha} \end{aligned} \quad (5.8)$$

the relation 5.7 take the form of relation 5.9.

$$\frac{I^2 R}{H - 1} = A(\rho \tau_p)^{1/3} + B \quad (5.9)$$

The anemometer is a constant temperature one and at his output a voltage and not a current is obtained; hence by applying the Ohm's law in the Wheatstone bridge the anemometer's output voltage can be detailed by the relation 5.10.

$$V = I \cdot (R_{var} + R_{int} + R_c + R_1) = I \cdot R_{tot} \quad (5.10)$$

In this way, the relation 5.9 can be rewritten as:

$$\frac{V^2 R}{R_{tot}^2 (H - 1)} = A(\rho \tau_p)^{1/3} + B \quad (5.11)$$



and the calibration curve becomes:

$$\tau_p = \frac{1}{\rho} \left( \frac{V^2 R}{R_{tot}^2 (H-1) A} - \frac{B}{A} \right)^3 \quad (5.12)$$

The 2 coefficients of the calibration curve,  $A$  and  $B$  are determined considering the relation between wall shear-stress and the friction velocity, see relation 4.36, and the relation determined between the friction velocity and the flow velocity, see relation 4.38. One example of calibration coefficients determination is illustrated in figure 5.9 and their values in 5.13.

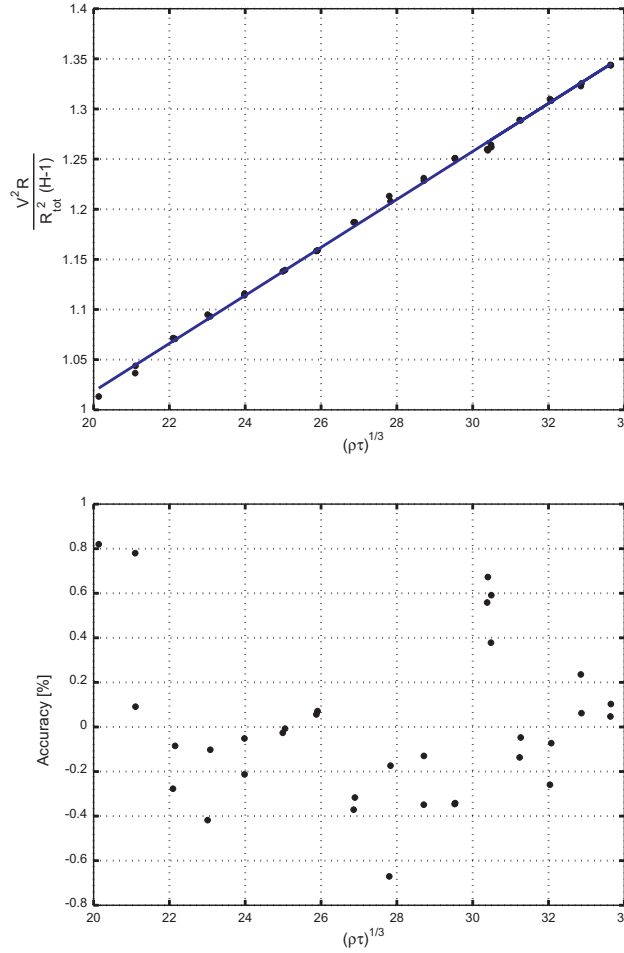


Figure 5.9: Calibration coefficients,  $A$  and  $B$ , determination

$$\begin{aligned} A &= 0.025606 \\ B &= 0.437984 \end{aligned} \quad (5.13)$$

Finally, the calibration curve is obtained, figure 5.10, and the global accuracy of the calibration is less than 2% of the measured value. Its final equation is illustrated by the equation 5.14.

$$\tau_p = \frac{1}{\rho} (1.149879 \cdot V^2 - 17.104741)^3 \quad (5.14)$$

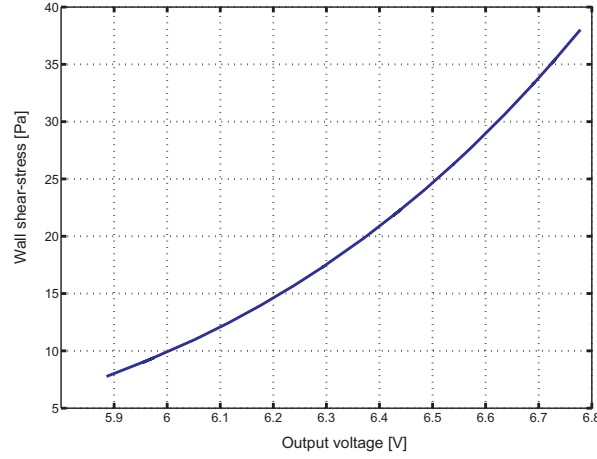


Figure 5.10: Hot-film probe calibration curve

Observation The measurements accuracy, for a parameter  $a$ , is calculated using the relation 5.15:

$$\text{Accuracy} = \frac{a_{\text{calculated}} - a_{\text{measured}}}{a_{\text{measured}}} \cdot 100 \quad (5.15)$$

### 5.2.2 Sensitivity parameters

The heat transfer by convection between the hot-film probe and the flow is not depending only on the flow velocity, but also on three supplementary parameters:

1. the difference between the water and probe temperature;
2. the angle between the hot-film probe direction and the flow direction;
3. the contamination of the hot-film probe.

All these three parameters represent noise sources for the wall shear-stress measurement and their effects must be evaluated and integrated in the calibration procedure for the hot-film probe, because their variations can introduce wall shear-stress measurement errors of many percentages (10 to 50).

#### 1. Temperature gradient influence

The temperature of the water gives one of the major impact over the measurements. This is due to the fact that between the water and hot-film probe takes place a heat exchange.

The hot-film probe is actually an electrical resistance maintained at a constant temperature and by its physical property, depends linear on the temperature difference between film and medium where it is placed.

The constant-temperature anemometer is adjusted for an established temperature gradient between the water and the hot-film. But since in the hot-film probe calibration, the water temperature can't be controlled and kept constant at a initial calibration value, this temperature varying continuously, with about  $0.1^\circ\text{C}$  every 30 minutes, the overheating rate for which the anemometer was calibrated is, also changing. So, it becomes obvious

the necessity of a correction of the calibration relationship when the water temperature modifies from its calibration value. For these reasons, the influence of this parameter over the measurements should be known.

For every hot-film sensor there are performed 2 steps:

1. anemometer calibration;
2. relationship estimation used to correct the data.

The description of the procedure for the calibration of the CTA and the results are presented in the annexe B.

Once the anemometer calibration performed, the measurements are done by fixing the pump speed and through it, the velocity of the flow. The water temperature is acquired together with the voltage coming from the hot film probe, and it is determined the relationship between those 2 parameters, see figure 5.11.

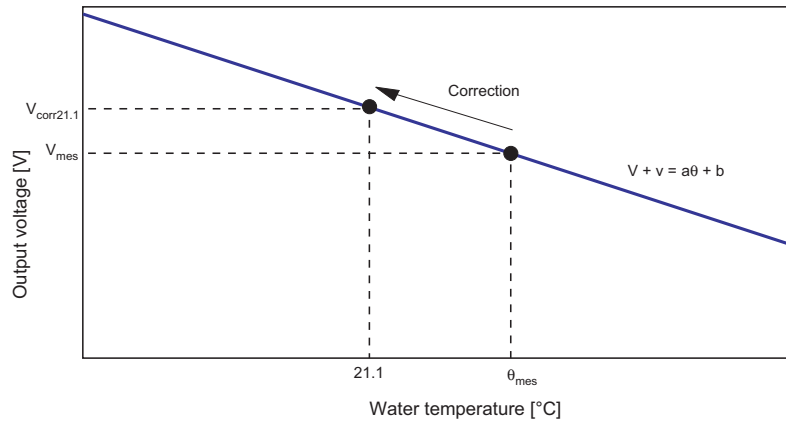


Figure 5.11: Method used to adjust the voltage drift due to the water temperature changes

The variation of the electrical resistance versus temperature is a linear one, so that the relation between the voltage and temperature can be considered also a linear relationship, given by equation 5.16.

$$V = a \cdot \theta + b \quad (5.16)$$

Further, having found the 2 constants  $a$  and  $b$ , it is found the relation that allows the correction of the output voltage given by the hot-film probe with the water temperature. All the data will be reported to the temperature of the anemometer's calibration, that is  $21,1^\circ\text{C}$  and all the time they will be corrected to the values corresponding to this temperature.

For finding the coefficients values and for establishing the relation that allows the correction of the voltage values given by the hot-film probe, it is assumed that it is measured a value  $V_{mes}$ , for the flow velocity of  $C_\infty$  and at the temperature  $\theta_{mes}$ , different from the anemometer's calibration temperature of  $21,1^\circ\text{C}$ .

Moreover, it is known that the output voltage changes with the temperature according to the relation:

$$V + v = a \cdot \theta + b \quad (5.17)$$

For a measurement point it is found the value of  $v$ :

$$v = a \cdot \theta_{mes} + b - V_{mes} \quad (5.18)$$

Starting from the relation 5.18, it can be deduced that the voltage measured for a different temperature will be corrected using the following relation:

$$V_{cor21,1} = a \cdot (21.1 - \theta_{mes}) + V_{mes} \quad (5.19)$$

For this calibration, the influence of the water temperature on the output voltage of the hot-film probe is illustrated by the relation 5.20 and it is represented in figure 5.12.

$$V = -0.1233 \cdot (21.1 - \theta) + 9.6222 \quad (5.20)$$

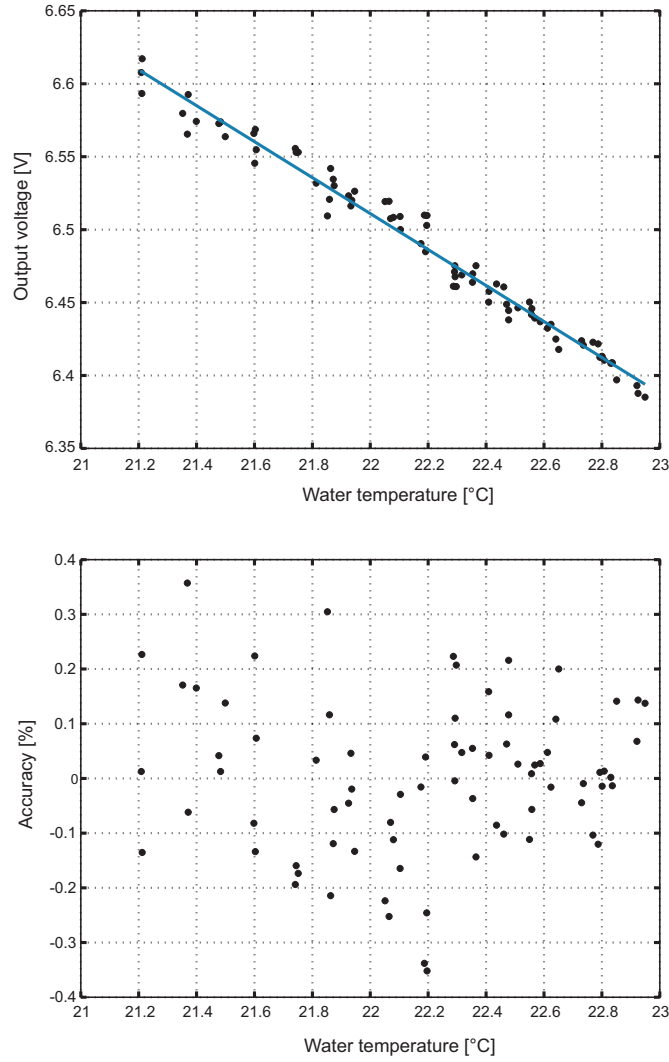


Figure 5.12: Hot-film probe output voltage evolution with the water temperature

## 2. Orientation of the hot-film probe in the flow

The maximal heat dissipation is obtained when the longitudinal direction of the film is perpendicular to the flow direction; this means maximum voltage value at the output of the anemometer.

For finding the maximum value of the voltage it is imposed the value for the flow velocity and kept constant, while the angle made by the film's sensor with the direction of the flow is modified, step by step, by  $10^\circ$ , considering that when the sensor is turned on the left side, the angle is negative and, in the other side, positive. For a constant wall shear-stress value, the variation of the measured voltage with the probe angle is presented in the figure 5.13.

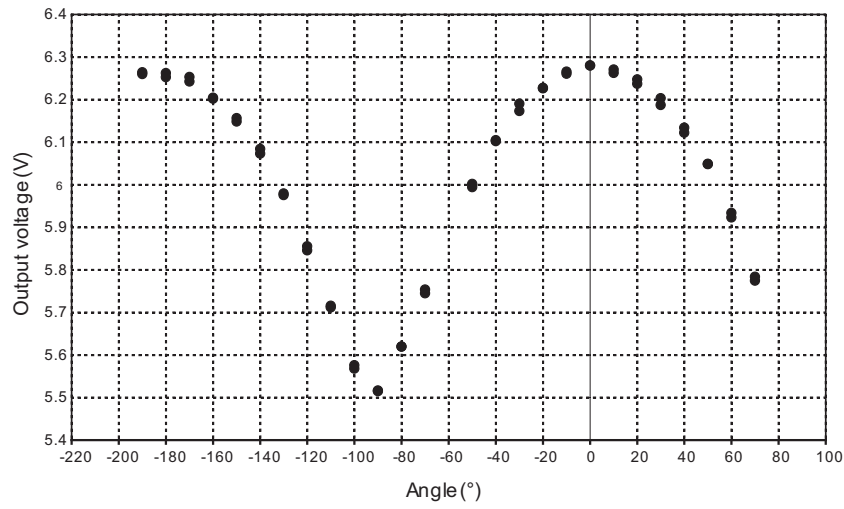


Figure 5.13: Angular variation of the voltage given by the sensor

Taking into account that the film was aligned with the support, while this one was mounted initially perpendicular to the flow in the tunnel, corresponding to  $0^\circ$  in the graphic, it is found that the hot-film probe reaches the maximum value of the voltage for the angle  $\alpha = 90^\circ$  between the direction of the film and the mean direction of the flow. Another observation concerns the non-symmetry of the 2 maxima/minima of the angular validation curve, see figure 5.13. An explanation for this thing can be the non-symmetry of the sensor geometry, linked to the insulating layer which surrounds the film.

To determine the angle of the probe in the cone there was approximated the evolution of the voltage versus the angle with a function composed by an constant and a sum of 2 sinus and the results obtained are presented in the figure 5.14.

Observation It is detailed only the variation of the angle between  $-30^\circ$  and  $+30^\circ$ , because it is known that the maximum value for the voltage is around  $0^\circ$ , see figure 5.14.

It can be concluded that for the calibration, the film's sensor should make with the direction of the flow  $90^\circ$ .

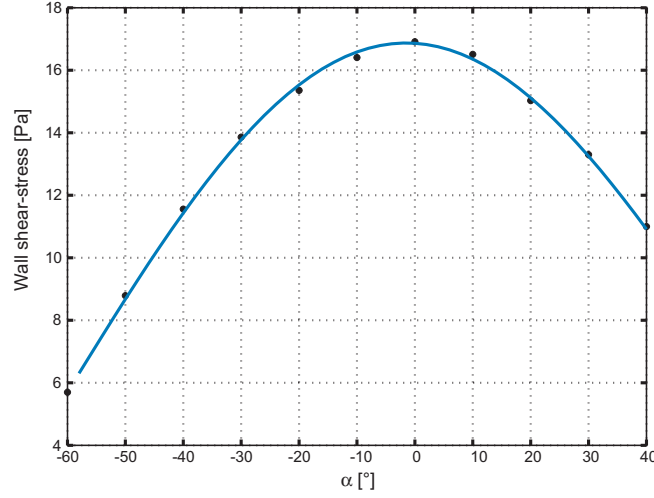


Figure 5.14: Angular variation of the wall shear-stress

### 3. Contamination of the hot-film probe

The third parameter taken into account is the contamination of the hot-film probe with the water impurities. For finding the influence of this parameter, the calibration curve is repeated after a measurement day and the 2 calibration curves obtained are compared in the figure 5.15 and the figure 5.16. The coefficients of the 2 calibration curves are presented in the table 5.2.

Measurement day	$A'$	$B'$
First day	0.0256	0.4379
Following day	0.0248	0.4945

Table 5.2: Calibration curves coefficients

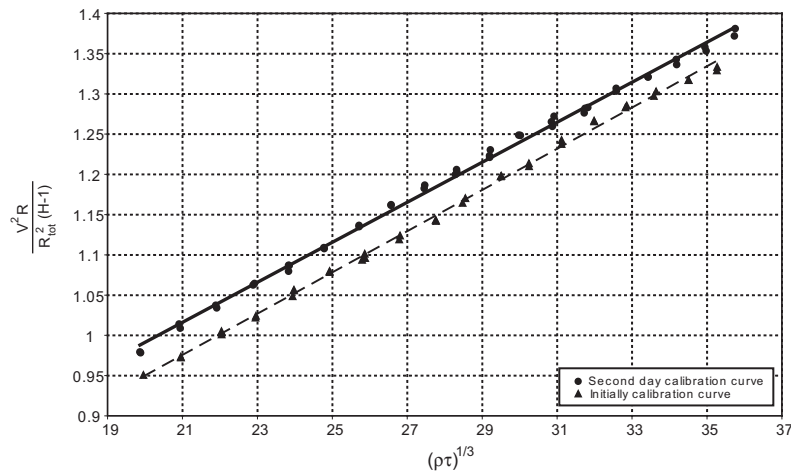


Figure 5.15: Coefficients calculation of the 2 calibration curves

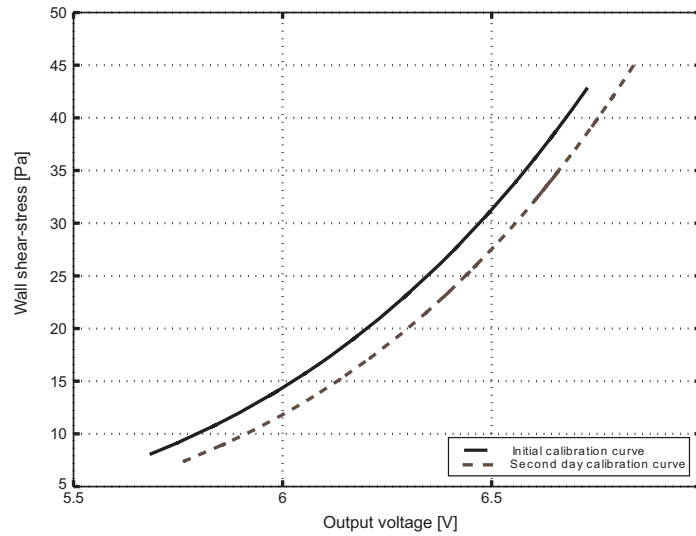


Figure 5.16: Probe contamination influence on the calibration curves

By comparison between the 2 calibration curves it can be noticed that the calibration curve changes day by day. The magnitude of the contamination error is about 1,4% of the measured value. The reasons for this are the impurities from the water, which are laid on the hot-film probe's surface.

This inconvenient can be eliminate in 2 ways:

- if the difference between the 2 calibration curves is smaller than 3%, a cleaning of the hot-film probe is enough;
- if the difference is, yet, bigger than 3%, the calibration of the hot-film probe must be redone.

## 5.3 MEASUREMENT OF THE WALL SHEAR-STRESS IN A FRANCIS TURBINE'S CONE

### 5.3.1 Experimental set-up

In the framework of FLINDT, Flow Investigation in Draft Tubes, research project, EUREKA no. 1625, the wall shear-stress measurements are performed, Berca and Ciocan [2002], in the cone of a  $\nu = 0.56$ ,  $n_q = 92$ , industrial high specific speed Francis turbine scale model, located in the test rig PF III from the EPFL, Laboratory for Hydraulic Machines, see figure 5.17.

The general characteristics of this turbine are:

- impeller blades number: 17;
- stay vanes: 10;
- guide vanes: 20;
- runner's diameter:  $0.4m$ .

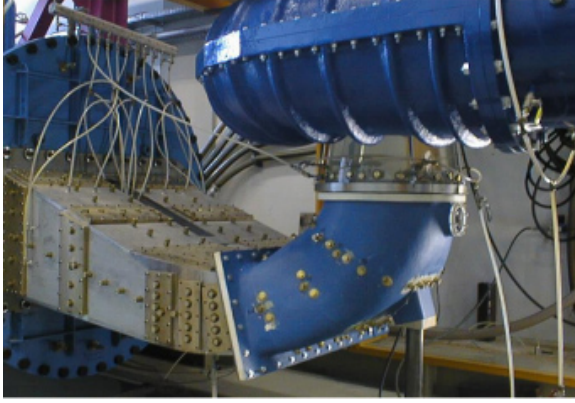


Figure 5.17: FLINDT Francis turbine scale model

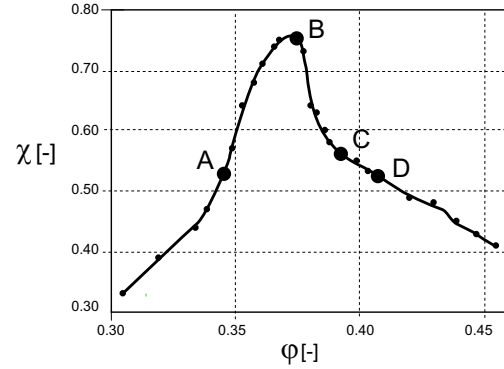


Figure 5.18: Draft tube pressure recovery model

The global measurements of flow, specific energy and efficiency are performed according to IEC recommendations \*\*\*\* [1993] at the EPFL, Laboratory for Hydraulic Machines. Four standard operating points are selected to characterize the draft tube characteristic, see figure 5.18, and 1 off-design operating point for  $2\sigma$  values, to characterize the drop of the draft tube efficiency, see table 5.3. The model characteristics and the selected operating points are described in Arpe [2003].

	Discharge coefficient $\varphi[-]$	Energy coefficient $\psi[-]$	Thoma number $\sigma[-]$
OP A	0.34	1.18	-
OP B	0.368	1.18	-
OP C	0.38	1.18	-
OP D	0.41	1.18	-
OP with vapor phase	0.256	1.18	0.38
OP without vapor phase	0.256	1.18	0.26

Table 5.3: Studied operating points characterization

For the wall shear-stress measurements, two sections are investigated, inlet and outlet sections of the turbine model cone, figure 5.19. The wall shear-stress distribution in the turbine's cone is realized by embedding the hot-film probe, see figure 5.20, at the cone inlet section in 9 different locations, and at the cone outlet section, in 7 different locations.

The data acquisition for the measurements in the cone was performed using the same acquisition module CA-1000 from the National Instruments, as for the calibration. However, for acquiring measurements synchronous with the runner rotation, the sampling frequency was limited at 3kHz, during 9 seconds. So, there were acquired 11 sets of 27000 data samples for each operating point as well as for each spatial position of the sensor.



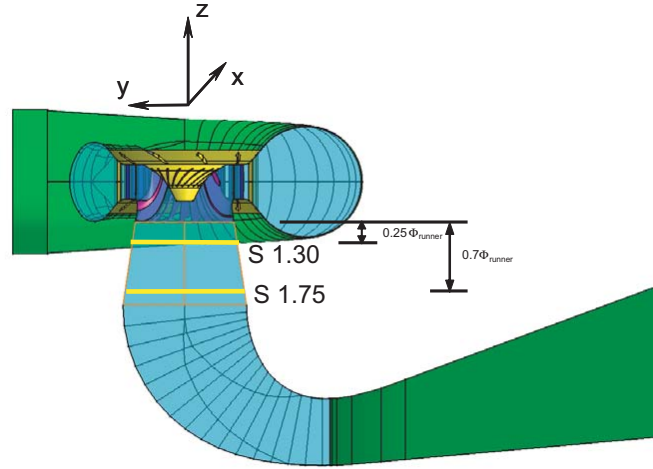


Figure 5.19: Wall shear stress measurement sections

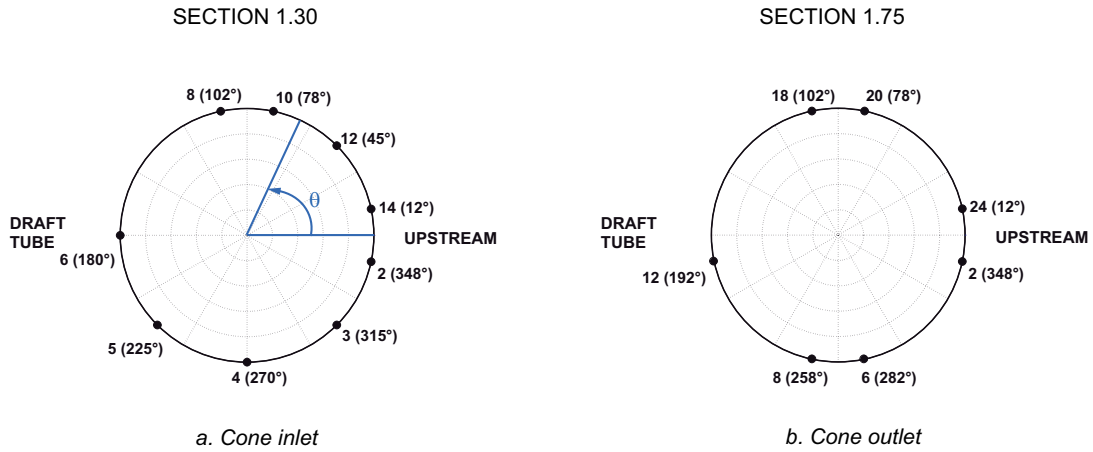


Figure 5.20: Wall shear stress sensors locations

### 5.3.2 Wall shear stress measurements procedure

For the wall shear-stress measurements in a Francis turbine, the influence of the three calibration parameters must be quantified in the cone configuration, Ciocan et al. [2002].

#### Water temperature correction

The first parameter to be taken into account during all the measurements is the water temperature. In the turbine test rig the temperature control step is  $2^\circ$ , that transposed in wall shear-stress represents a 30 Pa variation, meaning 15% of the mean wall shear-stress value.

The main reason for evaluation of this parameter is explained by water temperature variation, as mentioned above, in the turbine. Moreover, there must be taken into account

the change in sensor's mounting configuration. In the hydrodynamic water tunnel, the hot-film probe is mounted on a steel plate, while in the Francis turbine's cone it is mounted on a plexiglas interface. As the sensor's interface is bronze, it's expected a change in the heat transfer due to the 2 different configurations, which should be quantified.

To eliminate the influence of this parameter in the wall shear-stress measurements, the water temperature is acquired simultaneous with the wall shear-stress. Each instantaneous value of shear-stress is corrected with the instantaneous water temperature.

The relationship between the voltage given by the hot-film probe and the water temperature in the cone, see figure 5.21 is given by relation 5.21.

$$V = -0.1382 \cdot \theta + 10.5236 \quad (5.21)$$

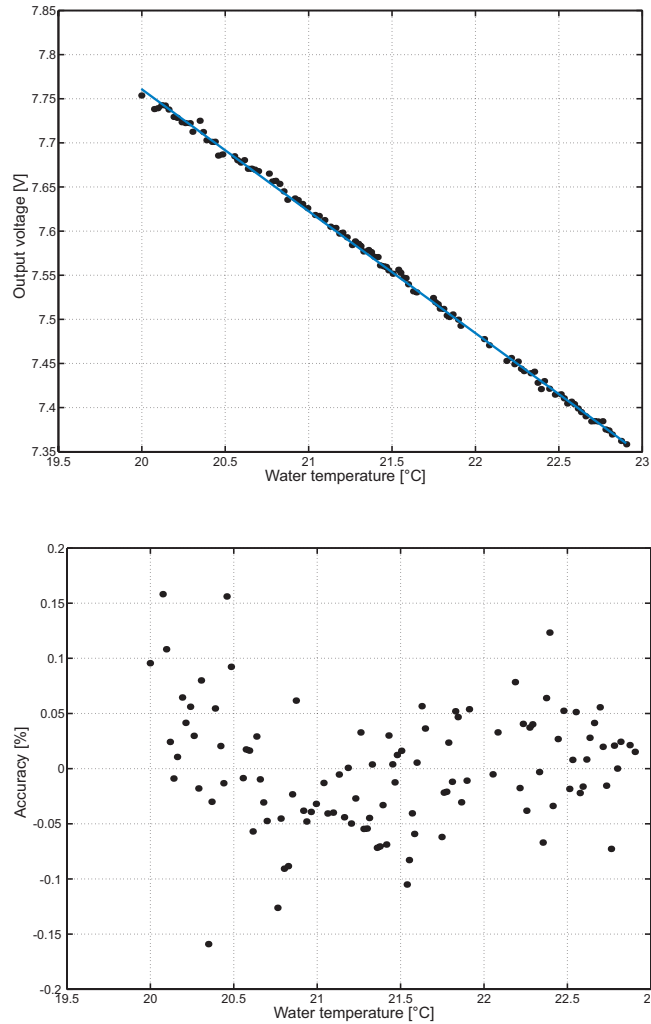


Figure 5.21: Variation of the output voltage of the hot-film probe with the water temperature in the cone

By comparison between the 2 temperature curves, see figure 5.22, in the calibration tunnel and in the cone of the Francis turbine, there can be noticed that the hot-film

probe is more sensible in the cone - the sensibility of the hot-film probe in the cone being  $0.138V/^{\circ}C$ , related to the one in the tunnel,  $0.123V/^{\circ}C$ . As sensor's interface is from bronze, the heat transfer between the bronze and steel, the hot-film probe being mounted on a steel plate in the tunnel, is higher than the heat transfer between the bronze and plexiglas, the hot-film probe being mounted on plexiglas in the cone.

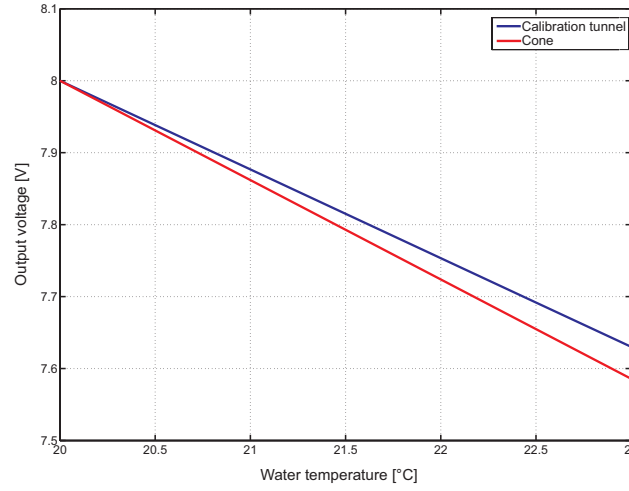


Figure 5.22: Temperature curves comparison obtained in the cone and in the calibration curve

For wall shear-stress measurements performed in the cone of a Francis turbine, the relation used to correct the measurements related to the anemometer's calibration temperature is illustrated by relation 5.22.

$$V_{cor} = -0.1382 \cdot (21.1 - \theta_{mes}) + V_{mes} \quad (5.22)$$

### The orientation of the hot-film probe in the flow

As the calibration showed, the maximal heat dissipation is obtained when the longitudinal direction of the film is perpendicular to the flow direction, meaning maximum voltage value at the output of the anemometer. For each operating point and for each spatial position of the probe in the cone, it is researched the maximum value for the voltage coming from the hot-film probe. For a constant mean wall shear-stress value, the variation of the measured wall shear-stress with the probe angle in the flow is presented in figure 5.24.

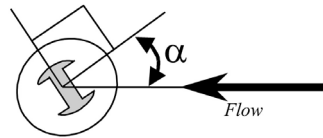


Figure 5.23: Angle made by the longitudinal direction of the hot film with the flow direction

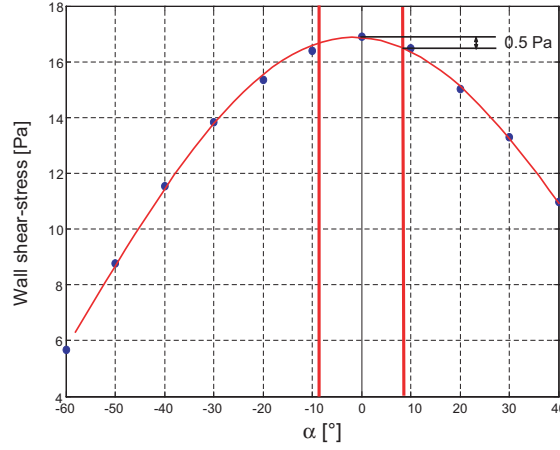


Figure 5.24: Influence of the hot-film probe orientation on the wall shear-stress

For the explored operating points, see Iliescu et al. [2002], the flow at the runner outlet is unsteady and the velocity angle variations near the wall are  $\pm 8^\circ$ , see figure 5.24, Ciocan et al. [2000]. As for the unsteady measurements, the hot-film probe was orientated on the mean flow direction, the change of the flow velocity direction with  $\pm 8^\circ$  leads to an estimated error for the unsteady component of about  $\pm 0.5\text{Pa}$ . Related to the mean wall shear-stress value of  $17\text{Pa}$ , this represents a systematical error of 3 %.

### Water contamination influence

As the calibration procedure has shown, due to the contamination of the hot-film probe with water impurities, during the measurements, the calibration curve changes. Due to the slope of the curve, deviations are observed and a calibration before and after each measurement, in a turbine configuration, can't be performed. To eliminate this inconvenient, one has to control and correct the slow drift of the calibration curve in the measurement zone. This inconvenient can be eliminated in 2 ways:

- if the difference between the wall shear-stress analogue values corresponding to the 2 calibration curves is smaller than 3%, the drift correction is performed, corresponding to figure 5.25;
- if the difference between the wall shear-stress analogue values corresponding to the 2 calibration curves exceed 3%, the coefficients of the calibration curve should be corrected.

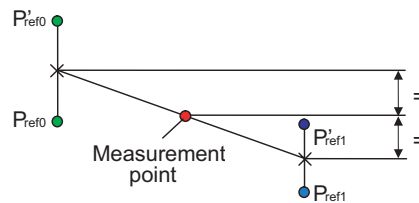


Figure 5.25: Drift correction scheme

For the turbine, 4 operating points, the nominal point for 4 different runner speeds, for each spatial position, are measured after the calibration and the wall shear-stress values are considered as reference. The reference operating points are measured at the beginning and at the end of the measurements day, corresponding to an spatial position of the hot-film probe in the cone.

For the first case mentioned above, the scheme for calculating the drift correction is presented in the figure 5.25. Because the difference between the analogues points does not exceed 3%, it can be applied the linear drift method, assuming that the measurement point it is placed on the line that gets together the middle of the distance between those analogue points, see figure 5.26.

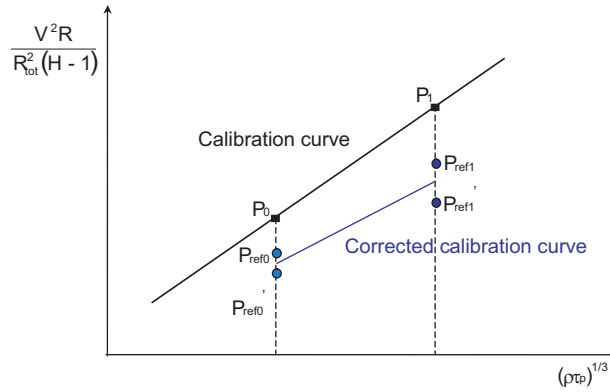


Figure 5.26: Method for correction the measurements

If the difference between the wall shear-stress analogue values corresponding to the 2 calibration curves exceeds 3%, the coefficients of the calibration curve are corrected in the way to obtain the same wall shear-stress values for the reference points before the drift, see figure 5.27.

These operations are repeated before and after every new operating point and for each spatial position of the hot-film probe in the cone.

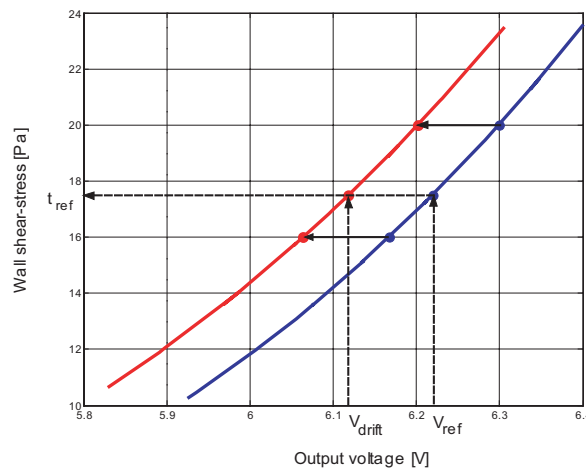


Figure 5.27: Measurements correction procedure

## 5.4 THE ANALYSIS OF THE RESULTS AT THE RUNNER OUTLET

Wall shear stress measurements are performed at the runner outlet for 4 standard operating points and 1 "partial load" operating point for  $2\sigma$  values. 9 spatial positions in the cone are explored, see figure 5.28.

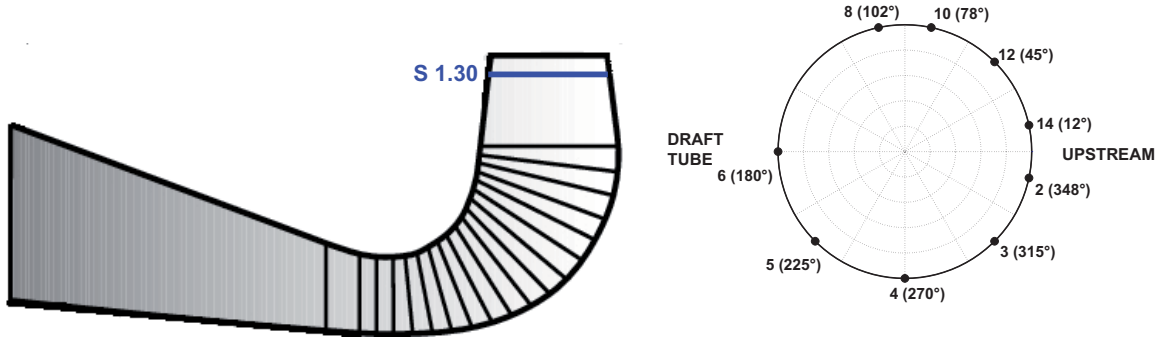


Figure 5.28: The spatial positions of the wall shear-stress probe in the measurement section at the runner outlet

The measurement system used for the signals acquisition in the cone is the same as the one used in the calibration procedure, right arm, see figure 4.4. The only difference is the synchronization of the signals acquisition with the runner position, realized by an optical encoder mounted on the runner shaft.

For the cone measurements, it is used the sampling frequency of  $3kHz$ ; there are acquired samples of 27000 data, meaning an acquisition time of 9 seconds. For every measurement, corresponding to an operating point, there were performed 11 acquisitions.

### 5.4.1 Near BEP operating points

#### Steady analysis

The purpose of the steady analysis regarding the wall shear-stress values, is to evaluate the distribution of the mean wall shear-stress and to offer informations regarding the boundary layer's tendencies of separation.

An analysis of the evolution of the wall shear-stress related to the operating points is proposed. The first representation, see figure 5.29, is related to the distribution of the wall shear-stress values with the spatial position and operating point. For each operating point the repartition is quite uniform. The same tendency is noticed for the mean pressure distribution, in the same section, at the cone inlet, see 5.30.

In a constant section, without separation tendencies, the wall shear-stress increases proportionally with the mean flow velocity. For all positions, in the present case, the tendency is opposite: the wall shear-stress decreases with the increasing of the mean flow velocity, see figure 5.31; this shows a separation tendency of the boundary layer.

As the draft tube characteristic, see figure 5.18, evidenced an important drop between  $\varphi_B = 0.368$  and  $\varphi_C = 0.38$  operating points, it is interesting to see, if this drop is due to a boundary layer separation. As figure 5.31 shows, the boundary layer is quasi identical

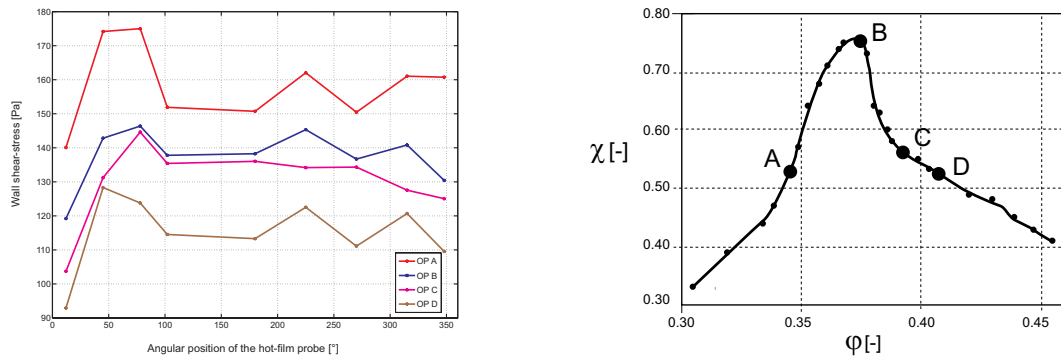


Figure 5.29: Steady wall shear-stress distributions at a distance of  $0.25\phi_{\text{runner}}$  from the runner outlet

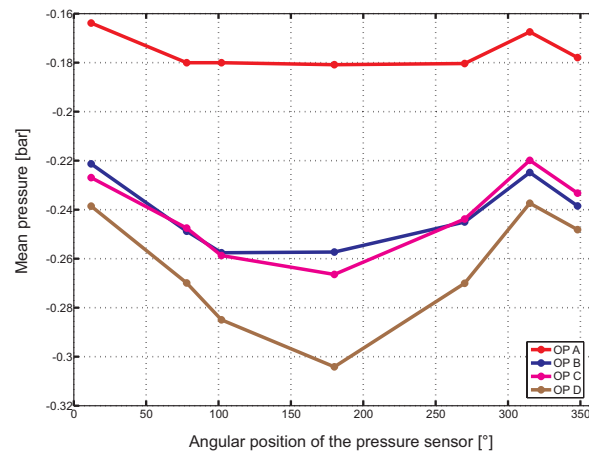


Figure 5.30: Mean pressure distribution with the operating point and the pressure sensor spatial position

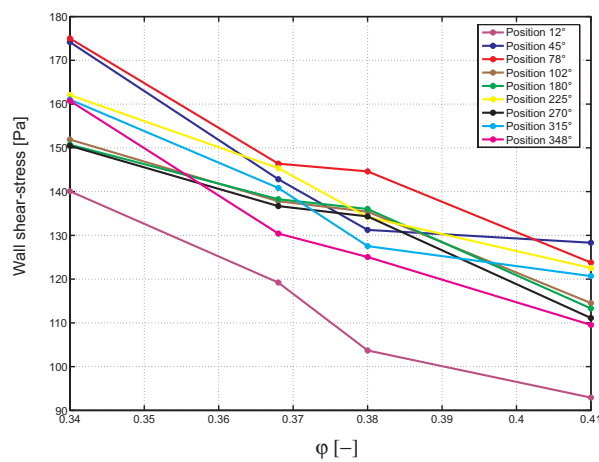


Figure 5.31: Wall shear stress distribution with the operating point and the hot-film probe spatial position

between  $\varphi_B = 0.368$  and  $\varphi_C = 0.38$  operating points, meaning that the boundary layer is not very sensitive to the velocity distribution in the section, Ciocan et al. [2000].

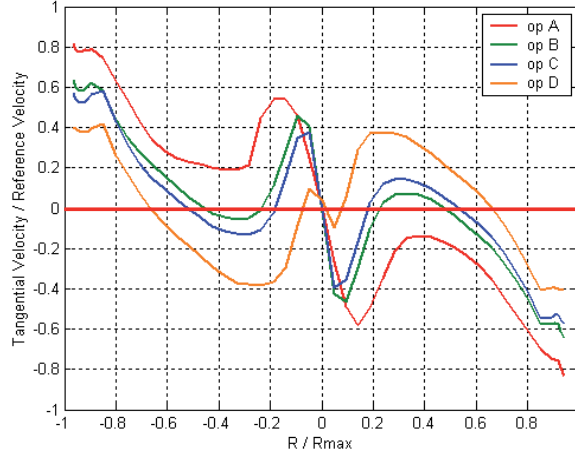


Figure 5.32: Tangential velocity components at the runner outlet

The stability of the runner outlet velocity profile, see figure 5.32, can be the main reason of the characteristic drop and not a boundary layer separation, see Susan-Resiga et al. [2006]. For this stability analysis of the runner outlet velocity profile, the boundary layer is no considered.

A comparison with the classical models of boundary layers, see figure 5.33, used by the classical CFD codes, is also presented, for 4 angular positions:  $78^\circ$ ,  $180^\circ$ ,  $270^\circ$  and  $348^\circ$ , see Mauri [2002]. The computed wall shear-stress values are underestimated with about 25% and there is not a significant difference between the different spatial positions of the hot-film probe.

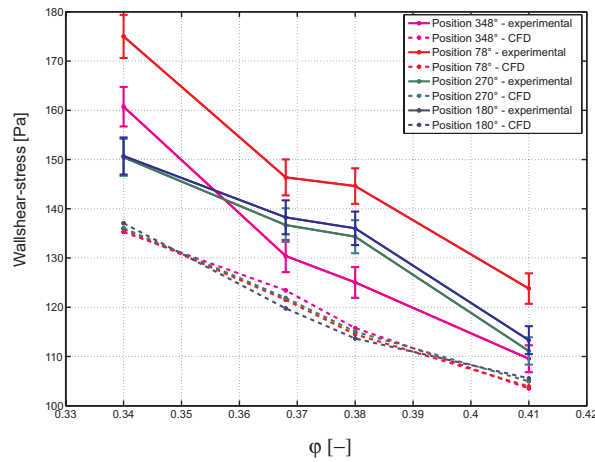


Figure 5.33: Comparison with the numerical approaches



### Unsteady analysis

The method used to separate the periodical fluctuations from the general fluctuations of the wall shear stress is called *synchronous average (phase average)*. This method allows to notice the influence of the runner position over the shear-stress distribution.

Thus, the instantaneous wall shear stress may be decomposed, for a period  $T$  of the blades passage, as it follows:

$$\tau(t) = \bar{\tau} + (\tilde{\tau}(t_1) - \bar{\tau}) + \tau'(t) \quad (5.23)$$

expression where:

- $\tau(t)$  - instantaneous value of the wall shear-stress;
- $\bar{\tau}$  - statistical average;
- $\tilde{\tau}(t_1)$  - synchronous average for an instant  $t_1$  of the period;
- $\tau'(t)$  - random turbulent fluctuations;
- $t_1$  - an instant of the period  $T$ , corresponding to an angular position,  $\varphi$  of the runner:  

$$t_1 = \frac{\varphi T}{2\pi}$$

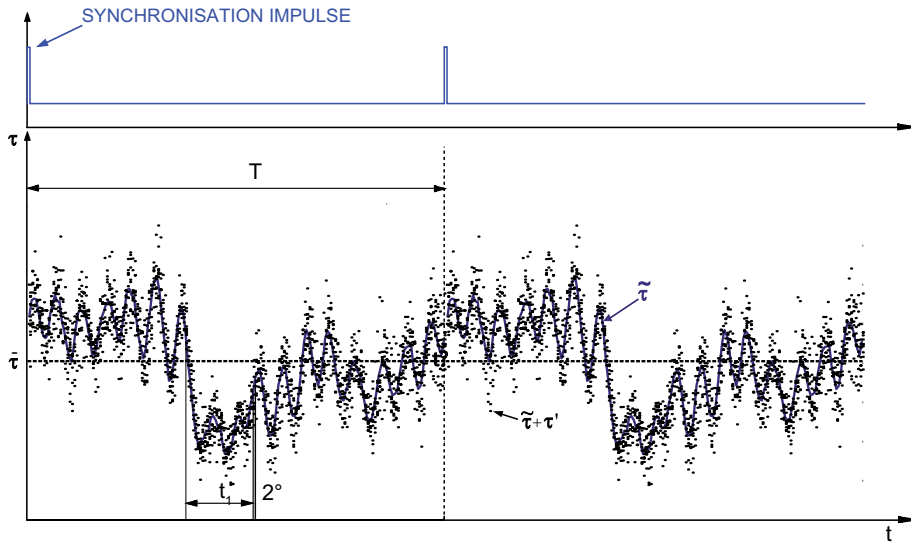


Figure 5.34: Phase average scheme

The spectral analysis evidences, for all spatial positions of the hot-film probe, two main characteristic frequencies: runner's rotating frequency and the blade passage frequency, see figures 5.35, 5.36, 5.37 and 5.38. The guide vanes frequency exists for several spatial positions of the probe, but with a small amplitude.

The synchronization of the signal acquisition and the runner position is realized by an optical encoder mounted on the runner shaft. It delivers a synchronizing signal with 1 pulse per rotation and a second signal with 9000 pulse per rotation. In this way, a phase average is performed for each of these characteristic frequencies.

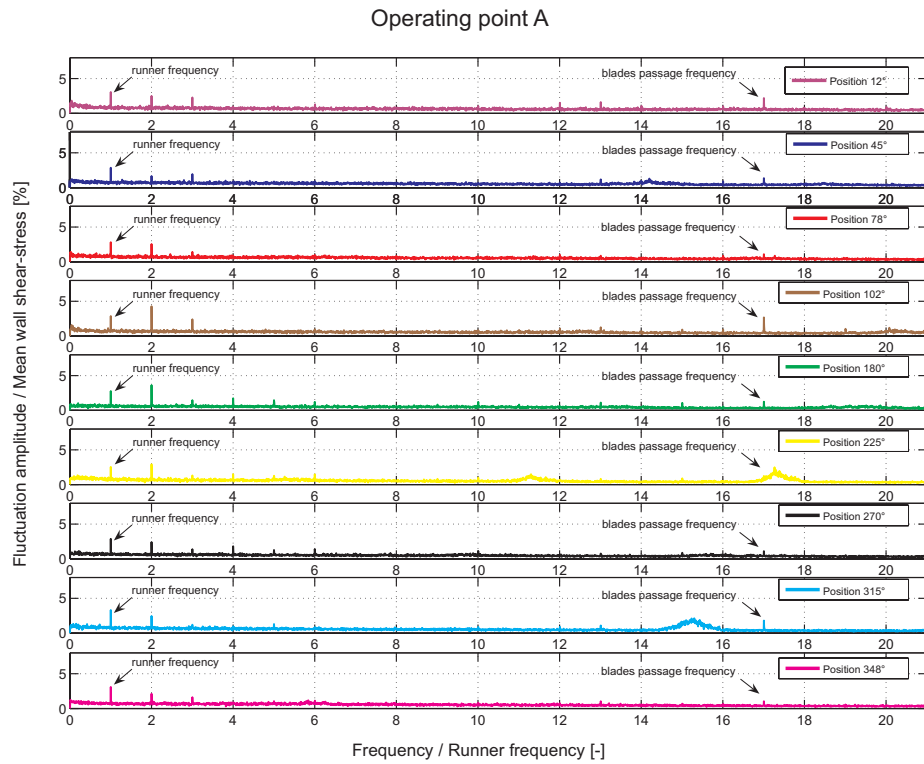


Figure 5.35: Spectral analysis of the wall shear-stress for operating point A

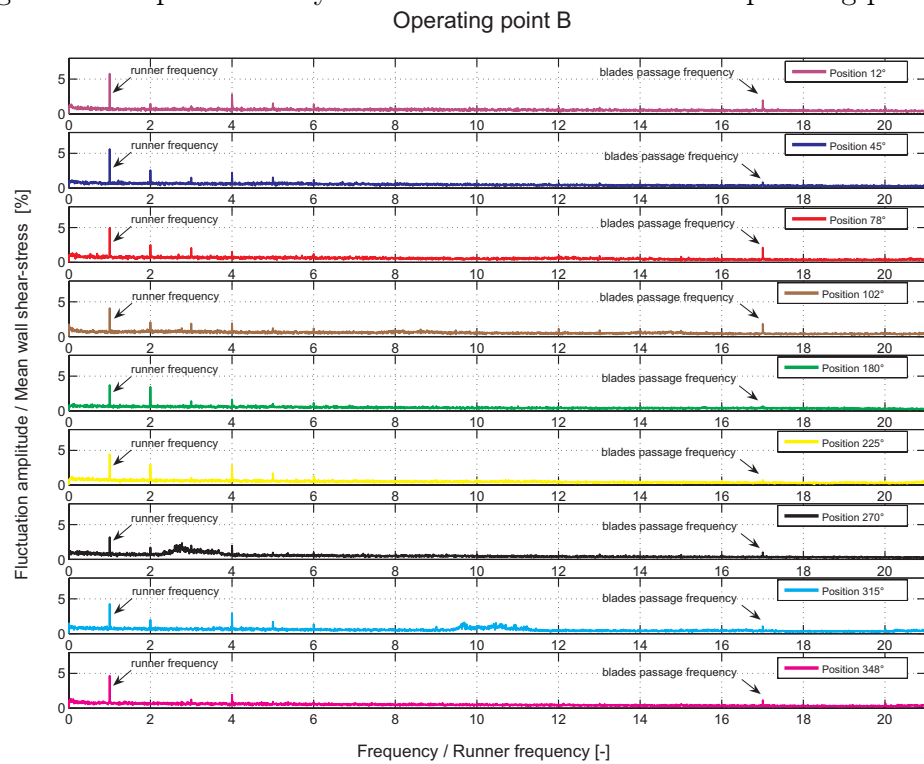


Figure 5.36: Spectral analysis of the wall shear-stress for operating point B

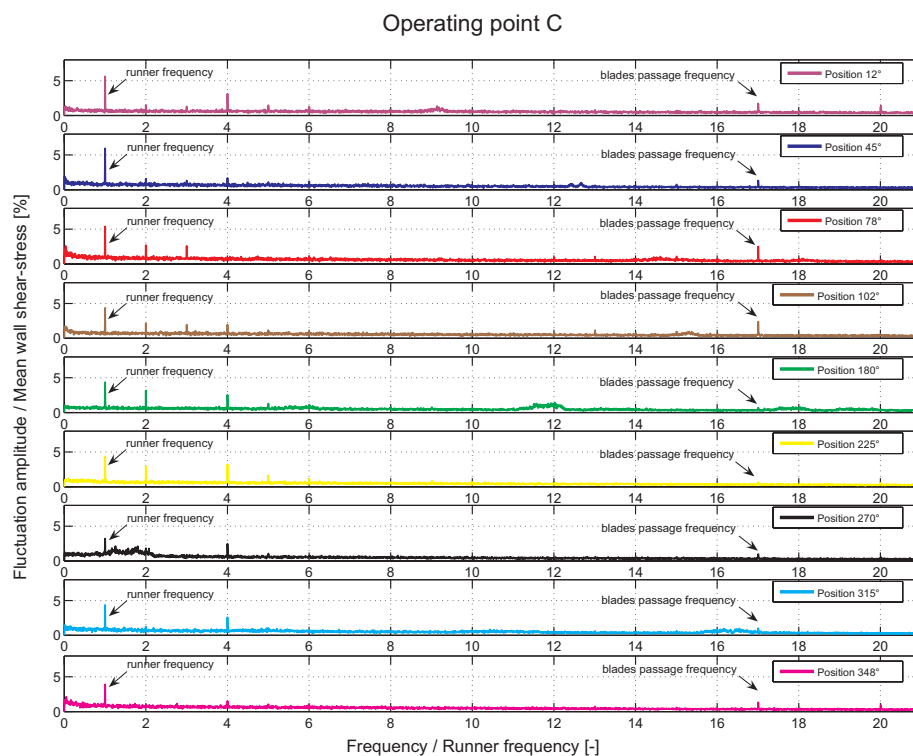


Figure 5.37: Spectral analysis of the wall shear-stress for operating point C

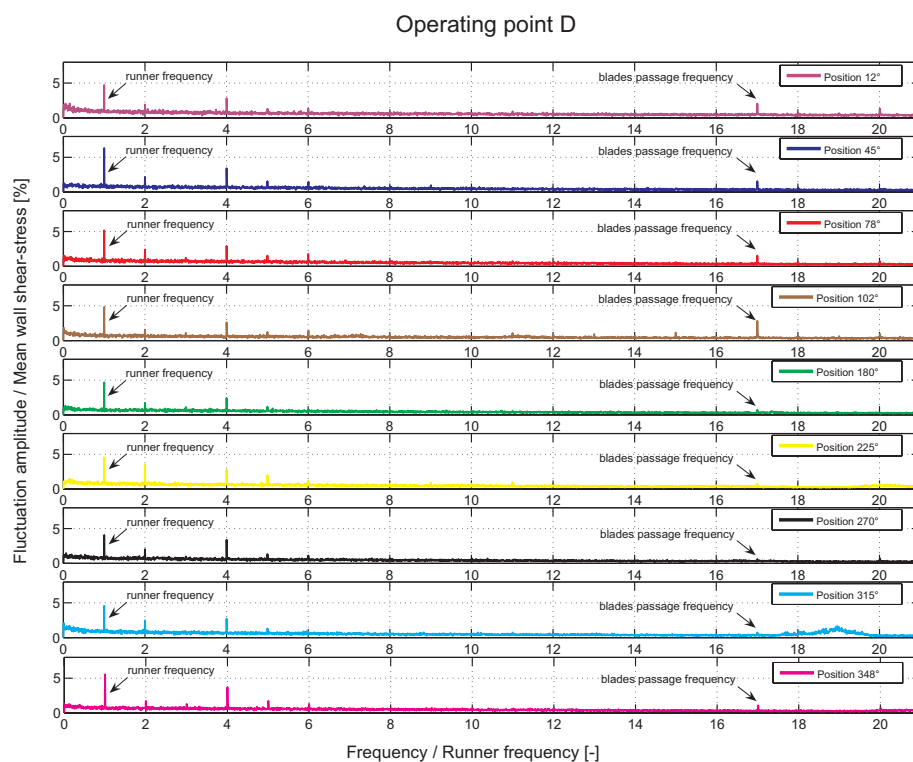


Figure 5.38: Spectral analysis of the wall shear-stress for operating point D

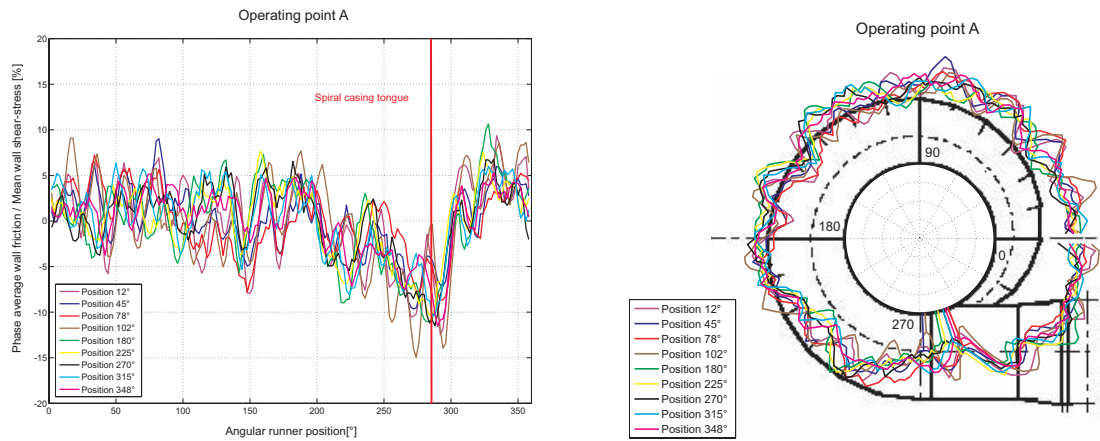


Figure 5.39: Wall shear stress phase average with runner rotation, operating point A

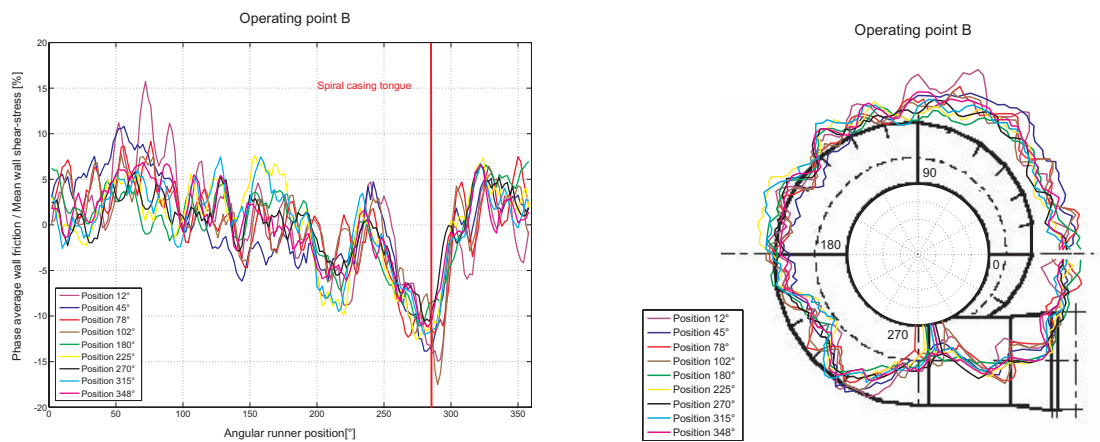


Figure 5.40: Wall shear stress phase average with runner rotation, operating point B

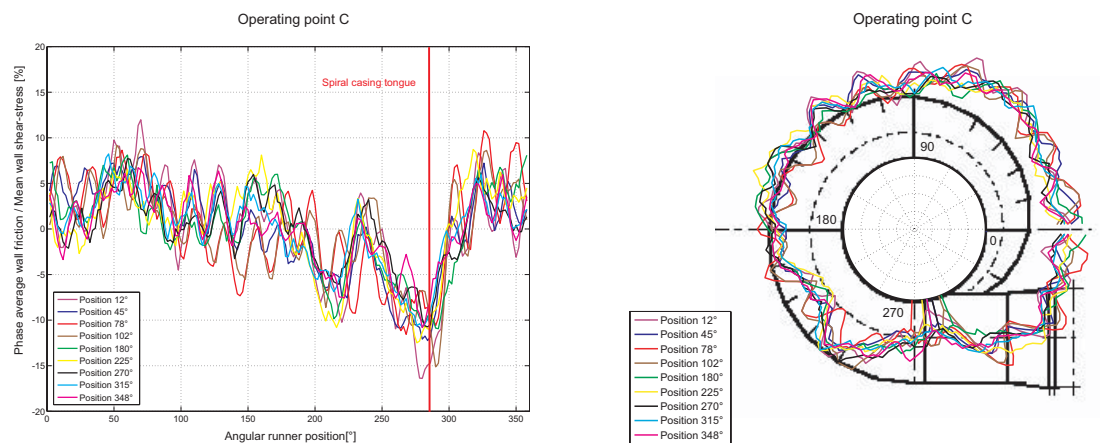


Figure 5.41: Wall shear stress phase average with runner rotation, operating point C

A drop is evidenced for the phase average performed with the runner's rotating frequency, corresponding to all spatial positions, see figures 5.39, 5.40, 5.41 and 5.42.

As all acquisitions are started at the same spatial runner position, and the angular position of the sensor are known in the cone, there are represented all the phase averages

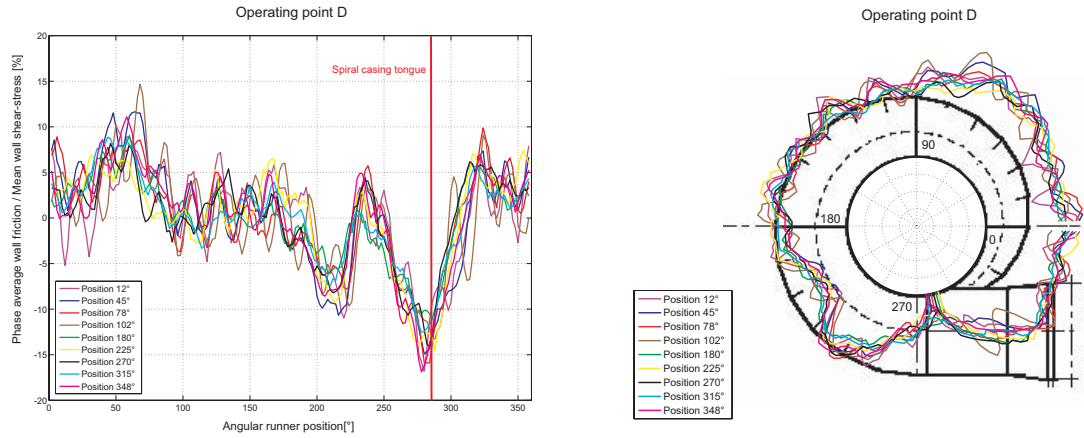


Figure 5.42: Wall shear stress phase average with runner rotation, operating point D

for the same absolute angular position. So, the drop position corresponds spatially at the spiral casing tongue location.

At the runner outlet, the wall shear-stress distribution reproduces the non-uniformity in the spatial pressure and velocity distributions in the same section, see Ciocan [1998], modulated with the runner speed.

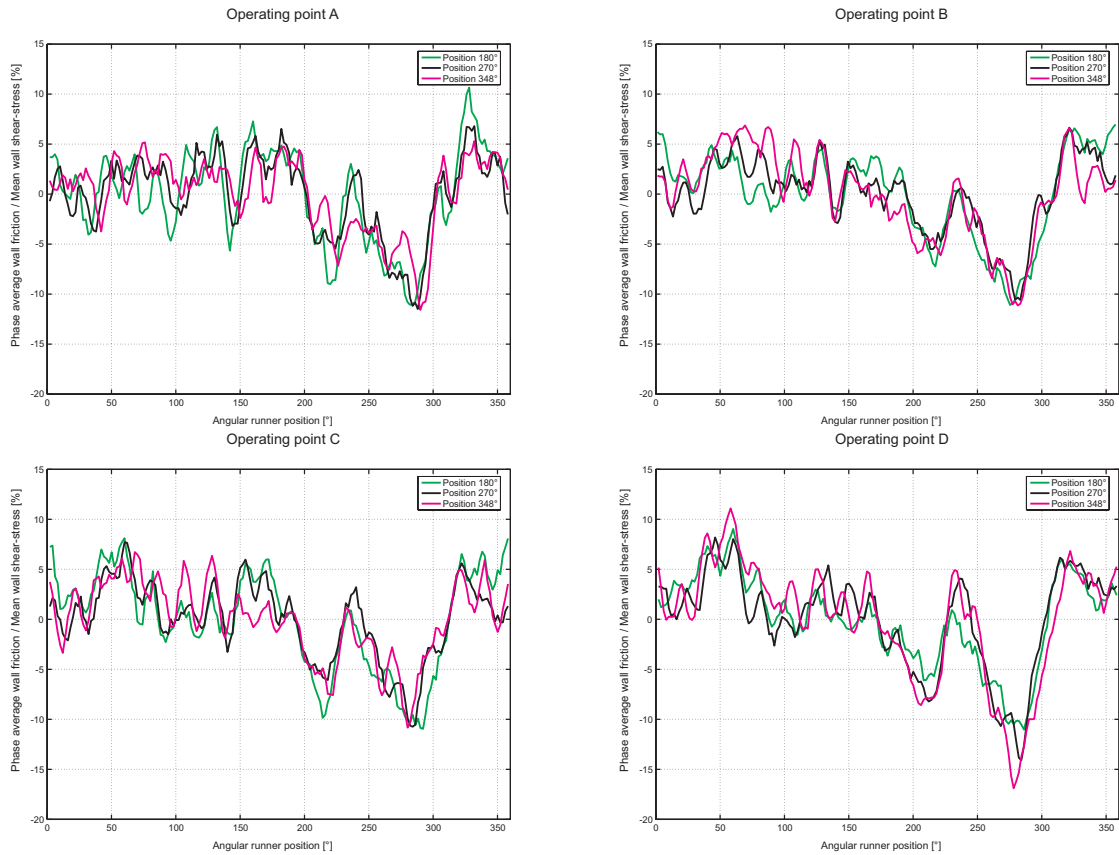


Figure 5.43: The signals in phase corresponding to all standard operating points

The fluctuation magnitudes are 20% of the wall shear-stress mean value for the values synchronous with the runner rotation.

The phase average performed for the runner's rotating frequency has evidenced also that a signal was shifted related to the others; figure 5.43 shows 3 signals corresponding to 3 sensor's positions:  $180^\circ$ ,  $270^\circ$  and  $348^\circ$  which are in phase for all 4 operating points; for the  $78^\circ$  position, the signal is shifted with a half of the blade passage period, see figure 5.44, explained by the elbow effect. The phase shift represents a flow deceleration or acceleration related to the hot-film spatial position and induced by the pressure gradient between the elbow's upstream and downstream sections. The same characteristics are obtained on the unsteady wall pressure measurements, see Ciocan et al. [2001].

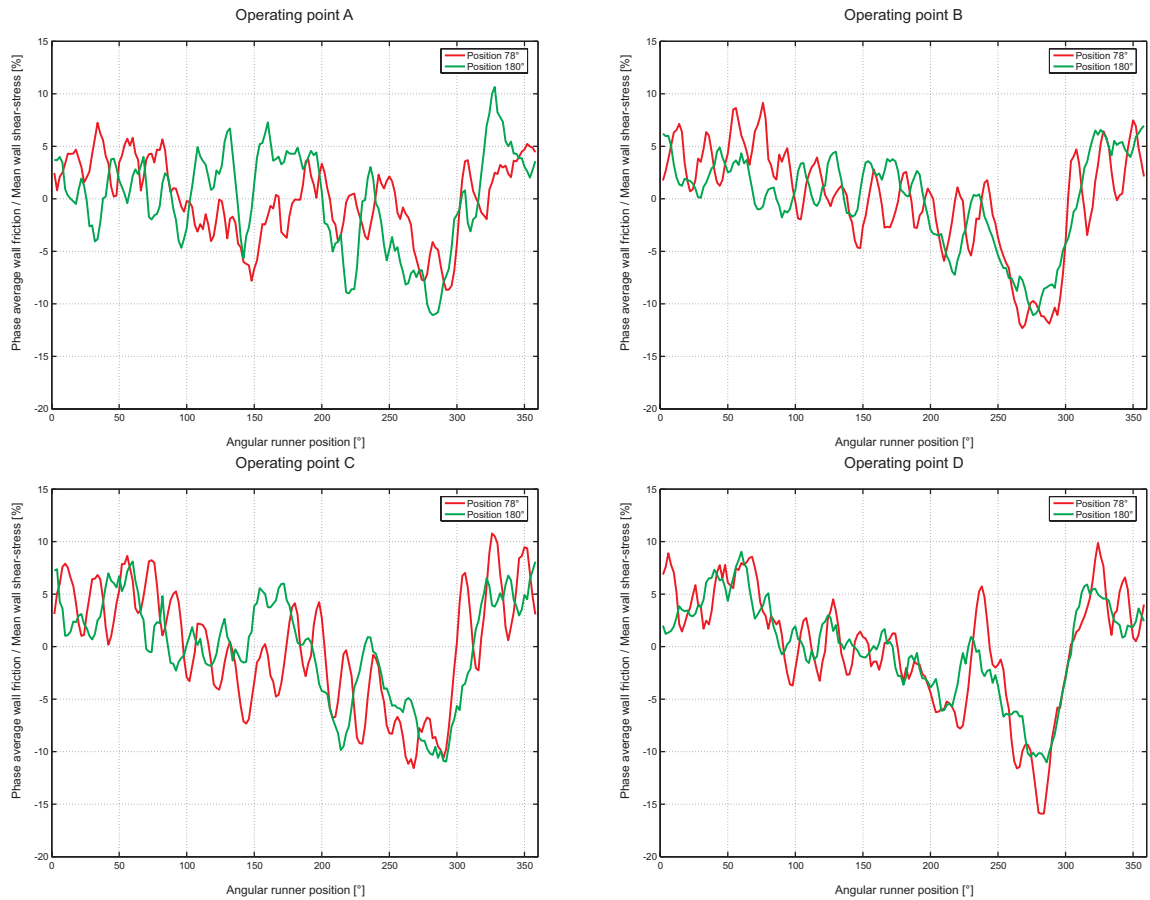


Figure 5.44: The signal shifted evidenced for all standard operating points

The phase average, made on the blade passage evidences that the fluctuation amplitude represents 2.5% of the mean wall shear-stress value, see figure 5.45, for all standard operating points. These results are coherent with the phase average velocity measurements - see Ciocan et al. [2000].

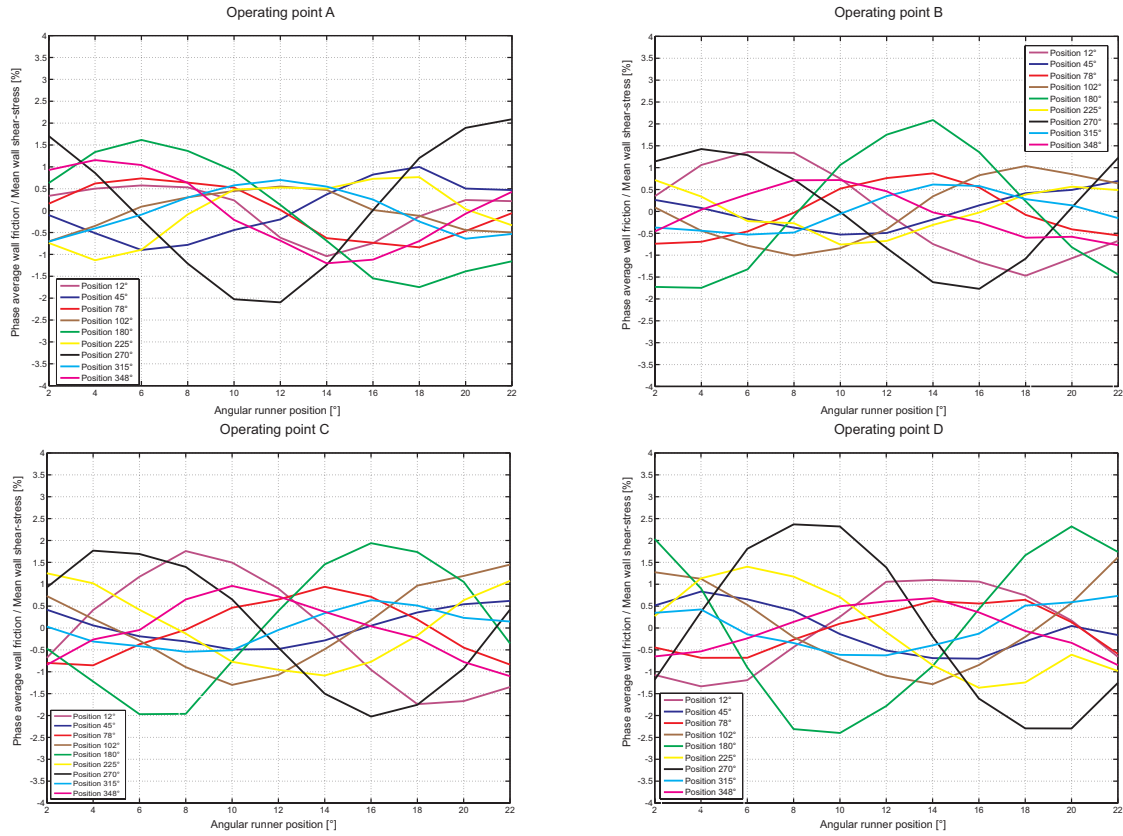


Figure 5.45: Wall shear stress phase average with the blade passage

### 5.4.2 Partial load operating points

#### Steady analysis

The distribution of the wall shear-stress values with the spatial position related to the partial load operating points at the cone's inlet is shown in figure 5.46.

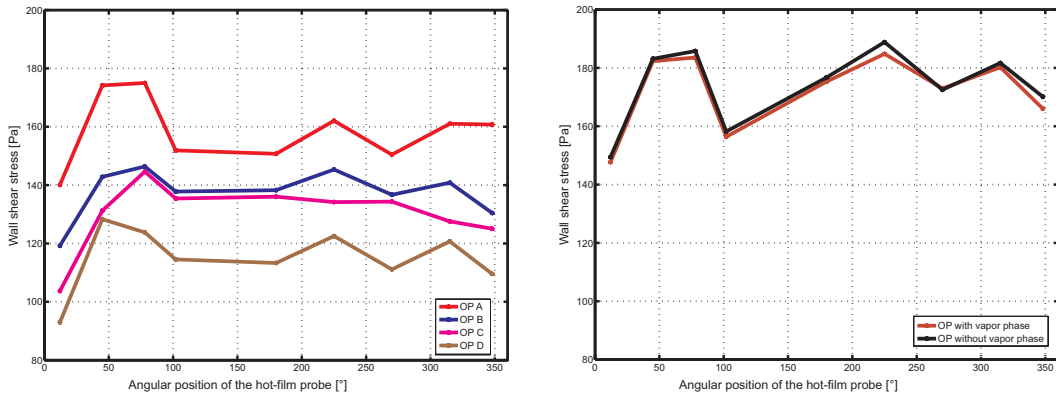


Figure 5.46: Steady wall shear-stress distributions at the cone's inlet, for both the near BEP and partial load operating points



It is noticed that the steady wall shear-stress values obtained for both partial load operating points, with and without vapor phase, are higher than the ones obtained for the standard operating points. Moreover, it is evidenced that for every spatial position of the hot-film probe in the section there is no difference between the steady wall shear-stress values corresponding to the 2 partial load operating points, with high  $\sigma$  and low  $\sigma$ .

### **Unsteady analysis**

The spectral analysis performed for every partial load operating points evidences one characteristic frequency: vortex's rotating frequency, see figures 5.47, 5.49, 5.51, 5.53, 5.55, 5.57, 5.59, 5.61 and 5.63, corresponding to every angular position of the hot-film probe at the runner outlet.

For this characteristic frequency there was performed the phase average, for every spatial position of the probe at the cone inlet, and for every partial load operating point, see figures 5.48, 5.50, 5.52, 5.54, 5.56, 5.58, 5.60, 5.62 and 5.64.

For every angular position of the probe, the same tendency is noticed: the rope frequency is dominant and its amplitude is higher (15%) for the high  $\sigma$  value (without vapor phase); it decreases with the increasing of the vapor phase. This higher amplitude is explained by the proximity of the rope to the wall.



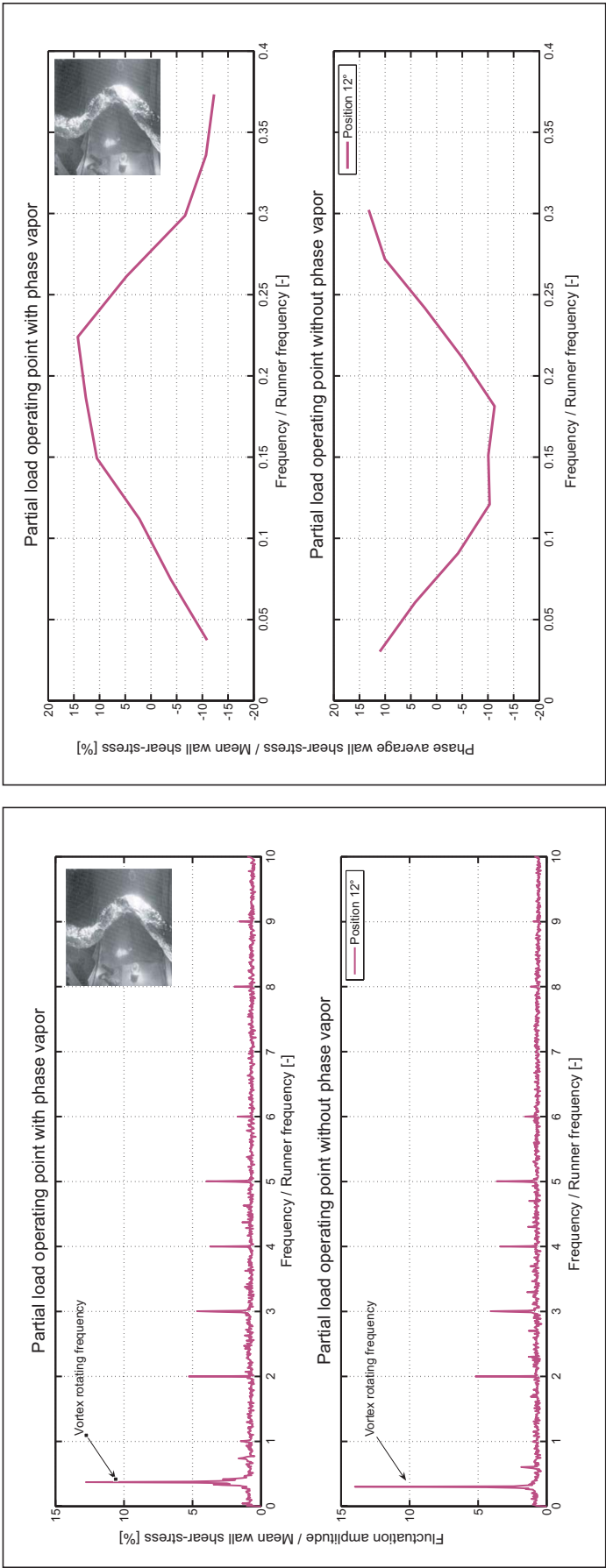


Figure 5.47: Spectral analysis for partial load operating points, corresponding to angular position 12°

Figure 5.48: Wall shear stress phase average with the vortex frequency for angular position 12°

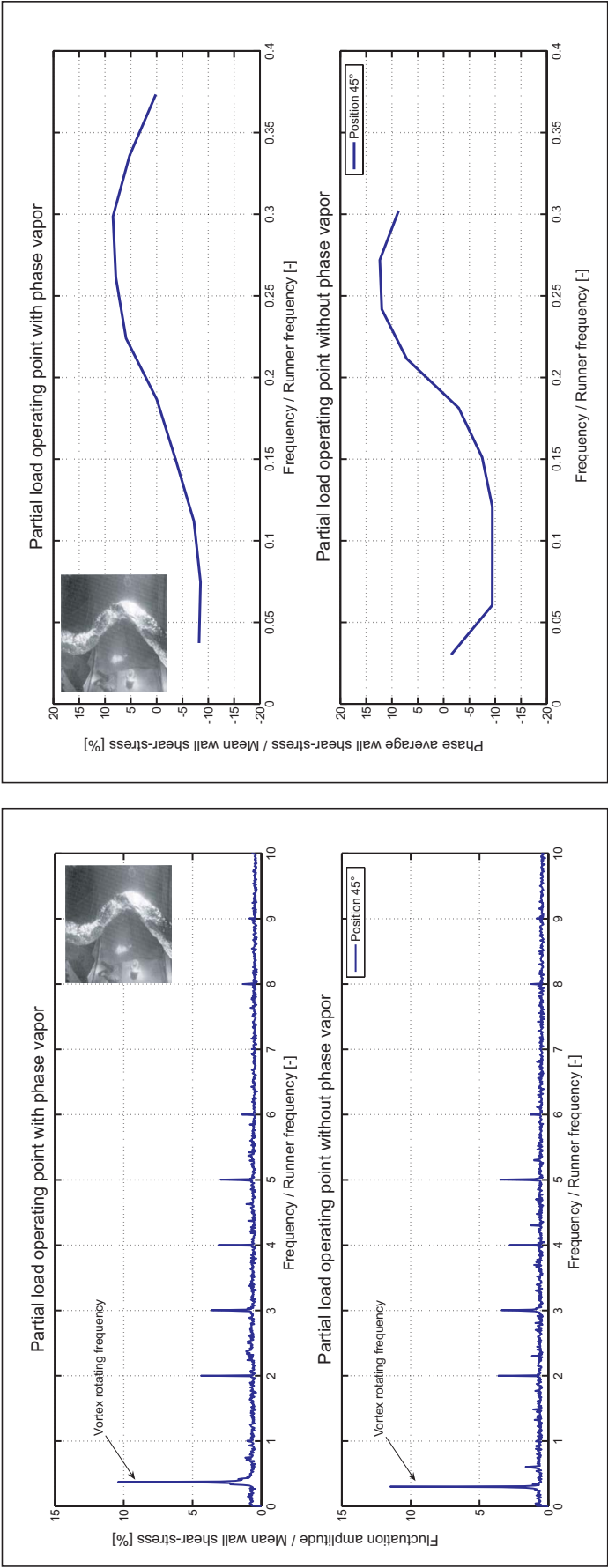


Figure 5.49: Spectral analysis for partial load operating points, corresponding to angular position 45°

Figure 5.50: Wall shear stress phase average with the vortex frequency for angular position 45°

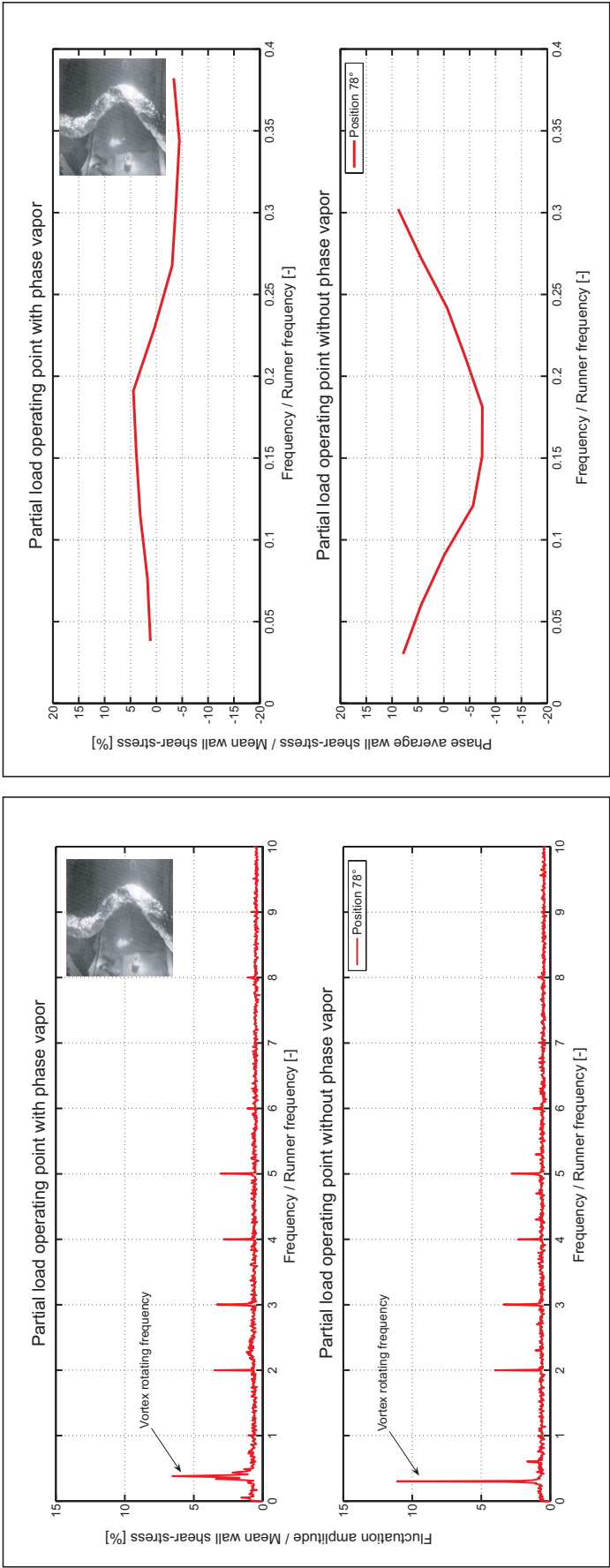


Figure 5.51: Spectral analysis for partial load operating points, corresponding to angular position 78°

Figure 5.52: Wall shear stress phase average with the vortex frequency for angular position 78°

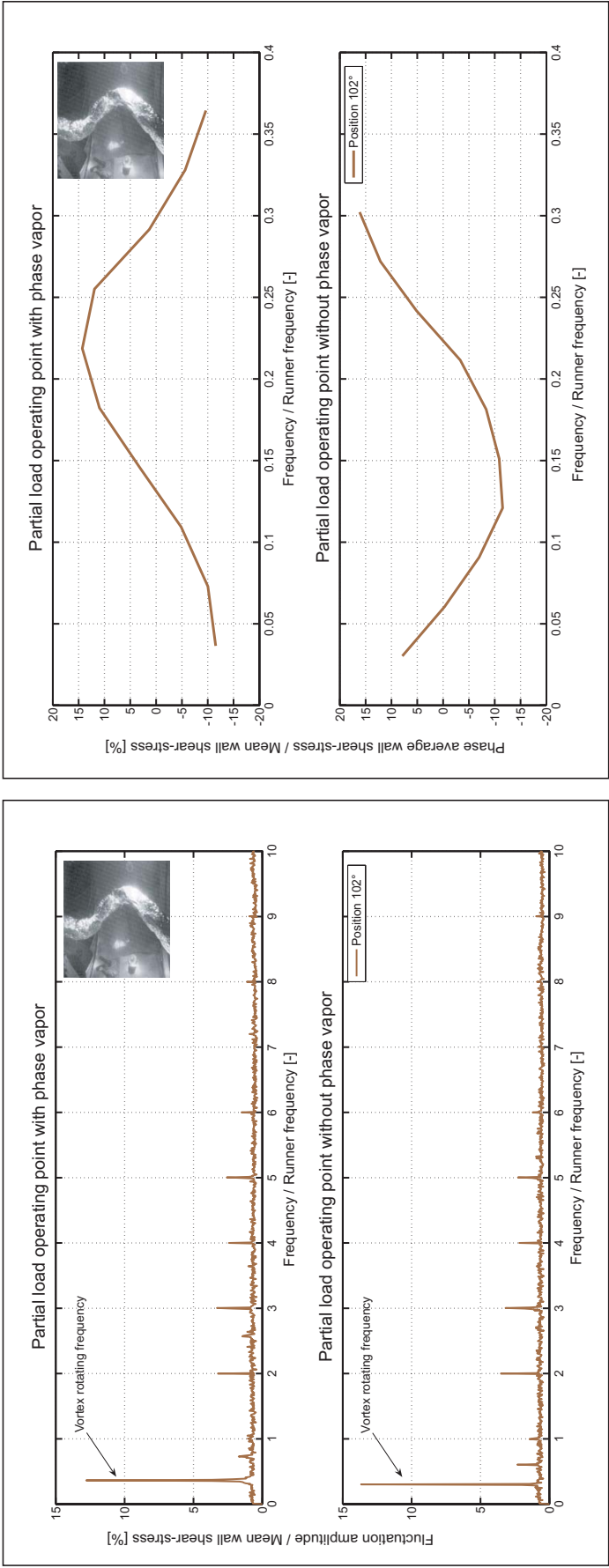


Figure 5.53: Spectral analysis for partial load operating points, corresponding to angular position 102°

Figure 5.54: Wall shear stress phase average with the vortex frequency for angular position 102°

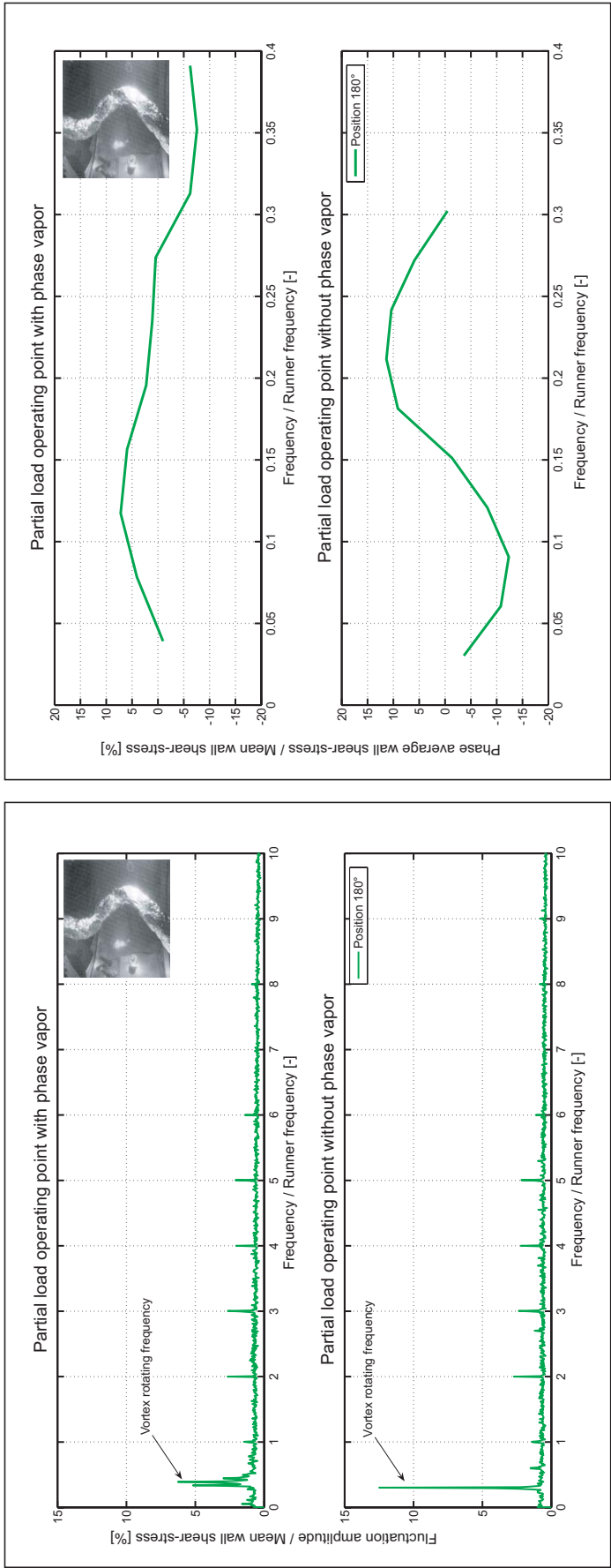


Figure 5.55: Spectral analysis for partial load operating points, corresponding to angular position 180°

Figure 5.56: Wall shear stress phase average with the vortex frequency for angular position 180°

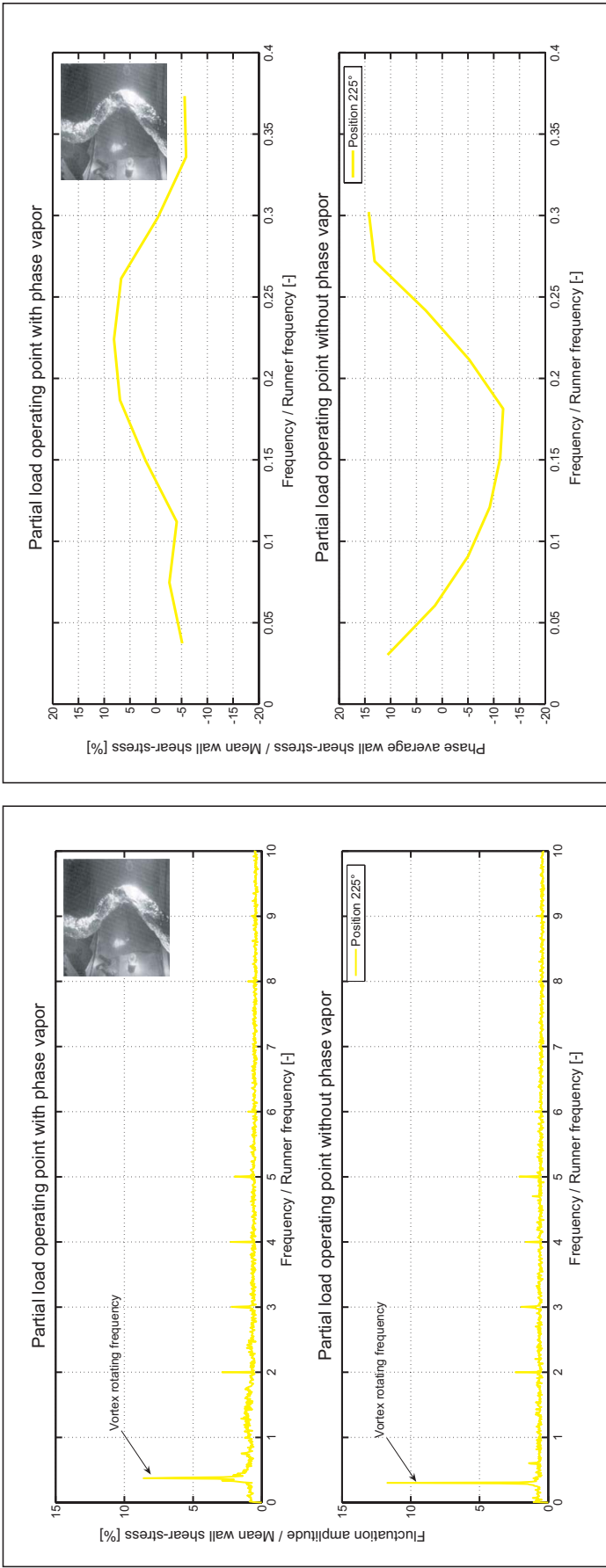


Figure 5.57: Spectral analysis for partial load operating points, corresponding to angular position 225°

Figure 5.58: Wall shear stress phase average with the vortex frequency for angular position 225°

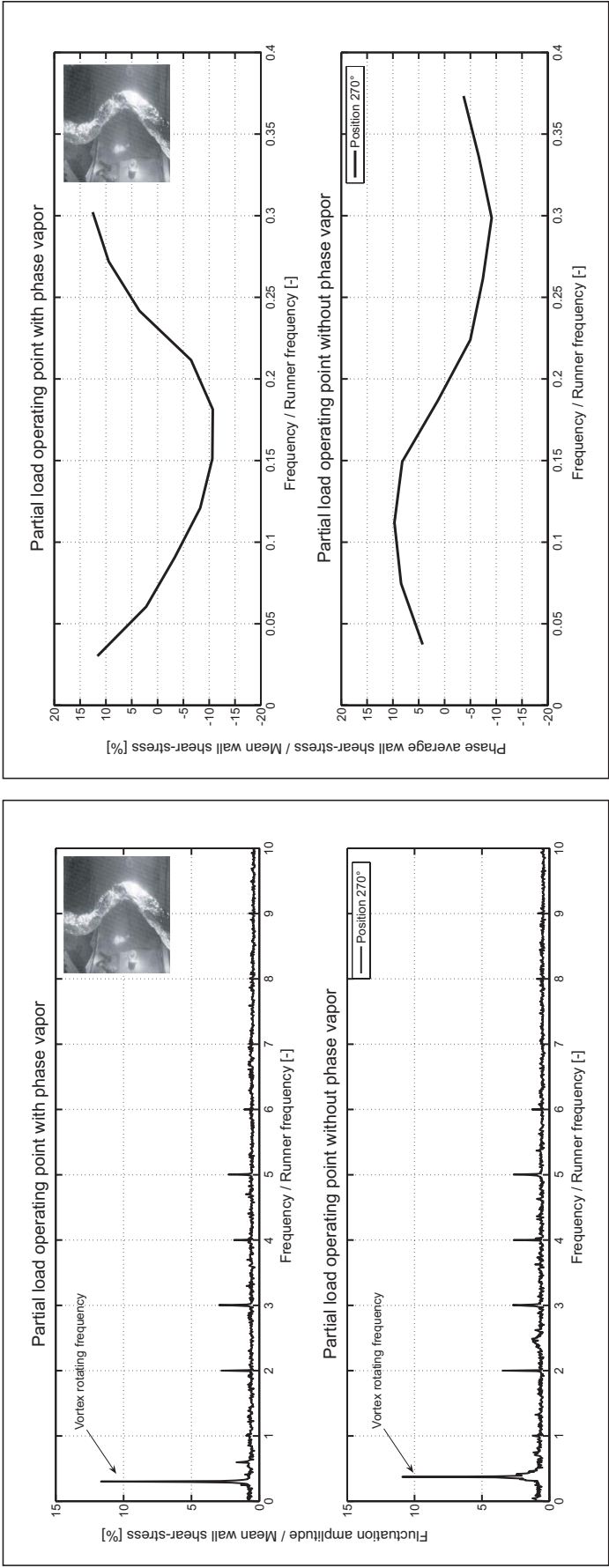


Figure 5.59: Spectral analysis for partial load operating points, corresponding to angular position 270°

Figure 5.60: Wall shear stress phase average with the vortex frequency for angular position 270°

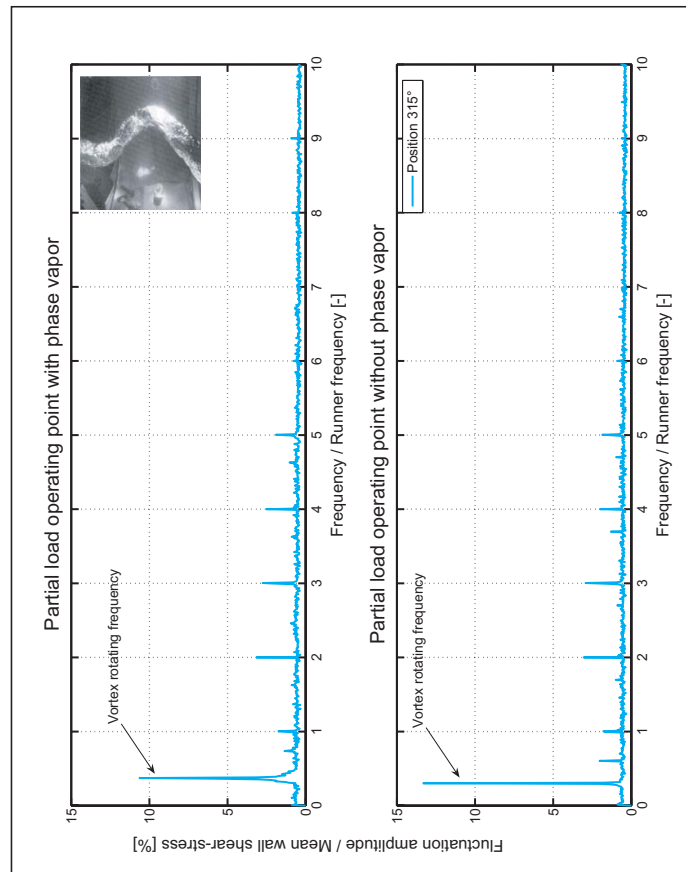


Figure 5.61: Spectral analysis for partial load operating points, corresponding to angular position 315°

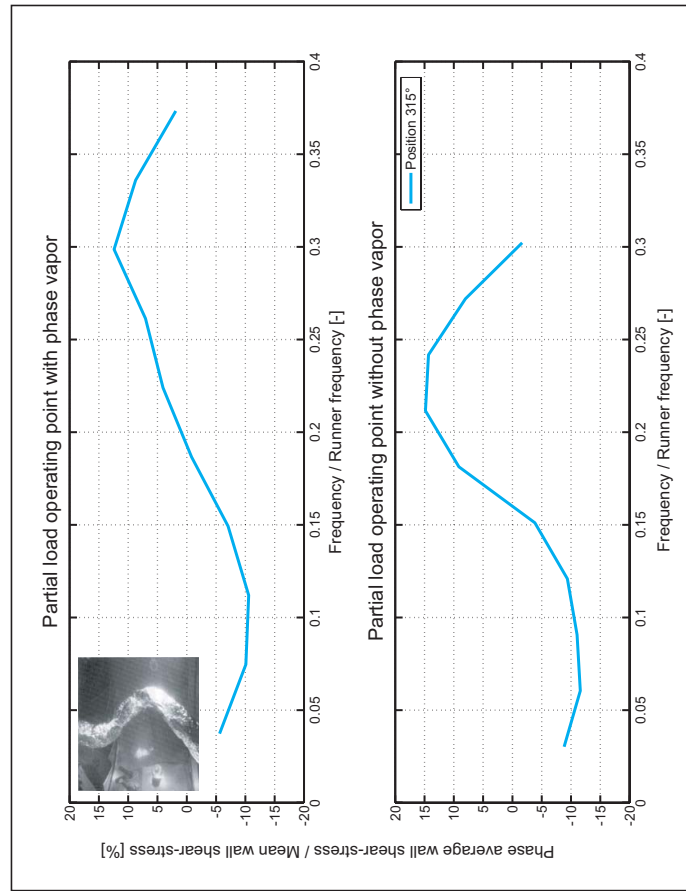


Figure 5.62: Wall shear stress phase average with the vortex frequency for angular position 315°



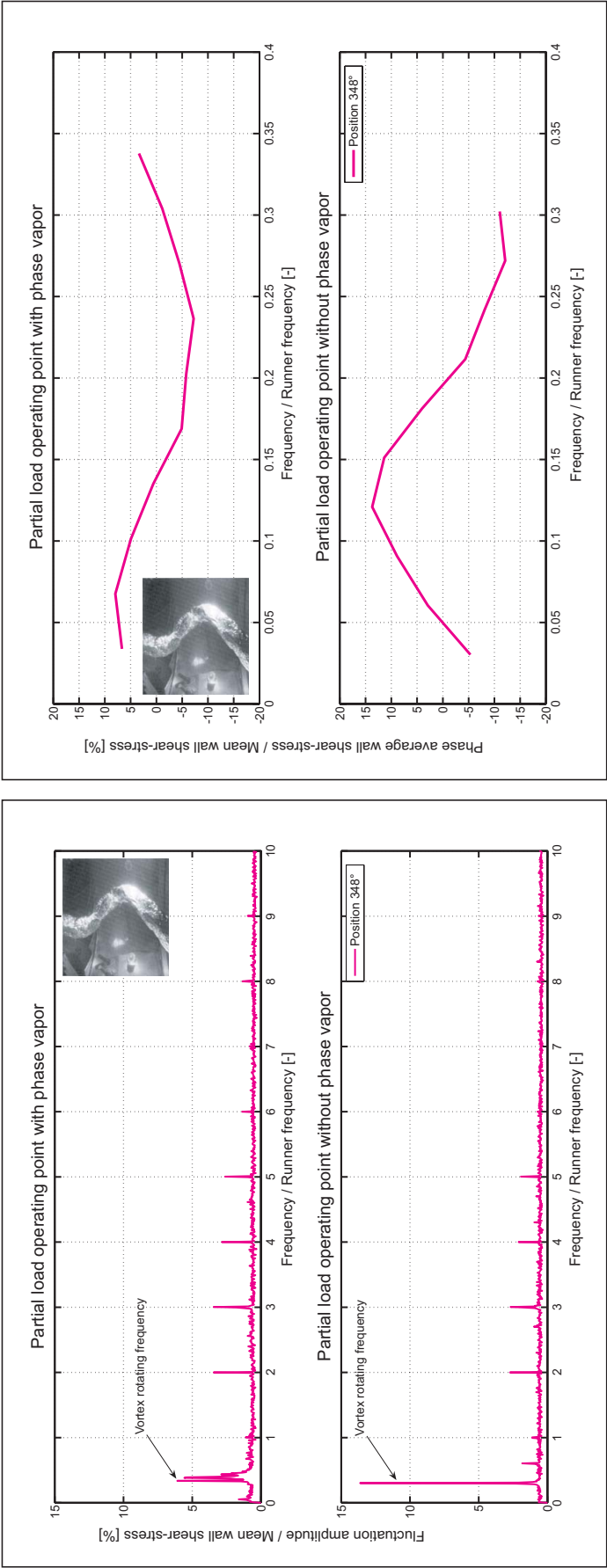


Figure 5.63: Spectral analysis for partial load operating points, corresponding to angular position 348°

Figure 5.64: Wall shear stress phase average with the vortex frequency for angular position 348°

## 5.5 THE ANALYSIS OF THE RESULTS AT THE CONE OUTLET

Wall shear stress measurements are also performed at the cone outlet for the same 4 standard operating points and 1 partial load operating point for  $2\sigma$  values, as at the runner outlet; 7 spatial positions in this cone section are explored, see figure 5.65.

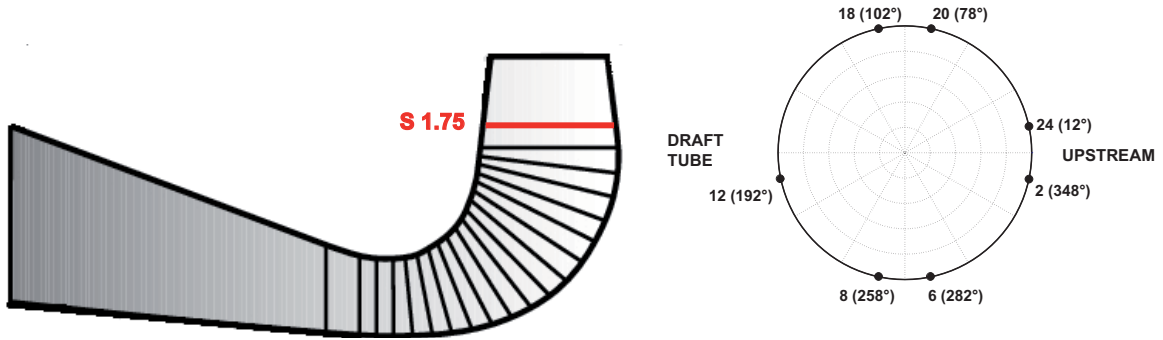


Figure 5.65: The spatial positions of the wall shear-stress probe in the measurement section at the cone outlet

### 5.5.1 Near BEP operating points

#### Steady analysis

An analysis of the evolution of the wall shear-stress related to the operating points at the cone's outlet is proposed. The first representation, see figure 5.66, is related to the distribution of the wall shear-stress values with the hot-film probe's spatial position and operating point. In this section it is remarked the bend influence over the wall shear-stress distribution. As a matter of fact, around  $180^\circ$  position, that corresponds to the bend position, the wall shear-stress values are 25% less than the values corresponding to the upstream positions. As at the cone inlet, at the cone outlet, the wall shear-stress distribution has the same tendency as the mean pressure distribution, see figure 5.67.

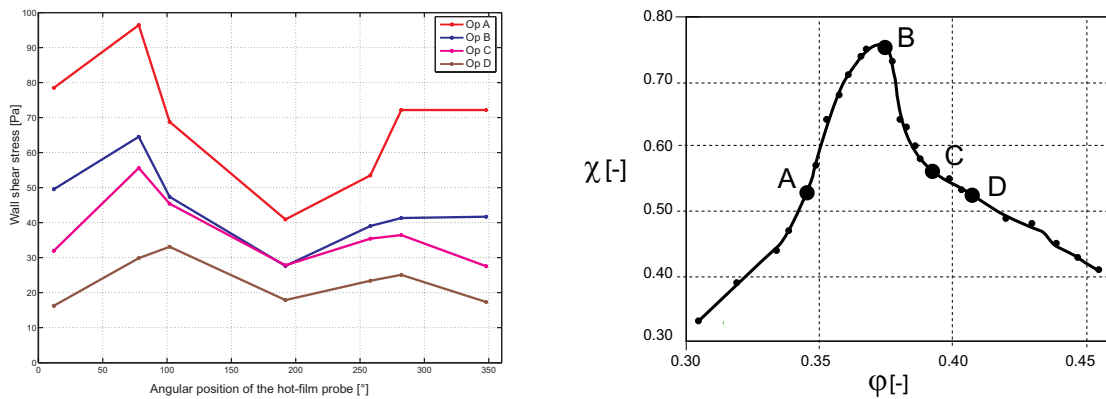


Figure 5.66: Steady wall shear-stress distributions at the Francis cone outlet

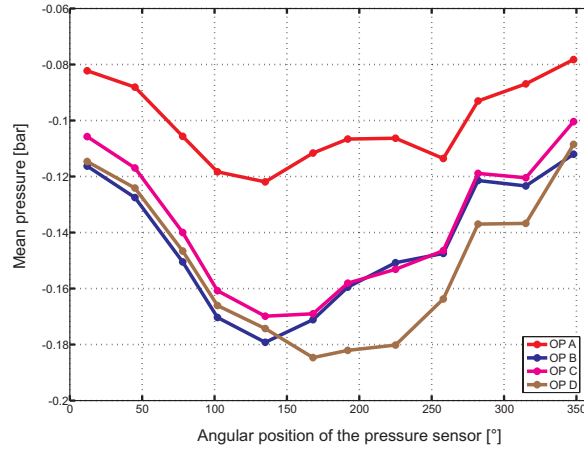


Figure 5.67: Mean pressure distribution at the cone outlet with the operating point

The second representation, see figure 5.68, concerns the comparison between the steady wall shear-stress distributions with the angular position and operating point, for the 2 measurement sections, the cone inlet and outlet. The wall shear-stress values are about 1/3 of the runner exiting values for all standard operating points.

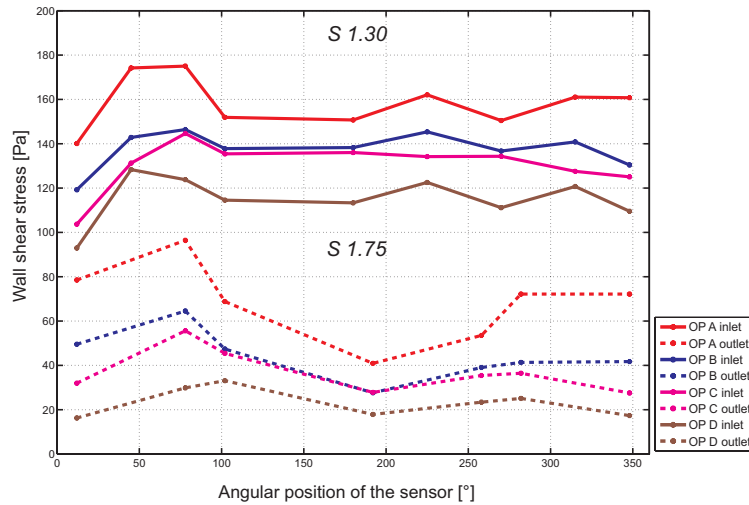


Figure 5.68: Steady wall shear-stress distributions at the cone inlet and outlet

For the cone outlet the same tendency like at the runner outlet exists: the wall shear-stress decreases with the increasing of the mean flow velocity, see figure 5.69; this shows a separation tendency of the boundary layer with the flow rate increasing.

As in the runner outlet section, the boundary layer is quasi identical between  $\varphi_B = 0.368$  and  $\varphi_C = 0.38$  operating points.

It is noticed that the hot-film probe was placed in 4 common spatial positions in the 2 measurement sections: positions  $12^\circ$ ,  $78^\circ$ ,  $102^\circ$  and  $348^\circ$ . By comparison between those common angular positions of the hot-film probe, see figure 5.70, it is remarked the major difference in the wall shear-stress values obtained at the same angular position of the

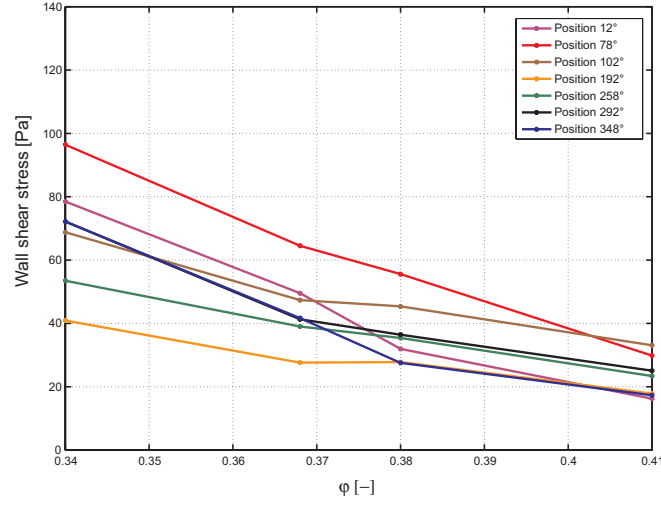


Figure 5.69: Wall shear stress distribution with the operating point and the spatial position, at the cone outlet

probe in the 2 sections and that the values obtained at the inlet are 3 times higher than the ones obtained at the outlet.

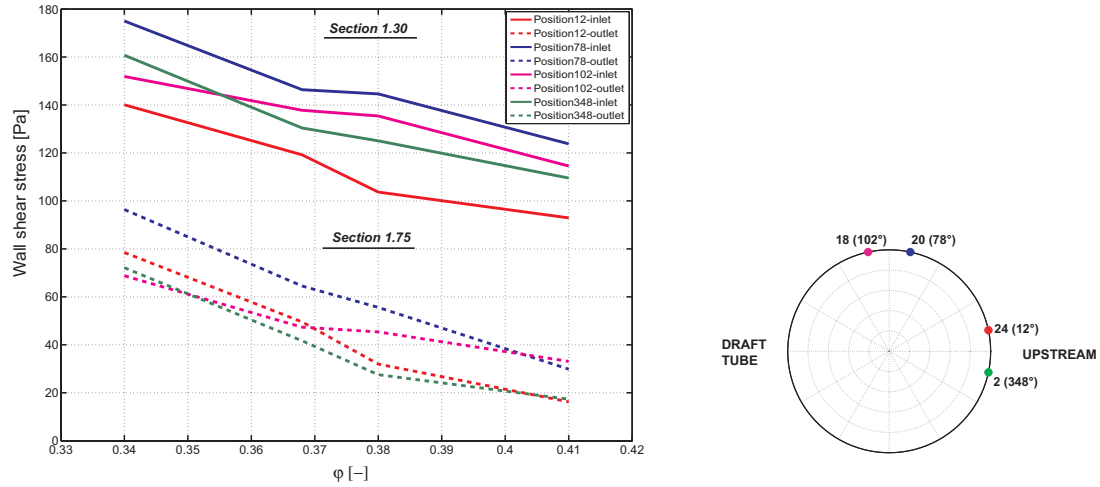


Figure 5.70: Wall shear stress distribution with the operating point for the same spatial positions, at the cone inlet and outlet

### Unsteady analysis

The spectral analysis performed for the near BEP operating points does not evidence, for any spatial position, any characteristic frequency see figures 5.71 to 5.77. The runner characteristic frequency appears, for some operating points and several angular positions of the hot-film probe at the cone outlet; its amplitude is rather small - around 3% of the mean wall shear-stress value.

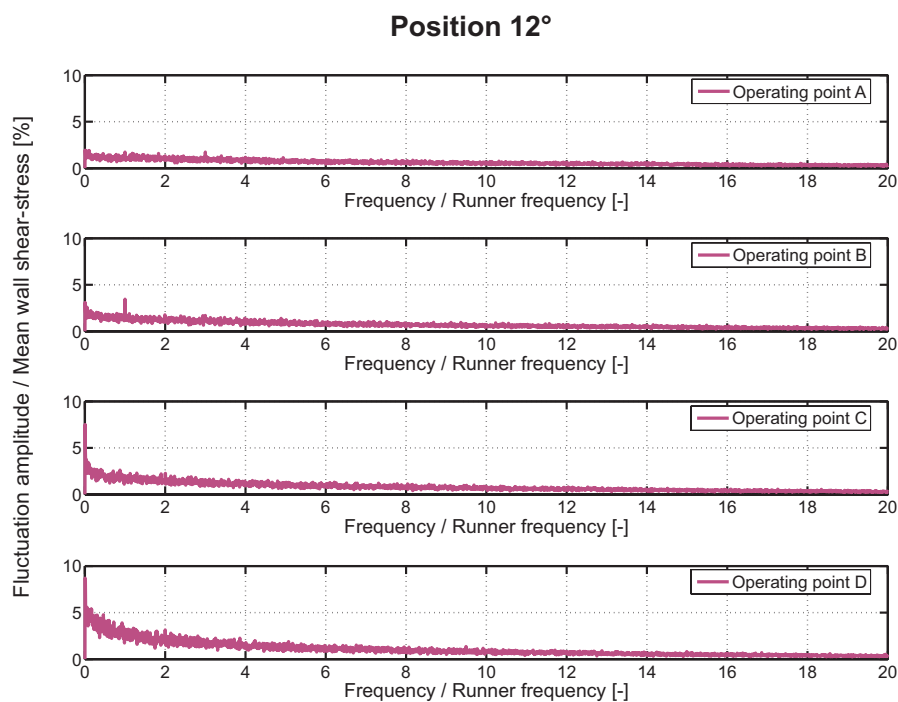


Figure 5.71: Spectral analysis of the wall shear-stress corresponding to the 12° angular position of the hot-film probe

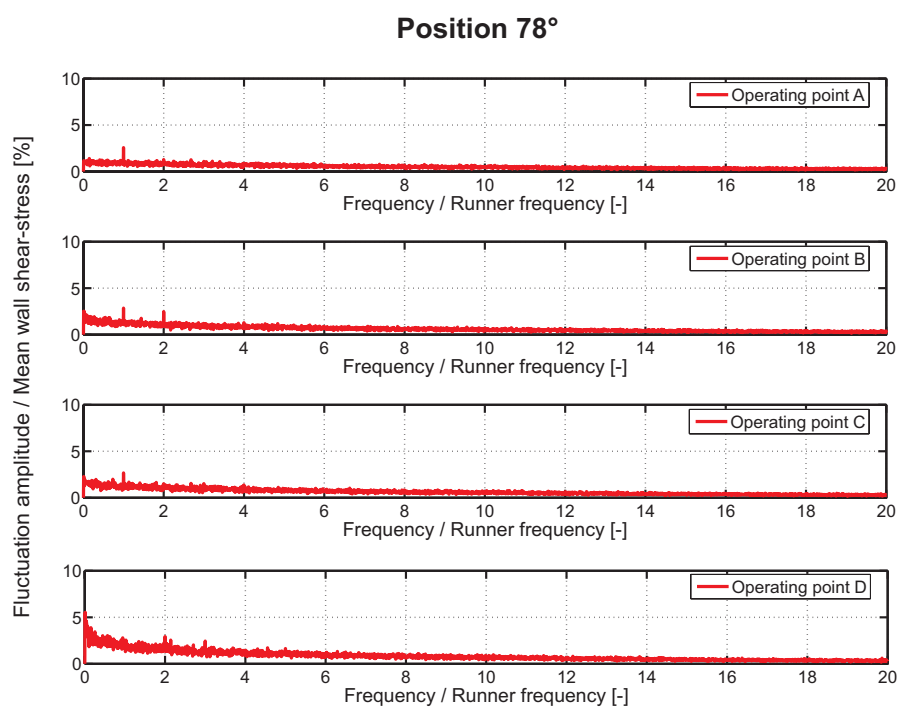


Figure 5.72: Spectral analysis of the wall shear-stress corresponding to the 78° angular position of the hot-film probe

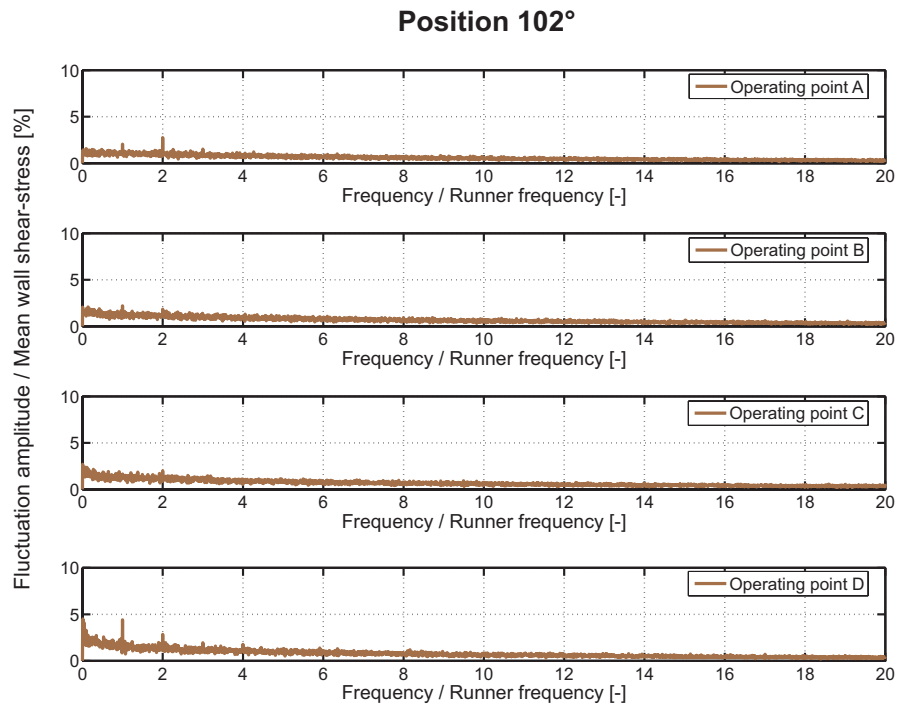


Figure 5.73: Spectral analysis of the wall shear-stress corresponding to the 102° angular position of the hot-film probe

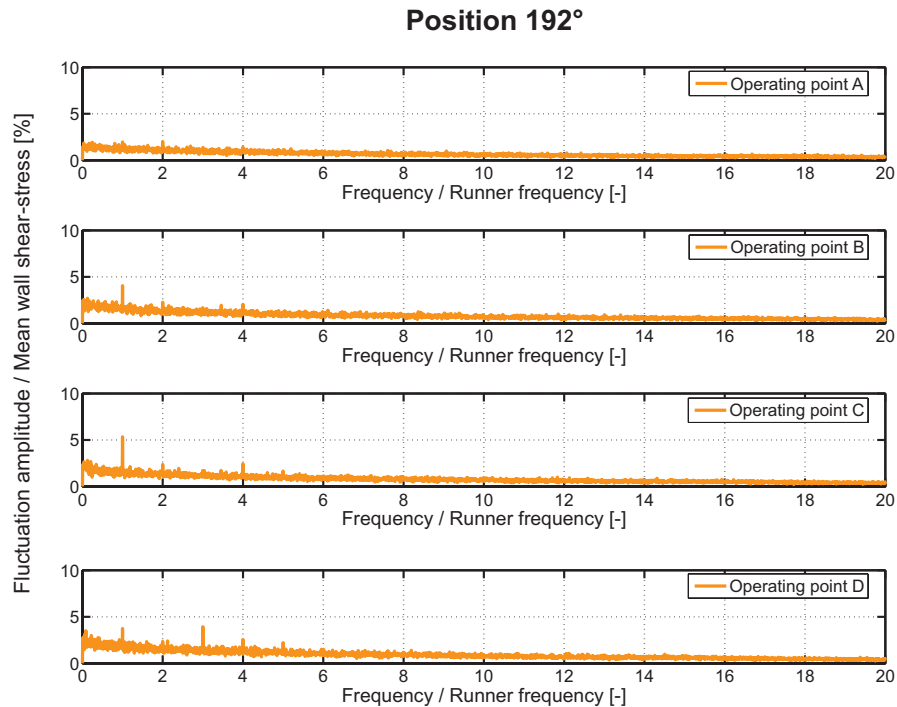


Figure 5.74: Spectral analysis of the wall shear-stress corresponding to the 192° angular position of the hot-film probe

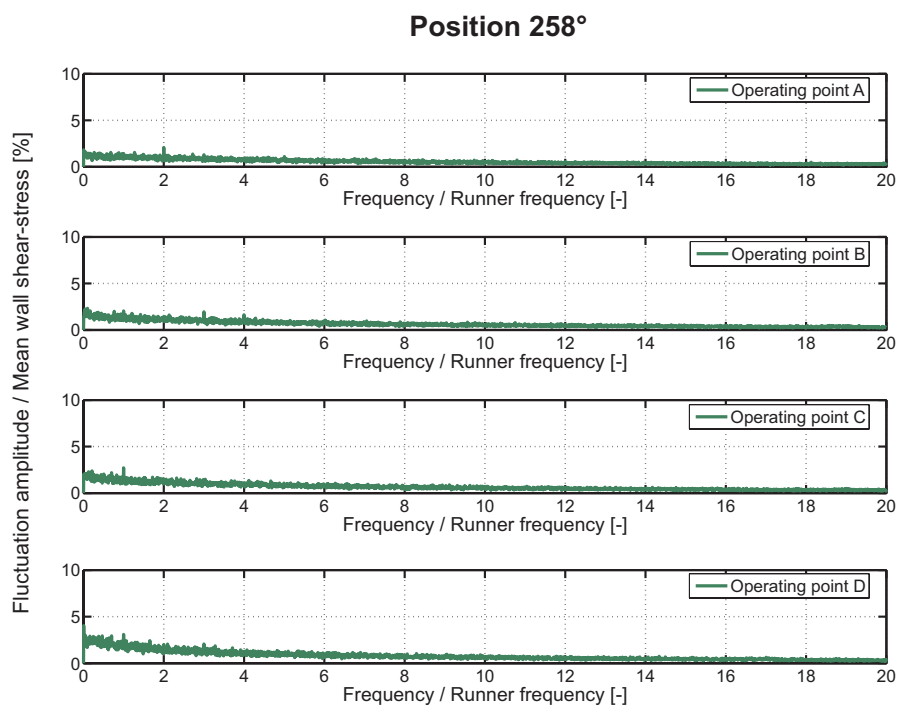


Figure 5.75: Spectral analysis of the wall shear-stress corresponding to the 258° angular position of the hot-film probe

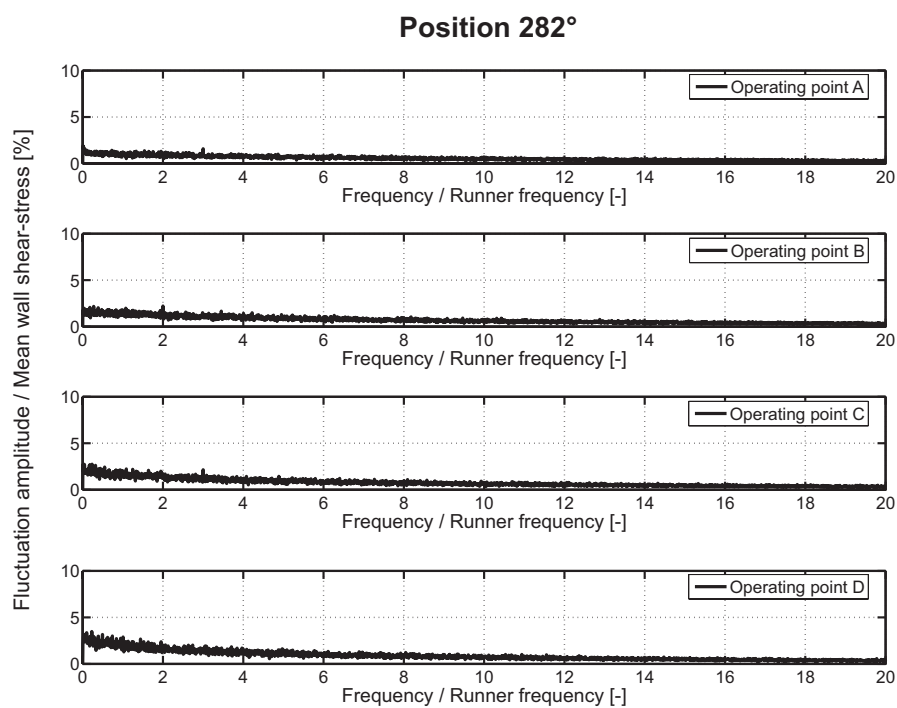


Figure 5.76: Spectral analysis of the wall shear-stress corresponding to the 282° angular position of the hot-film probe

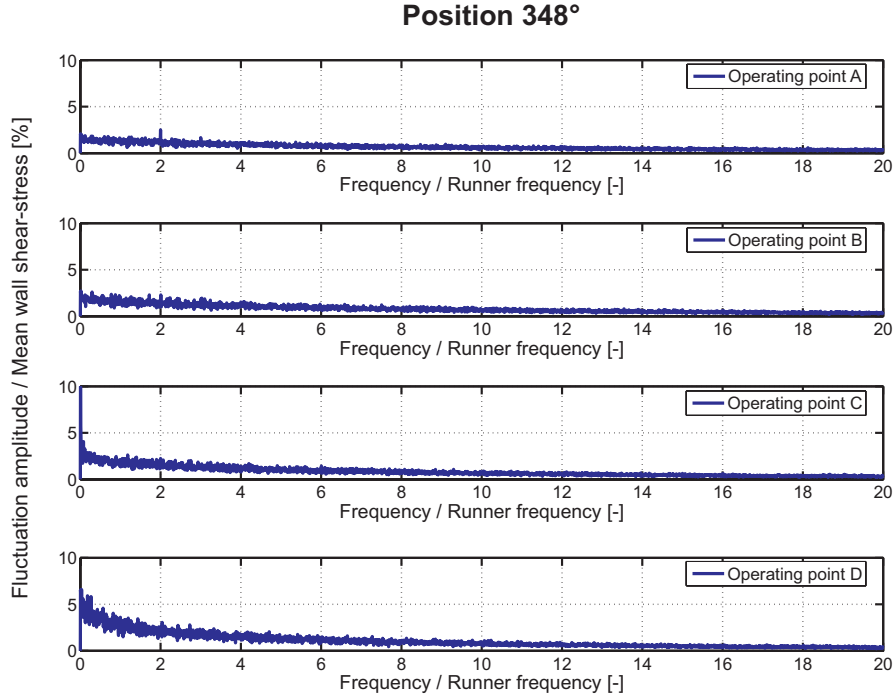


Figure 5.77: Spectral analysis of the wall shear-stress corresponding to the 348° angular position of the hot-film probe

### 5.5.2 Partial load operating points

#### Steady analysis

The same tendencies, regarding the steady wall shear-stress distribution, as for the standard operating points, are observed for the off-design operating point, for the  $2\sigma$  values, at the cone outlet, see figures 5.78 and 5.79. The bend influence is evidenced.

Moreover, the vortex present in the center of the measurements section, defines a "dead flow zone", inducing a decreased flow cross sectional area and, hence, leading to high flow velocity near the wall. Thus, the absolute values of the wall shear-stress are higher than for the standard operating points but, in mean values, the wall shear-stress is independent on the  $\sigma$  value, similar to the cone inlet - see figure 5.80. The mean wall shear-stress values at the cone outlet are smaller than at the inlet.

#### Unsteady analysis

The spectral analysis performed for the partial load operating points evidences the same characteristic frequency as in the inlet section: vortex's rotating frequency, for every spatial position of the probe in the measurement section, see figures 5.81, 5.83, 5.85, 5.87, 5.89, 5.91 and 5.93.

For this characteristic frequency there was performed the phase average, see figures 5.82, 5.84, 5.86, 5.88, 5.90, 5.92 and 5.94, corresponding to every angular position of the probe.



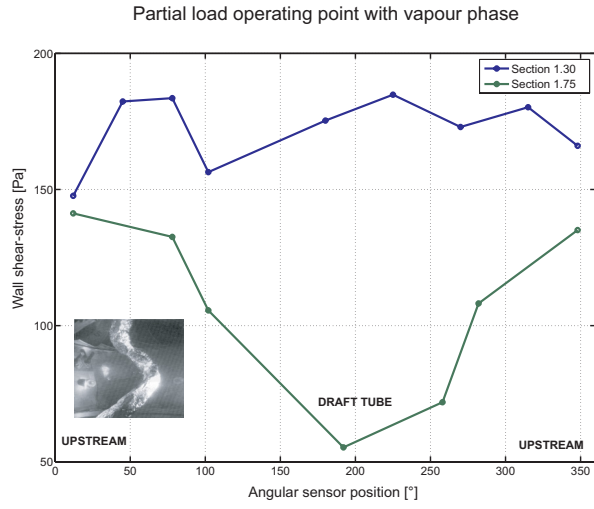


Figure 5.78: Steady wall shear-stress distribution for the part load operating point with vapor phase

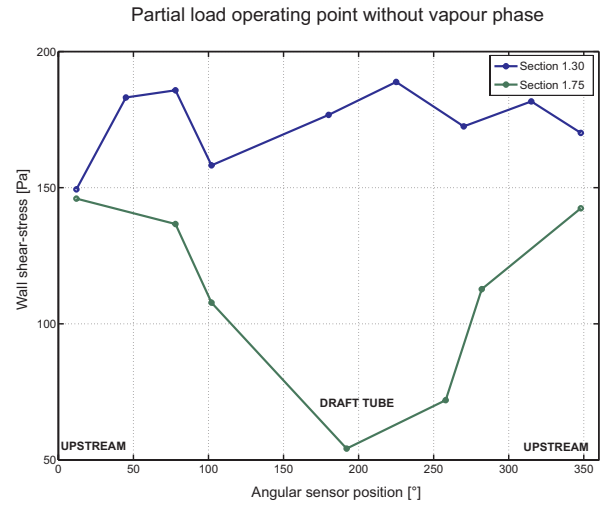


Figure 5.79: Steady wall shear-stress distribution for the part load operating point without vapor phase

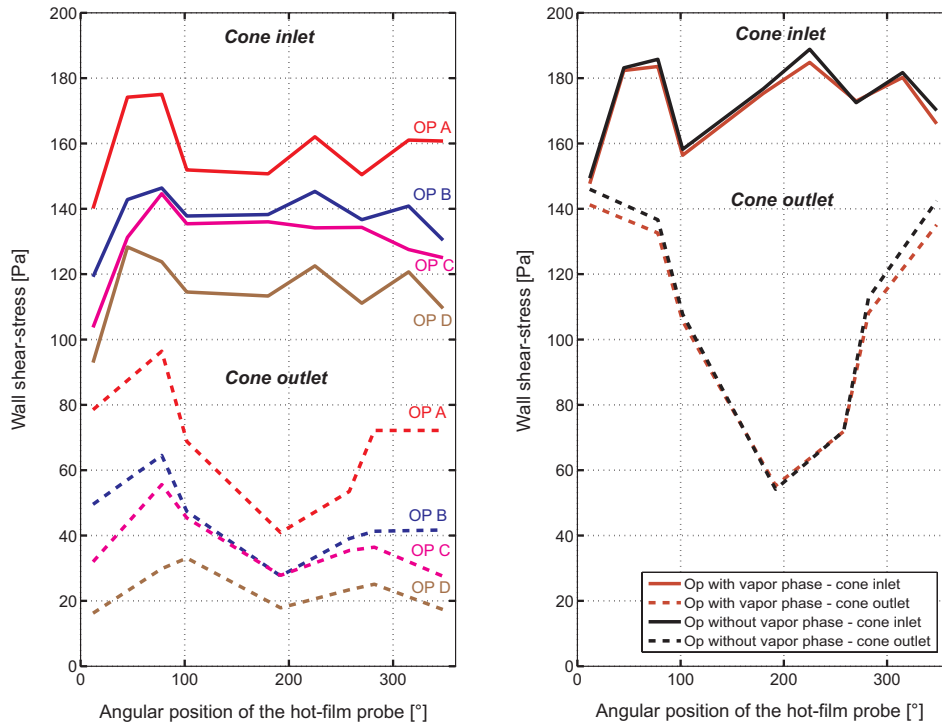


Figure 5.80: Wall shear stress distribution with the operating point and the spatial position, both at the cone inlet and outlet

The rope frequency is dominant and its amplitude is higher (50%) like in the cone inlet, section 1.30. This higher amplitude is explained by the proximity of the rope to the wall.

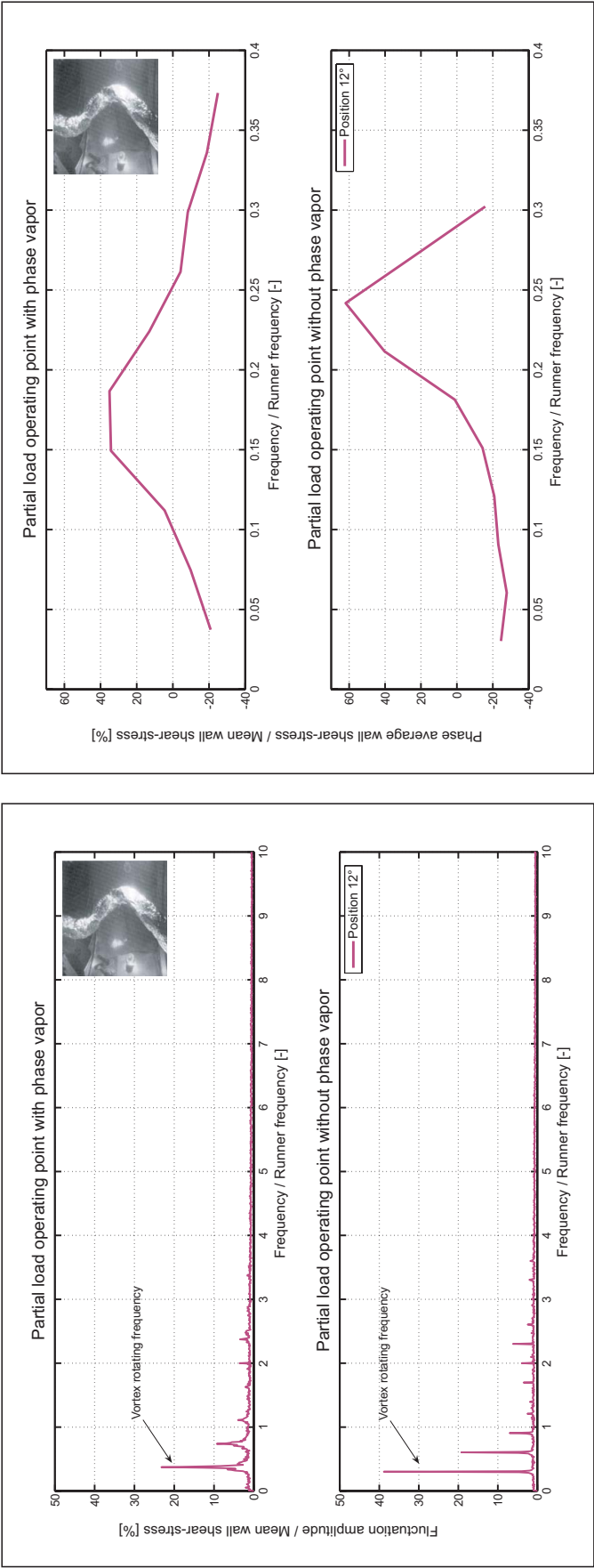


Figure 5.81: Spectral analysis, at the cone outlet, for partial load operating points, corresponding to angular position 12°

Figure 5.82: Wall shear stress phase average with the rope frequency for angular position 12°

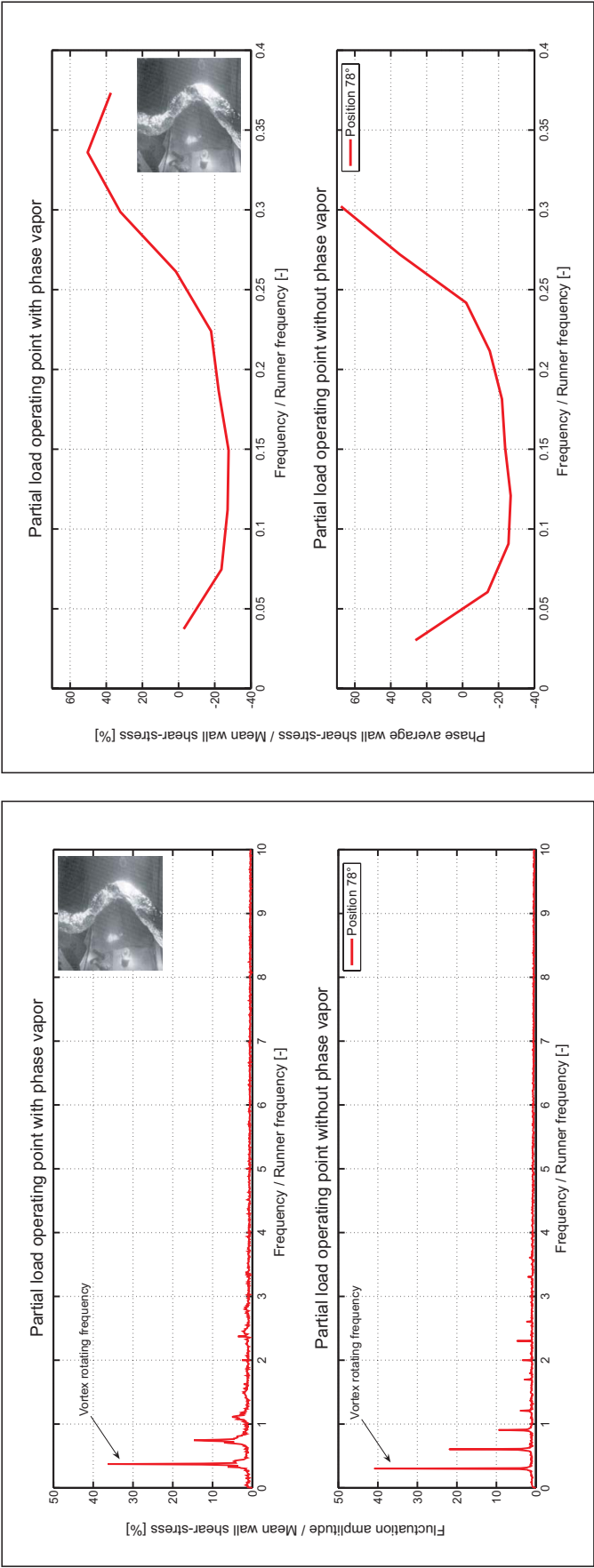


Figure 5.83: Spectral analysis, at the cone outlet, for partial load operating points, corresponding to angular position 78°

Figure 5.84: Wall shear stress phase average with the rope frequency for angular position 78°

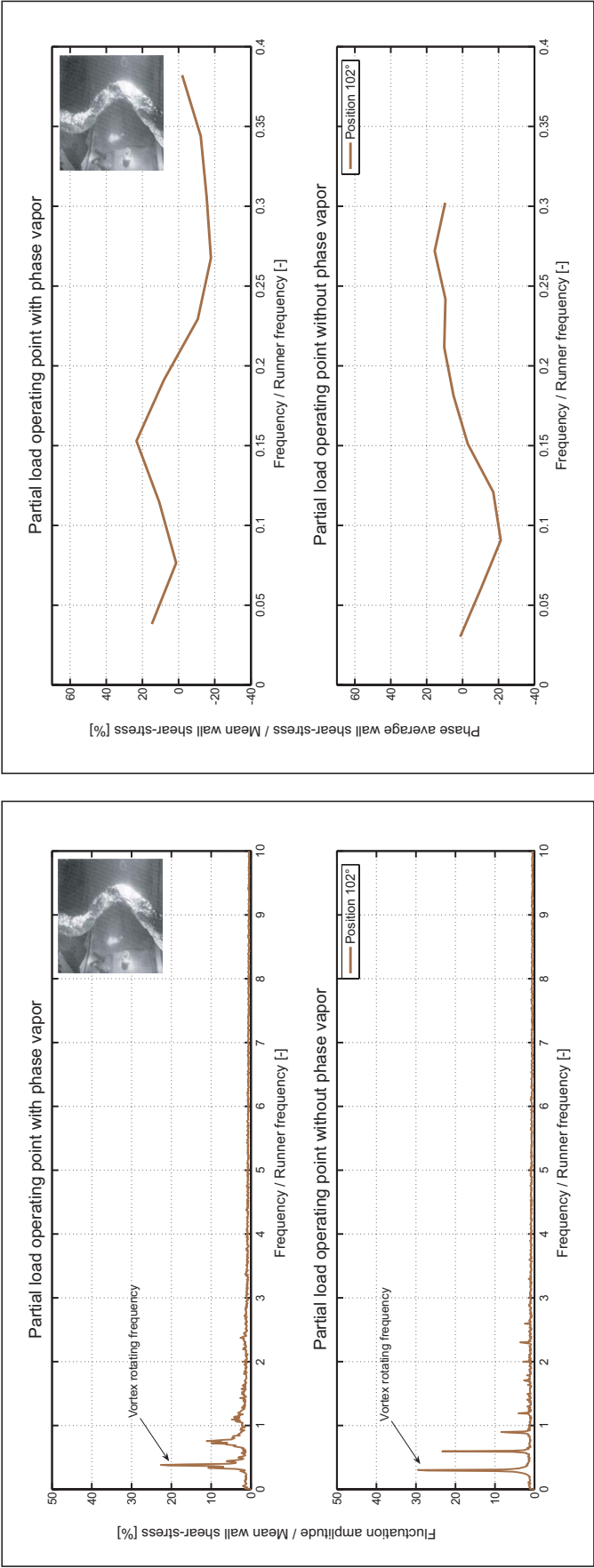


Figure 5.85: Spectral analysis, at the cone outlet, for partial load operating points, corresponding to angular position 102°

Figure 5.86: Wall shear stress phase average with the rope frequency for angular position 102°

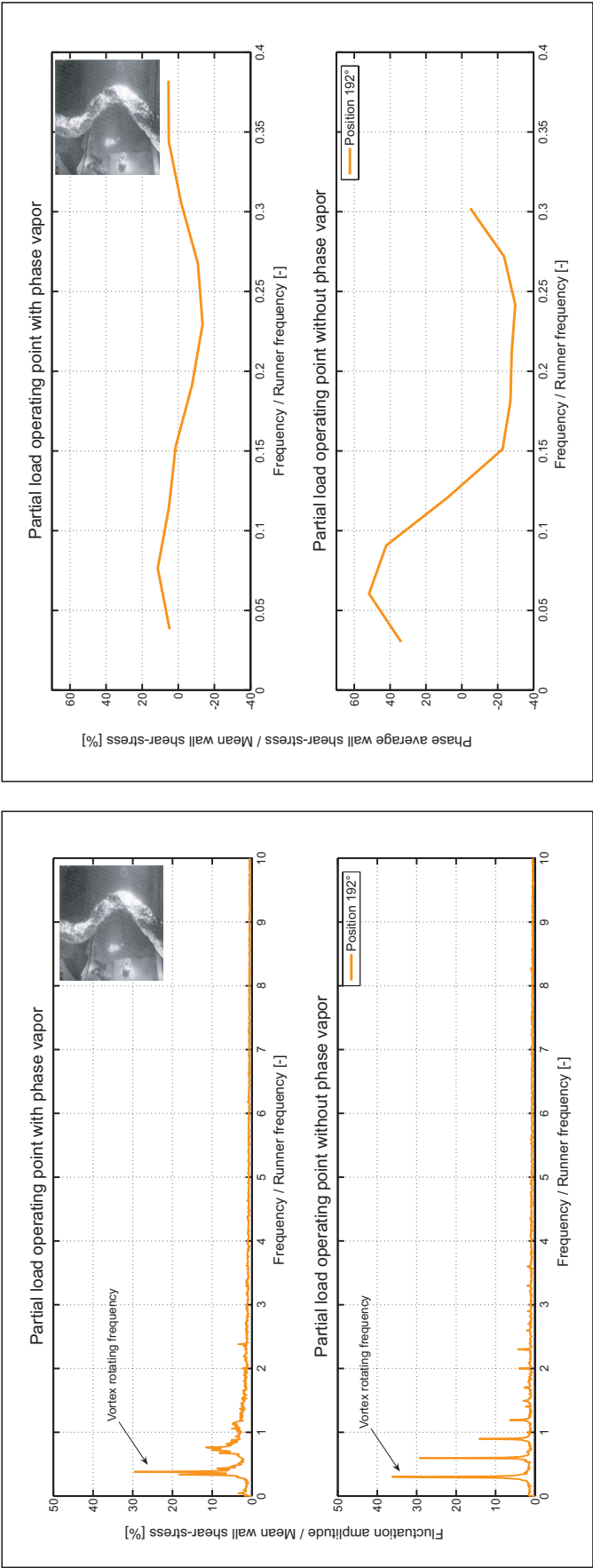


Figure 5.87: Spectral analysis, at the cone outlet, for partial load operating points, corresponding to angular position 192°

Figure 5.88: Wall shear stress phase average with the rope frequency for angular position 192°

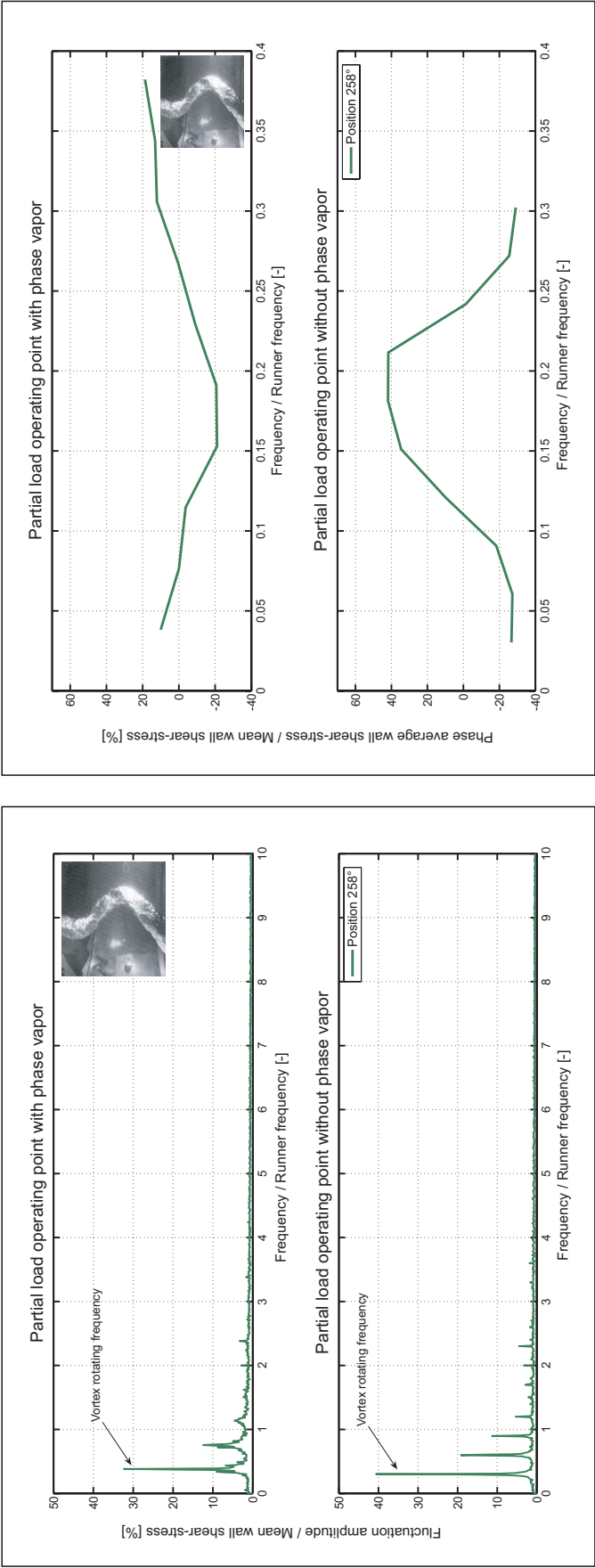


Figure 5.89: Spectral analysis, at the cone outlet, for partial load operating points, corresponding to angular position 258°

Figure 5.90: Wall shear stress phase average with the rope frequency for angular position 258°

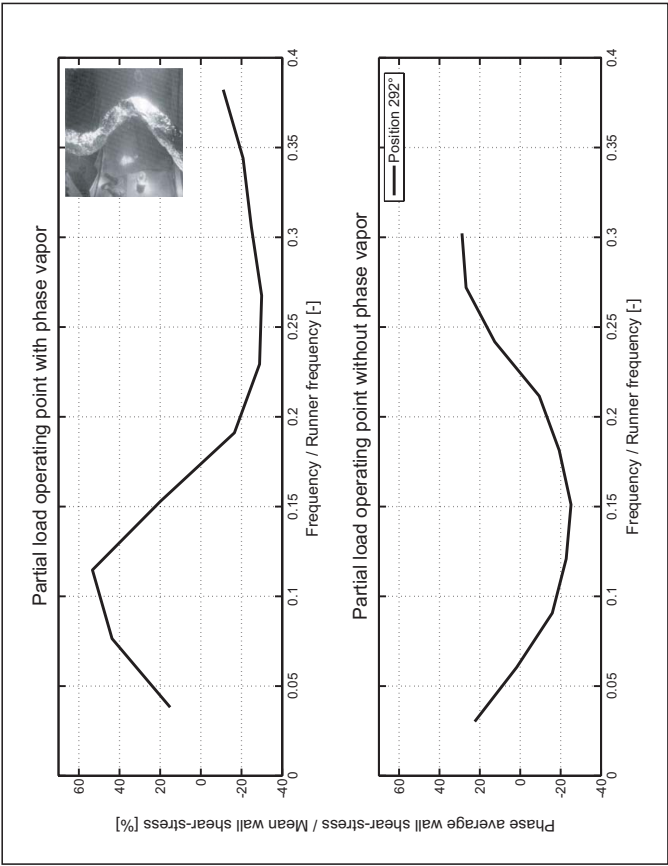


Figure 5.91: Spectral analysis, at the cone outlet, for partial load operating points, corresponding to angular position 292°

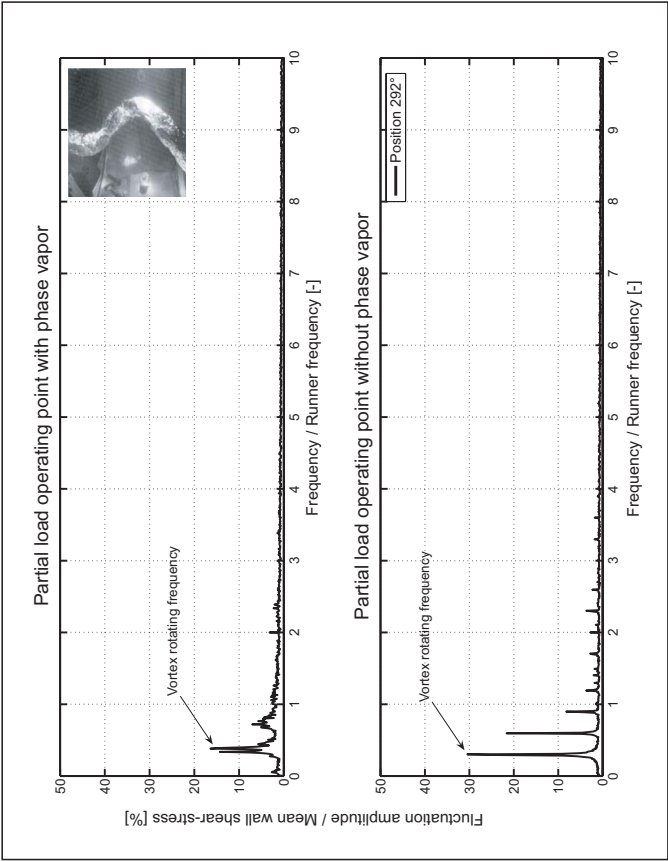


Figure 5.92: Wall shear stress phase average with the rope frequency for angular position 292°

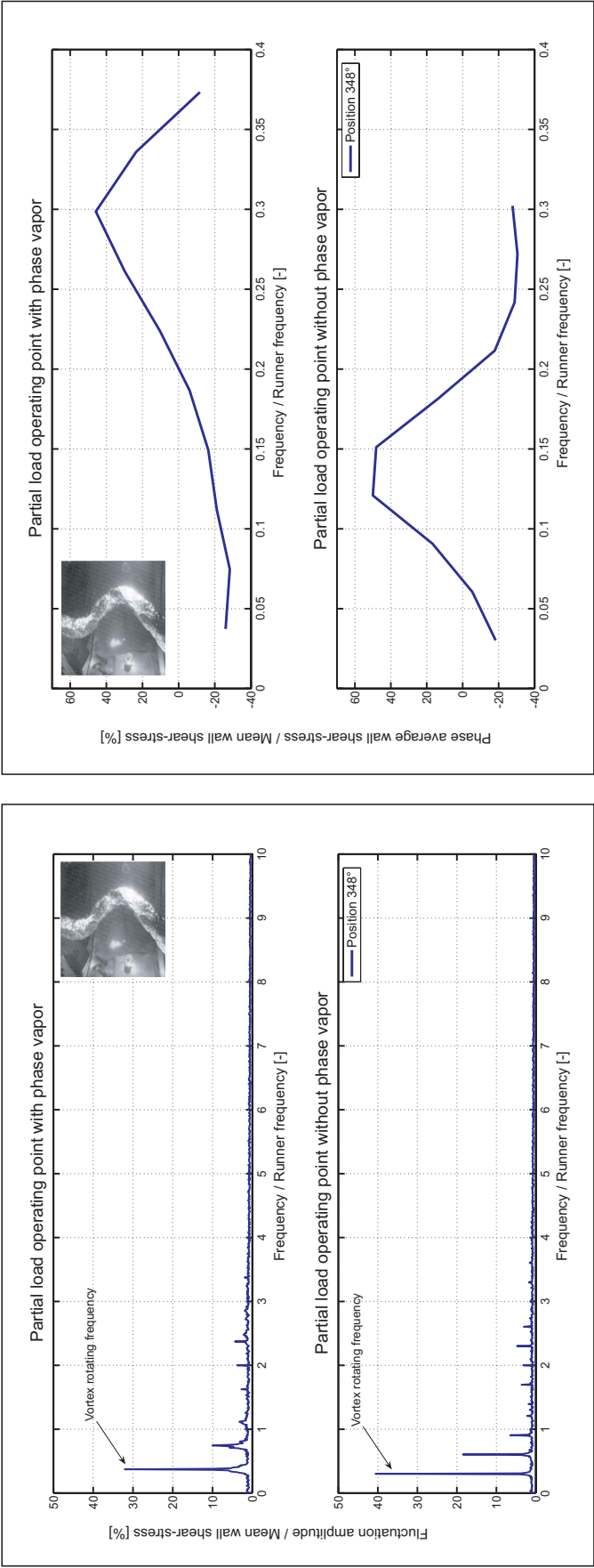


Figure 5.93: Spectral analysis, at the cone outlet, for partial load operating points, corresponding to angular position 348°

Figure 5.94: Wall shear stress phase average with the rope frequency for angular position 348°



# Chapter 6

## BOUNDARY LAYER CHARACTERIZATION IN THE CONE

The challenging problem in fluid mechanics, nowadays, is still the control of the behavior of the turbulent boundary layers, with regard to their separation or detachment. All existing results in turbulence theory depend on assumptions which should be reconsidered as knowledge develops.

von Kármán [1930] and Prandtl [1932] are the first, since 1930, who proposed a model for the turbulent boundary layer. Their model describes the wall region by means of a universal logarithmic law, by assuming that outside the viscous sublayer, the contribution of viscosity can be neglected. In 1950, Clauser [1954] and Coles [1956] proposed a model for turbulent boundary layers at large Reynolds number, based on the assumption that the transition from the wall region, described by Karman-Prandtl law, to the external flow, called "wake region", is smooth. This model, called classical, is widely accepted and used, especially for the zero-pressure gradient turbulent boundary layer.

Using analytic and experimental arguments, since 1991, Barenblatt et al. [2002] developed a new model for the turbulent boundary layer. This model shows that the intermediate region in turbulent boundary layers at large Reynolds number, between the viscous sub-layer and the external flow consists on two self-similar structures, described by different and substantially Reynolds-number-dependent scaling laws. However, the boundary between them is sharp. Actually, according to this model, the mean velocity profile in the transition region has a characteristic form of a "chevron". This model was validated for both zero-pressure and non- zero-pressure gradient flows.

The recent progresses in the boundary layer investigation show that, for the flows with adverse pressure gradient, the standard log-law velocity profile does not hold, near-wall distributions of r.m.s. velocity fluctuations cannot be scaled with the wall parameters, friction velocity and kinematic viscosity and that the response time of turbulence to the imposed adverse-pressure-gradient, changes among streamwise wall-normal and spanwise velocity components.

In Francis turbine, the evolution of the boundary layer in the cone is complex due to the rotating flow at the runner outlet, the adverse pressure gradient, the interaction with the leakage flow and the unsteady perturbations due to the runner blade-to-blade shared flow or vortex rope.

This part of the thesis intends to characterize the boundary layer present in the cone of the Francis turbine scale model, by wall shear-stress and near wall velocity measurements and to provide the best-fitted model for the boundary layer model. Meanwhile, the boundary layer thicknesses are determined for the cone inlet and outlet, for different spatial positions and for 6 operating points of the turbine .

## 6.1 NEAR WALL 2D LDV MEASUREMENTS AND RESULTS

To characterize the boundary layer analysis Berca et al. [2004b], a 2D velocity profile survey is performed near the cone wall by LDV measurement method, in 2 locations in the cone, situated at the same spatial position related to the hot-film probe,  $0^\circ$  for the 2 measurements sections, see figure 6.1.

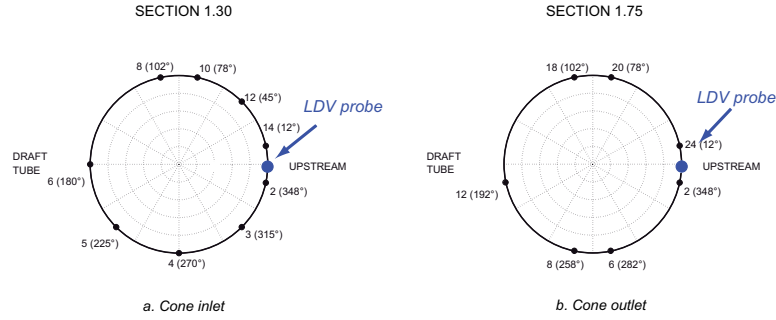


Figure 6.1: LDV measurement location in the measurements sections related to the wall shear-stress locations

The LDV system is a Dantec 2 components system, using back-scattered light and transmission by optical fiber, with a laser of 5W Argon-ion source. The main characteristics of the LDV probe are detailed in table 6.1.

	Laser wave lengths	Probe diameter	Beam spacing	Focal length	Fringe spacing	Measuring volume $\sigma_x = \sigma_y$	Measuring volume $\sigma_z$
LDV probe	488 nm 514.5 nm	60 mm	38 mm	159.4 mm	2.15 nm	0.1 mm	0.8 mm

Table 6.1: Main optical probe characteristics

An optical window with plane and parallel faces is used as interface. The geometrical reference position of the measurements is obtained by positioning the laser beams on the windows faces with an accuracy of better than  $0.05mm$ .

Two components are measured: the tangential component of the velocity  $c_x$  and the axial one  $c_z$ , see figure 6.2. An exploration of the complete diameter of the cone was

already performed, see Ciocan et al. [2000] and the comparison of the near wall measurements with the velocity profile showed a very good agreement, see figure 6.3. The uncertainties of the laser measurements are estimated to 2%, according to the method of Mofat [1985].



Figure 6.2: Near wall LDV measurements

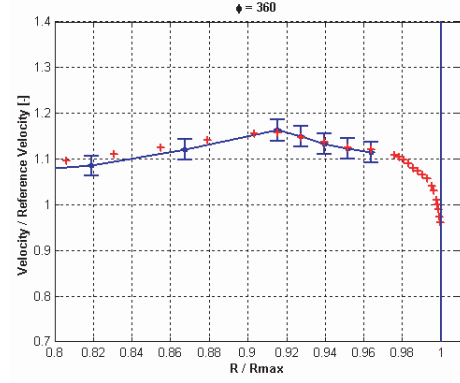


Figure 6.3: Velocity distribution in the cone near wall region

## 6.2 BOUNDARY LAYER ANALYSIS

The velocity measurements in the vicinity of the cone wall between  $0.2\text{mm}$  and  $20\text{mm}$ , corresponding to  $y^+$  values between 100 and 10'000, allow obtaining the boundary layer law, for both the near BEP operating points, at the cone inlet and outlet, see figure 6.4, and for the partial load operating points, in the 2 sections, see figures 6.5. It is considered that  $y/R = 1$  corresponds to the wall.

### 6.2.1 Boundary layer representation

Using inner variables,  $c^+$  and  $y^+$ , defined by relationship 6.1, and the measured values of the wall shear-stress and near wall velocity, the boundary layer can be represented for

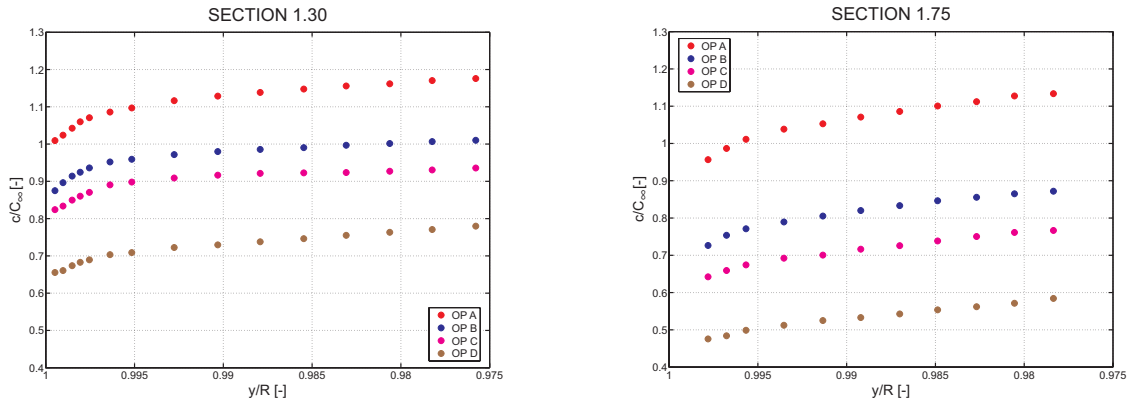


Figure 6.4: Near wall velocity measurements for near BEP operating points at the runner and cone outlet

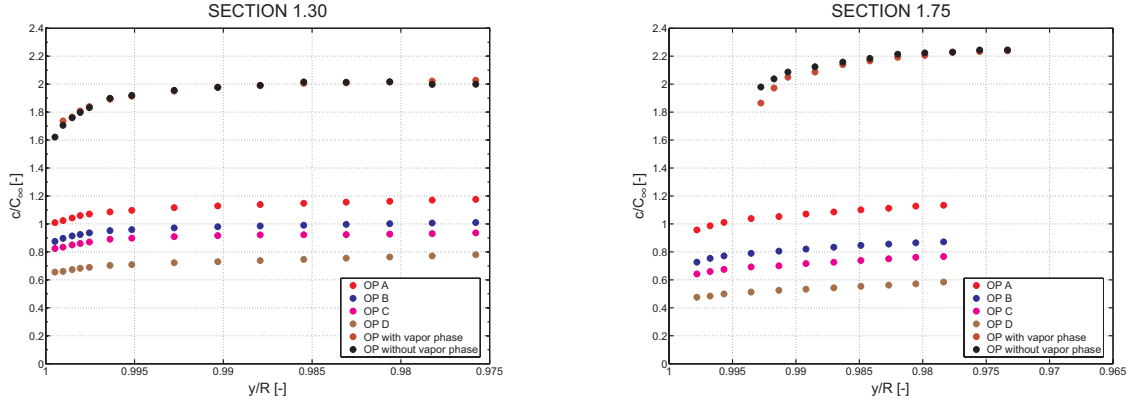


Figure 6.5: Near wall velocity measurements for near BEP and 2 off-design operating points at the runner and cone outlet

the inlet and outlet section of the cone, see figures 6.6 to 6.7.

$$c^+ = \frac{c}{c_\tau} \quad c_\tau = \sqrt{\frac{\tau_p}{\rho}} \quad y^+ = \frac{yc_\tau}{\nu} \quad (6.1)$$

In Section 1.30, at  $0.25D_{Ie}$  from the runner outlet, the boundary layer thickness and shape are very similar, for both the standard and the 2 off-design operating points.

In Section 1.75, at 0.7 from the runner outlet, due to the adverse pressure gradient values, see Arpe [2003], the boundary layer thickness is proportional to the flow rate for the near BEP operating points. At the cone outlet, the boundary layer developed at the operating points with and without vapor phase is identical.

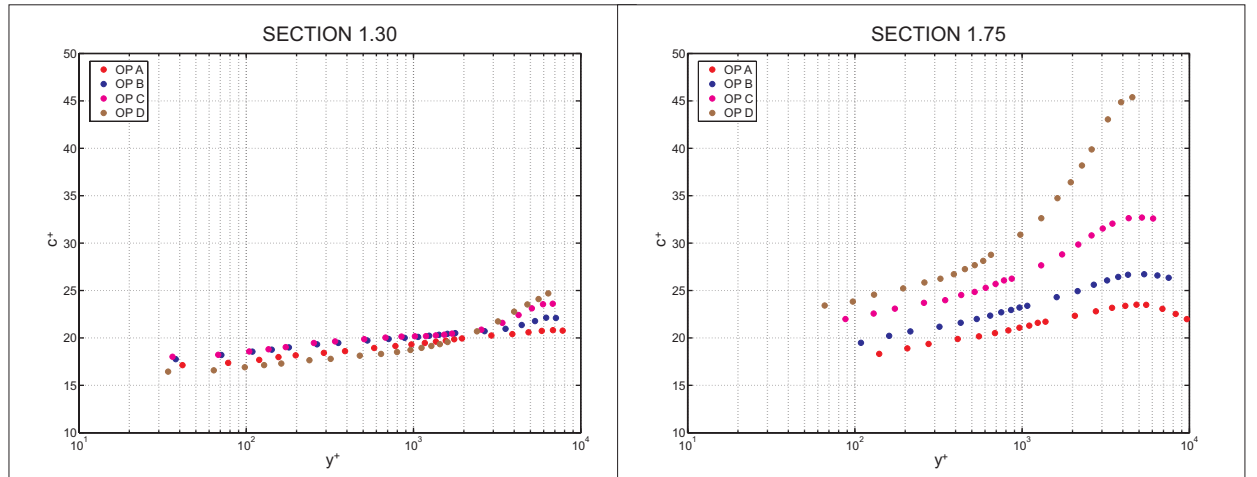


Figure 6.6: Velocity profile distribution, in boundary layer inner variables, for the near BEP operating points

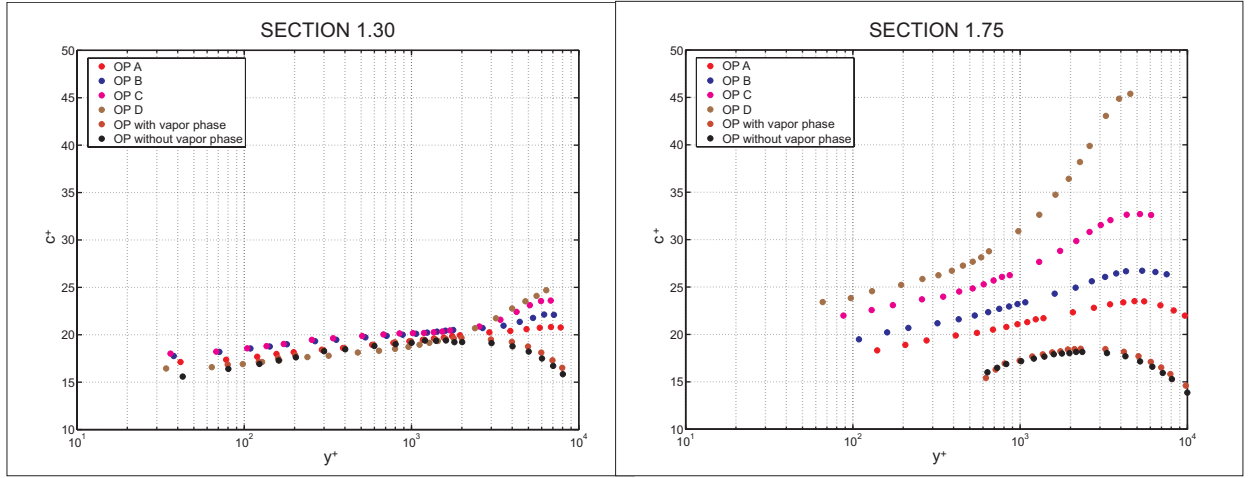


Figure 6.7: Velocity profile distribution, in boundary layer inner variables, for the near BEP and 2 off-design operating points

### 6.2.2 Scaling laws for turbulent flows

Turbulence at very large Reynolds numbers is considered as one of the happier provinces of the entire turbulence domain. Scaling laws are an important topic in turbulence research, leading, mainly in a direct way to wall shear-stress laws.

The distribution of the mean velocity in intermediate region of a turbulent flow was intensively studied over sixty years and, finally, two totally different laws were obtained and coexist, actually, in the literature. Both of them are obtained by assuming that, in the intermediate region of the boundary layer, see figure 6.8, the velocity gradient,  $\frac{\partial c}{\partial y}$ , depends on several variables:

$$\frac{\partial c}{\partial y} = f(y, \tau_p, d, (\nu, \rho)) \quad (6.2)$$

where:  $y$  represents the coordinate,  $\tau_p$  - wall shear-stress,  $d$  - diameter and  $(\nu, \rho)$  - the fluid properties, the kinematic viscosity and the density.

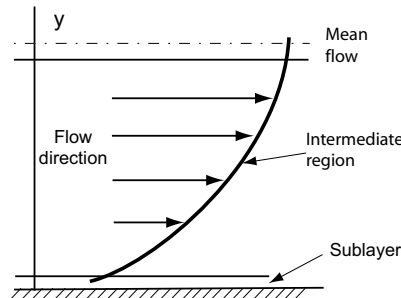


Figure 6.8: The intermediate region of wall-bounded shear flow

By a dimensional analysis, see Barenblatt et al. [1997b], the relation 6.2 become:

$$\frac{\partial c}{\partial y} = \frac{c_\tau}{y} \Phi(\eta, Re) \quad (6.3)$$

where  $Re$  is the Reynolds number,  $\Phi$  is an unknown dimensionless function of 2 parameters, and  $\eta$  is defined by relation 6.4.

$$\eta = \frac{yc_\tau}{\nu} \quad (6.4)$$

By assuming:

$$\phi = \frac{c}{c_\tau}, \quad (6.5)$$

the equation 6.3 can be rewritten in the form:

$$\frac{\partial \phi}{\partial \eta} = \frac{1}{\eta} \Phi(\eta, Re) \quad (6.6)$$

The first scaling law is obtained by assuming that at viscous sublayer's outside,  $\eta$  is very large,  $\eta \rightarrow \infty$ , and that in turbulent flows, the Reynolds number is also considered large,  $Re \rightarrow \infty$ . In this way, the function  $\Phi$  depends no longer on its parameters and it can be replaced by a constant  $1/\kappa$ . The equation 6.6 becomes:

$$\frac{\partial \phi}{\partial \eta} = \frac{1}{\eta} \frac{1}{\kappa} \quad (6.7)$$

In this way, the first scaling law obtained and considered as reference in the turbulent boundary layer theory is a logarithmic law.

Meanwhile, as it is unknown if that, regarding the Reynolds number, such a limit exists, it may be considered that at large  $\eta$ ,  $\Phi$  function can be represented as a power law, see relation 6.8.

$$\Phi(\eta, Re) = A\eta^\alpha + M, \quad (6.8)$$

where  $M$  represents smaller quantities, but as  $\eta$  is large, this term  $M$  can be neglected and the relation 6.8 becomes:

$$\Phi = A\eta^\alpha, \quad (6.9)$$

and, thus, the equation 6.7 can be rewritten, see relation 6.10.

$$\frac{\partial \phi}{\partial \eta} = A\eta^{\alpha-1} \quad (6.10)$$

By integration, the equation 6.10 becomes:

$$\phi = \frac{A}{\alpha} \eta^\alpha + constant \quad (6.11)$$

Assuming  $\frac{A}{\alpha}$  as a constant and the constant term as zero, from experiments comparison, it is obtained the second scaling law, a power law, illustrated by relation 6.12.

$$\phi = A'\eta^\alpha + constant \quad (6.12)$$

Finally, it was shown that the 2 scaling laws, can be derived with equal rigor, but from different assumptions. For the present case, the intermediate region of boundary layer developed in the cone was evaluated with the 2 scaling laws and the results are presented below.

### 6.2.3 Comparison with the classical model of boundary layer

The first scaling law studied for the present case is the model of the turbulent boundary layer at large Reynolds number, proposed by the Clauser [1954] and Coles [1956], based on the assumption that the velocity distribution in the intermediate region follows the Karman-Prandtl universal logarithmic law. The mean velocity distribution follows, according to this classical model, the universal logarithmic law:

$$c^+ = \frac{1}{\kappa} \ln y^+ + C \quad (6.13)$$

where following the derivation,  $\kappa$  and  $C$  are universal constants, independent of Reynolds number and, generally,  $\kappa = 0.41$  and  $C = 5$ , values illustrated in figure 6.9.

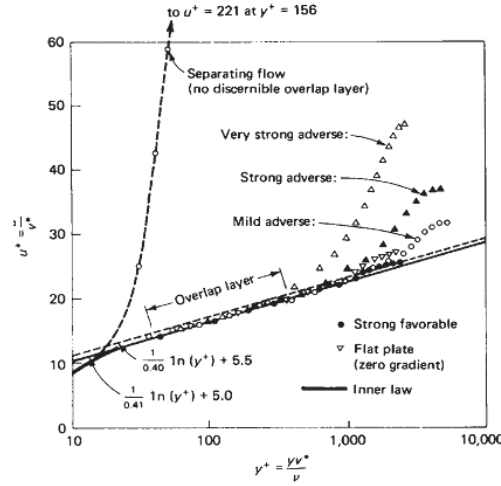


Figure 6.9: Velocity profiles using inner-variables, White [1991]

Generally, it is thought that this universal logarithmic law agrees, satisfactory, with the experimental data in turbulent boundary layers.

For the case studied, the measurements results could be approximated with a logarithmic law but differences appear for the two constants values. The friction velocity based on the wall shear-stress measurements is about 3 times larger than the one obtained with the classical log-law. This means, transformed in wall shear-stress, that the ratio between the measured values and the calculated one is about 10.

The results are coherent with the one obtained by Nagano et al. [1998], for the adverse pressure gradient in turbulent boundary layers.

In this way, it is noticed that using the log-law, see figure 6.10, for all studied operating points, the boundary layer shape is inadequately approximated and, in the same time, the Karman-Prandtl universal logarithmic law is not valid for the turbine cone flow conditions.

The boundary layer in the Francis Turbine cone, for all studied operating points, is strongly three-dimensional, fact illustrated by the flow angle distribution in the boundary layer, see figures 6.12 and 6.14. The absolute flow angle representation, related to the local system attached to the hot-film probe,  $x'$  and  $z'$ , for the LDV velocity field, see figure 6.11 shows a strong gradient in the boundary layer - see figure 6.13 .

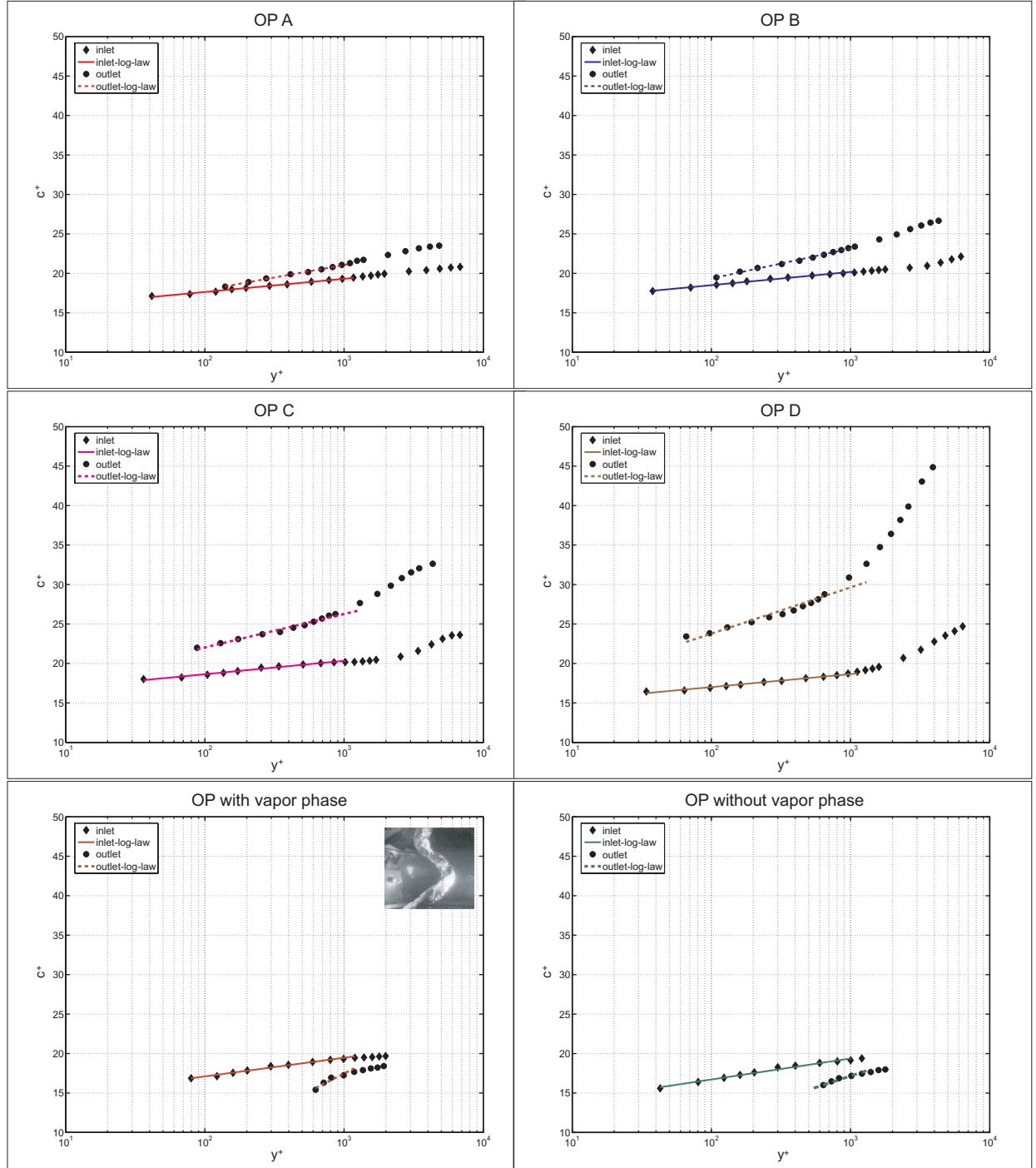


Figure 6.10: Velocity profile distribution, in boundary layer inner variables, for the near BEP and 2 off-design operating points

Superposed with the three-dimensionality, an adverse pressure gradient, see Arpe [2003], is governing the flow, and its influence is clearly visible for  $y^+ > 10^3$ .

The comparisons of the measured boundary layer with the von Karman-Prandtl universal logarithmic law showed that the classical model is not valid. The logarithmic law shape exists but the constants are different. Two raisons are invoked and quantified:



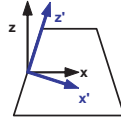
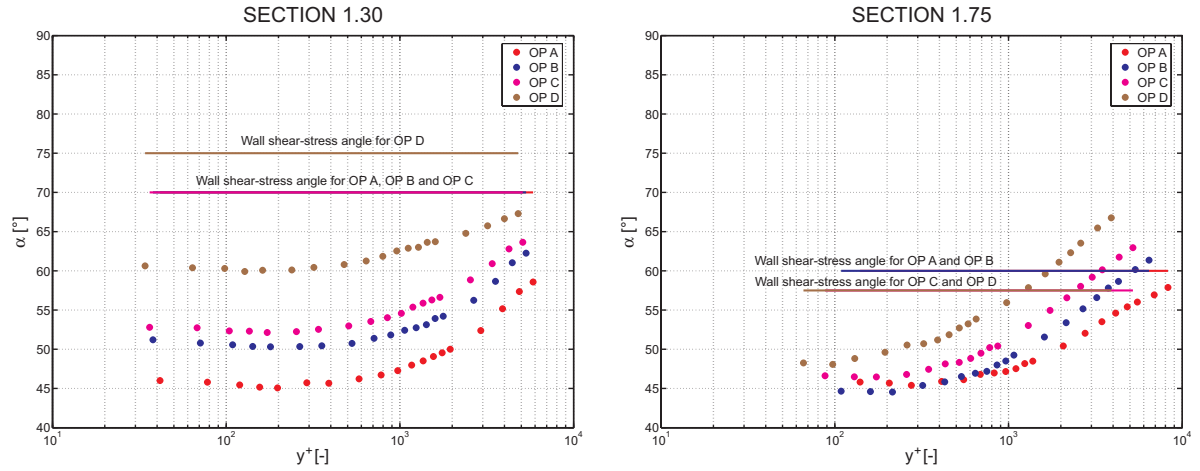
Figure 6.11: Local system attached to the hot-film probe,  $x'$  and  $z'$ 

Figure 6.12: Boundary layer flow angle distribution, for the near BEP operating points

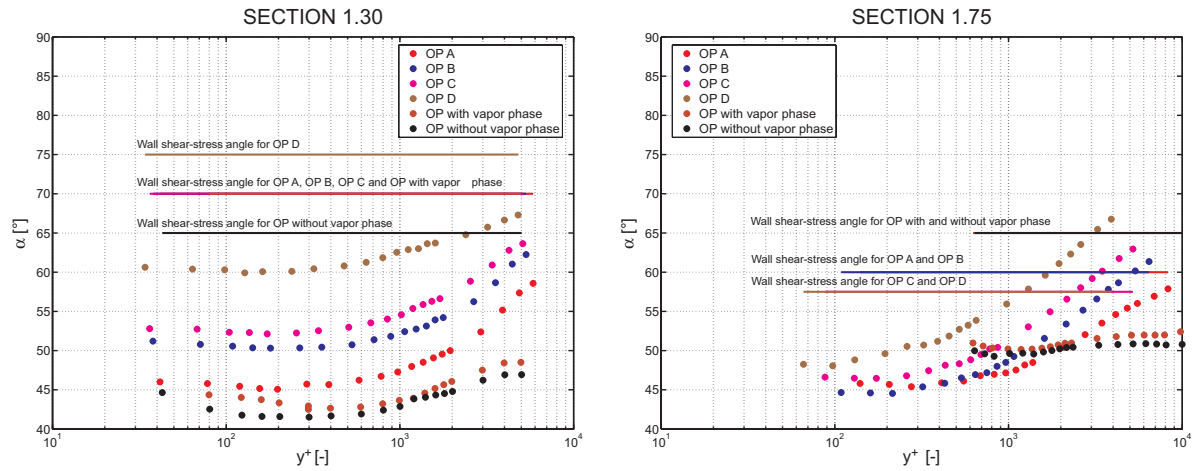


Figure 6.13: Boundary layer flow angle distribution, for the near BEP and 2 off-design operating points

the strongly 3D character of the boundary layer and the adverse pressure gradient. Two other possible raisons: the runner outlet leakage flow and the unsteady character of the sheared flow must be investigated in the future.

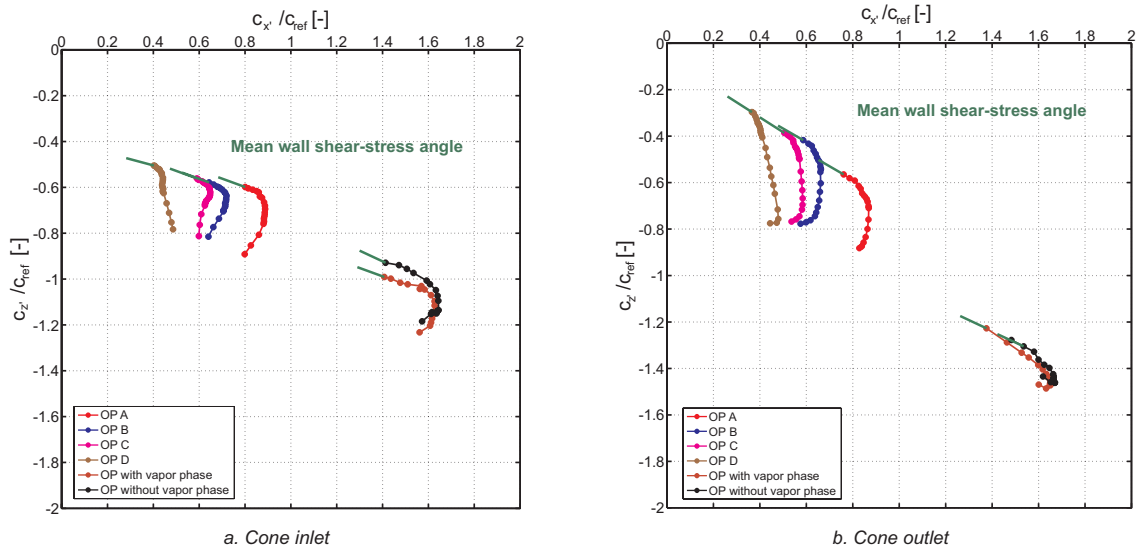


Figure 6.14: Comparison between the shear-stress angle and flow angle distribution in the boundary layer, for all operating points studied

#### 6.2.4 Comparison with the power model of the boundary layer

According to a model of the turbulent boundary layer proposed by Barenblatt et al. [2002], and based on the second scaling law presented above, in the absence of the external turbulence, the transition region between the viscous sublayer and the external flow is composed by 2 sharply separated self-similar structures where the velocity distribution follows 2 different scaling laws, see figure 6.15. Actually, the characteristic form of the velocity distribution in this region is a broken line called "chevron".

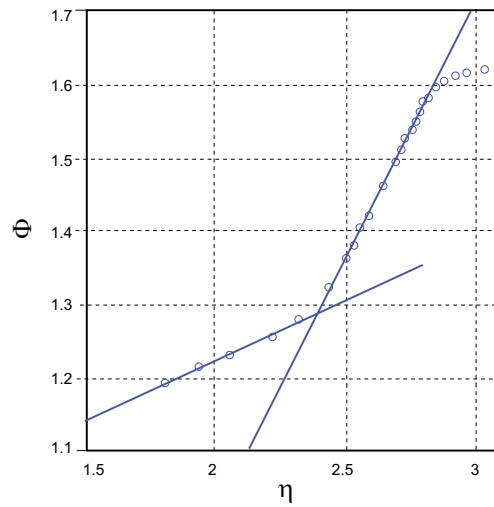


Figure 6.15: Velocity distribution by 2 different scaling laws

In the adjacent part to the viscous sublayer, the scaling law describes the mean velocity distribution:

$$\Phi = A\eta^\alpha, \quad (6.14)$$

while in the other one, adjacent to the free stream, the scaling law becomes:

$$\Phi = B\eta^\beta, \quad (6.15)$$

where:

$$\Phi = \frac{c}{c_\tau} \quad \eta = \frac{yc_\tau}{\nu} \quad (6.16)$$

In the first "layer", the influence of viscosity is transmitted to the main part of the flow via "strips" separated from the viscous layer. In the second "layer", the upper boundary of the boundary layer is covered by large-scale "humps". In the same time, it is known that the upper layer is influenced by the external flow via the form drag of theses humps and also, by the wall shear-stress.

The approximation with a power law shows a good agreement with the measured velocity profiles, corresponding to the 3D fully turbulent flow in adverse pressure gradient conditions taking place in a Francis turbine cone, see figure 6.16.

An interesting parameter of the flow, which influences the slopes of the mean velocity distribution is the Reynolds number based on the momentum displacement thickness; it has been calculated for each operating point:

$$\text{Re}_\theta = \frac{\theta c}{\nu} \quad (6.17)$$

The parameters  $A$ ,  $\alpha$ ,  $B$  and  $\beta$  of the scaling laws are determined from the experimental data, see table 6.2, based on wall shear-stress and near wall velocity measurements by standard statistical processing of the data. The results are coherent with the Barenblatt et al. [2002] analysis. The coefficients  $A$  and  $\alpha$  are Reynolds-number-dependent. In the second region, the parameter  $\beta$  of the scaling law has values significantly different from 0.2, the value obtained for the same parameter in zero-pressure-gradient boundary layer, see Barenblatt et al. [1997a].

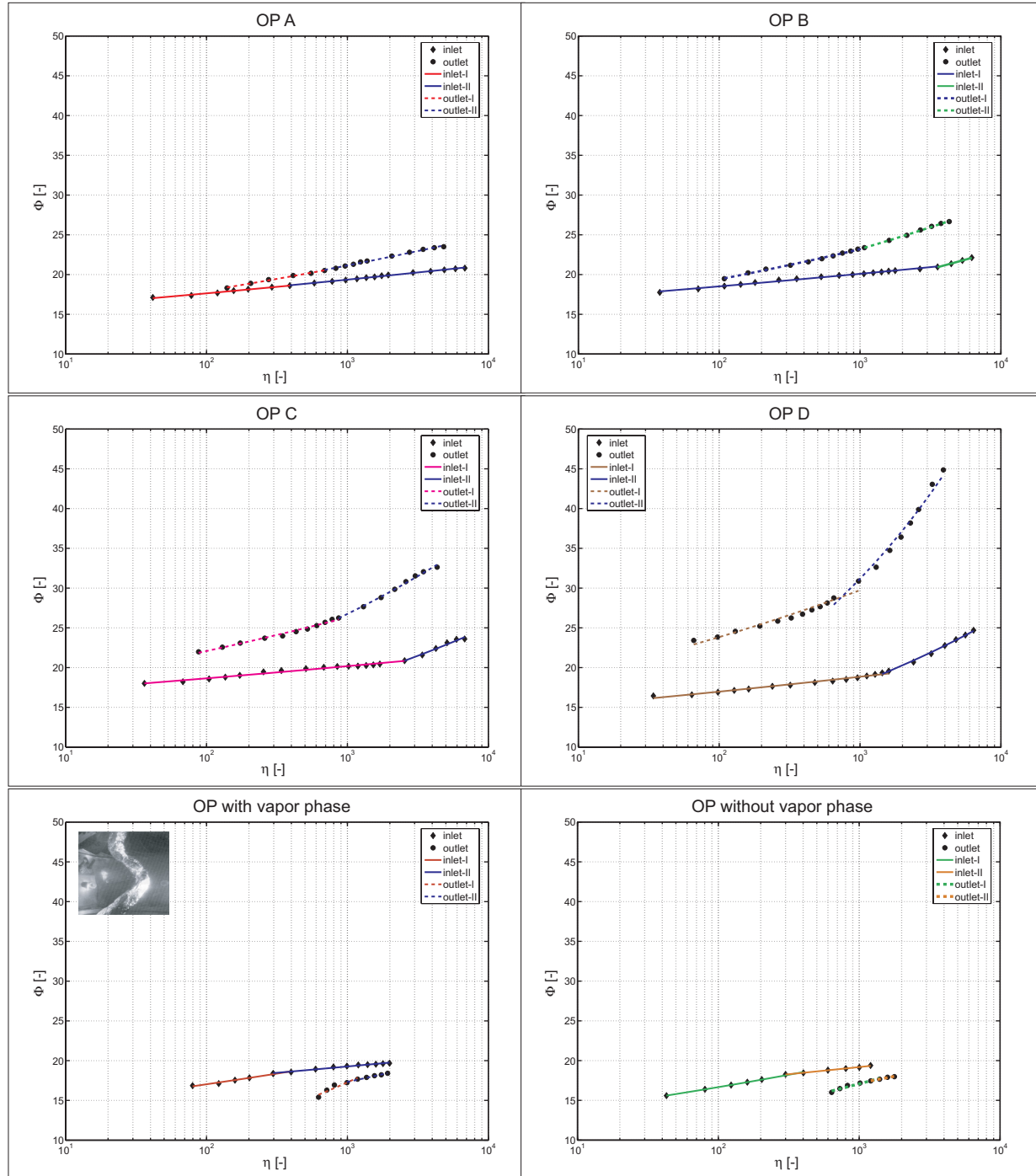


Figure 6.16: Boundary layer's "chevron" in the cone, both at the outlet and at the inlet, for all operating points studied

Section	Operating point	$Re$	$Re_\theta$	$A$	$\alpha$	$B$	$\beta$
1.30 (inlet)	A	$2.73 \cdot 10^6$	11244	14.712	0.0394	14.727	0.0396
	B	$2.98 \cdot 10^6$	12255	15.714	0.0356	9.4243	0.0976
	C	$3.07 \cdot 10^6$	14444	15.923	0.0343	7.2035	0.1356
	D	$3.31 \cdot 10^6$	15600	13.766	0.0455	5.7154	0.1666
	With vapor phase	$1.6 \cdot 10^6$	1878	12.573	0.0659	14.994	0.0363
	Without vapor phase	$1.6 \cdot 10^6$	1502	11.661	0.0775	14.377	0.0418
1.75 (outlet)	A	$2.44 \cdot 10^6$	8983	13.041	0.0695	12.904	0.0715
	B	$2.66 \cdot 10^6$	13992	13.567	0.0776	11.876	0.097
	C	$2.74 \cdot 10^6$	17310	15.53	0.0764	10.013	0.1422
	D	$2.96 \cdot 10^6$	21810	15.319	0.096	5.2872	0.2568
	With vapor phase	$1.43 \cdot 10^6$	1849	4.3496	0.1996	8.9878	0.095
	Without vapor phase	$1.43 \cdot 10^6$	1849	7.4902	0.1193	9.8156	0.0812

Table 6.2: The power scaling law constants

For the present case study, the composite power law of Barenblatt and Chorin gives a better description of the boundary layer for fully turbulent flow in adverse pressure gradient.



# Chapter 7

## DESIGN AND DEVELOPMENT OF THE NEW HOT-FILM PROBE

### 7.1 BACKGROUND

Flow sensors for fluid mechanics studies must satisfy a number of performance requirements, such as fast response speed, directional, low detection limit, least intrusion to the flow field of interests, and preferably low costs. For certain applications, it is also desirable that two dimensional arrays of such sensors can be made for boundary layer flow studies.

Many engineered flow sensors have been developed in the past, based on a number of sensing principles, including thermal anemometry, hot-wire or hot-film anemometers, and indirect inference from pressure differences. A hot-wire or hot-film anemometer uses flow-induced, forced convection to indirectly infer the flow velocity. The availability and performance of flow sensors have been seriously limited by traditional fabrication techniques. The majority of existing hot-wire anemometers are made using conventional manufacturing methods. The sizes of such sensor devices are generally large. It is difficult to miniaturize conventional sensors because their manufacturing typically requires handicraft. In the same time, mass-production with good device repeatability was very challenging.

During the past decade, micromachining technology had been developed to fabricate miniaturized mechanical parts and to produce large quantities of sensors with uniform geometry and performance. Generally, a typical MEMS device has a characteristic length of more than  $1\mu m$  but less than  $1mm$ . It combines mechanical and electrical components and can be either individual units or parts of a more complex mechanical system with integrated electronics. Motors, turbines, valves, gears and transducers of less than  $100\mu m$  size have been successfully fabricated. Integrated microelectronics and micro-machines constitute the micro-electro-mechanical-system - MEMS - , which can execute sense-decision-actuation on a monolithic level. During the last years there has been a tremendous interest in developing MEMS, with major impacts in many disciplines: biology, medicine, optics, aerospace, and mechanical and electrical engineering.

MEMS devices are fabricated using manufacturing processes that have been developed specifically for MEMS applications. Some of these commonly used processes are: anisotropic etching of silicon, fabrication of high-aspect ratio microstructures, anodic bonding of silicon to glass, etc. The micromachining process uses the lithography to expose the designed photoresist patterns on the chip; after, the unwanted portion is selectively etched away. By repeating the deposition-removal processes, sensors and actuators with intricate geometry can be produced, see Ho and Tai [1996, 1998]. These procedures are similar to those used in integrated circuit (IC) fabrication but with a difference: 3-D and freestanding structures are common features, because of the nature of mechanical parts. Several manufacturing technologies such as bulk micromachining, surface micromachining, and LIGA - Lithographie, Galvanoformung, und Abformung - have been developed to make various micromachines. A brief introduction of these technologies can be found in a paper by Ho and Tai [1996].

Micromachines have several unique features. First of them concerns the typical micromachined transducer sizes, which are on the order of 100 microns and which can be one or more orders of magnitude smaller than traditional sensors and actuators. The drastic reduction in inertia resulting from these smaller sizes equalize with a substantial increase in the frequency response. Second, batch processing, characteristic of IC fabrication, can be used to make many transducers for distributed sensing and actuation over a wide area. This capability enables to observe certain flow characteristics in a 2-D domain and to perform control at the proper locations. Potential application areas include, among all, the reduction of surface shear stress in a turbulent boundary layer. Third, micromachine manufacturing technology is derived from IC fabrication so it is possible to integrate the IC with microtransducers to provide logic capability.

### 7.1.1 MEMS wall shear-stress sensors - historical survey

In the last two decades, several research groups have developed micromachined flow sensors based on a diversity of sensing principles. Microfabrication offers the advantages of high-spatial resolution, fast time response due to low mass and thermal mass, integrated signal processing, and potentially low costs. Microsensors based on various principles including thermal transfer - de Bree et al. [1999]; Ebefors et al. [1998]; Jiang et al. [1994a]; Lofdahl et al. [1992]; van Baar et al. [2001]; van der Wiel et al. [1993]; van Honschoten et al. [2001] -, pressure distribution - Boillat et al. [1995]; Kalvesten et al. [1996]; Lofdahl et al. [1996] - and torque transfer - Enoksson et al. [1996]; van der Wiel et al. [1995]; Svedin et al. [1998]; Svedin et al. [2001] -, have been developed. There is an important aspect of microsensors: being small, and, generally, producing small signals, they do not necessary interface with the macro-world. Therefore, micromechanical sensors cannot be considered as separate entities but they should actually be viewed as microsystems involving, in the same time, the sensing microstructure and the interfacing together with the packaging. Hence, the microsensors design and development-process should include, simultaneously, the interfacing and packaging aspects, to assure a successfully working micro-sensor-system. In addition to flow sensors, boundary-layer shear stress sensors have been realized using floating element methods - Padmanabhan et al. [1996] - and thermal transfer principles - Xu et al. [2002].

The wall-shear stress, as we have shown in chapter 5, is an essential quantity to compute, to measure or to infer in wall-bounded turbulent flows. Knowledge of such wall



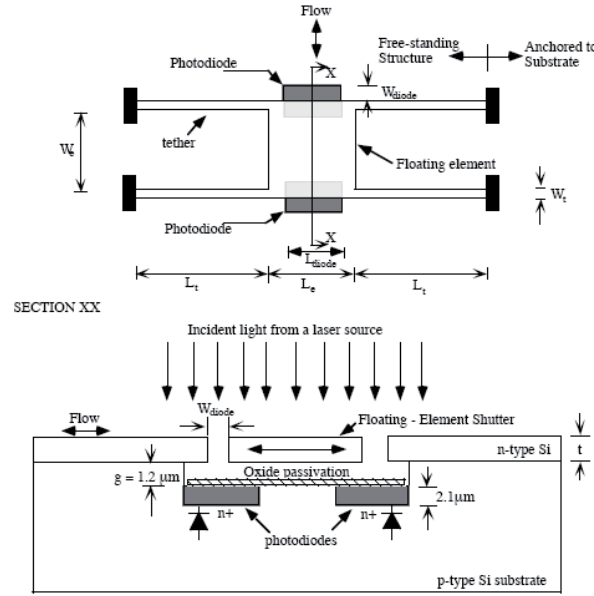


Figure 7.1: Schematic presentation of the floating element balance, Padmanabhan et al. [1996]

shear stress is essential, and its measurement holds great importance for investigating and controlling wall-bound turbulence and flow separation both in aerodynamic and in hydrodynamic fields. The time-averaged values of this quantity indicate the global state of the flow along a surface and it can be used for control purposes, drag-reduction or separation delay. The time resolved part of the wall shear stress is a measure of the unsteady structures in the flow, responsible for the individual momentum transfer events and is an indicator of the turbulence activities.

For a reliable measurement of turbulent wall shear-stress over a large range of Reynolds numbers two main conditions need to be satisfied. The first requirement concerning protruding sensors is that the result must be independent on the type of boundary layer; the method cannot use non-universal models for specific boundary layer regions, such as the log-law, shown in chapter 6, where the constants depend on the pressure gradient, for example. The second requirement is that the sensor must be small enough to avoid spatial resolution which leads to an underestimation of the fluctuating shear stress.

Measurement of shear stress, as well as temperature, in complex flows is of great importance and interest for understanding the dynamics of fluid flow. Accurate, time-resolved measurements of wall shear stress are essential for a physical understanding of complex flow phenomena. At moderate Reynolds numbers, typical length scales of interest are in the order of  $100 \mu m$  or less, and the typical timescales require an usable bandwidth of  $10 kHz$  to capture the spectrum of turbulent fluctuations. Manufacturing techniques and mechanical constraints limit the size of traditional hot-wire sensors. Many techniques have been developed over the years and their potential and limitations have been explored. Hence, the MEMS-sensors are well suited for wall-shear stress measurements, in particular for tracing local coherent structures in turbulent boundary layers. Micromachined wall shear stress sensors calculate the shear stress from measurements performed at the surface, mechanically, by using a floating element, or thermally, by using heat dissipation, or infer

the shear stress at the wall from velocity measurements performed within the viscous sublayer of the boundary layer.

Miniaturized shear-stress sensors fabricated by using MEMS technology offer superior spatial resolution, high performance, fast time response, minimized interference with fluid flow and they are low cost sensors. In the same way, the micromachined shear-stress sensors can be grouped into two distinct classes: direct techniques, such as floating-element devices or indirect techniques, such as hot wires or hot films. The floating element sensor, see Schmidt et al. [1988], Padmanabhan et al. [1996], Pan et al. [1995], offers many advantages by the fact that the measurement is a direct one and not reliant on indirect correlations between shear and some other phenomena. However, these techniques are also complex and require a complex mechanical devices fabrication and accurate transductions of small motions. In the second category, the most common approach is the use of the thermal anemometry, where the shear is related to the convective cooling of a heated element. This technique, while reliant on the convective properties of the flow, offers the advantages of simplicity, lack of moving parts and relatively good sensitivity. MEMS-based thermal sensors evidence some interesting properties, both for measuring fluctuating flow quantities and for detecting coherent structures in reactive control purposes. The MEMS technology makes it feasible to fabricate miniature sensors in such a small scale that even high wave-number-range eddies in technically interesting turbulent flows can be resolved. The significant advantages of MEMS are: the possibilities to operate sensors at low overheat temperatures and improved methods for insulation of the heated sensing parts, high accuracy in the manufacturing process, the possibilities to fabricate closely spaced multi-sensor probes integrated on one chip, and once the design and fabrication method has been developed, production of sensors in a large quantity at a low cost.

For almost 10 years, MEMS-based wall-shear stress sensors with low overheat temperatures and improved thermal insulation, related to conventional sensors, to the surrounding substrate have been fabricated. Most of MEMS devices fabricated along these years have typically used polysilicon as the sensing element, see Lui et al. [1994], Kälvesten et al. [1996].

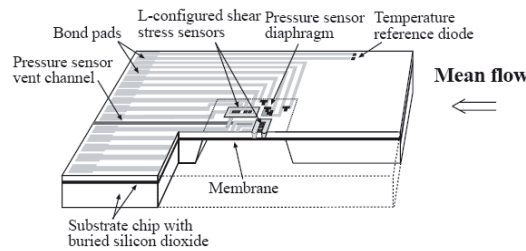
Since their initial demonstration, much progress has been made in further development of MEMS thermal sensors for shear-stress measurements. There were tested different sensing element configurations and materials, and there were investigated different sensor characteristics such as thermal insulation, frequency response, pressure sensitivity and noise floor spectra. Recently, there have also been numerical simulations on MEMS thermal shear-stress sensors to study the effect of natural convection on the fluid velocity profile and, in the same time, the effect of heat conduction in the sensor substrate on frequency response. The numerical simulations evidence, mainly, that even for a perfectly insulating solid, the surface temperature is affected a large distance downstream the heated part, and they are showing that the heat conduction to the substrate is completely dominant for almost all possible choices of surrounding material. A short summary of micromachined sensors available for shear stress measurements, is presented in table 7.1, offering a brief description of each device.

Author	Sensor type	Description
Oudheusden and Huijsing [1988]	Thermal	The sensor surface was 4mm x 3mm and was fabricated in silicon. The sensing element is a thermopile (with directional sensitivity). The sensor was tested in a turbulent boundary layer, for a range of 0-2Pa. Its frequency response was poor due to the substrate conduction, ( $< 1Hz$ ).
Schmidt et al. [1988]	Floating element	The floating element size was $500\mu m \times 500\mu m$ and was fabricated in polyimide. Its working principle is based on the differential capacitive sensing. It was tested in a laminar channel flow, for shear-stress values up to 1Pa, but it showed mainly drift problems during the tests. The bandwidth was about 10kHz.
Ng [1990]	Floating element	The floating element size was $120\mu m \times 140\mu m$ and was fabricated in silicon. Its working principle is based on a piezoresistive transduction scheme. It was conceived for shear-stress applications in polymer extrusion for values between 1kPa and 100kPa.
Goldberg et al. [1994]	Floating element	This floating element has the size of $500\mu m \times 500\mu m$ and was fabricated in silicon; it is working on the same principle as the one developed by Ng. [1] and was designed for the same applications. Main difference were the backside electrical connections for packaging facilitation.
Jiang et al. [1994b]	Thermal	The sensor has the size of $10 - 160\mu m \times 1\mu m$ and was fabricated in polysilicon. It is a hot wire anemometer; it was tested in a wind tunnel and there are presented only flow velocity data. Sensor's bandwidth was 500 kHz in constant current mode.
Liu et al. [1994]	Thermal	The sensor, a hot wire anemometer, has a surface of $200\mu m \times 200\mu m$ , fabricated in polysilicon; it was tested in a wind tunnel, for wall shear-stress values between 0-1.4Pa showing a sensitivity of 15V/kPa. Sensor's bandwidth was 500 Hz in CCT mode.
Kalvesten [1995]	Thermal	The sensor is a hot film anemometer with direction-sensitivity; it has a size of $300\mu m \times 60\mu m$ and was fabricated in polysilicon. It was tested in a turbulent boundary layer. Sensor's bandwidth was noticed in constant temperature mode, at about 40kHz.
Pan et al. [1995]	Floating element	The floating element size had $100\mu m \times 100\mu m$ and was fabricated in polysilicon; it is a capacitive sensor. It was tested in laminar channel flows for wall shear-stress values up to 10Pa. No bandwidth reported.
Jiang et al. [1996]	Thermal	This sensor is actually a hot wire sensor array made up of 25 sensors with pitch of $300\mu m$ , the whole having a size of $150\mu m \times 3\mu m$ . It was fabricated in polysilicon. and was tested extensively turbulent boundary layers detecting a "streak" structure and providing instantaneous wall shear stress distributions. Sensor's bandwidth was 30 kHz.
Padmanabhan et al. [1996]	Floating element	The floating element size had $120\mu m \times 120\mu m$ , it was fabricated in silicon and it is based on an optical position sensing scheme. It was tested in laminar boundary layer for wall shear-stress values of 0.005Pa. Theoretical bandwidth was 52 kHz.

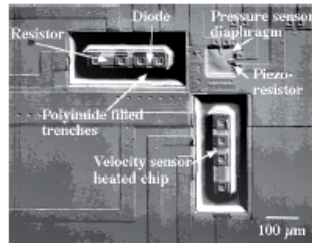
Table 7.1: Progress in micromachined shear-stress sensor technology

### 7.1.2 MEMS wall shear-stress sensors - examples

Two of the MEMS thermal wall-shear stress sensors used were, mainly, evidenced. Kalvesten [1995] has developed a MEMS-based, flush-mounted wall shear stress sensor, see figure 7.2. The heated portion is relatively small,  $300 \times 60 \times 30 \mu m^3$ , and is thermally insulated by polyimide-filled, KOH-etched trenches. The sensitive part of the chip is electrically heated by a polysilicon piezoresistor and its temperature is measured by an integrated diode. For the ambient temperature, a reference diode is integrated on the substrate chip, far away from the heated portion of the chip. The power consumed to maintain the hot part of the sensor at a constant temperature was evaluated. For a step wise increase of electrical power, the response time was about  $6ms$  which is double the calculated value. This response was considerably shortened to  $25\mu s$  when the sensor was operated in a constant-temperature mode using feedback electronics. The main advantage of this sensor is that it can operate at relatively low temperature on the heated diode, of the magnitude 100 degrees.



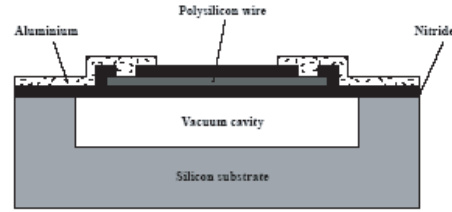
a. Schematic cross-section



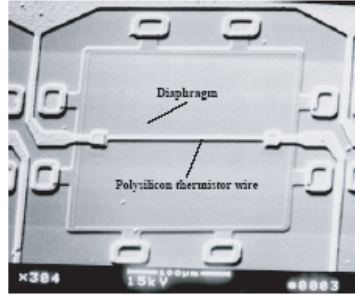
b. SEM photo

Figure 7.2: MEMS flush-mounted wall shear-stress sensor, Kalvesten [1995]

Jiang et al. [1996] developed an array of wall shear stress sensors based on the thermal principle. Each sensor was made smaller than a typical streak width. For a Reynolds number of  $10^4$ , the width of the streaks was estimated at around  $1mm$ , so that each sensor was designed to have a length less than  $300\mu m$ . Figure 7.3 -a- shows a schematic diagram of one of these sensors. The polysilicon resistor wire, is located on the diaphragm, having  $3\mu m$  wide and  $150\mu m$  long. Below the diaphragm there is a  $2\mu m$  deep vacuum cavity for heat conduction loss reduction to the substrate. When the wire is heated electrically, heat is transferred by heat convection to the flow resulting in an electrically measurable power change which is a function of the wall shear stress. Figure 7.3 -b- shows a photograph of a portion of the  $2.85 \times 1.00 cm^2$  streakimaging chip, containing just one probe.



a. Schematic cross-section



b. SEM photo

Figure 7.3: MEMS shear-stress sensor developed by Jiang et al. [1996]

### 7.1.3 Motivation

As the experiments show, the main frictional losses of a turbomachine take place in the runner. Thus, it becomes very interesting to be able to explore the flow in this part of the turbomachines and to validate the CFD codes. This analysis will offer informations on the boundary layer separation tendency, on the losses prediction and thus will facilitate the characterization and the understanding of the flow. Yet, the availability and performance of the commercial hot film sensors, in this region of a turbomachine, have been seriously limited by several specific constraints. First of all the complex character of the flow in the runner must be taken into account: the strongly 3D flow, the turbulence and the Coriolis forces influence.

On the other hand, there is the accessibility problem, which rises. It is due to the fact that the dimensions of the actual hot film probes are not adequate for mounting it on the runner blades surface. Direction founding of the hot-film probe in the flow, the aging of the probe are another disadvantages in using it for exploring the flow in the runner.

Motivated by these issues, and taking into account the progress achieved in MEMS technology, the aim of this PhD thesis is to design and to develop a new multidirectional miniature hot film probe able to measure the wall shear-stress in the runner. The design, fabrication stages, and testing of such sensors, which contains new thermal insulating structures development, are presented below. Moreover, we also present three dimensional simulations of the new MEMS thermal wall shear-stress sensor to gain a quantitative understanding of these devices.

## 7.2 CONCEPTION OF THE NEW HOT-FILM PROBE FOR WALL SHEAR-STRESS MEASUREMENTS

The choice of development and fabrication of a new wall shear stress sensor for specific water turbomachines applications was stimulated by personal exigencies and, in the same time, by profound study of the actual wall shear stress sensors industrial market. There were also taken into account considerations of cost, manufacturing time and technical informations point of view.

As explained in chapter 3, the most adequate technique for wall shear-stress in a turbomachine is the hot-film.

The design of the new probe is an important step for the development, unfortunately restraint by several criteria. The first one deals with the size of the probe: the sensors should be thin enough, so that they do not perturb the flow.

Meanwhile, a probe consists of the following:

- *Sensor*, forming the heating element;
- *Sensor supports*, prongs or substrate, carrying the sensor and leading current to it;
- *Probe body*, carrying the sensor supports;
- *Connector*, providing electrical connection to the probe support or probe cable.

Main limitations in support and heated element are essential and there will be studied further.

### Sensor substrate

A hot-film sensor is made up by a metallic film deposited on an insulating substrate which serves to minimize the heat losses by conduction. If the substrate is not sufficiently insulating it can lead to an extension of the heated surface. These 2 reasons determine the choice of the substrate material, characterized by a reduced thermal conductivity. The main materials available in the microtechnology, with a relative reduced thermal conductivity are presented in table 7.2.

Material	Density $\rho[kg/m^3]$	Specific heat $C_p[J/(m \cdot K)]$	Thermal conductivity $k[W/(m \cdot K)]$
Pyrex	2220	728	1.1297
Silicon	2330	702.9	125.52

Table 7.2: Main thermal properties for the available substrate materials

Moreover, regarding the substrate, its thickness becomes another interesting parameter which must be quantify.

### Sensitive element

The development of a new hot-film sensor should imply a compromise between the length of the heated element and the thickness of the substrate, for obtaining a high performance probe.

Another limitation in the use of the commercial wall shear-stress probes is based on a high frequency response. A relative extended heated zone in the substrate related to the metallic film size leads to a relative high reduction of the sensor's frequency response. This means that the length of the main element of the probe should be as small as possible. In the flow, near the heated film it is developed a thermal boundary layer; this is imposing the film size. The boundary layer's thickness is determined by the local parameters of the flow. The thermal boundary layer developed over the hot film surface should be included in the viscous sublayer, according to the Reynolds analogy. This limitation, imposed to the thermal boundary layer's thickness means a limitation for the longitudinal extend of the heated zone on each hot film. In the literature there are presented many different limitations concerning the maximum longitudinal extend of the heated zone, see Hanratty and Campbell [1996], Haritonidis [1989], Löfdahl and Gad-el Hak [1999].

The geometry of the heated film is also an interesting parameter for the performance of the sensor. Although, the heated film's geometry, in itself, doesn't have an influence over the sensor's sensitivity, there are some limitations regarding its thickness: it should be less than  $1\mu m$ , so that it doesn't modify significantly the heat transfer at the wall. 3 designs were proposed, see figure 7.4.

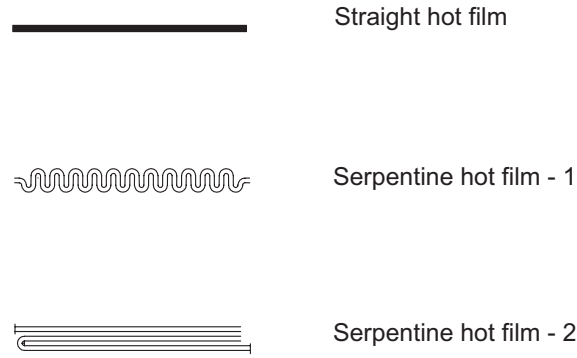


Figure 7.4: Different designs proposed for the hot film

Finally this new hot-film probe, to suit to all components measurement requirements for a turbomachine, taking into account all the limitations presented above, needs to satisfy more conditions:

1. The probe has to be small enough, so that, together with the entire encapsulation system, the dimension should not exceed  $\Phi = 4mm$ ;
2. The sensor should not perturb the flow, which means that the electrical connections should be realized on the backside, the surface of the probe should not have any protuberances;
3. Hot-film impedance  $\sim 100\Omega$ ;
4. It should have a good electrical isolation between the surface of the probe, which comes in contact with the water, and the hot-film;
5. It should have isolation between the upside and the backside of the probe;
6. It should be water-tight;
7. The sensor should be conceived in a 3D configuration, for detecting flow direction;
8. The sensors should measure a wide velocity range;

9. They should have high accuracy and resolution;
10. They should be low cost and easy to use.

It was chosen a 3 hot-films configuration in one shear-stress sensor, due to the fact that in the turbine the flow is unsteady and the purpose is to be able to measure both the value of the wall shear-stress, and in the same time to be able to determine the flow sense and direction. Taking into account all the conditions above, there was developed the new design for the hot-film probe, which has 3 hot-films positioned in triangle, in a way that there isn't any heat transfer between.

## 7.3 HOT-FILM DEPOSING TECHNOLOGY AND FABRICATION STEPS

The new flow sensor was conceived and manufactured using the most adequate techniques based on MEMS. The general description of the microtechnology techniques used, is presented in annexe C. The development of this new multidirectional sensor implies technological developments together with the Center of MicroNanoTechnology, in EPFL, which allows microsystems design and manufacturing for both industrial and research applications.

### 7.3.1 The center of MicroNanoTechnology - overview

The CMI, Center of MicroNano Technology, in Swiss Federal Institute of Technology (EPFL), has a assembly of clean rooms and high technology processing equipments, used for training and experimentation of the microtechnologies scientific users, guided by a professional staff.

The availability of a clean room is mandatory for the microtechnology research and product miniaturization. It's exploitation is managed by a staff of specialists in microtechnology, ensuring the equipment accessibility and the help needed in performing the experimental work, as well as they evaluate, install and operate the equipment, develop new processing steps and improve the existing ones. Meanwhile, each new clean room user gets a training on processing equipments operation.

Practical works, diploma works, PhD thesis works, microtechnology experimental researches are the main activities of CMI.

The user's access in the clean room is regulated in the way that it is promoted in the first place the educational activities, then the research ones, and afterwards, the partnership research with the other academic institutions.

### 7.3.2 First new hot-film probes generation

One important step before the fabrication of the new sensors is the choice of the material for the heated element. The main constraint which should be respected is that it must have a linear resistance vs. temperature characteristic. Common heated element materials used because of their properties as well as for their availability in small dimensions, are platinum, nickel and combinations of platinum with different metals, like tantalum or titanium. Table 7.3, presents their main thermal properties.



Material	Density $\rho[kg/m^3]$	Specific heat $C_p[J/(m \cdot K)]$	Thermal conductivity $k[W/(m \cdot K)]$	Temperature coefficient of resistivity TCR[ppm/°C]
Platinum	21400	133.9	69.036	3000
Nickel	8900	443.5	87.864	6800
Tantalum	16600	138.1	71.128	-
Titanium	4500	523	20.92	-

Table 7.3: Main thermal properties for the available heated element materials

**Platinum** is a precious metal possessing a very stable and, most interesting, a near linear resistance versus temperature function. A heavy, malleable, ductile, precious, platinum is resistant to corrosion and occurs in some nickel and copper minerals along with some native deposits. Platinum possesses remarkable resistance to chemical attack, excellent high-temperature characteristics, and stable electrical properties. All these properties have been exploited for industrial applications. Platinum is used in jewelry, laboratory equipment, electrical contacts, dentistry, and automobile emissions control devices. While intrinsically less sensitive than thermistors or other metals, thin films in platinum provide very high base resistance and high device sensitivity.

**Nickel** is a silvery white, hard, malleable, ductile metal, being a good conductor of electricity and heat. Nickel metal is relatively resistant to corrosion. Water solubility of nickel compounds vary. The nickel is used, mainly, in alloys, which are used in the making of metal coins and jewelry and, in industry, for making metal items. It is used to make stainless steel and other metal alloys. Nickel and nickel compounds are used, generally, for nickel electroplating, to color ceramics, to make batteries, for permanent magnet materials, and as catalysts. In the same time, on account of its permanence in air and inertness to oxidation, it is used in the smaller coins, for plating iron, brass, for chemical apparatus.

**Tantalum** is gray, dense, ductile, very hard, easily fabricated, and highly conductor of heat and electricity. The metal is known and appreciated for its resistance to corrosion by acids. Because it resists attack by body liquids and is non irritating, Ta is widely used in making surgical appliances. Meanwhile, the major use for tantalum, as the metal powder, is in the production of electronic components, mainly capacitors. Because of the size and weight advantages, tantalum capacitors are attractive for portable telephones, pagers, personal computers, and automotive electronics. Tantalum is also used to produce a variety of alloys that have high melting points, are strong and have good ductility. Alloyed with other metals, it is also used in the production of super-alloys for jet engine components, chemical process equipment, nuclear reactors, and missile parts. Because of its ductility, Ta can be drawn into fine wires or filaments, which are used for evaporating metals such as aluminium.

**Titanium** is a light, strong, glossy, easy to work, corrosion-resistant transition metal; it is used in strong light-weight alloys and its most common compound, titanium dioxide, is used in white pigments. One of titanium's most notable characteristics is that it is as strong as steel, having only 60% its density. Titanium is well known for its excellent corrosion resistance, almost as resistant as platinum, being able to withstand attack by acids, moist chlorine gas, and by common salt solutions. It is a metallic element, also

well-known for its high strength-to-weight ratio. Titanium is as strong as steel, but 43% lighter; it is 60% heavier than aluminium, but twice as strong. These properties make titanium very resistant to the usual kinds of metal fatigue. It is paramagnetic, weakly attracted to magnets and has a very low electrical and thermal conductivity. Because of its very high tensile strength, even at high temperatures, light weight, extraordinary corrosion resistance, and ability to withstand extreme temperatures, titanium alloys are principally used in aircraft, armor plating, naval ships, spacecraft and missiles. It is also used in cement, and as a strengthening filler in paper. Recently, it has been put to use in air purifiers or in window film on buildings which when exposed to UV light. Welded titanium pipe is used in the chemical industry for its corrosion resistance. When alloyed with vanadium, it is used to make the outer skin of aircraft, fire walls, landing gear, and hydraulic tubing.

After a detailed analysis of all these metals and considering also the constraints imposed by the application of the new development it was chosen as initial configuration for the heated element: Ti/Ni, Ti serving as adhesion layer between the heated element and the substrate.

### Manufacturing Steps

A first configuration for the new miniature hot-film sensor, after considering all the restrictive criteria presented above is presented. It consists of 3 very thin films of alloy titanium/platinum, about 100nm deposited by sputtering on a pyrex support, of 1mm thickness. For the conducting tracks, there is deposited Au, 500nm, by evaporation, on the front side of the wafer. The electrical access to the sensor's films was thought as backside wire bonds, in copper, to not disturb the flow. An additional  $SiO_2$  coating, at about  $1\mu m$  protects the film from against electrolysis effects. The main fabrication steps are presented in figure 7.6. The wafer used are characterized by a thickness of  $500\mu m$  and a diameter of 100 mm.

As explained in section 7.2, there were implemented on the same wafer, sensors corresponding to the 3 different designs for the heated film, allowing to obtain an impedance of about  $100\Omega$ , see figure 7.6.

Meanwhile another difficulty related to the pyrex electrodischarge needed in the electrical connections realization appeared. It is used a electrochemical discharge machining technology, which combines good surface quality, in the same way as obtained by HF etching, and the flexibility of laser machining. Otherwise, it is a manually procedure, needing a precise tool handling for every hole, while the positioning relatively to the workpiece is not precise. Moreover, another imprecisions appear related to the accuracy of machining tool's motion, machining tool wear, vibrations of machining tool and workpiece. Taking into account the fact that, for each wafer there were developed 100 probes, meaning about 400 holes for each wafer, this process becomes an inconvenient. So, the substrate material has to be changed.

Although the term MEMS is not restricted to silicon micromachining, most of today's MEMS technology is based on silicon. Silicon mono-crystalline wafers offer a good combination of qualities, ranging from ideally elastic, no mechanical hysteresis, to a good heat conductor, from low to intermediate electrical conductivity, depending on type, from having a small thermal expansion coefficient to being stable up to high temperatures.

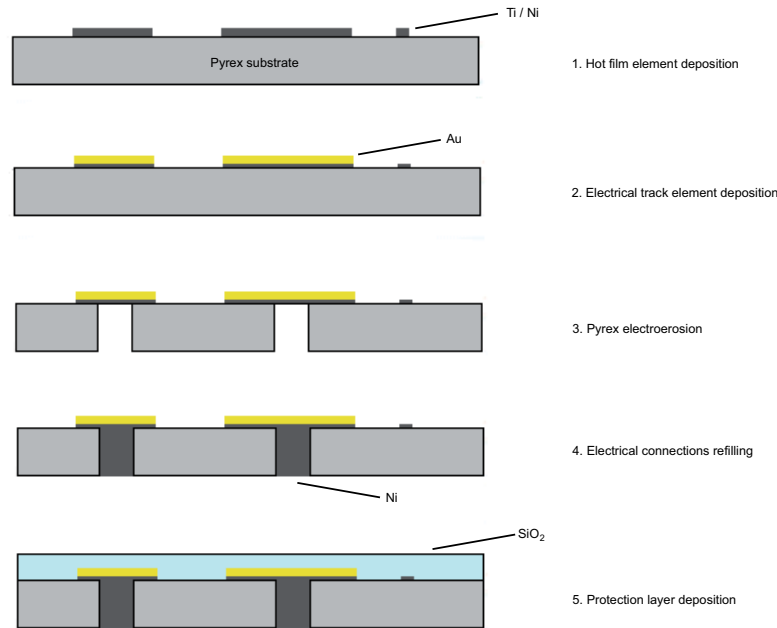


Figure 7.5: Main fabrication steps for the initial configuration of the new hot-film sensor

More interesting, silicon wafers are produced and used on a large scale for integrated microelectronics resulting in low prices and compatible equipment. Therefore, the majority of MEMS devices are made on silicon wafers as the starting substrate.

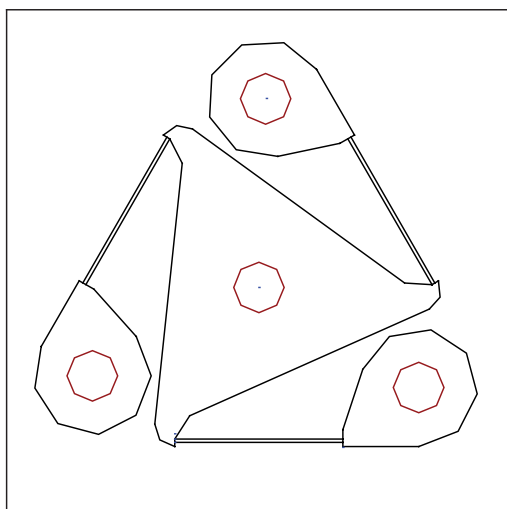
Finally, the substrate material was replaced by silicon. Due to the fact that the thermal conductivity of the silicon is about 100 times more than the one of the pyrex, risking to obtain heated plates, there were added around the hot-films, holes serving as gates for the heat transfer by conduction. Moreover, due to the fact that the silicon wafers used are 3 times less thicker than the ones in pyrex,  $380\mu\text{m}$  related to  $1\text{mm}$ , the structure of the new probe has to be reviewed, see figure 7.7.

Main change was produced for the conducting tracks, where the Au layer thickness was reduced from the initial  $500\text{nm}$  to about  $300\text{nm}$ . Simultaneously, for the electrical connections on the backside it will be used copper instead of nickel.

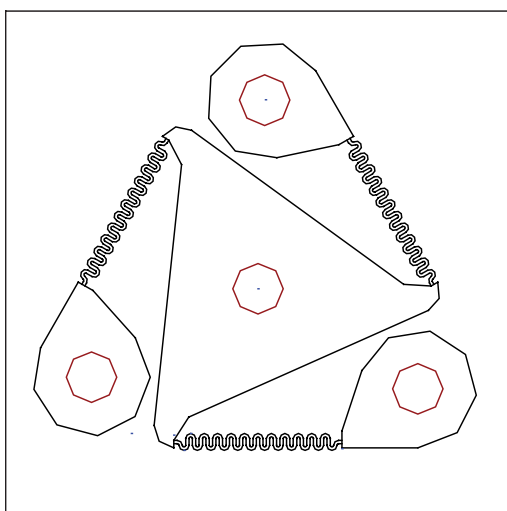
### 1. Masks design and fabrication

The first step, in the development of the new miniature hot-film probe is the masks fabrication. Generally, as explained in annexe C.1, a mask is used to print the desired pattern on the photoresist by photolithography. It acts as a screen between the light source and the photosensitive surface, during the exposition to a light with parallel beams. The mask is made up by a glass plate supporting a chromium layer, on which the desired patterns are transferred. In the same time, using L-Edit software, the patterns to be transferred on masks and, afterwards on the wafer, constituting the new components of the new hot-film probe, are designed and transferred on the machine used to write these masks, namely Direct Laser Writer, DWL200.

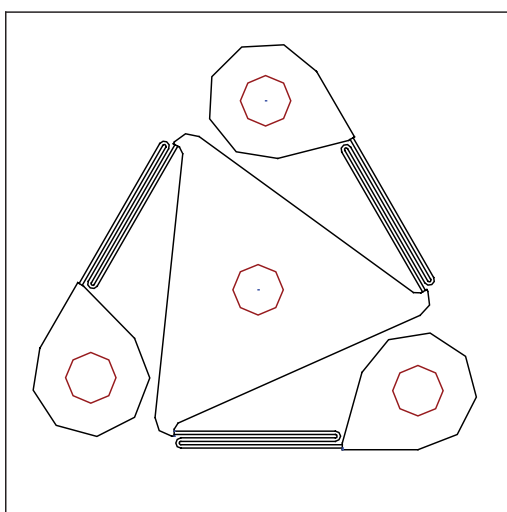
The DWL is a high precision machine using raster technology to impression on divers substrates like silicon, glass, etc. The DWL 200 is a high resolution laser lithography system, with active write area of  $195 \times 195 \text{ mm}$ . It can be used for semiconductors



*I. Straight hot film design*



*II. Serpentine hot film - 1 - design*



*III. Serpentine hot film - 2 - design*

Figure 7.6: Top view of the new sensor, corresponding to different designs for the hot-film probe

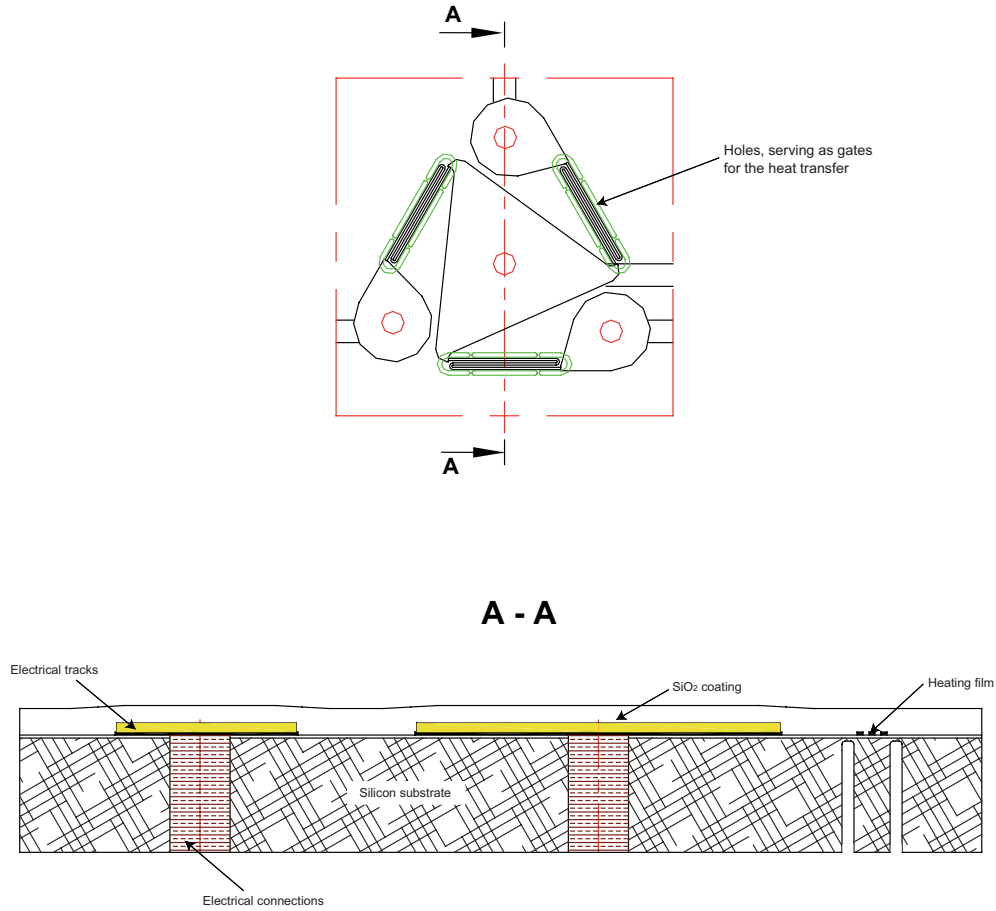


Figure 7.7: Top schematic view and cross-section in the new sensor

mask and direct writing, integrated optics and any application where high precision, high resolution images must be produced and obtained. The DWL can accommodate various write heads. Masks with dimensions of 195 x 195mm, as well as, wafers with a diameter of 195mm may be used and an alignment precision of less than  $\pm 250nm$  may be achieved.

Afterwards, the photoresist covering the chromium mask is developed in a tank of Microposit CD 26, discovering the designed patterns. This process is followed up by chromium etch using an acid bath and the remaining resist is eliminated by immersion in a solvent tank.

New sensor fabrication process is a 3 masks process, illustrated by figure 7.8:

1. The first one is used to define the films and electrical track layers, all the subsequent mask layers being aligned to this layer;
2. the second one is dedicated to the electrical track layers increasing,
3. the 3<sup>rd</sup> one is used to pattern the electrical connections holes and the gates provided for reduce the thermal conduction.

Meanwhile, on a wafer there are placed about 100 sensors. For the wafers dicing it is used a Nd-YAG zig-zag-slab laser, presented in annexe C, while the design used is presented in figure 7.9. The wafers are diced in 4mm diameter sensors.

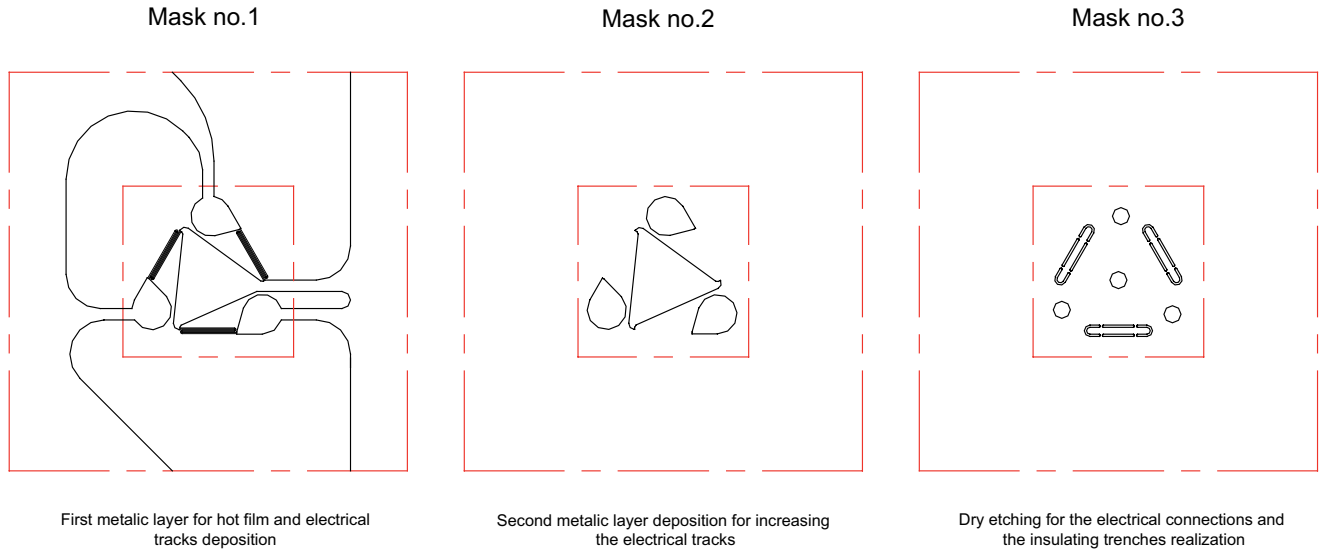


Figure 7.8: The 3 masks used for first generation sensors fabrication

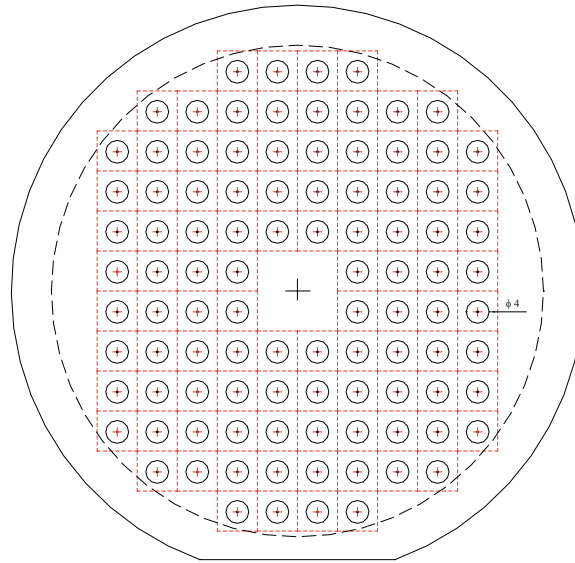


Figure 7.9: Wafer design used for laser dicing

First generation of sensors was developed from wafers with substrates in silicon, 4", 380 $\mu m$  thickness, DSP, 1 $\mu m$  wetox, with resistivity 1-10  $\Omega cm$ .

A preliminary stage in the fabrication process is the reducing of the wetox layer on a face of the device from initial 1 $\mu m$  to 0.2 $\mu m$ , using a wet etching in a HF bath, see figure 7.10. The protection of the backside face is ensured by a relatively thick photoresist, namely S1818.



Figure 7.10: Wetox reducing on the front side of the device

## 2. Heated elements and the first electrical track layer deposition

The first process in the new wall shear-stress sensor generation fabrication is the heated elements and a first metal layer corresponding to the electrical tracks performance.

Photolithography is a first step. A HMDS processing is planned. This technique consists in an adherence promoter vaporization, HMDS, in a automatic vapor prime oven, for improving photoresist adhesion to oxides. The HMDS - hexamethyldisilazane - reacts with the oxide surface forming a strong bond to the surface. The HMDS coating process is performed for all photolithography steps. Afterwards, the photoresist is deposited on the wafers by centrifugation.

The photoresist used, MAN 1410, is a negative photoresist. The MAN 1400 series is a photoresist especially designed to generate undercut patterns. The edge profile is easily controlled by variation of the exposure and development parameters. Pattern sidewalls can be produced from nearly vertical to extremely undercut ideally qualifying the resist for metallization processes using lift-off. The chemical composition of MAN 1400 allows easy and residue-free resist removal. For coating it on a wafer's side, it is used a *Ritetrack coater & developer*, where it is processed by spincoating. Afterwards, a thermal processing which ensures photoresist's hardening on the wafer is performed, on a heated plate at  $98^{\circ}\text{C}$ , during 90s.

The second step is the pattern transfer from the mask to the wafer. The mask aligner, *MA150*, allows the accomplishment of this procedure. Usually in a development, several different layers must be superposed, requiring several alignment marks, both on the front side and on the backside. Meanwhile, for the first photolithography, the alignment is not needed.

In the end of the photolithography process, the photoresist containing the patterns is developed automatically, using the developing line of the *Ritetrack coater & developer*, the results being shown in figure 7.11.

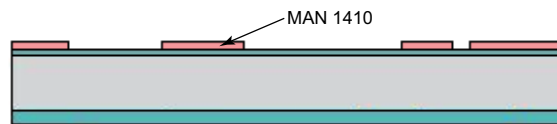


Figure 7.11: First photolithography illustration

The second step is the heated elements and the first electrical track layer physical deposition. A first test was to evaporate Ni, for the heated element. Yet, after processing one wafer, one inconvenient was noticed during the evaporation: a partial detachment of the metal. Mainly, for this reason, it was replaced Ti with Ta. Meanwhile, as the resistance vs. temperature characteristic for nickel is less linear than the one corresponding

to platinum, there was decided to replace Ni in the initial choice with Pt, this representing the final configuration for the heated film.

As the platinum temperature evaporation is about  $1772^{\circ}\text{C}$ , a vacuum evaporation is not possible. For this reason the sputtering technique is used. There were deposited  $10\text{nm}$  of Ta and another  $100 - 150\text{nm}$  of Pt, in the *SPIDER 600* machine, see figure 7.12.

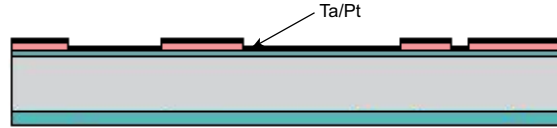


Figure 7.12: Heated elements deposition

Furthermore, a lift-off must be performed for obtaining the shape of the heated elements, see figure 7.13. This lift-off, meaning the photoresist removal on the unwanted structures, is performed by wafers immersion in an acetone bath. The sputtering is a non-directional deposition technique which is complicating however the lift-off procedure. A supplementary energy source is used, namely an ultrasonic agitation. During this process, several microscopic observations were needed for detecting the lift-off advancement stage and also, the eventual problems and to ensure a good quality of the process.



Figure 7.13: Heated elements pattern

### 3. The second electrical tracks layer deposition

The second process in the new wall shear-stress sensor fabrication, after the heated element deposition, is the increasing of the metal layer corresponding to the electrical tracks.

For transferring the patterns on the wafer, a second photolithography is performed. For this second photolithography, it is used, identically, the same photoresist with the same thickness. Furthermore the procedure is the same: the photoresist is coated on the wafers, then the thermal processing is performed. Before the photoresist exposition step through the second mask, the existing structures on the wafer are aligned with the mask, thanks to alignment marks layout on the mask, so called a normal frontside alignment. Once the alignment done, the wafer exposition is performed and afterwards developed.

The second metallic layer, about  $300\text{nm}$ , used for the electrical tracks increasing, is gold, which deposition is made by vacuum evaporation. The evaporation is performed in an high vacuum enclosure,  $10^{-4} - 10^{-5}\text{Pa}$ , by Joule effect. The equipment used was the *E-gun evaporator, Alcatel EVA600*. The planetary rotation is used to achieve a uniform thickness of metal across all the wafers.

Finally, as in the previous step, a lift-off is performed, in acetone, for removing the unwanted metal from the wafer's surface, see figure 7.14.



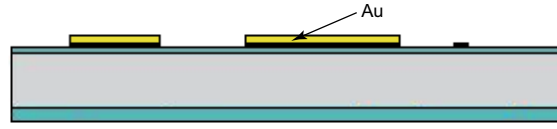


Figure 7.14: Second metallic layer used for increasing electrical tracks

#### 4. Protection layer deposition

Next step in the fabrication of the new wall shear-stress is the deposition of a  $\text{SiO}_2$  layer, on the side facing the flow, for protection against electrolysis effects. Meanwhile a thick resin, SJR,  $7.8\mu\text{m}$ , is applied, both to protect the face of the probe in the electroplating process and to ensure the integrity of the metal layers, once the Si dry etching is carried out, see figure 7.15.



Figure 7.15: Protection  $\text{SiO}_2$  layer and photoresist deposition

#### 5. Electrical connections realization

The final major step in the fabrication of the new device is the electrical connections realization, meaning the etching of the holes representing the electrical connections and, in the mean time, of the holes serving for the conduction heating reduction, and the refilling of this holes with a conductive metal.

The procedure for fulfilment of this step is briefly presented and it is detailed afterwards. A substep for transferring the patterns corresponding to the electrical connections and trenches, a third photolithography is performed. This photolithography comported another photosensitive resin, S1818  $2.4\mu\text{m}$ , laid down on the wafer's unprotected face. The photoresist is coated on the wafers. For the photoresist exposition, using the third mask, a new alignment is needed. The existing structures on the top surface of the wafer are aligned with the mask, this time on the backside.

In the same way as previous, once the alignment done, the wafer is exposed and, afterwards, it is developed.

The oxide layer, of  $1\mu\text{m}$  is withdrawn by wet etching in HF bath. Afterwards, the Si dry etching for engraving the whole  $380\mu\text{m}$  is performed and then, using the same procedure, the  $0.2\mu\text{m}$  oxide found on the holes bottom are withdrawn, reaching, in this way, the metal film, see figure 7.16.

A  $\text{SiO}_2$  layer is deposited by sputtering, before holes refilling, serving as electrical insulation of the lateral walls. Another anisotropic etching by plasma is performed to reach the metal film and to allow the electrical contact.

Finally, the holes metal refilling is performed, by electrodeposition Cu-HL, see figure 7.17.

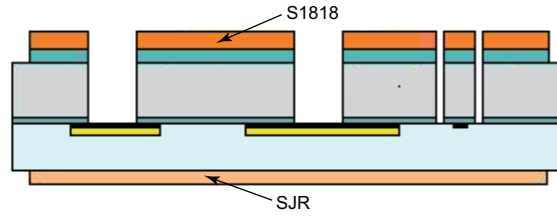


Figure 7.16: Protection  $\text{SiO}_2$  layer and photoresist deposition for holes refilling

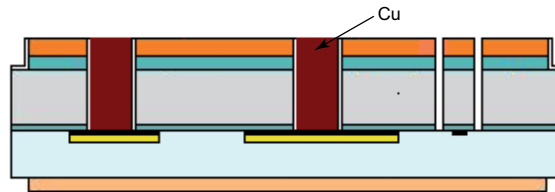


Figure 7.17: Electrical connections refilling, schematic view

Nevertheless, the results observed on the SEM, showed a very unsatisfying and unsuccessfully refilling. This is the main reason for undertaking a process having for goal to study the feasibility of electrical contacts crossing a silicon substrate. It is searched the optimum hole diameter for the refilling process, corresponding to the electrical connections.

### Detailed description of the cross-section electrical connections realization and validation in a silicon substrate

As explained previous, within the framework of the project aiming at the development of a sensor for the measurement of wall shear-stress in hydraulic machines, it is essential to have the electrical contacts on the backside, as the front face of the sensor is in contact with the liquid medium. Moreover, any bump on the front face would disturb the fluid flow along the wall and would largely deform the shear stress measurement, exerted by the fluid on the wall.

Having encountered difficulties for the metal filling by electrodeposition of holes of low diameter, initially planned at  $200\mu\text{m}$ , on a first serie of sensors, it is decided to undertake a process to validate the feasibility of this process. For this first serie of sensors, the filling by electrodeposition was a failure, less than 2% of the holes being filled correctly. The purpose of this process is illustrated by figure 7.18, see Béguin et al. [2002].

For acquiring the hot-film impedance of  $\sim 100\Omega$ , the diameter of holes plays an important function in the success of this process. It is decided to test different diameters for holes, by forming a network of more than 400 holes, corresponding to the future contacts electrical crossing, having a variable diameter between 250 and  $700\mu\text{m}$ . The mask used for this validation is presented in figure 7.19.

For these tests, there were used silicon wafers of 4 inches, polished double face (DSP), with a thickness of  $380\mu\text{m}$  and resistivity of  $1 - 10\Omega\text{cm}$ . These wafers are covered on the both sides of  $1\mu\text{m}$  oxide coating - wetox.

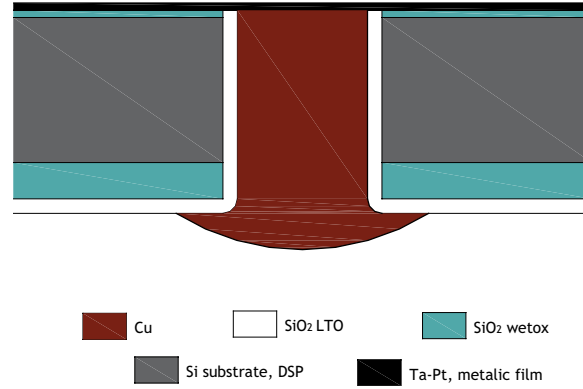


Figure 7.18: Schematic view of the holes refilling purpose

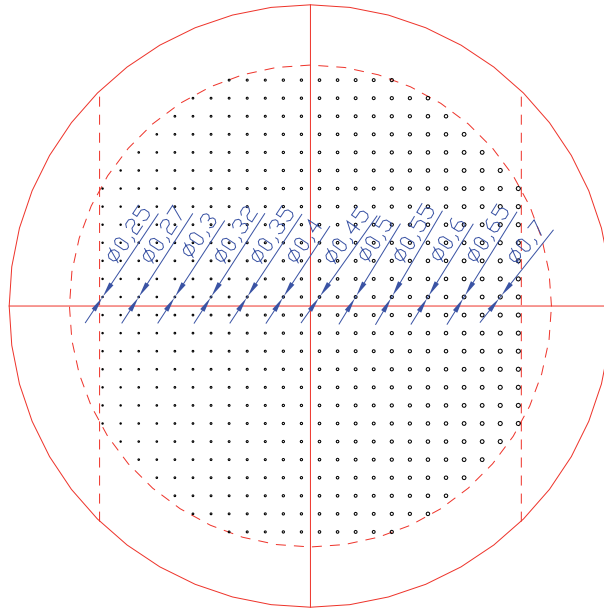


Figure 7.19: Schematic view of the mask used for metal filling validation by electrodeposition

The oxide coating, on the side where will be deposited the metal film, is thinned to 200nm, by engraving HF. For performing this, the other face is protected with a S1818 resin layer, 1.75 $\mu m$  thickness. After the engraving operation this resin is withdrawn.

Afterwards, the metal layer is deposit by sputtering. For these tests, this layer is made up of a Ta film, thickness 10nm, used as explained earlier, as an adhesion support, and a Pt film, with thickness varying between 100 and 150  $nm$  according to wafers.

A thick resin, SJR, 4 $\mu m$ , is then applied, to guarantee the integrity of the metal membranes once that drilling by engraving with-through Si is carried out, on wafer's face supporting the metal film.

A mask for engraving oxide is realized and a photosensitive resin, S1818 2.4  $\mu m$  is laid down on the wafer's unprotected face, on the side on which it remains 1  $\mu m$  of  $SiO_2$  wetox. A process of photolithography by direct writing is then applied to structure this resin.

On the places where the silicon will be drilled, the oxide is withdrawn by wet etching in HF bath. Afterwards, a dry etching by plasma, for engraving the  $380\text{ }\mu\text{m}$  of anisotropic silicon is performed. In the end of this process, the  $200\text{ nm}$  of  $\text{SiO}_2$  wetox, established between the metal film and the silicon substrate are reached. Another process of dry etching by plasma allows the withdraw of the  $200\text{ nm}$  oxide, reaching the metal film. After this step, the metal film is discovered and the images from SEM, see figure 7.20, prove that.

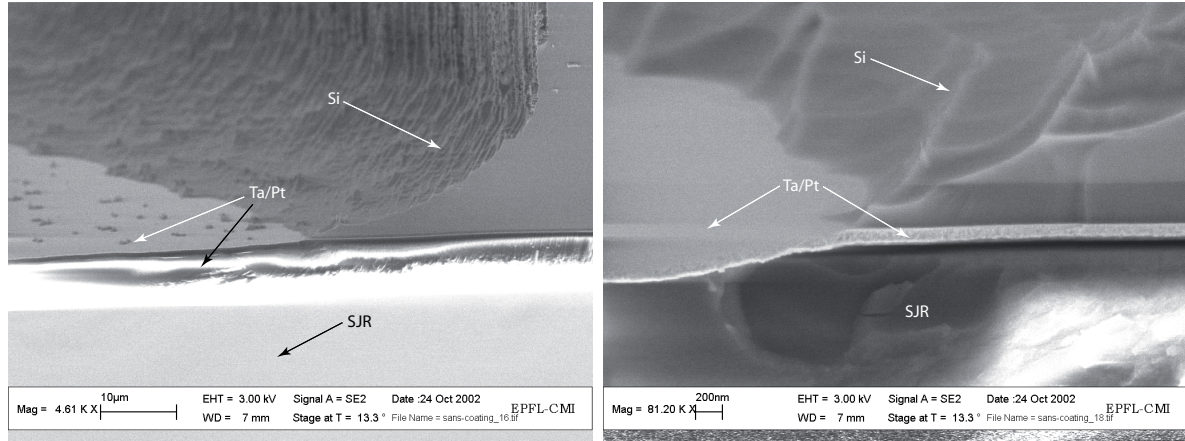


Figure 7.20: Views in a hole, after the silicon and wetox layers etching, showing a complete removal of the  $\text{SiO}_2$  layer

Due to a relatively high electrical conductivity of silicon, it is deposited, by sputtering, a  $\text{SiO}_2$  layer, before metal refilling of the holes, serving as electrical insulation of the lateral walls. The layer's thickness deposited on the surface is  $1\text{ }\mu\text{m}$ , while on the hole's bottom and on the lateral walls, for a hole with a diameter of  $250\text{ }\mu\text{m}$ , a thickness of  $200\text{ nm}$  was measured, see figure 7.21.

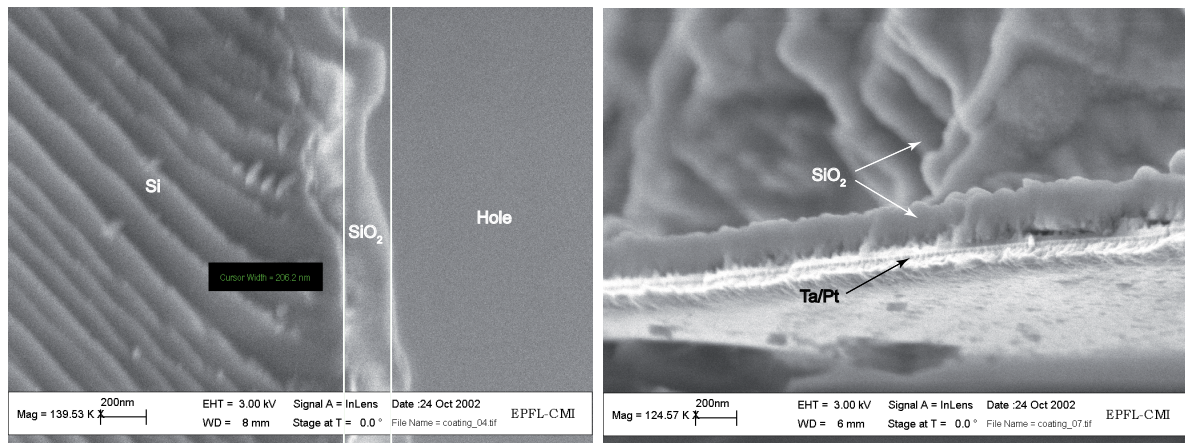


Figure 7.21: Cross-sections showing the  $\text{SiO}_2$  layer thickness deposited on the lateral walls of a hole, on the left side, and general view of the  $\text{SiO}_2$  layer deposition in a hole, both on the bottom and on the lateral walls



To reach again the metal film and to allow the electrical contact, it is performed another anisotropic etching by plasma to withdraw the oxide coating deposited on the holes bottom, see figure 7.22.

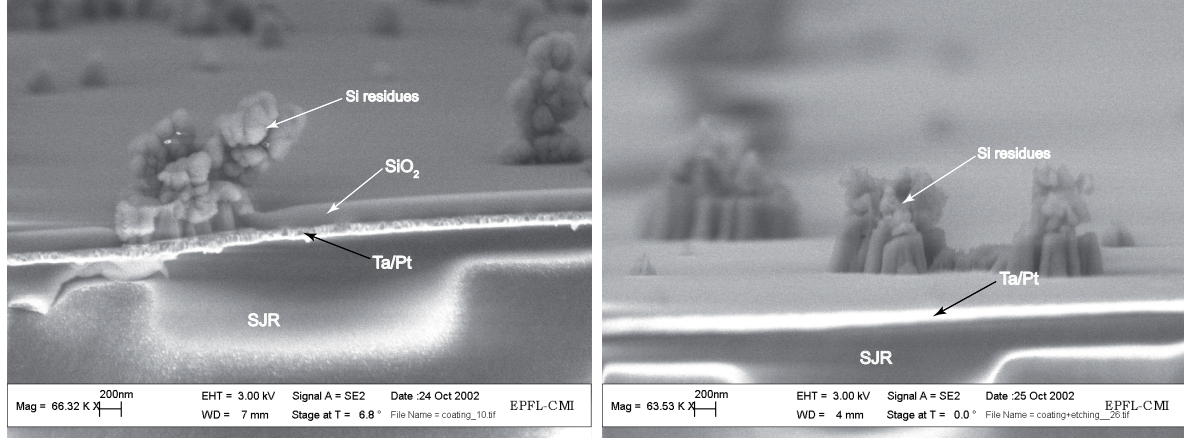


Figure 7.22: Cross-section through a hole, before - left side - and after - right side -,  $SiO_2$  dry etching on the bottom

Thanks to the anisotropy of the process, it is withdrawn only the oxide covering the metal film, without touching the oxide layer on the lateral walls, guaranteeing the electric insulation of the hole walls. By electronic microscopy measurements it is observed that, on the holes lateral walls, it remains a sufficient oxide layer thickness to ensure a good electric insulation, see figure 7.23.

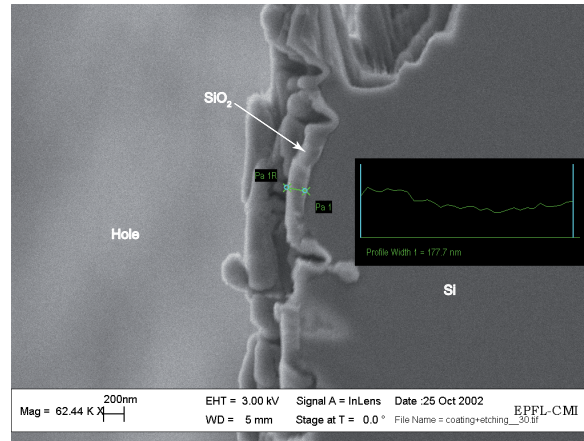


Figure 7.23: Lateral walls observation, showing a sufficient oxide layer thickness

Finally, the holes metal refilling is performed, by electrodeposition. Supposing that the nonpenetration of the electrolyte in the holes of low diameter is at the origin of the first sensors failure, it is worked out a procedure supporting the penetration of the electrolyte in the holes. A first step is the wetting of the wafers holes with Isopropanol. The electrolyte is used for its excellent absorptivity. The wafer is then rinsed with deionized water, for not contaminating the deposition bath with Isopropanol, by gradually replacing Isopropanol which has penetrated in the holes, by water. Following this rinsing, the wafer is placed

in the electrodeposition bath, Cu-HL. The results show a very good and compact refilling with Cu, see figure 7.24 ; meanwhile the Si- $\text{SiO}_2$ -Cu interface geometry is very rough, see figure 7.25. Otherwise, the  $\text{SiO}_2$  layer stands together with the copper, ensuring a very good adhesion.

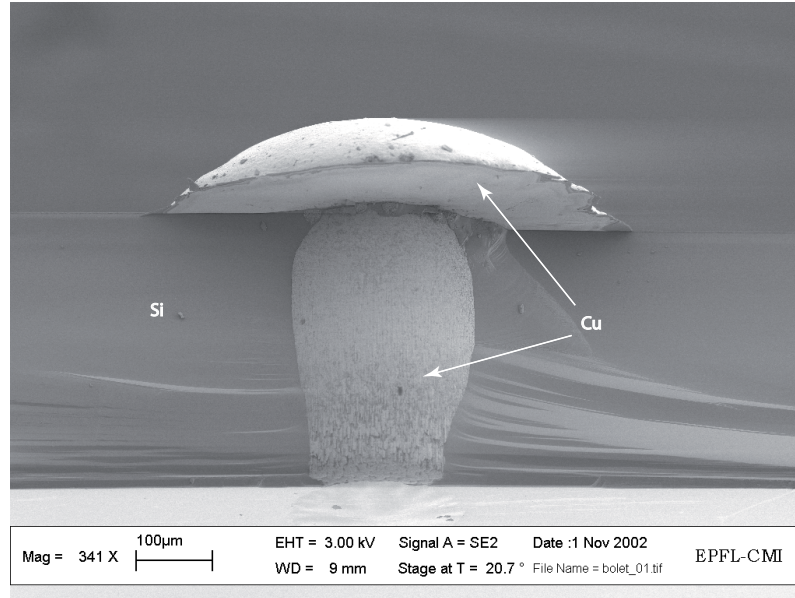


Figure 7.24: Cross-section through a hole refilled with Cu

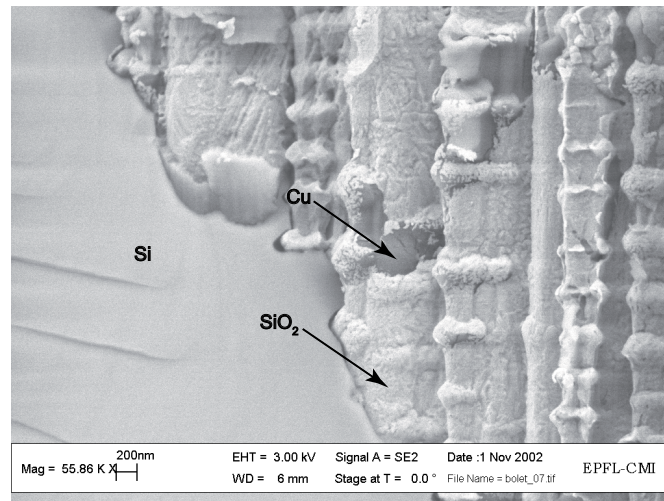


Figure 7.25: Detailed view of the silicon- $\text{SiO}_2$ -copper interface, from the left to the right side)

The results showed that a good refilling of the holes with the copper was obtained starting from a hole diameter of  $250\mu\text{m}$ . Yet, for the new sensor, it was chosen an optimum hole diameter of  $300\mu\text{m}$  and, in this way, there was fabricated a new mask containing the holes for the electrical connections which is replacing the former one.

Afterwards, having done the validation of all the manufacturing stages needed for the hot-film probe development, the first generation of sensors was fabricated, see figure 7.26.

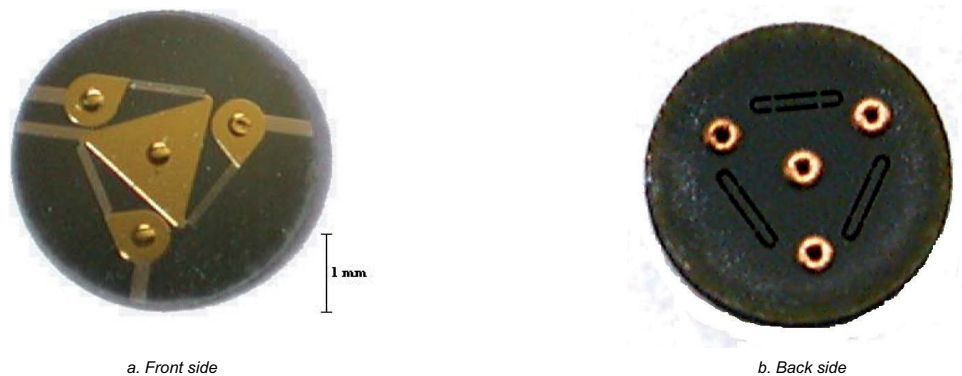


Figure 7.26: First generation of the new hot-film sensors

### Tests and conclusions on the first generation

The first generation of sensors has the films resistances values between 100 and 150  $\Omega$ . As the previous CTA used together with the commercial hot-film probe could be used only for maximum film resistance values of 99.99 $\Omega$ , a preliminary electronically device has to be realized, namely a constant temperature anemometer adapted to the new resistances values, see figure 7.27.

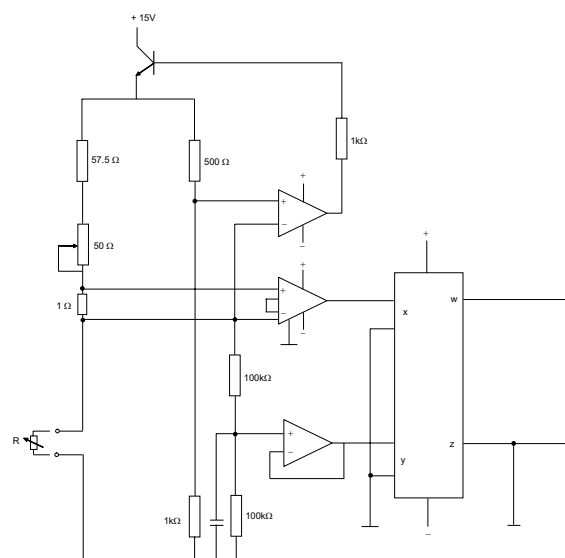
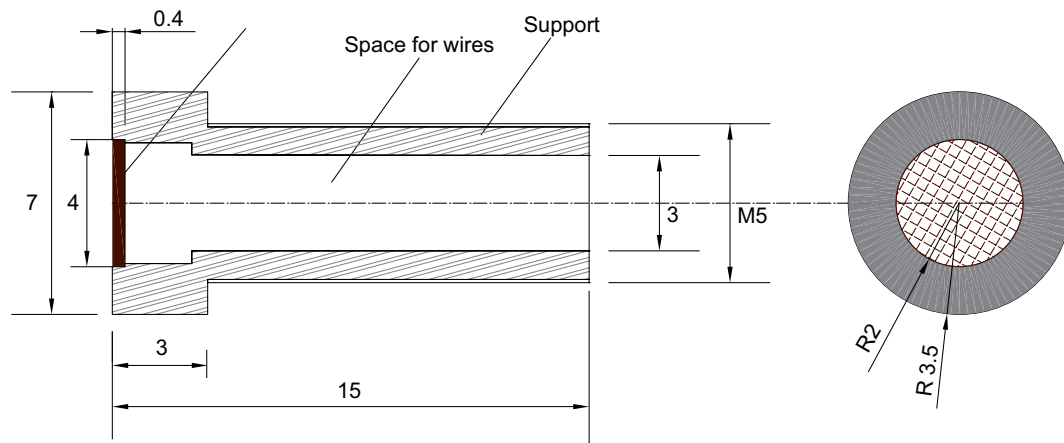


Figure 7.27: CTA development for preliminary tests

The sensor's package, used for calibration of the new wall shear-stress sensors in the hydrodynamic water tunnel is presented. The main requirements on the sensor package are:

- flush-mounting of the sensor device to the package and, in the same time, the package to the wall of the test facility. The effect of protruded or recessed sensor implies a perturbation of the flow around the element and, hence, a disturbed boundary layer on the sensor. Sensor's chip should not protrude or be recessed by more than 0.05% of the channel height.
- minimization of any gap between the sensor device and the package, as well as between the package and the wall of the test tunnel, as gaps around the wall shear-stress sensor leads to flow field perturbation on the chip, causing errors in shear-stress measurements. The gap between the sensor chip and package were filled with express glue, while a copper ring is ensuring a good waterproofs between the sensor package and the test facility wall.

The package of this probe has been designed, see figure 7.28, and realized, by using an plastical material, based on a polyetherethercetone resin, a linear polymer, used for special requirements applications in temperature, chemical and hydrolysis attacks, UV resistance, high erosion, mechanical and fatigue resistance. It ensures a good thermal isolation from the place where it will be implemented, namely the wall of the water tunnel.



All the dimensions are in mm

Figure 7.28: Detailed view of the packaging system

Temperature coefficient of resistance, TCR, is the first testing stage. An oven is used to heat up the sensor's films and, then, it is measured the resistance at different temperatures. An adequate time delay, about 20 minutes, is allowed between each temperature change to reach thermal equilibrium. The TCR of the heated films,  $\alpha$  is obtained by derivating the slope of linear curves, illustrated in figure 7.29 and its value is, for all films,  $0.24\%/^{\circ}C$ . The behavior of the new wall shear-stress probe used together with the new anemometer, implemented identically with the Dantec probe used previous in the calibration tunnel, is observed, see figure 7.30. Afterwards, for this first sensors generation, there were performed only preliminary tests and not a proper calibration.

The results evidenced a very good sensitivity of the new wall shear-stress with the new electronical device. Meanwhile a relatively high power is needed with the mean flow velocity increasing which leads to a general heat up of the device. Actually, the hot-film probe becomes a heated plate. In the same time, it becomes obvious that, in these



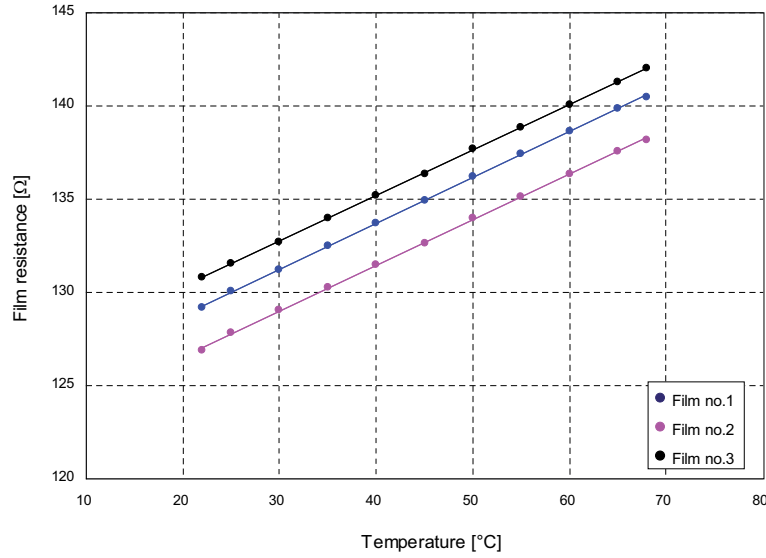


Figure 7.29: Temperature coefficient of resistance determination

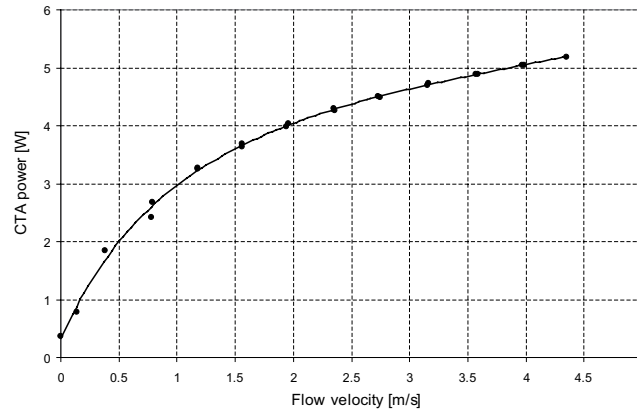


Figure 7.30: Power variation, at the wall shear-stress sensor, with the mean flow velocity, in the hydrodynamic tunnel

conditions, the technical tests of stability - the new probe is let in the water, without any flow and then observed on a microscope -, sensitivity - meaning the angular sensitivity of the films with the flow direction -, repetitivity in the calibration tunnel at the LMH were unsuccessfully. The main results of these preliminary tests, of the first miniature hot-film probe realized can be summarized:

- a high thermal conduction, even with the gates;
- the detachment of the protecting  $SiO_2$  layer on the electrical connections, see figure 7.31;
- a very short life time in the water, about 2-3 days, due to the high thermal conduction, which affected the entire structure of the probe.

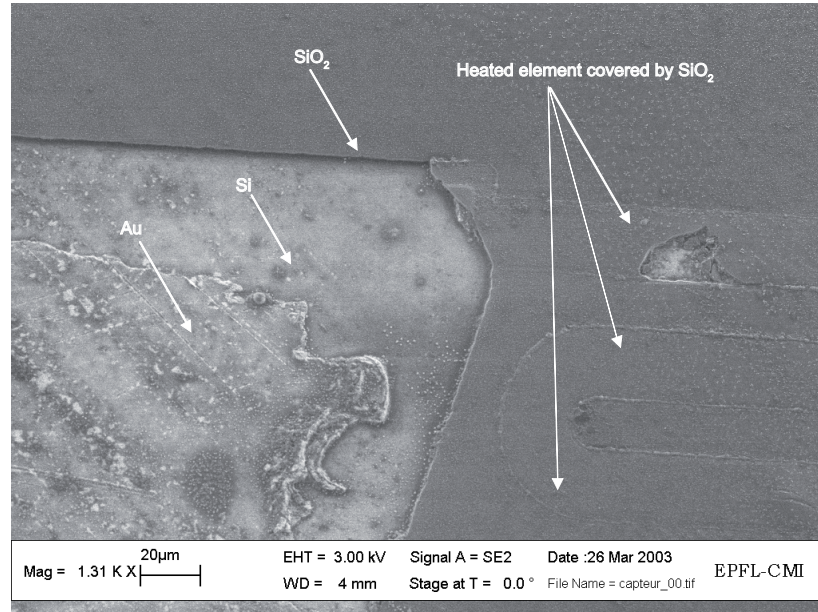


Figure 7.31: Detailed view on a first generation sensor, after tests in the water tunnel

## 7.4 SECOND GENERATION

The aim of fabricating the second generation sensors was to eliminate the inconveniences observed on the first generation of sensors, namely to develop a solution for reducing heat conduction in the substrate and to eliminate the holes used as gates against the heat conduction. All the other aspects of the design of the second generation sensors are kept similar to the first generation devices.

### 7.4.1 Improvements

After considering all the inconveniences remarked on the first generation of sensors, new improvements were done to achieve and to succeed in this development:

- new design to reduce the heat transfer by conduction;
- the increasing of the  $SiO_2$  layer thickness covering the new sensor, from  $1\mu m$  to  $2.5\mu m$ .

The solution, found for reducing the heat transfer, was to create an insulating surface on which it will be deposited the heated element, Berca et al. [2004a]. The main idea was to obtain a configuration for the new probe, in the way illustrated by figure 7.32.

One of the commonly used MEMS materials, due to its good mechanical strength and, mainly to its low thermal conductivity, is  $SiO_2$ . For the new device, it may provide a very good thermal insulation, but still ensuring a good mechanical support, taking into account the turbulent flow where the probe will be implemented. There are some approaches for fabricating the thick  $SiO_2$  insulating surfaces. One involves converting a portion of a silicon substrate to porous silicon by anodization - Lehmann [1996], and then oxidizing the porous silicon - Ou et al. [1999], Nam and Kwon [1996]; another approach uses a spin-

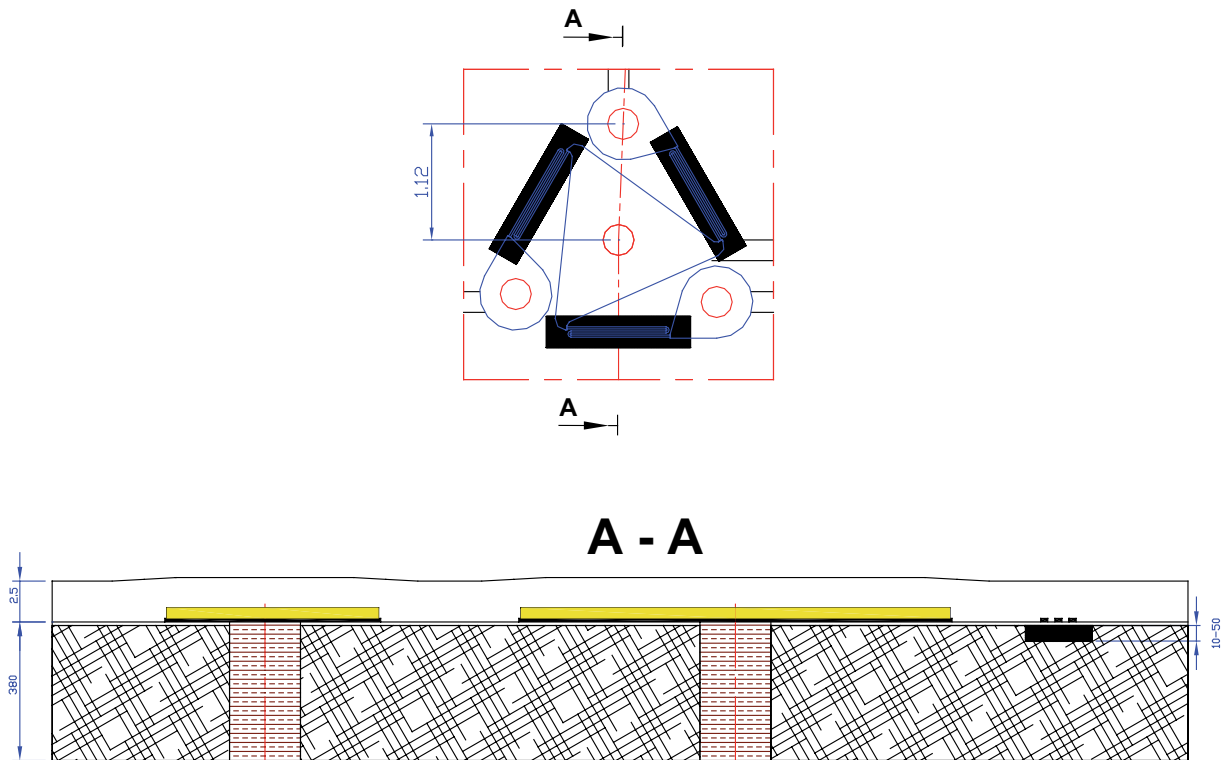


Figure 7.32: Cross-section for the new generation of hot-film sensors

on glass method (sol-gel technique) - Kucherenko and Leaver [2000], Liu et al. [2003], but the resulting films are not strong enough from mechanical point of view.

The initial idea, for fabricating an insulating surface was based on the results presented by Zhang and Najafi [2002]. The major difference with their fabrication is the filling of the trenches. Meanwhile, for developing this fabrication, there was necessary the study of 2 parameters:

1. The optimum thickness of the insulating cavity, and of the silicon pillars in the same time, to ensure a reduced substrate conduction for the particular configuration and for the optimization of the LTO filling;
2. The optimum silicon pillars forms and dimensions, as well as trenches dimensions, for realizing a compact and solid substrate, which can be used for the small devices placed in the water and must support strong pressures.

### Thermal modelling of the new hot-film sensor

To estimate the thermal insulation for the substrate conduction, there were carried out numerical computations of the device. There were taken into account variations of the film and fluid properties with the temperature, by the numerical simulation, handles variable fluid properties, and the results are summarized in this section. There were studied 2 cases, using 2 different CFD codes:

1. Steady case without flow velocity, using ANSYS v.6.1;
2. Steady case with mean flow velocity, using CFX 5.7.1;

A great attention was paid to the near-wall modelling. Numerical treatment of the equations in the near wall region is an important issue for turbulent flows accurate predictions as wall shear-stress and heat transfer are influenced. Nevertheless, boundary layers development, as well as the onset of separation are influenced. 2 methods may be used for near-wall flow modelling: wall-function and low-Reynolds-number.

The method used for the calculation was the wall-function method with scalable wall-functions, where the wall shear-stress is connected to the dependent variables in the near-wall grid nodes, placed in the turbulent region of the boundary layer. As this method allows valuable computer resources and no viscosity effects estimation in the turbulent model are needed, it was preferred to the low-Reynolds-number method, which needs a very fine mesh in near-wall region, as well as restrictions in the grid resolution.

The origin of the coordinate system for the sensor are considered from the center of the heated film. The insulating cavity, which generally takes on an irregular shape, is approximated to have the shape of a rectangular block defined by several thickness values. Both the insulating cavity and substrate sections were discretized in the  $z$  direction, for the 2 studied cases. The model considers heat conduction in the substrate induced by the platinum hot film. For both calculations, the thermal conductivities of materials used in the device are in accordance with the ones used in sensor manufacturing.

### 1. Steady case without flow velocity

The thermal transfer for 1 film is considered as representative for the 3 films. Thus, the heat transfer was studied on only one part. The computational domain was split in 5 parts: fluid, the protection layer, film,  $SiO_2$  and substrate. The model meshing was performed using ANSYS v8.1, the mesh comports 149909 nodes. Due to the fact that the new device is placed in the water, with no velocity, the environment was built as a solid element. The silicon pillars thickness was varying for 10, 20 and 50  $\mu m$ .

Initial conditions for the calculation are:

- zero flow velocity,  $C_\infty = 0$ ,
- film temperature constant,  $T_f = 65^\circ C$ ,
- temperature at the bottom surface of the insulating surface,  $T = 20^\circ C$ .

Boundary conditions:

- temperature at the bottom surface of the substrate,  $T = 20^\circ C$ ,

The computation is considered converged to the steady solution, for the maximal normalized equation residual value less than  $10^{-4}$ .

The results, presented in figures 7.33 and 7.37, showed a very good thermal insulation for the substrate conduction.

Figure 7.33 evidences the temperatures distribution in the streamwise vertical plane of symmetry for the film sensor with nominal material properties and geometric dimensions, when operating at a constant average hot-film temperature of  $65^\circ C$ .

Thermal numerical analysis shows that such thick silicon dioxide layers allow a very good thermal isolation between the heated structures and the surrounding neighbouring structures starting with a minimum height of 10  $\mu m$ , due to the reduced thermal conductivity of the thick  $SiO_2$ .

The conclusion is that the thermal isolation is ensured and the entire heat transfer quantity by conduction is dissipated in the substrate.

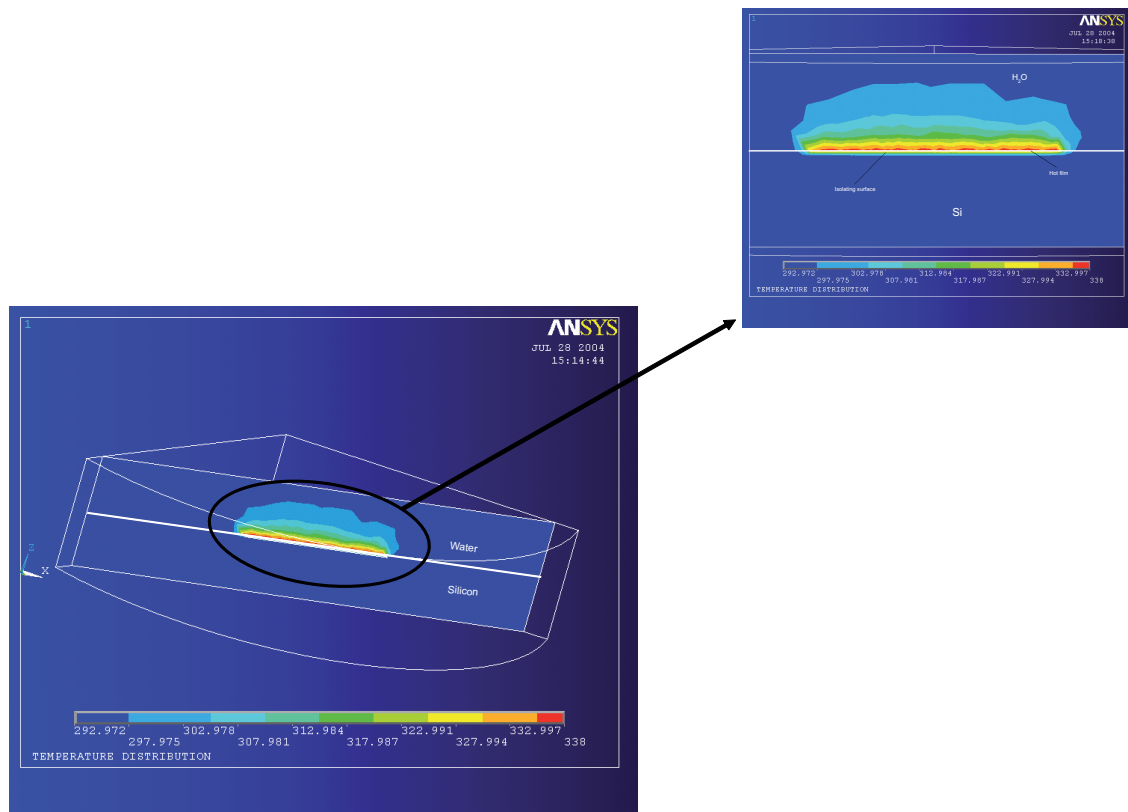


Figure 7.33: Numerical simulation of the heat transfer in the device, improved with an insulating surface

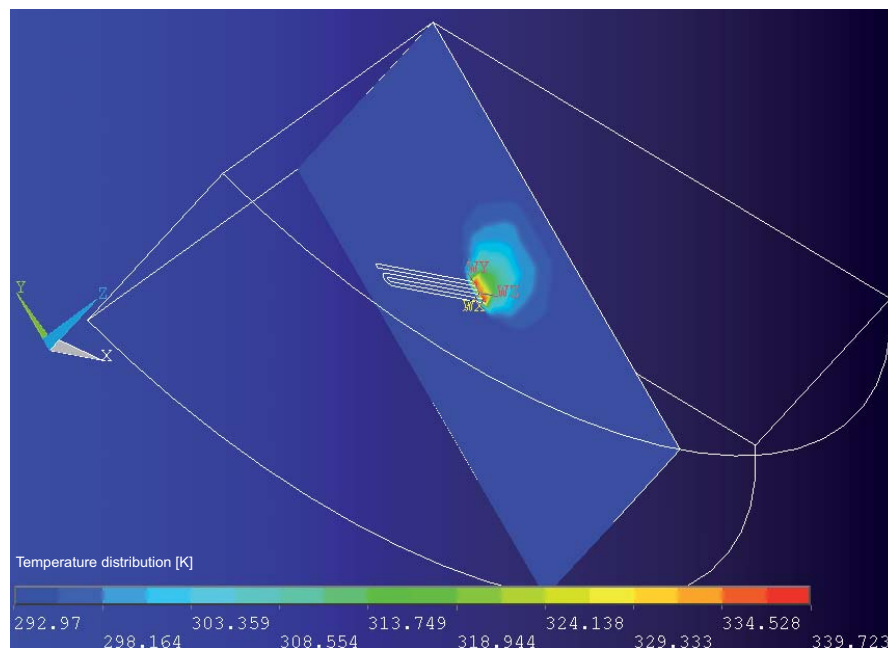


Figure 7.34: Cross-section in the device, illustrating the heat transfer

## 2. Steady case with flow velocity

A schematic presentation of the computational domain including the boundary conditions is shown in figure 7.35.

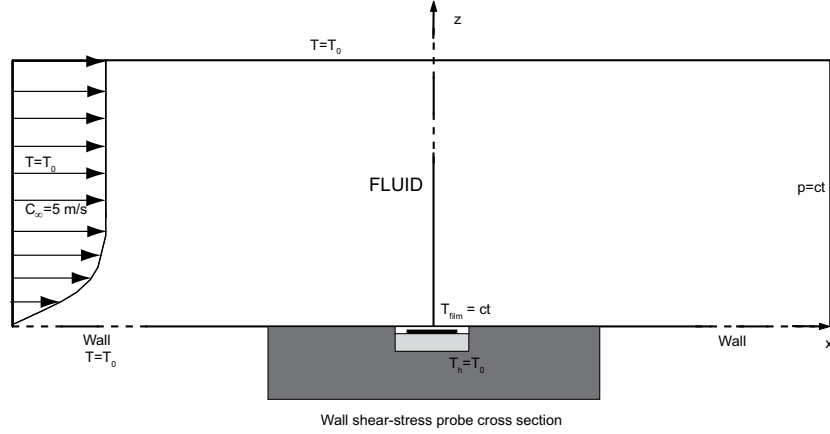


Figure 7.35: Computational domain presentation

Forced convection in the water flow above the protection layer and hot film is included in the model, assuming a mean flow velocity far upstream from the device of about 5m/s. The water temperature was considered 20°C, as well as the temperature at the bottom of the substrate. The hot-film temperature is kept constant, at 65°C, in the present simulation. The coupled conduction-convection heat transfer problem is solved numerically using CFX v.5.7.1.

The turbulence model used is SST integrated into the viscous sublayer  $y^+ = 0.2$ , due to its capacity of accurate separation and heat transfer predictions. The SST model combines the best elements of the  $k - \epsilon$  and  $k - \omega$  models using a blending function, F1, which is equal to 1, near the surface and 0 in the outer part. Moreover, an additional feature is introduced in the SST model, namely an upper limit for the turbulent shear stress in boundary layer, for avoiding excessive shear-stress values. Compared to the  $k - \epsilon$  model, its main advantage is represented by the adverse gradient pressure conditions.

The heat transfer model used in calculation was Thermal Energy. As boundary conditions, symmetry on the lateral walls and zero velocity in the normal direction to the flow interface were imposed. Meanwhile for the interface region, flow IN and flow OUT, periodic translational conditions were chosen; the influence of the wall boundary on the flow was considered as no slip.

Boundary conditions are summarized, as it follows:

- constant water temperature far from the probe surface - 20°C;
- mean flow velocity, far upstream from the device - 5m/s;
- constant pressure gradient at the outlet surface of the computational domain;
- film temperature constant - 65°C;
- turbulence intensity - 1%.

In the figure 7.36, the x-axis is perpendicular on the film and aligned with the flow, while the z-axis is perpendicular to the insulating surface and points to the flow. In the

same way, as for the first case, the system origin is considered at the center of the hot film.

The total calculation domain was split in 4 main subdomains, detailed in table 7.4, while the total mesh had 27799 elements.

Subdomain	Nodes number	Elements number	Equations
Sensor	1998	880	Heat transfer
Fluid	46800	23067	Heat transfer + Navier-Stokes
LAYER	2040	845	Heat transfer
SUBSTRATE	6416	3007	Heat transfer

Table 7.4: Detailed calculation domain

For the convergence control, regarding the steady solution monitoring points for the velocities were chosen. The residual target was set to  $1e-4$ , while the physical timescales were fixed at 0.1s for both heat transfer and Navier-Stokes equations. The total number of iterations required to achieve an adequate convergence was 63.

The calculations results was qualitatively validated by comparison with previous results, obtained with DANTEC probe. As it is known, for an imposed mean flow velocity, the wall shear-stress should be the same, for sensor placed in the same location and in the same flow conditions in the test tunnel, no matter the device used for measuring its value. The wall shea-stress value obtained within this case, is 30.76 Pa. By comparison with the value obtained in the previous experimental work, using a commercial hot-film probe, estimated at about 38Pa, the calculation results value obtained is underestimated with about 25%, in the same way as for the wall shear stress measurements performed in the cone. This confirms that model provides a valid quantitative description of the new wall shear-stress sensor manufactured.

The main conclusions were that the silicon pillars surface ensure a very good heat dissipation, providing a minimum thermal conduction and, in the same time, a maximum thermal convection and that it is noticed very well the development of the thermal boundary layer.

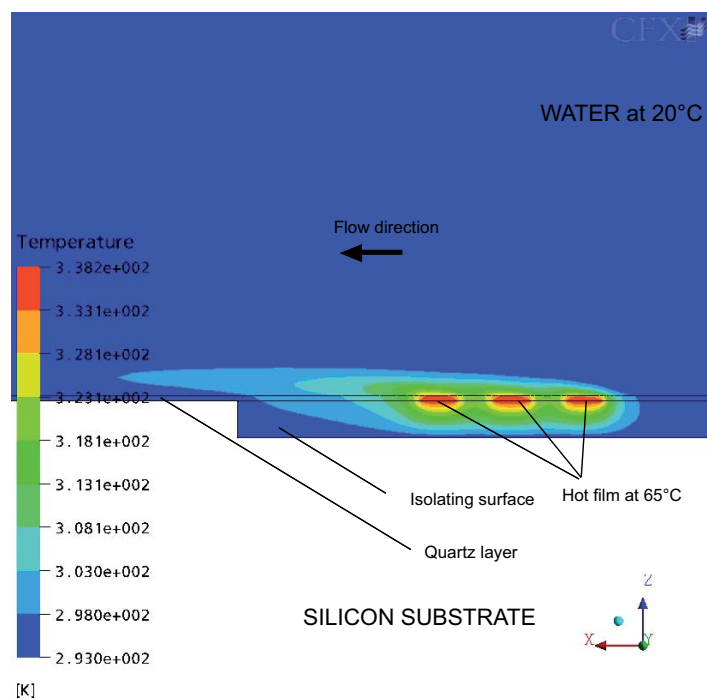


Figure 7.36: Heat transfer calculation results for the steady case, with flow velocity

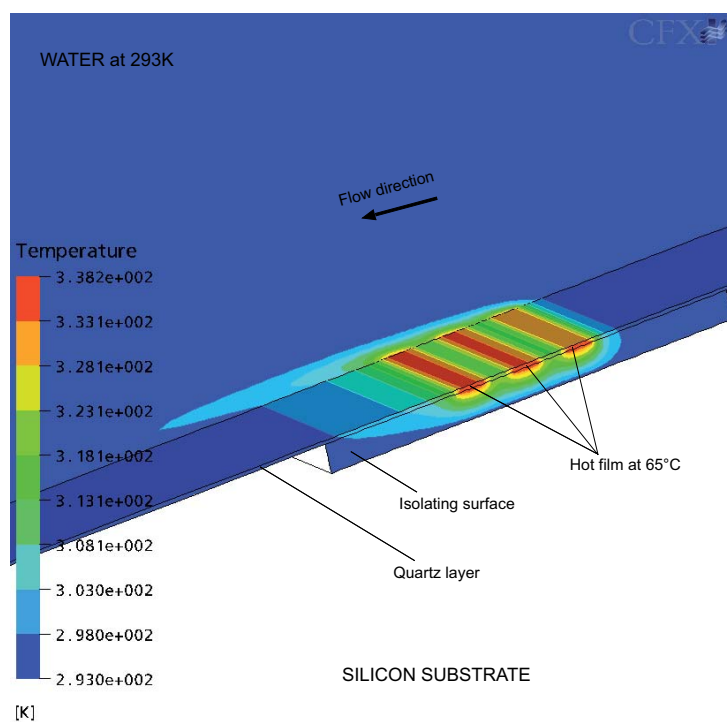


Figure 7.37: Detailed view over the heated element, illustrating the conduction heat transfer



### 7.4.2 Thick silicon dioxide fabrication

A method for fabricating silicon dioxide layers is presented, see Zhang and Najafi [2002], thanks to the deep reactive ion etching (DRIE), used for creating high-aspect-ratio silicon pillars. Then these pillars are oxidized and/or refilled with LPCVD oxide or nitride. The silicon pillars are realized in an ALCATEL 601E, fluorine chemistry high density plasma etcher with a Bosch process. The pillars thickness in a first configuration varied between 10 and 20  $\mu m$ . Meanwhile, another question rises: which are the optimum dimensions and forms for the silicon pillars, for achieving a complete filling. In this way, there were proposed, as illustrated figure 7.38, several pillars design having different widths, as well as different trenches openings.

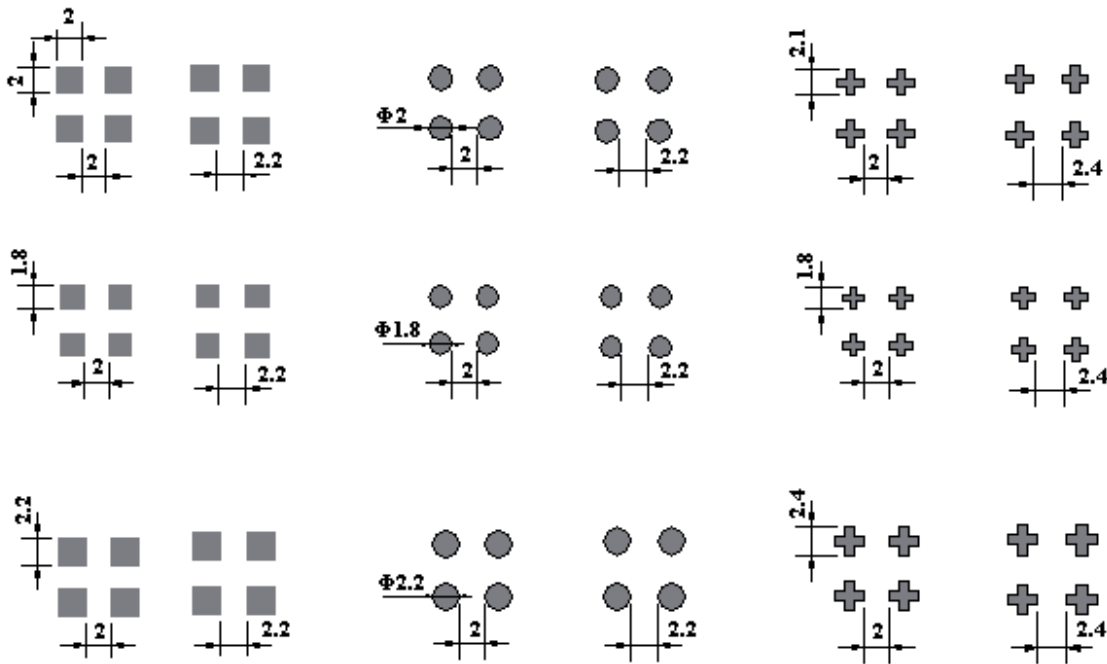


Figure 7.38: Pillars design and trenches dimensions studied

The process of trench filling is experimented by several different methods: by oxidation only, by oxidation and LPCVD oxide, by polysilicon deposition and by oxidation and LPCVD nitride. There will be shown that the complete filling of the trenches is very difficult, depending on several parameters like the trenches profile, the silicon pillar width and dimensions, etc.

#### 1. Trench filling by oxidation only

The trench refilling in this case is performed by consuming the Si pillars through oxidation and outgrowth of the oxide into the trench, see figure 7.39. Meanwhile, to obtain a complete refill by oxidation only, the ratio of silicon pillar width to trench opening should be  $\sim 0.85$ , but in practice, the ratio should be larger than this for ensuring a good

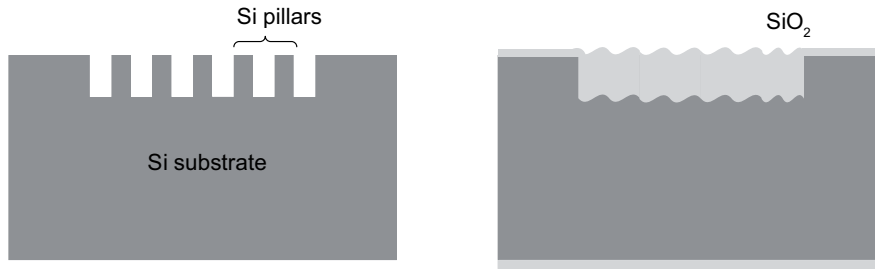


Figure 7.39: Pillars design and trenches dimensions studied

mechanical resistance. In this way, after trenches realization, the wafers are wet oxidized for 3h at 1050°C in order to refill them, figure 7.40.

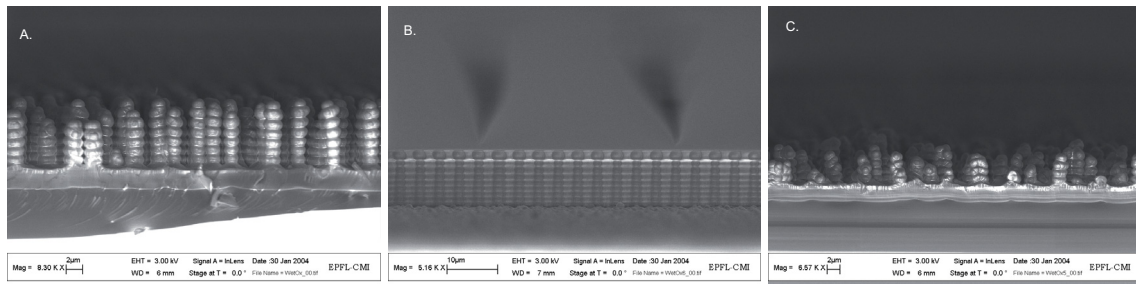


Figure 7.40: SEM photos showing the trenches filling depending on the Si pillars design: a) square design, b) circle design, c) cross design

It can be concluded, that for all silicon pillars designs, the behavior of the trenches filling is almost the same: for the square and cross silicon pillars designs, the trenches filling by oxide procedure was unsuccessfully, while for the round design of the pillars, the top and the bottom of the thick oxide layer have the tendency to join together, but voids are formed in the middle, and it can be noticed that the oxidation is not enough. This is explained by sidewall profile formed during the DRIE. Yet, for the new application, where a very good mechanical strength is required, it is necessary to obtain a solid insulating surface. Thus, new investigations are carried out.

## 2. Trench refill by oxidation and LPCVD oxide

One of the solution proposed by Zhang and Najafi [2004], in order to avoid voids formation, is the use of both oxidation and further filling of the trenches using LPCVD oxide, method illustrates in figure 7.41.

After 3h of wet oxidation at 1050°C, 1-2  $\mu\text{m}$  of LPCVD oxide is deposited to fill the openings, see figure 7.42.

The results obtained are similar for all the designs. Yet, as one can notice in the SEM photos, the thick oxide layer produced does still have voids in the middle. That is the reason, why it is proposed another different designs and tried different filling methods.

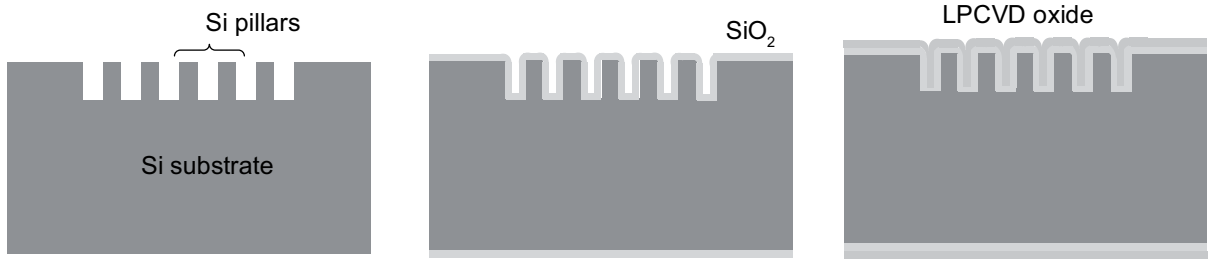


Figure 7.41: Schematic view of the trench filling by oxidation and LTO deposition

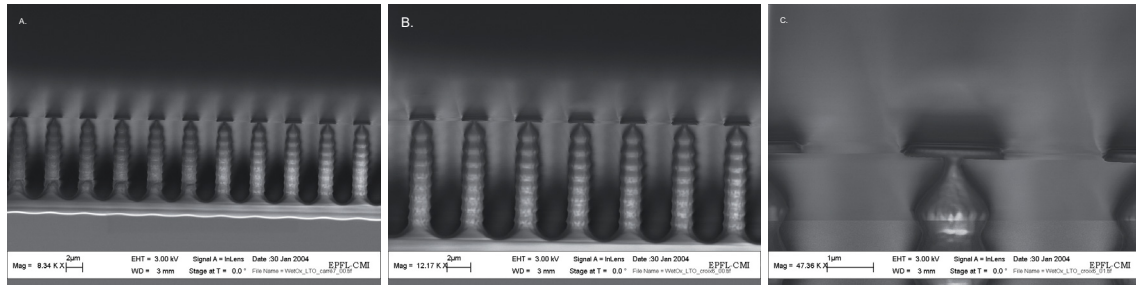


Figure 7.42: SEM photos showing the trenches filling by this method depending on the Si pillars design: a) square design, b) and c) cross design

### 3. Trench refill by oxidation, polysilicon layer deposition and again oxidation

The main stages in the trenches refilling using these techniques are illustrated in figure 7.43.

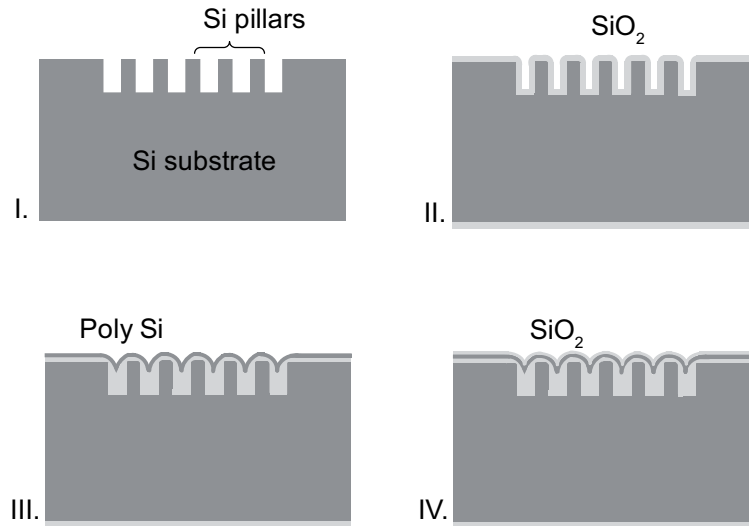


Figure 7.43: Schematic view of the trench filling by oxidation, polysilicon deposition and oxidation

As it has been noticed, the different designs used for silicon pillars before were unsuccessfully, there were conceived another ones, see figure 7.44. In the same time, the pillars thickness was varied from 10, 20, 40 and 60  $\mu m$ .

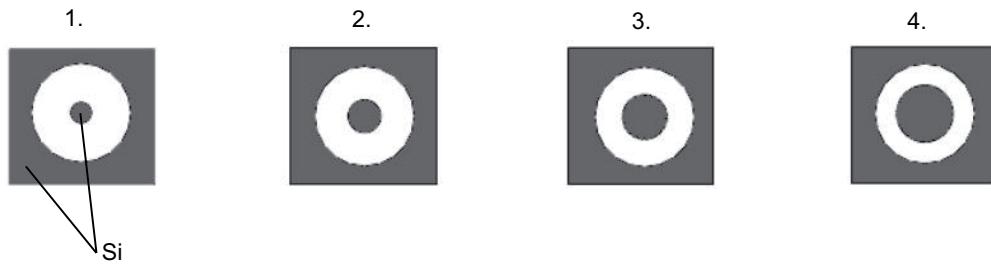


Figure 7.44: New designs for the silicon pillars

For the new designs there was also performed a filling by oxidation only. The results, see figure 7.45, showed that the trenches filling only by oxidation, for the new designs, was partially realized, the most successfully design being the 3rd one.

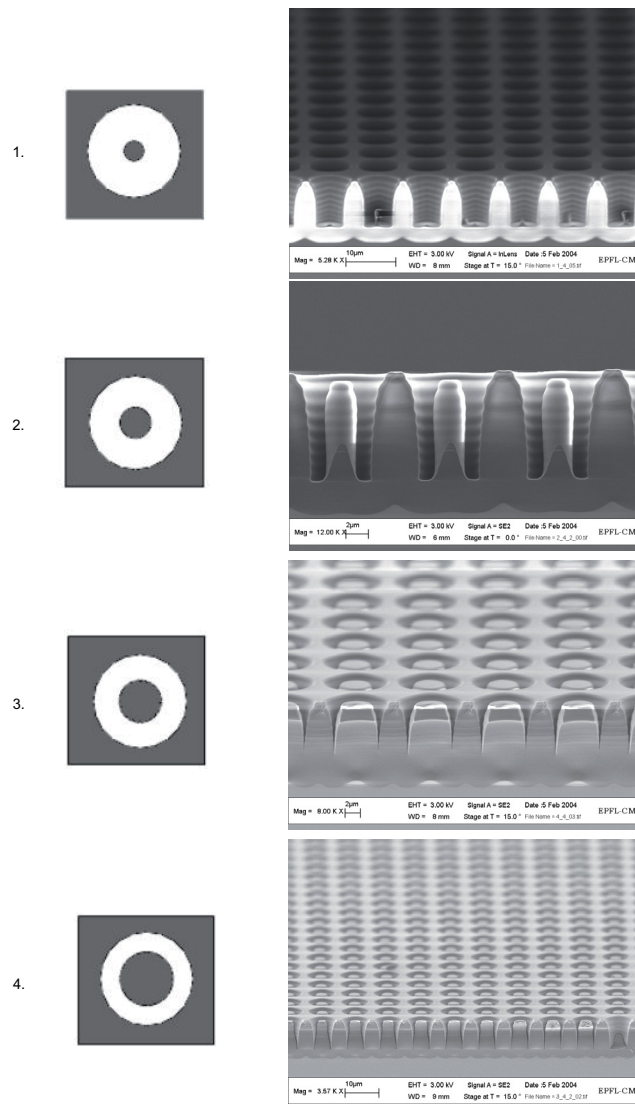


Figure 7.45: SEM photos showing the trenches filling by oxidation only in the new designs configuration

Furthermore, the filling procedure chosen, afterwards was more complex: the silicon pillars were oxide at  $1250^{\circ}\text{C}$  for 9h, then for facilitating the trenches filling, as well as the surface planarity, there was deposited a narrow layer of polysilicon, and then the procedure was completed by a new oxidation, during about 6h. The results are presented in figure 7.46, for all the new designs.

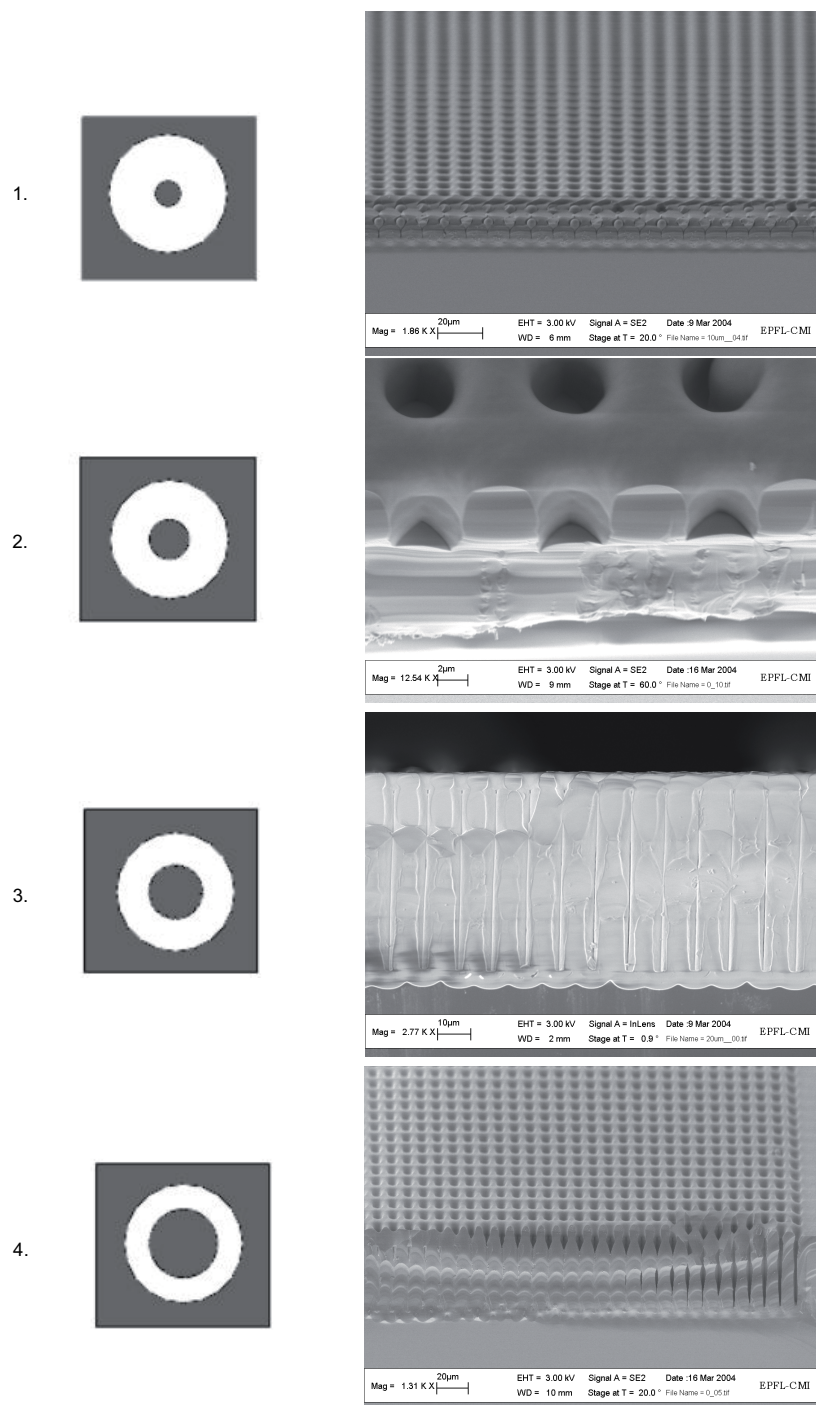


Figure 7.46: SEM photos showing the trenches filling by the complex method corresponding to the new designs

It is noticed a good resolution for the silicon pillars going from 4 to 5  $\mu m$  diameter and very unsatisfactory results for the silicon pillars diameters of 2 and 3  $\mu m$ . Thus, there was developed a final configuration, having the silicon pillars diameter of 4  $\mu m$ .

#### 4. Trench refill by oxidation and LPCVD nitride

There was chosen a final design and the final trenches filling method tested was composed by an oxidation, followed by a nitride deposition by LPCVD, for improving the trenches filling, schematized in figure 7.48.

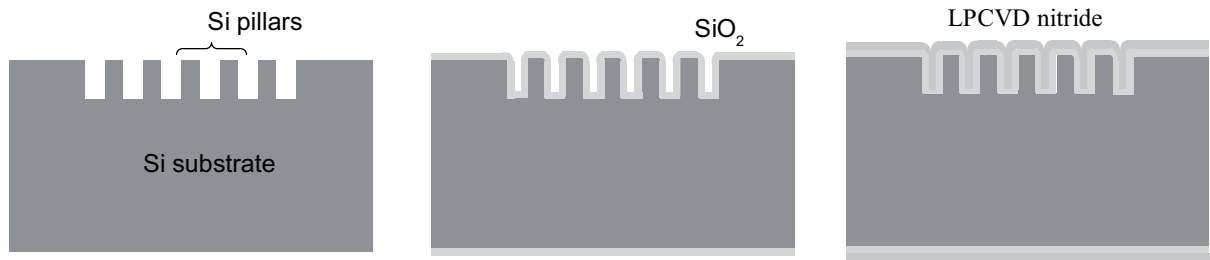


Figure 7.47: Schematic view of the trench filling by oxidation and nitride deposition

The results presented in figure 7.48 show that the level of trenches filling performed by this method is higher than any other method presented before.

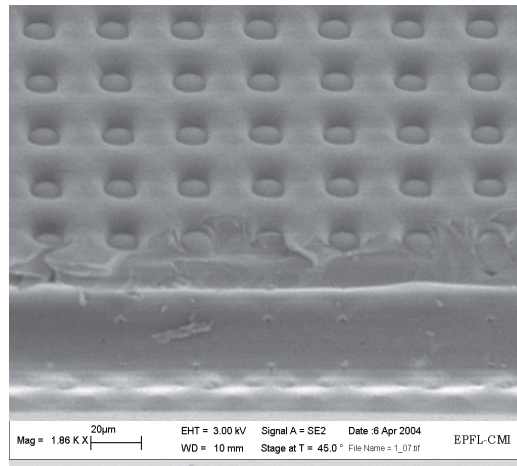


Figure 7.48: SEM photos showing the trenches filling by oxidation and nitride deposition

For the same design of the silicon pillars and trenches, there were compared the refilling methods using the deposition of nitride in parallel with the one of oxide, illustrated by figure 7.49. By comparison between the whole methods presented, it is remarked that this is optimum method for filling the trenches.



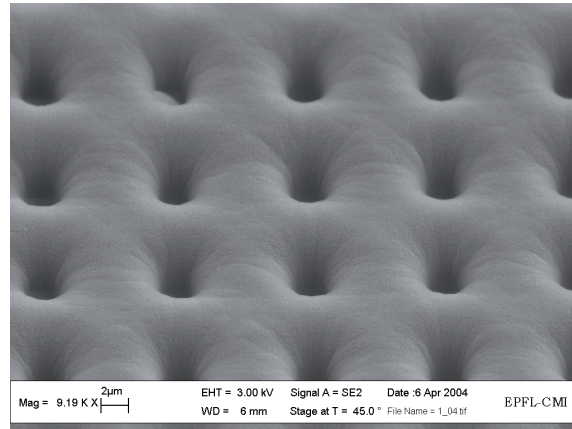


Figure 7.49: SEM photos showing the trenches filling by oxidation and LTO deposition

### 7.4.3 Sensors second generation fabrication

The refilling validation process leaves an corrugated surface. Nevertheless, due to the fact that the sensor's surface must be an uniform one, without no protuberance to disturb the flow, a chemical-mechanical polishing is planned. The results, as the figure 7.50 show, are very uniform and the process is a successful one.

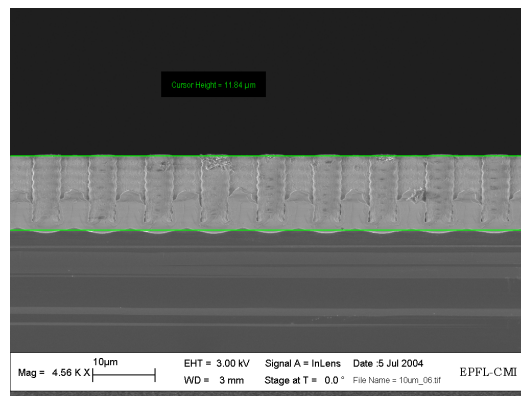


Figure 7.50: Chemical mechanical polishing results on a wafer surface

Finally, after choosing the optimum design and thickness of the insulating cavity, the first step was to fabricate a mask for the implementation of the new design in the configuration of the new sensor. Finally, the manufacturing process is a 4 masks layers, illustrated from figure 7.51 to 7.54.

The main fabrication steps for the second generation of new hot-film sensors are summarized in figura 7.55, while the new probe is illustrated in figure 7.56. The whole wafer after the laser dicing is shown in figure 7.57.

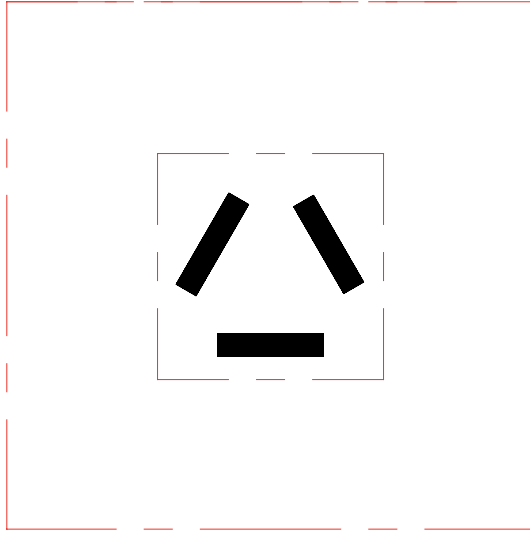


Figure 7.51: Mask no.1 used for creating the insulating surface in the substrate

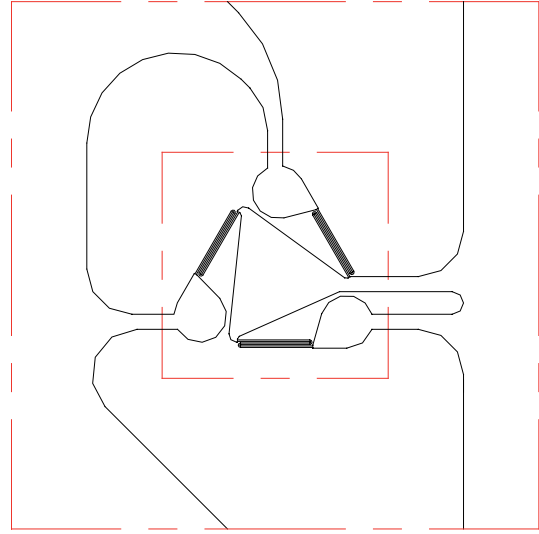


Figure 7.52: Mask no.2 for the heated film and a first layer corresponding to the electrical track deposition

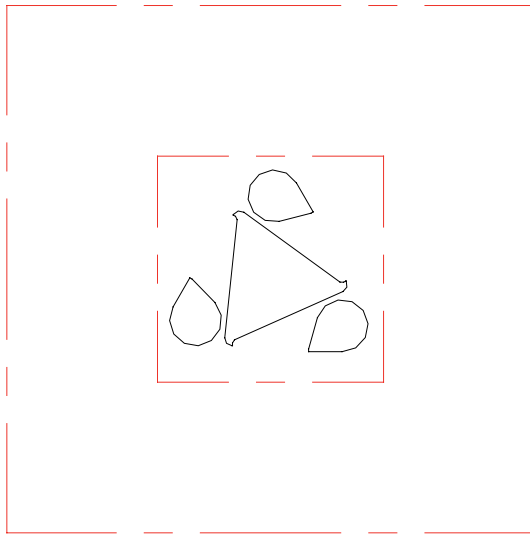


Figure 7.53: Mask no.3 corresponding to the second layer of the electrical tracks

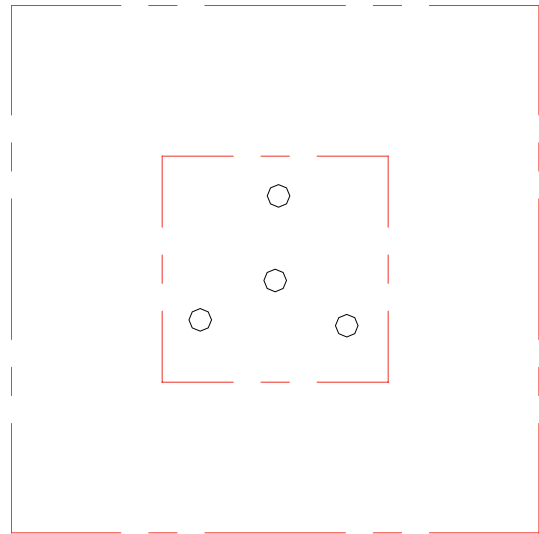


Figure 7.54: Mask no.4 for the holes realization, corresponding to the electrical connections

## 7.5 EXPERIMENTAL SET-UP

### 7.5.1 Probe encapsulation

A preliminary step after the fabrication procedure is the wires welding, for the electrical connections on the new miniature hot-film probe. The wires welding was performed in the Atelier de COncption, Réalisation et Test (ACORT), for about 10 probes on a wafer, for each of the 3 wafers. Copper wires soldered to the leads constitute the electrical connection between probe cable and probe, see figure 7.58.



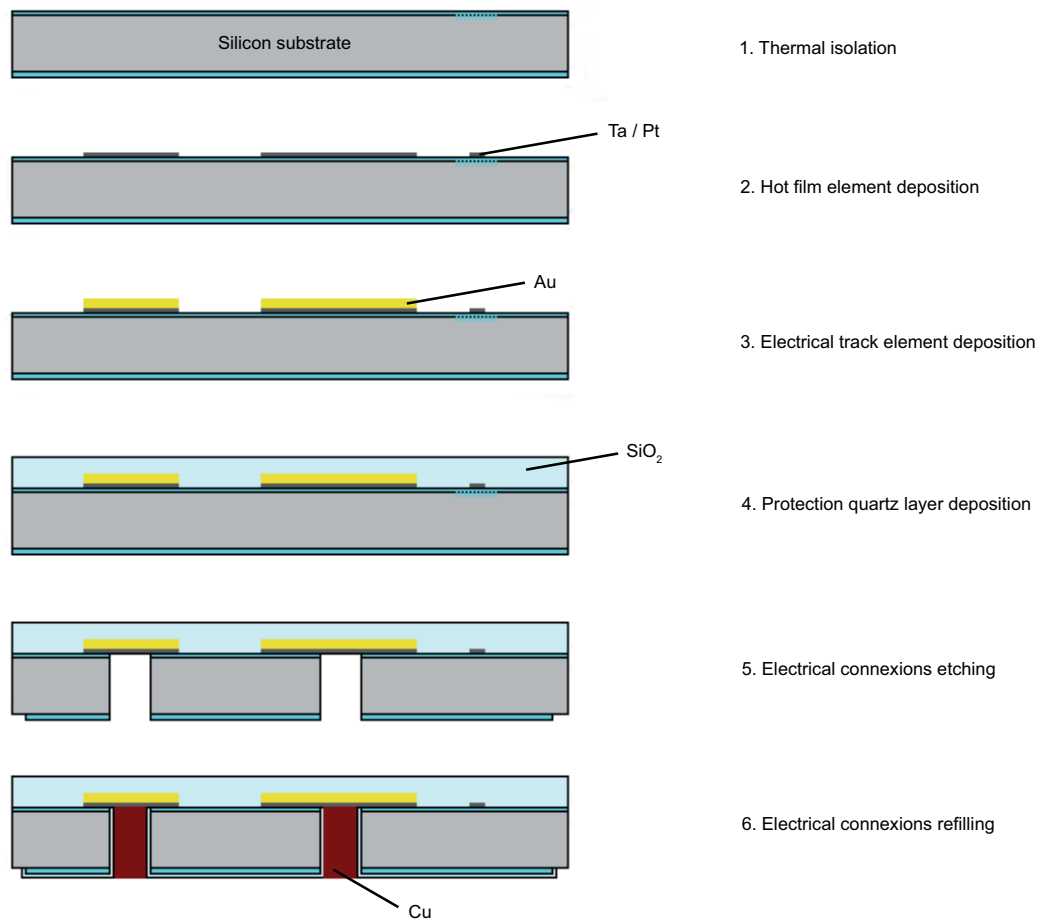


Figure 7.55: Main fabrication steps for the second generation of the new hot-film sensor



Figure 7.56: New multidirectional hot-film sensor

For testing this new wall shear-stress sensor, after the wires welding, the encapsulation is necessary. In the same way as for the first generation sensors, there were developed and manufacture several different plastic and stainless steel components, for preliminary testing and characterization of the probe in the hydrodynamic water tunnel in the LMH. A probe encapsulated is presented in figure 7.59. Nevertheless, a special attention should be paid to the flush mounting of the probe in its encapsulation system.

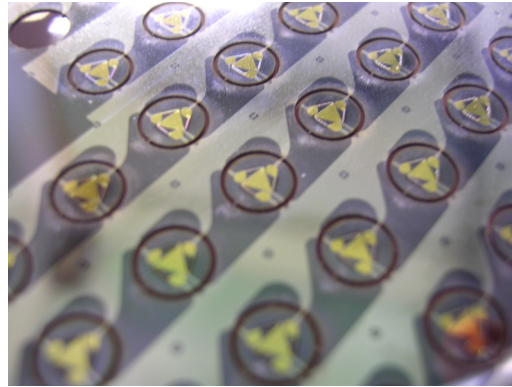


Figure 7.57: A processed wafer

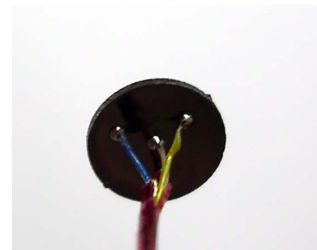
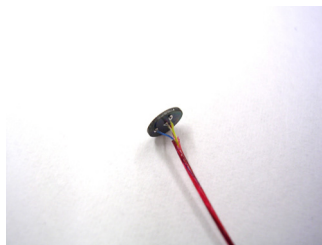


Figure 7.58: Wires welding on the sensor's backside

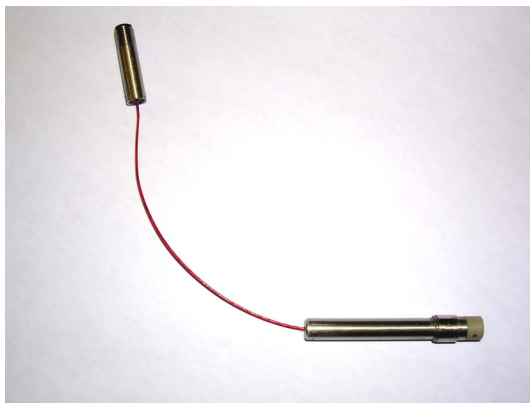


Figure 7.59: New wall shear-stress sensor's encapsulation

Another major parameter to be considered is the glue of the probe in its encapsulation system. Actually, this is a special version of the flush-mounting probe, where the sensor is deposited on an insulating plastic material, in the same way as for the first generation of sensors, see figure 7.28. The sensor's diameter is 4 mm. It is glued using a solidification glue, directly on the plastic, by total backside refilling, in this way ensuring a good property on the top surface of the probe, avoiding the glue to recover some part of the probe's face and to perturb the flow and the thermal boundary layer.

### 7.5.2 Design and manufacturing of the rotating support

Meanwhile, for the calibration procedure there was developed a new rotating support adapted to the new probe, which allows the rotating of the probe with  $360^\circ$ , to see the influence of the angle between the longitudinal direction of the films and the direction of the flow, on the measurements, corresponding to each of the hot-films, see figure 7.60.

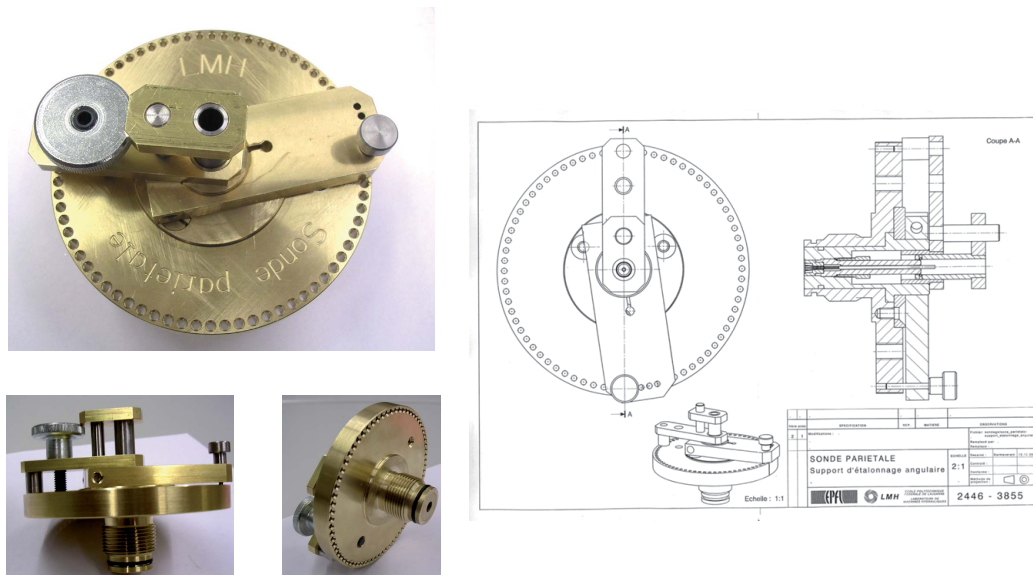


Figure 7.60: New rotating system design

A special care was provided for fitting of the probe encapsulation system in this new support, for allowing the flush mounting once, the plastic encapsulation together with the new probe glued, in the rotating system and, on the other side, the rotating system to the wall, see figure see figure 7.61.

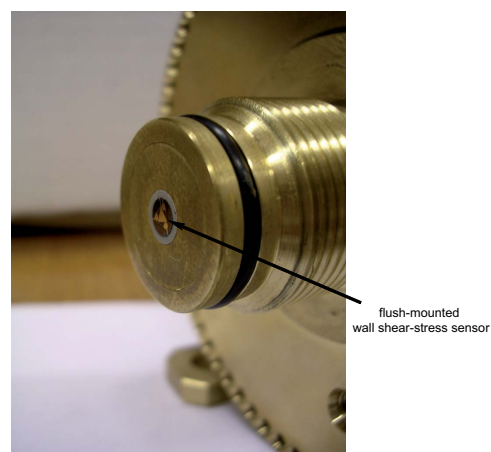


Figure 7.61: The whole encapsulating system used for the new wall shear-stress calibration



## Chapter 8

# MEASURES AND EVALUATION OF THE NEW PROBE

Several manufacturing procedures are not uniform, from one wafer to another, so that new hot-film sensors on each wafer have to be tested. The results of the manufacturing process are 3 wafers which can be investigated and tested.

The new wall shear-stress sensor testing can be divided in following categories: electrical functionality and behavior, time response study and sensor calibration.

### 8.1 PROBE CHARACTERIZATION

In the same way, as for the first sensors generation, the temperature coefficient of resistance evaluation constitutes the first testing step. Resistance with temperature behavior of the thin-film platinum sensor is necessary for calculating the sensor overheat ratio for a given resistance.

For the second wall shear-stress sensors this coefficient is evaluated for the 3 films of a probe, both in the air and in the water. The temperature was measured using a classical thermometer placed in the same environment with the new probe. For the air tests the same oven as previous is used, to heat up the sensor's films and, then, measured the resistance at different temperatures, see figure 8.1.

For TCR evaluation of the heated films in water, a container with water at an initial temperature, of 13 °C, is used. The water temperature is increased by adding hot water and the temperature and the 3 films resistances are acquired simultaneously. The acquisition is performed until the water temperature reaches 70°C. The same measurements were performed, in both directions, from hot to cold and from cold to hot, meaning that the hot water is cooled, little by little, until it reaches again about 16°C. The results are presented in figure 8.2.

The measurements values deviation from the mean value of the TCR,  $\pm 0.5\%$ , for all 3 heated films, as well as the differences in  $\alpha$  value,  $0.18\%/^{\circ}C$ , for the film no.1,  $0.15\%/^{\circ}C$  for the film no.2 and  $0.14\%/^{\circ}C$  for the film no.3, are explained by the non-uniformity of different procedure used in sensor's fabrication and also by the poor precision of the thermometer used for temperature read. Meanwhile, the increasing of the films resistances with the water temperature shows a good behavior and a good dynamic of the new probe, in both environments, around  $0.15\Omega/^{\circ}C$ . The response of the probe was repetitive.

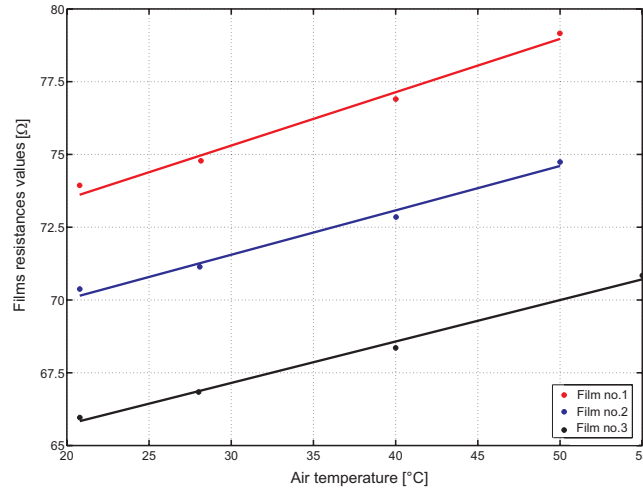


Figure 8.1: Temperature coefficient of resistance evaluation for air

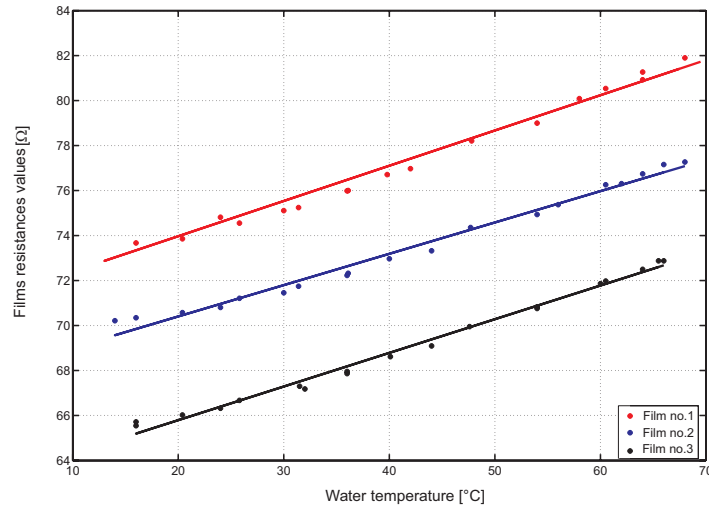


Figure 8.2: Temperature coefficient of resistance evaluation for water

## 8.2 TESTS IN THE WATER TUNNEL

### 8.2.1 Instrumentation

Validation of the new probe implies an electronically system development, made up of 3 constant-temperature anemometers, corresponding to the 3 films. The principle used for these anemometers involves automatic control of the current supplying the film so that the temperature of the hot-film probes should be maintain at a constant level, no matter the outer conditions for heat transfer, throughout the measurements. As said before, due to the non-uniformity of certain processus in the fabrication of the new design, films resistances change on all 3 wafers processed, from one wafer to another. Moreover, the films resistances values changed from 130-140  $\Omega$  in the first generation of sensors, to 10-90  $\Omega$ , for the second generation - depending on the wafer used. Thus, it became necessary the development of appropriate electronic device which integrates the 3 anemometers.

A first attempt was carried out and it is presented in figure 8.3. As this new development was carried out together with Wavemind, we will refer to the anemometer as Wavemind anemometer.

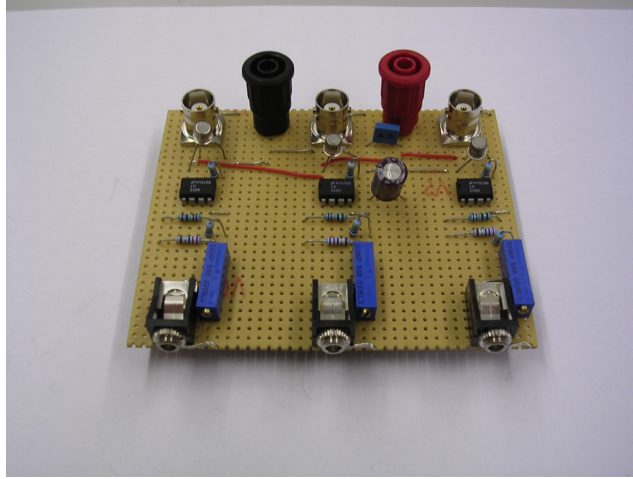


Figure 8.3: First electronical device developed

For the calibration of the new miniature hot-film sensor, it is used the same instrumentation as for the calibration of the commercial one, used in chapter 5 for the analysis of the wall shear stress in a Francis turbine. The same additional instruments are used, namely a Pitot tube, for the mean flow velocity acquisition and a temperature sonde for the temperature acquisition in the measurement section.

### 8.2.2 Calibration procedure

The calibration procedure for the new miniature hot-film sensor is the same as the one used for the preliminary calibration and measurements performance in the cone of a Francis turbine. The calibration procedure was detailed in chapter 4, section 4.3.

## 8.3 NEW PROBE CALIBRATION

There were, initially, tested 2 hot-film probes encapsulated with the initial version of anemometer. The preliminary tests results showed a success in improving the life time of the probe - the detachment of the protecting  $\text{SiO}_2$  layer on the electrical connections took no more place, even if the films were heated at about  $140^\circ\text{C}$ . Meanwhile, the Wavemind anemometer needs some improvements, as during the measurements high oscillations occur, difficult to eliminate, the system becoming, in this way, instable.

For establishing the sensor's dynamic, a new electronic device has to be developed, while for characterization of the maximum frequency for the velocities variations that the anemometer would be able to detect and measure, the sensor's time constant value must be evaluated. The time response of the sensor is limited by its thermal capacity, i.e. the thermal time constant of the active sensor mass. This time constant was evaluated theoretically and experimentally.

### 8.3.1 Time response calculation

The basic one-dimensional model for a non-cylindrical hot film, shown in figure 8.4, which includes also the heated losses across the substrate to surfaces adjacent to the film has been introduced by Bellhouse and Schultz [1967].

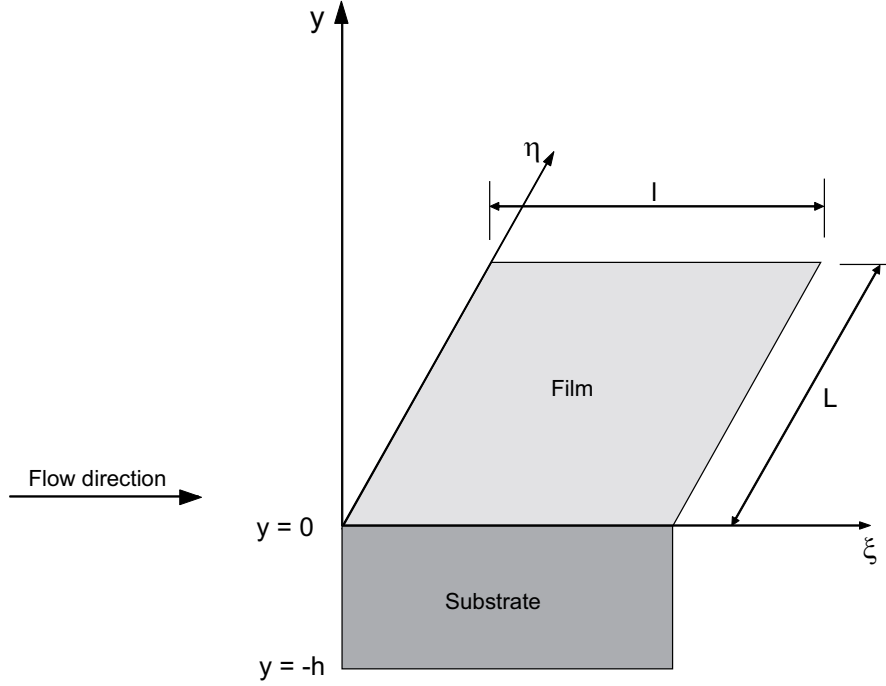


Figure 8.4: Model of non-cylindrical hot film

This model replaces the film surface of a sensor by a planar film surface at a temperature and it replaces the three-dimensional heat transfer across the substrate into areas adjacent to the film by one-dimensional heat transfer across the substrate to another planar surface below the substrate at temperature. In this model, and for the new wall shear-stress sensor, due to the fact that the film's thickness is  $150\text{nm}$ , and the substrate thickness is  $380\text{ }\mu\text{m}$ , it can be neglected the film thickness related to the substrate thickness  $h$ . The heat loss from the film through the substrate is in the opposite  $y$  direction. For the hot-film probe, it is also neglected the protecting  $\text{SiO}_2$  layer placed on the film surface, between the water and the film.

The energy balance at the upper surface, covered by the film characterized by a length,  $l$  and width  $L$  is evidenced, in the same way as in section 4.3, by relation 8.1.

$$\dot{Q}_J = \Sigma \dot{Q} + \frac{dQ_{film}}{dt}, \quad (8.1)$$

where:

- $\dot{Q}_J$  - heat power transferred by Joule effect;
- $\Sigma \dot{Q}$  - heat transfer by convection from film to surrounding fluid;
- $dQ_{film}$  - heat transfer by conduction to supports, which influences the dynamic response of the sensor.



Assuming that the film resistance  $R_f$  represents one arm of the Wheatstone bridge,  $R_1$  another arm in series with  $R_f$  and  $U$  the voltage over the bridge of the constant-temperature anemometer represented in figure 8.5, the heat transferred by Joule effect,  $\dot{Q}_J$  can be written as relationship 8.2.

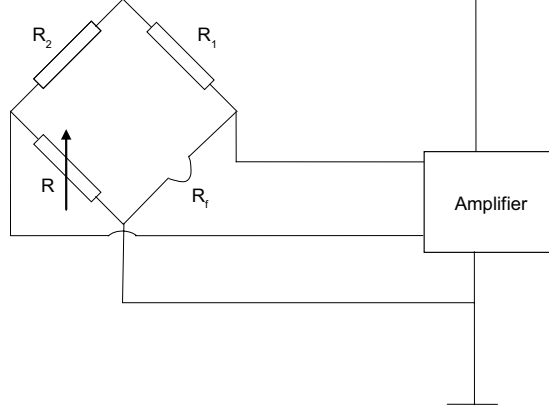


Figure 8.5: Principle of the constant temperature anemometer

$$\dot{Q}_J = \frac{R_f U^2}{(R_f + R_1)^2}, \quad (8.2)$$

The heat transfer by convection depends on the flow velocity and on the temperature difference between the film and the substrate. The heat transfer by conduction depends on the temperature variation in substrate; in this way, the thermal balance evidenced by relation 8.1 becomes, with the new parameters, relation 8.3.

$$\frac{R_f U^2}{(R_f + R_1)^2} = H(c) \cdot (T|_{y=0} - T_0) + l L k_{su} \frac{\partial T}{\partial y}, \quad (8.3)$$

where:  $T(y)$  is the temperature in the substrate,  $T|_{y=0} = T_f$  is the film temperature,  $T_0$  is the water temperature along the upper surface of the film,  $y = 0$ , as well as the temperature for the lower surface of the substrate,  $y = -h$ ,  $c$  is the flow velocity,  $k_{su}$  is the heat conductivity of the substrate and  $H(c)$  is the heat transfer function.

For the new wall shear-stress sensor, the substrate may be considered as being made of 2 different materials:

- an insulating surface at the lower surface of the film, made up by silicon pillars refilled with  $SiO_2$ , characterized by a thickness  $h_1$  and a heat conductivity  $k_{su1}$ ,
- initial silicon substrate characterized by heat conductivity  $k_{su2}$ .

The equivalent thermal conductivity of the substrate,  $k_{su}$ , is determined by assuming a linear dependence of the temperature in the substrate, see figure 8.6, and described by relation 8.4.

$$k_{su} = \frac{k_{su1} h_1 + k_{su2} (h - h_1)}{h} \quad (8.4)$$

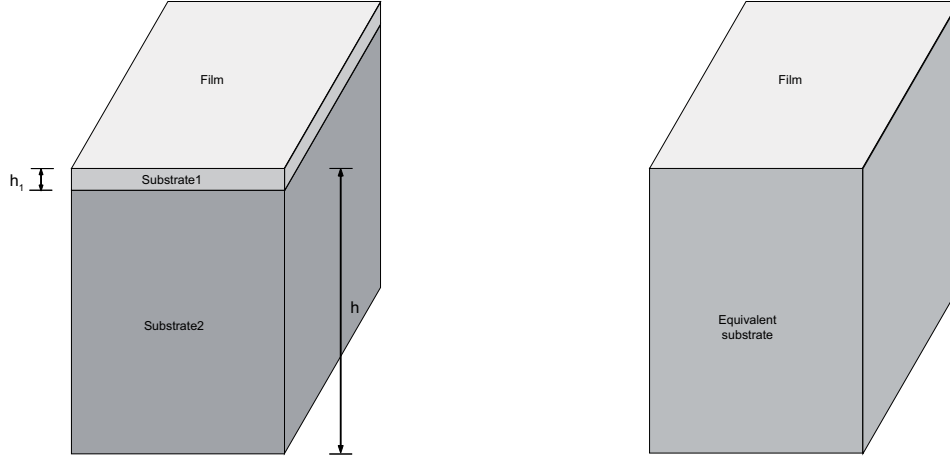


Figure 8.6: Equivalent substrate assumption

The thermal conductivity of the insulating surface is considered  $k_{su1} = 1.3807[W/(m \cdot K)]$ , while for the silicon substrate is  $k_{su2} = 125.52[W/(m \cdot K)]$ .

The heat transfer function,  $H(c)$ , described by relationship 8.5, involves the local heat transfer coefficient from the film to the flow,  $\hat{h}$ .

$$H(c) = \int_{\xi=0}^l \int_{\eta=0}^L \hat{h}(c, \xi, \eta) d\xi d\eta \quad (8.5)$$

For steady-state heat transfer, the relation 8.6 is available.

$$\frac{\partial T}{\partial y} = \frac{T_f - T_h}{h} \quad (8.6)$$

where  $T_h$  is the temperature of the lower substrate surface for static conditions and  $h$  is the substrate thickness.

Moreover, at the lower surface of the substrate the boundary condition is described by relation 8.7.

$$H(c) \cdot (T|_{y=-h} - T_0) = lLk_{su} \frac{\partial T}{\partial y}|_{y=-h} \quad (8.7)$$

It is introduced the dimensionless quantity,  $x$  called the Biot number of the non-cylindrical sensor, see relation 8.8.

$$x = \frac{h}{lLk_{su}} H(c) \quad (8.8)$$

Taking into account the relationship 8.9, expressing the temperature difference, the boundary conditions 8.3 and 8.7 are simplified to relation 8.11.

$$T_f - T_h = \frac{x}{x+1} (T_f - T_0) \quad (8.9)$$

$$\frac{R_f U^2}{(R_f + R_1)^2} = H(c) \cdot (T_f - T_0) + \frac{1}{x} H(c) \cdot (T_f - T_h) \quad (8.10)$$

Furthermore, combining equations 8.9 and 8.11 yields:

$$\frac{R_f U^2}{(R_f + R_1)^2} = \frac{2+x}{1+x} H(c) \cdot (T_f - T_0) \quad (8.11)$$

The heat transfer function, for the new wall shear-stress case, can be developed, in the relationship 8.12, by considering the Nusselt number,  $Nu$ , and its simplest expression is given by "King's law", see relation 8.13.

$$H(c) = Nu \cdot lL \quad (8.12)$$

$$Nu = A + Bc^n \quad (8.13)$$

where  $A$ ,  $B$ ,  $n$  are constants. The heat transfer function becomes:

$$H(c) = lL(A + Bc^n) = A' + B'c^n \quad (8.14)$$

For a hot film, which is an electrical resistance, the temperature dependence may be expressed as:

$$R_f = R_0[1 + \alpha \cdot (T_f - T_0)] \quad (8.15)$$

where  $R_0$  is the resistance at the reference temperature  $T_0$ ,  $\alpha$  being the temperature coefficient of the electric resistivity of the film. The temperature coefficient's value for the new wall shear-stress, as the heated film is in platinum is considered about  $0.0035^\circ C^{-1}$ . The temperature difference can be expressed by relationship 8.16.

$$T_f - T_0 = \frac{R_f - R_0}{\alpha R_0} \quad (8.16)$$

Replacing the relations 8.16 and 8.14 in 8.11 it is obtained the relation 8.17,

$$\frac{U^2}{R_f(R_f - R_0)} = \frac{lL}{\alpha R_0} \frac{2+x}{1+x} (A + Bc^n) \quad (8.17)$$

and replacing 8.14 in 8.8, the relation 8.17 becomes:

$$\frac{U^2}{R_f(R_f - R_0)} = \frac{lL}{\alpha R_0} \left(1 + \frac{k_{su}}{k_{su} + h(A + Bc^n)}\right) (A + Bc^n) \quad (8.18)$$

Meanwhile the derivation of the relation 8.18 allows the achievement of the relationship 8.19.

$$\frac{U^2(2R_f - R_0)}{R_f^2(R_f - R_0)^2} \frac{\partial R_f}{\partial t} = nBc^{n-1} \frac{lL}{\alpha R_0} \left[1 + k_{su} \frac{h(k_{su} - 1)(A + Bc^n) + k_{su}}{[k_{su} + h(A + Bc^n)]^2}\right] \frac{\partial c}{\partial t} \quad (8.19)$$

It is introduced the time constant,  $M$ , detailed for the new wall shear-stress sensor in the expression 8.20.

$$M = nBc^{n-1} \frac{lL}{\alpha R_0} \frac{R_f^2(R_f - R_0)^2}{U^2(2R_f - R_0)} \left[1 + k_{su} \frac{h(k_{su} - 1)(A + Bc^n) + k_{su}}{[k_{su} + h(A + Bc^n)]^2}\right] \quad (8.20)$$

The limit frequency of the hot-film response is defined by relationship 8.21, while the time response is found as relation 8.22.

$$f = \frac{1}{2\pi M} [\text{Hz}] \quad (8.21)$$

$$\tau = \frac{1}{f} [\text{s}] \quad (8.22)$$

For the same wall shear-stress probe containing 3 heated elements, there were calculated, for each of them, the time constant, the limit frequency and the time response, for 2 different cases: without considering the conduction losses, illustrated in table 8.1 and for the case with conduction losses, illustrated in table 8.2. For this calculations there were imposed a constant temperature for the hot-film, at about  $65^\circ\text{C}$  and the temperature value at the lower surface of the substrate, at  $20^\circ\text{C}$ .

As the calculations showed the heat conduction in the substrate plays an important role in the behavior of the new wall shear-stress probe. Meanwhile, even considering the conduction losses, the new probe responds to the expectations in time response.

### 8.3.2 Time response measurement

Moreover, to confirm this behavior there was measured the time constant, for all the 3 heated films, corresponding to the same probe used for the characterization of the probe's behavior regarding the time response. For this, there will be measured the relaxation time of a signal output as response to a controlled external perturbation.

For the measurements a preliminary CCA - constant current-anemometer - development was carried out, schematized in figure 8.7.

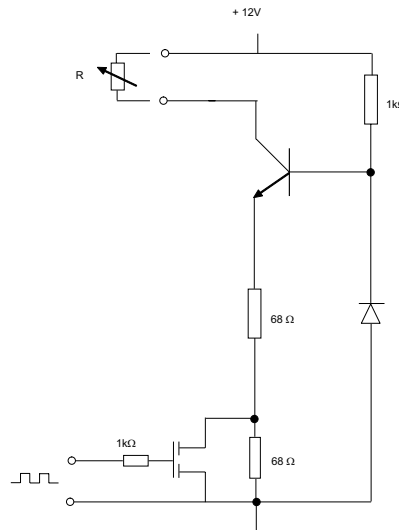


Figure 8.7: Constant-current anemometer

	n	U [V]	$R_0[\Omega]$	$R_f[\Omega]$	c [m/s]	A	B	A'	B'	M	f [kHz]	$\tau$ [ms]
Film no.1	0.5	5	73.97	81.0395	5	0.32	43.6394317	$2.74672 \cdot 10^{-11}$	$1.6856 \cdot 10^{-7}$	$1.12326 \cdot 10^{-5}$	14.169	0.071
Film no.2	0.5	5	70.404	76.6725	5	0.32	43.6394317	$2.88584 \cdot 10^{-11}$	$1.77098 \cdot 10^{-7}$	$8.8232 \cdot 10^{-6}$	18.038	0.055
Film no.3	0.5	5	65.791	72.523	5	0.32	43.6394317	$3.08818 \cdot 10^{-11}$	$1.89515 \cdot 10^{-7}$	$1.01961 \cdot 10^{-5}$	15.609	0.064

Table 8.1: Wall shear-stress sensor's thermal time constant calculation without considering conduction losses

	n	U [V]	$R_0[\Omega]$	$R_f[\Omega]$	c [m/s]	A	B	A'	B'	M	f [kHz]	$\tau$ [ms]
Film no.1	0.5	5	73.97	81.0395	5	0.32	43.6394317	$2.74672 \cdot 10^{-11}$	$3.74579 \cdot 10^{-9}$	$2.28723 \cdot 10^{-5}$	6.958	0.144
Film no.2	0.5	5	70.404	76.6725	5	0.32	43.6394317	$2.88584 \cdot 10^{-11}$	$3.93551 \cdot 10^{-9}$	$1.79662 \cdot 10^{-5}$	8.859	0.113
Film no.3	0.5	5	65.791	72.523	5	0.32	43.6394317	$3.08818 \cdot 10^{-11}$	$4.21145 \cdot 10^{-9}$	$2.07617 \cdot 10^{-5}$	7.666	0.131

Table 8.2: Wall shear-stress sensor's thermal time constant calculation with considering conduction losses

A preliminary test for this new development was its time response, meaning the time needed to obtain a stabilizing output signal. It was tested a film on a probe for 3 different mean flow velocity in the water tunnel, corresponding to the constant current value of 40 mA, see figure 8.8.

A second test is needed and performed for studying the system behavior. As the new CCA can function at 2 different current intensities,  $i = 40mA$  and  $i = 80mA$ , its behavior in time is relevant for the measurements. It is characterized the CCA time response with the same new probe used in the first test, by switching between the 2 current values, for a constant mean flow velocity, see figure 8.9.

The results show that, as expected, due to the thermal inertia, the time response of the CCA is higher than for CTA, and in the same time, due to fact that by inputting a current of 80mA, the film temperature is unknown, the CCA utilization leads to probe deterioration. For different flow velocity, the same voltage values are obtained at the anemometer's output. By operating the sensor at constant temperature, the response time of the sensor can be improved considerably.

Meanwhile, the Wavemind anemometer previous developed has been improved for measuring the time response of a new wall shear-stress sensor. It is used the *square wave test*, which consists in imposing a square wave at the anemometer's input and noticing the effects on the output voltage.

The square wave test has been and is still nowadays usually used, due to its easy operation, in most applications involving hot-wire and hot-film anemometry for optimizing and quantifying the frequency response of hot-element systems.

This method is based on the idea that the water velocity fluctuation leads to a temperature fluctuation which is equilibrated or after a time linked to the thermal inertia, by the use of a CCA, or by a feed-back compensation time, CTA case. In both cases, the square wave test simulates a velocity fluctuation by setting a temperature variation by Joule effect. The output voltage consists in a drop, which releases in an exponential form  $\sim e^{-t/t_0}$ , allowing the time response evaluation,  $t_0$ . This time response integrates all the response times of the system: thermal inertia, capacitive effects of the cables, time response of the electronical device.

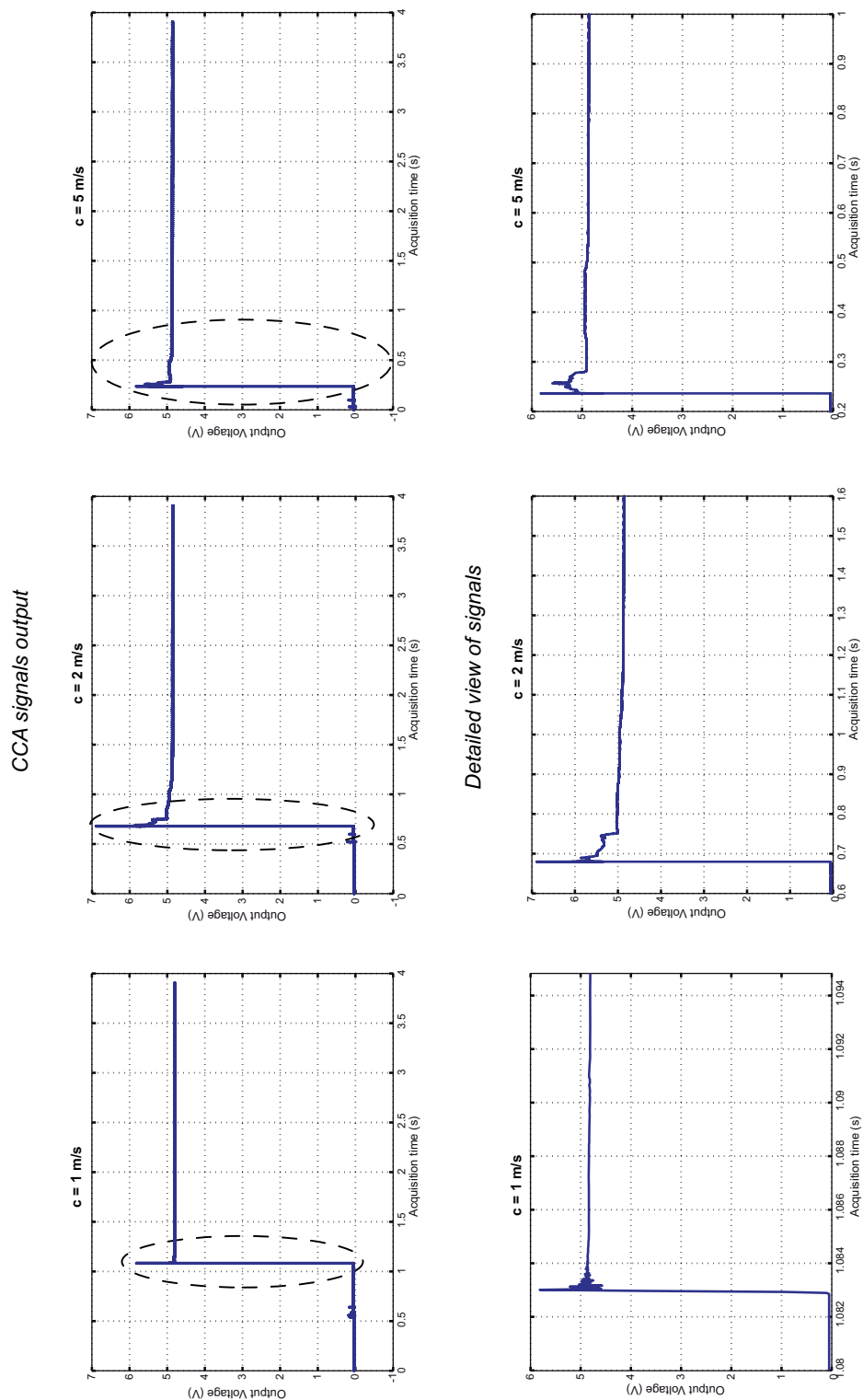
There were measured 2 different wall shear-stress probes, taken from 2 different wafers at 2 different mean flow velocity in the calibration tunnel.

The measurement results are presented in 2 different tables: 8.3 and 8.4.

The frequency response of the optimized hot film system, defined as the frequency at which the bridge voltage signal is attenuated by 3 dB, is given by relation 8.23.

$$f_s = \frac{1}{3\tau_s} \quad (8.23)$$

The results showed a good frequency response for the new wall shear-stress sensor, for the 2 mean flow velocity. By comparisons with the time response calculated, it can be noticed an important difference, the time response calculated is about 2 times smaller than the one measured. This difference is explained by the simplifying assumptions imposed in the calculations, related to the size of the film, of the equivalent substrate, and also, as explained above, the time response measured is made up of all the response times of the system, which there were not taken into account in the calculation.

Figure 8.8: Constant-current anemometer preliminary test for a film resistance of  $R = 71.5\Omega$

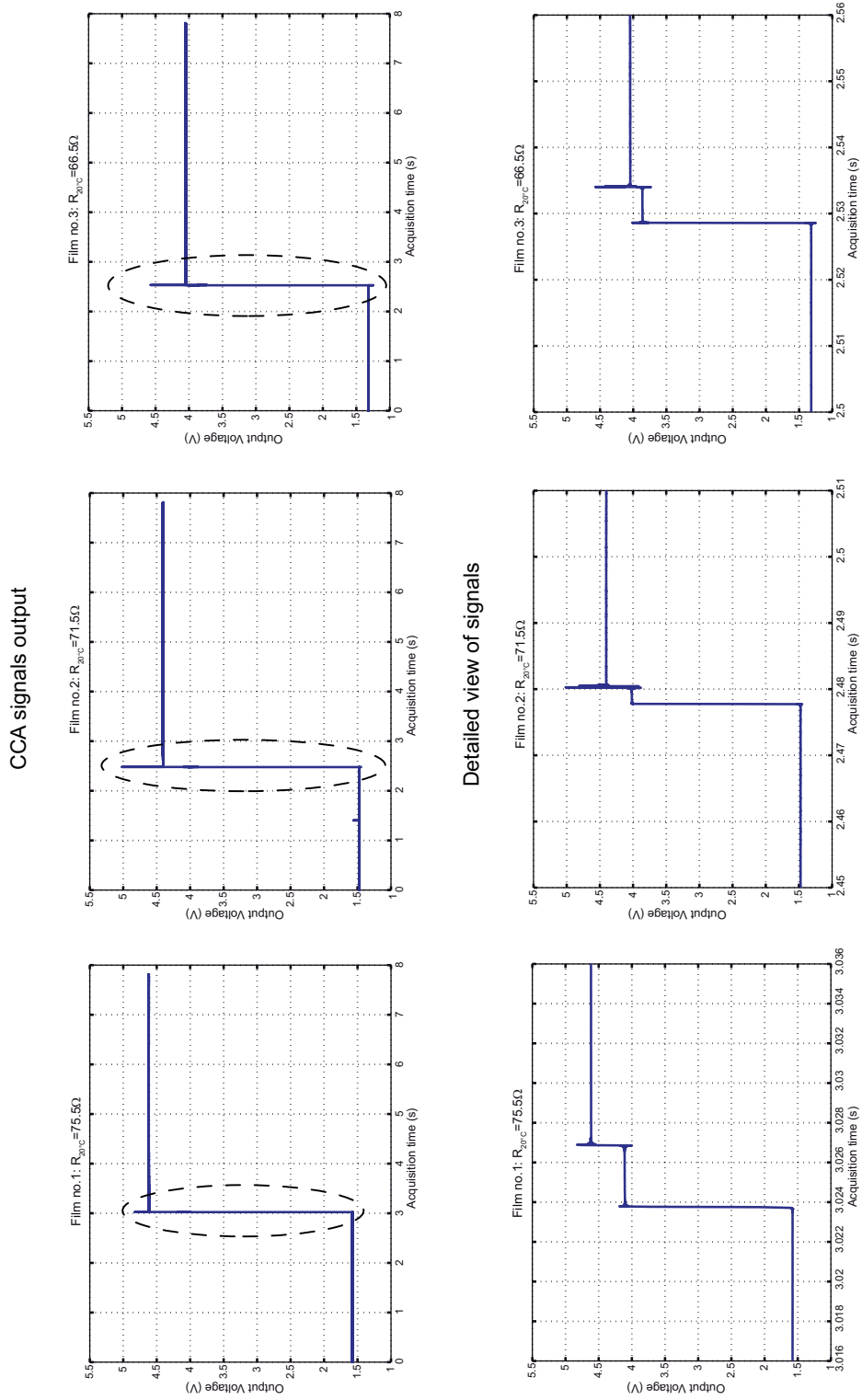


Figure 8.9: Constant-current anemometer's output from step input current



Sensor no.1	Square wave signal frequency	$t_{0,c=2m/s}$ [s]	$f_{0,c=2m/s}$ [Hz]	$t_{0,c=5m/s}$ [s]	$f_{0,c=5m/s}$ [Hz]
Film no.1, $R = 38.5 \Omega$	1 Hz	0.000355	448.36	0.000265	599.45
	10 Hz	0.000282	563.98	0.000255	625.36194
	100 Hz	0.000225	707.53	0.000304	522.89
	300 Hz	0.000312	510.93	0.000301	528.73
	500Hz	0.000285	559.34	0.000333	477.71
	1 kHz	0.000217	734.75	0.000203	785.7
	5 kHz	$1.41726 \cdot 10^{-5}$	11229.78	$2.64646 \cdot 10^{-5}$	6013.87
	10 kHz	$1.88974 \cdot 10^{-5}$	8422.05	$1.51241 \cdot 10^{-5}$	10523.25
Film no.2, $R = 26.2 \Omega$	1 Hz	0.000225	706.6	0.000287	554.15
	10 Hz	0.000398	400.33	0.000359	443.48
	100 Hz	0.000234	680.47	0.000284	560.83
	300 Hz	0.000419	379.95	0.000237	671.16
	500Hz	0.000295	539.06	0.000228	714.45
	1 kHz	0.000191	835.19	0.000188	847.54
	5 kHz	$2.51996 \cdot 10^{-5}$	6315.78	0.000021	7578.81
	10 kHz	$1.68014 \cdot 10^{-5}$	9472.7	$1.68003 \cdot 10^{-5}$	9473.35
Film no.3, $R = 40.6 \Omega$	1 Hz	0.000298	534.74	0.000272	584.82
	10 Hz	0.000176	906.45	0.00029	549.31
	100 Hz	0.000338	470.35	0.000305	521.96
	300 Hz	0.000311	511.98	0.000338	470.46
	500Hz	0.000314	507.17	0.000294	541.59
	1 kHz	0.000181	878.28	0.000181	880.59
	5 kHz	$1.76359 \cdot 10^{-5}$	9024.5	$1.76431 \cdot 10^{-5}$	9020.81
	10 kHz	$1.13385 \cdot 10^{-5}$	14036.74	$1.10239 \cdot 10^{-5}$	14437.23

Table 8.3: Time responses measurements for 1 new wall shear-stress sensors with medium resistance values

Sensor no.2	Square wave signal frequency	$t_{0,c=2m/s}$ [s]	$f_{0,c=2m/s}$ [Hz]	$t_{0,c=5m/s}$ [s]	$f_{0,c=5m/s}$ [Hz]
Film no.1, $R = 71.7 \Omega$	1 Hz	0.000286	555.75	0.000335	475.61
	10 Hz	0.000288	552.38	0.00027	590.44
	100 Hz	0.00028	567.77	0.000283	561.61
	300 Hz	0.000253	627.53	0.000262	606.64
	500Hz	0.0003	530.6	0.000295	539.31
	1 kHz	0.000223	714.11	0.0002	797.63
	5 kHz	$1.35141 \cdot 10^{-5}$	11776.97	$1.7653 \cdot 10^{-5}$	9015.73
	10 kHz	$1.49816 \cdot 10^{-5}$	10623.34	$1.37448 \cdot 10^{-5}$	11579.27
Film no.2, $R = 75.7 \Omega$	1 Hz	0.000257	620.17	0.000235	675.92
	10 Hz	0.000261	609.02	0.000241	660.19
	100 Hz	0.000308	516.85	0.000346	460.45
	300 Hz	0.000273	582.57	0.000224	710.02
	500Hz	0.00027	588.66	0.000301	527.88
	1 kHz	0.000201	791.81	0.000201	791.53
	5 kHz	$2.11238 \cdot 10^{-5}$	7534.41	$2.84172 \cdot 10^{-5}$	5600.65
	10 kHz	$1.4892 \cdot 10^{-5}$	10687.296	$1.71808 \cdot 10^{-5}$	9263.56
Film no.3, $R = 67.6 \Omega$	1 Hz	0.000259	613.55	0.000336	472.93
	10 Hz	0.000293	543.02	0.00025	636.4
	100 Hz	0.000302	527.19	0.000227	702.16
	300 Hz	0.000234	680.86	0.000288	552.12
	500Hz	0.000295	539.38	0.00025	635.9
	1 kHz	0.0002	793.79	0.000231	687.79
	5 kHz	$1.79986 \cdot 10^{-5}$	8842.65	$2.17779 \cdot 10^{-5}$	7308.11
	10 kHz	$1.15486 \cdot 10^{-5}$	13781.36	$1.03944 \cdot 10^{-5}$	15311.57

Table 8.4: Time responses measurements for another new wall shear-stress sensors with high resistance values

### 8.3.3 New wall shear-stress sensor calibration and sensitivity parameters study using miniCTA

Furthermore, after the probe characterization, the calibration procedure has to be carried out. As the CTA used was not totally adequate for all the probes fabricated, another option, for the calibration, was the use of a miniCTA, developed by DANTEC Measurement Technology. The inconvenient in using this instrumentation is that it can be used only with one film at once.

The MiniCTA, illustrated in figure 8.10, is designed in the same way as a classical constant temperature anemometer, having specifications and performance carried out for the ordinary low speed flows. It is intended for the measurement of velocity and turbulence in flows with moderate frequency content.

It is equipped with BNC connectors and operated via a 12-volt DC power adapter or by a battery. The bandwidth, maximum 10kHz is optimized for use with wire probes. The anemometer can be used with probes having the cold resistances up to 10  $\Omega$ . The overheat setting is defined via dip switches and jumpers inside the box.

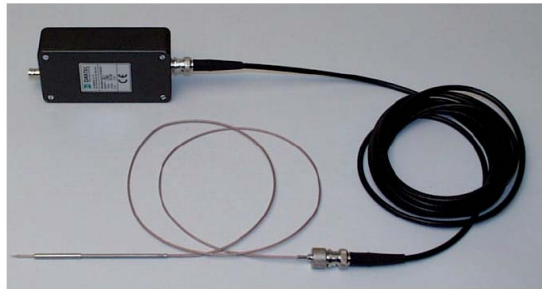


Figure 8.10: MiniCTA

A miniature Constant Temperature Anemometer, 54T30 type, was specially adapted for some probes resistances, 18 – 50 $\Omega$ , bridge ratio 1 : 10.

The calibration and the sensitivity parameters were studied, using this new instrumentation; all the measurements were performed in the water tunnel in the Laboratory for Hydraulic Machines, with respect to the same relations obtained in chapter 4 due to the same relative position of the new probe in the measurement section of the hydrodynamic tunnel. Calibration results and sensitivity parameters study are following up.

### 8.3.4 Sensitivity parameters

#### 1. Temperature gradient influence

In the same way, as for the commercial hot-film probe used for performing wall shear-stress measurements in a Francis turbine, the new sensor is made up by 3 hot-film probes, which are electrical resistances maintained at a constant temperature, about 65°C, and, which by their property, depend linear on the temperature difference between film and medium where it is placed.

For each of the 3 films on the same probe there are presented the results of the quantification of this parameter together with the measurements accuracy, see figure 8.11, 8.12 and 8.13.

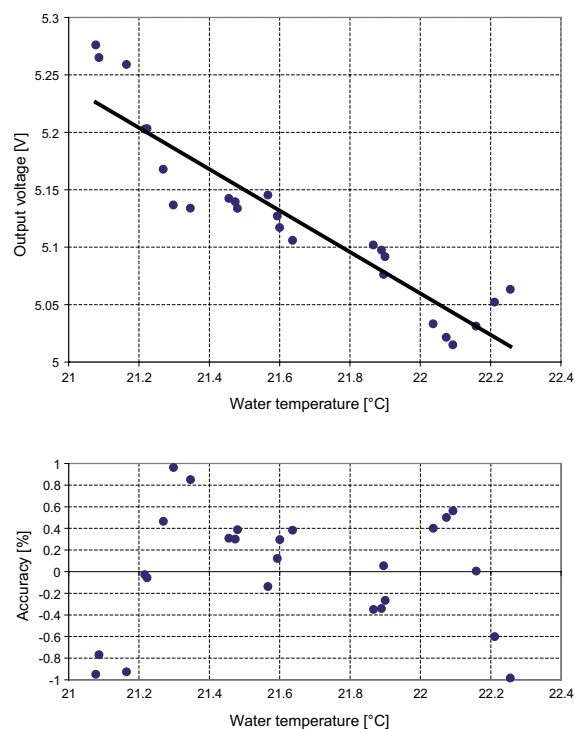


Figure 8.11: Film no.1,  $R = 37.2 \, \Omega$ , output voltage evolution with the water temperature

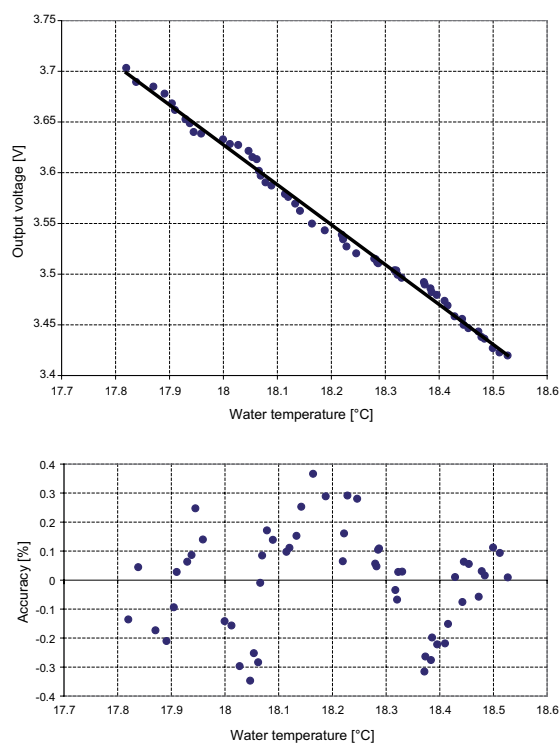


Figure 8.12: Film no.2,  $R = 29.5 \, \Omega$ , output voltage evolution with the water temperature

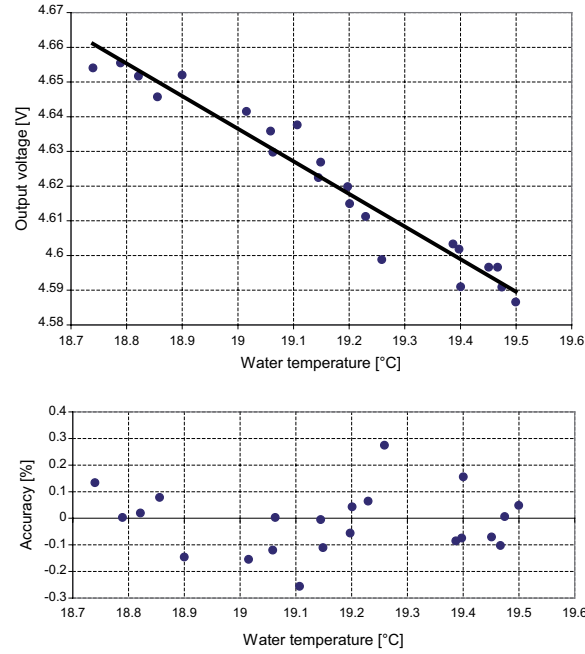


Figure 8.13: Film no.3,  $R = 33.1 \, \Omega$ , output voltage evolution with the water temperature

The influence of the water temperature on the output voltage of the wall shear-stress probe is expressed further, corresponding to each of the 3 films.

**Film no.1**,  $R = 37.2 \, \Omega$   $V = -0.1803 \cdot (21 - \theta) + 9.0267$ ;

**Film no.2**,  $R = 29.5 \, \Omega$   $V = -0.3937 \cdot (19 - \theta) + 10.714$ ;

**Film no.3**,  $R = 33.1 \, \Omega$   $V = -0.094 \cdot (18 - \theta) + 6.4218$ .

## 2. Orientation of the hot-film probe in the flow

The second parameter to study is the angular influence of the film direction with the flow direction. In the same way, as a ordinary hot-film, the maximal heat dissipation is obtained when the longitudinal direction of the film is perpendicular to the flow direction.

The influence of this parameter is presented in figures 8.14, 8.15 and 8.16, corresponding to each of the 3 films. Taking into account that a special configuration is presented for the new wall shear-stress sensor, film in triangle, the angle made by each film's sensor with the direction of the flow is modified over  $360^\circ$  with a step of  $5^\circ$ , starting from the same initial angle, for all 3 films,  $0^\circ$ .

It is observed that the maximum output voltage is obtained for the film no.1 at the relative angle  $-15^\circ$ , for the film no.2 at  $-120^\circ$ , while for the film no.3 an inconvenient was noticed, even if in this condition maximum is obtained at  $+120^\circ$ , in a good correlation with the other values. All the relative angular positions were reported to a same initial angular value for all the 3 films.

Due to the fact that the miniCTA's settings are changing for this wall shear-stress from one day to another, it is decided to not perform the contamination influence.

The voltage given by the heated films is acquired simultaneously with the water temperature and the flow velocity, see figure 8.17, 8.18 and 8.19, allowing to get the calibration curves, see figure 8.20, 8.21 and 8.22.

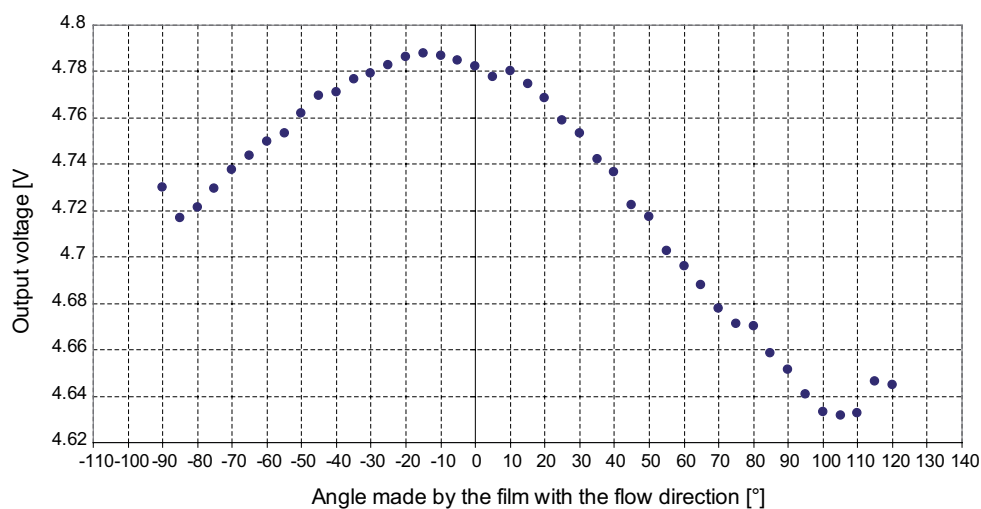


Figure 8.14: Angular variation of the output voltage given by the film no.1,  $R = 37.2 \Omega$

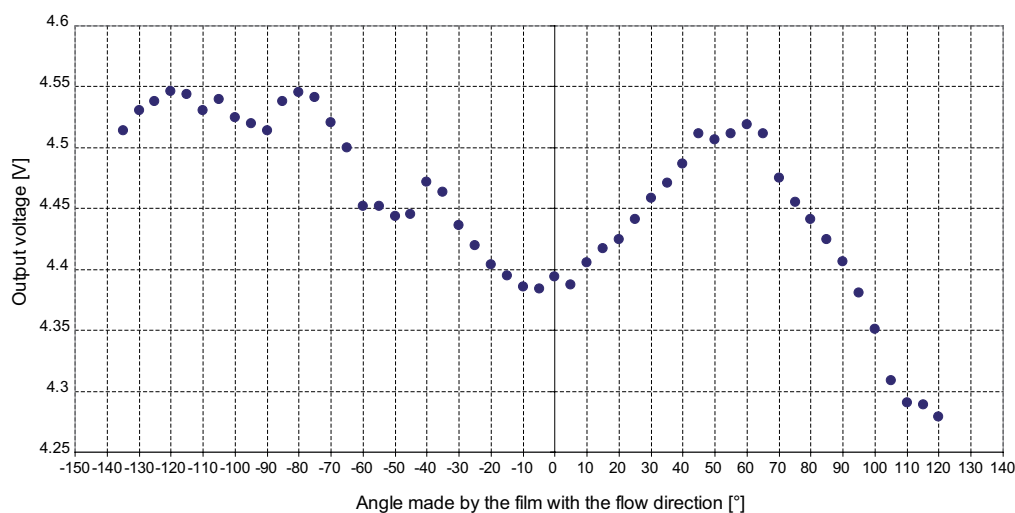


Figure 8.15: Angular variation of the output voltage given by the film no.2,  $R = 29.5 \Omega$

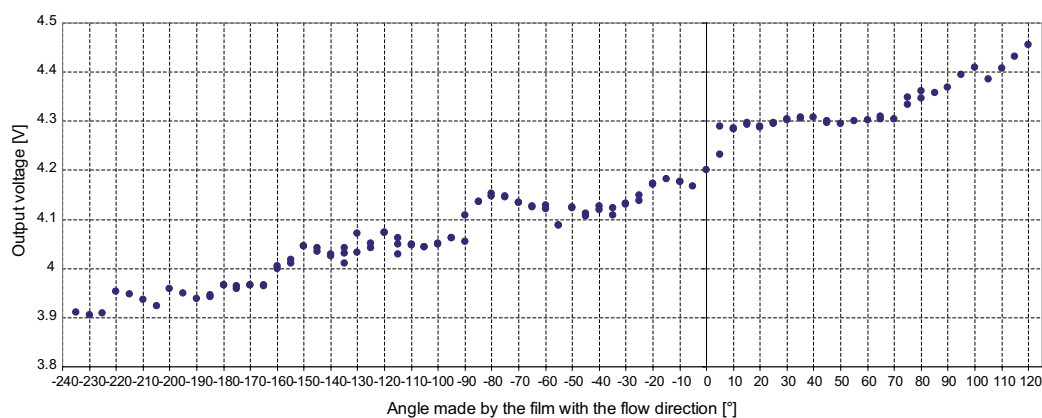


Figure 8.16: Angular variation of the output voltage given by the film no.3,  $R = 33.1 \Omega$

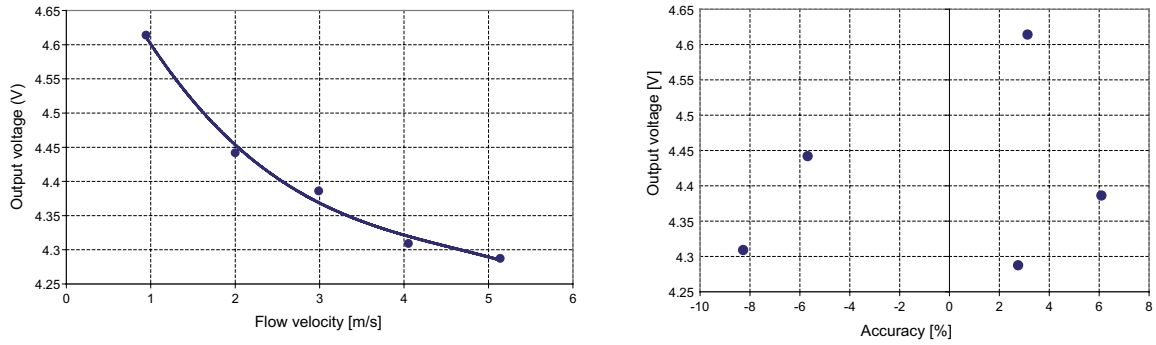


Figure 8.17: Output voltage variation with mean flow velocity, film no.1,  $R = 37.2 \Omega$

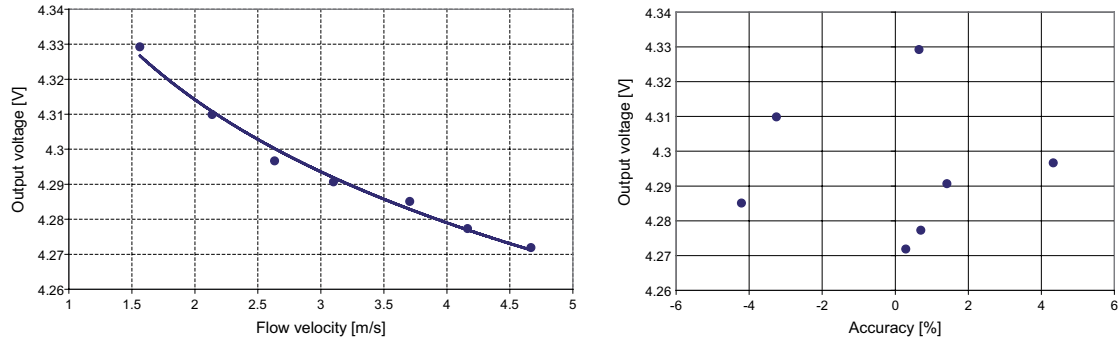


Figure 8.18: Output voltage variation with mean flow velocity, film no.2,  $R = 29.5 \Omega$

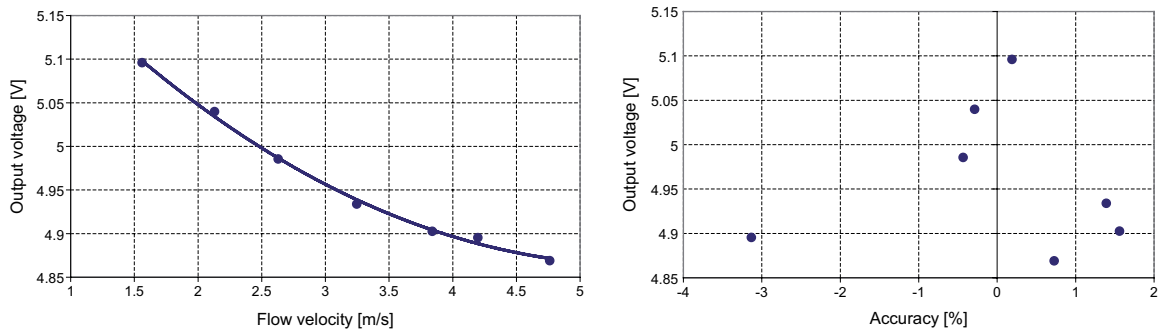


Figure 8.19: Output voltage variation with mean flow velocity, film no.3,  $R = 33.1 \Omega$

The calibration results showed that, as for all the 3 films was noticed the same behavior, the anemometer is not adequate for the present application, showing that as the flow velocity increases, the output voltage of the anemometer decreases. This means that the anemometer could no more introduce the power needed for keeping the film temperature constant, allowing, in the way, the cooling of the film.

As the new generation of wall shear-stress sensors comported 3 different wafers, one containing films with  $50\text{-}100 \Omega$ , the second one  $30\text{-}70 \Omega$  and the third one  $2\text{-}20 \Omega$  resistances values, the final calibration was performed using sensors on the last wafer which were used

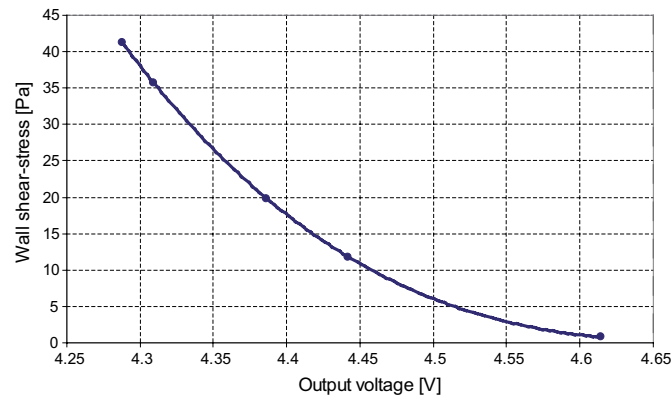


Figure 8.20: Calibration curve corresponding to film no.1,  $R = 37.2 \Omega$

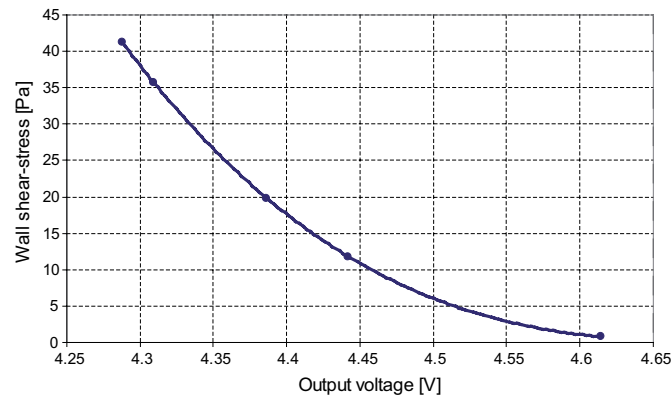


Figure 8.21: Calibration curve corresponding to film no.2,  $R = 29.5 \Omega$

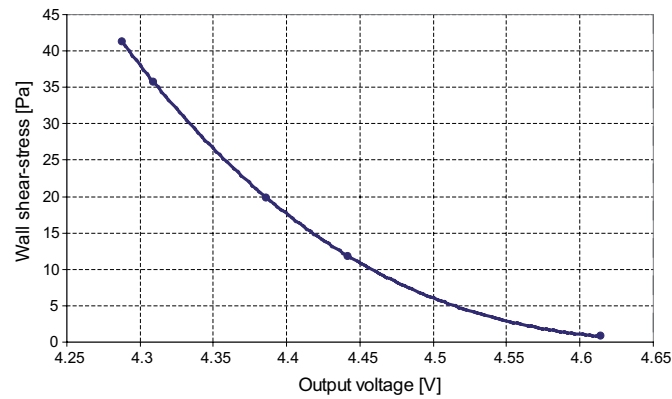


Figure 8.22: Calibration curve corresponding to film no.3,  $R = 33.1 \Omega$

with the DISA 55M System, previously used in the calibration of the commercial hot-film probe. The results with the sensitivity parameters influence study are presented.

For all the 3 films of a new wall-shear stress the results obtained were encouraging, and a good calibration was obtained for each one of them. The calibration global accuracy was  $\pm 1\%$ .

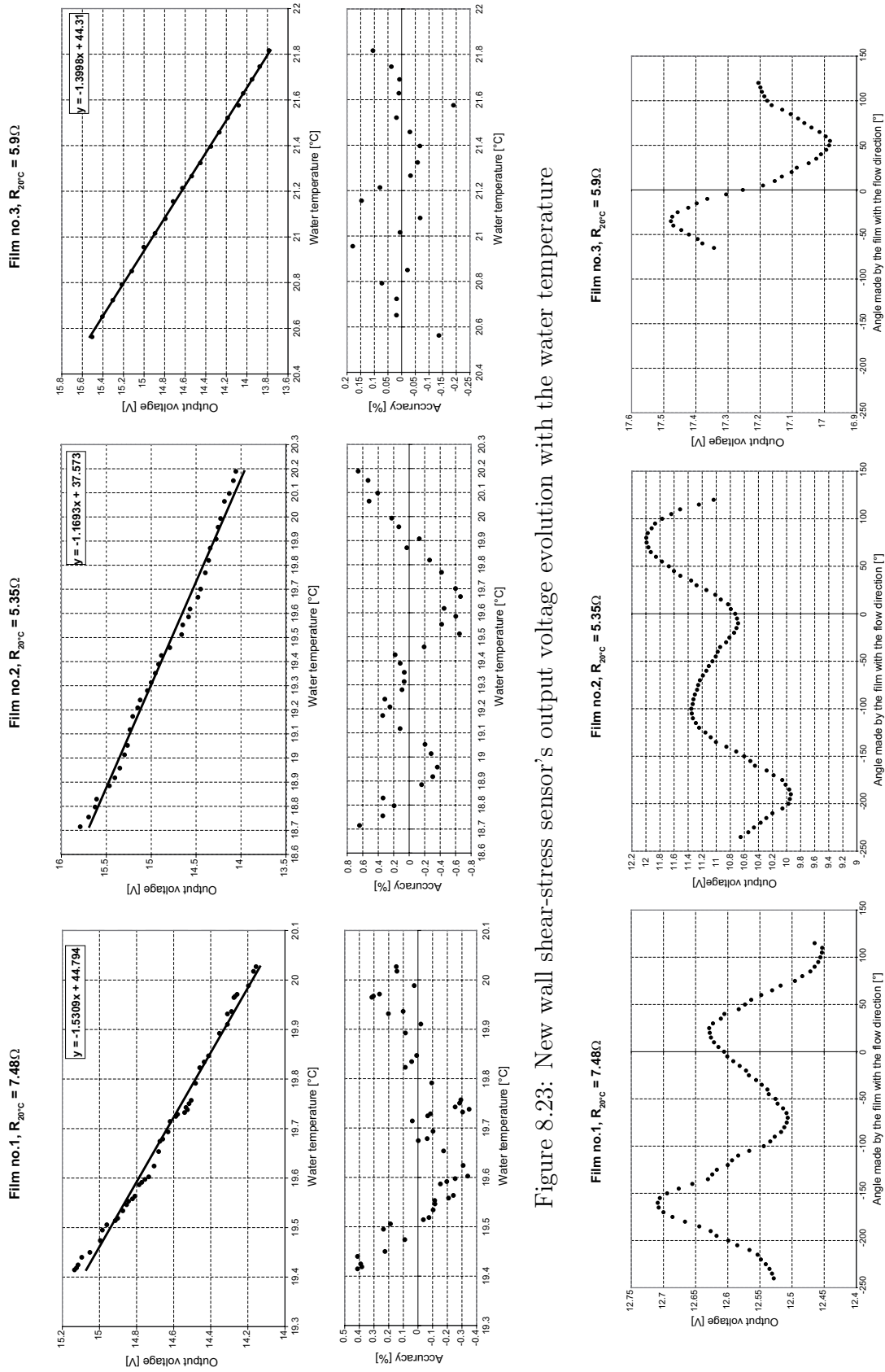


Figure 8.23: New wall shear-stress sensor's output voltage evolution with the water temperature

Figure 8.24: Angular variation of the voltage given by the new wall shear-stress sensor



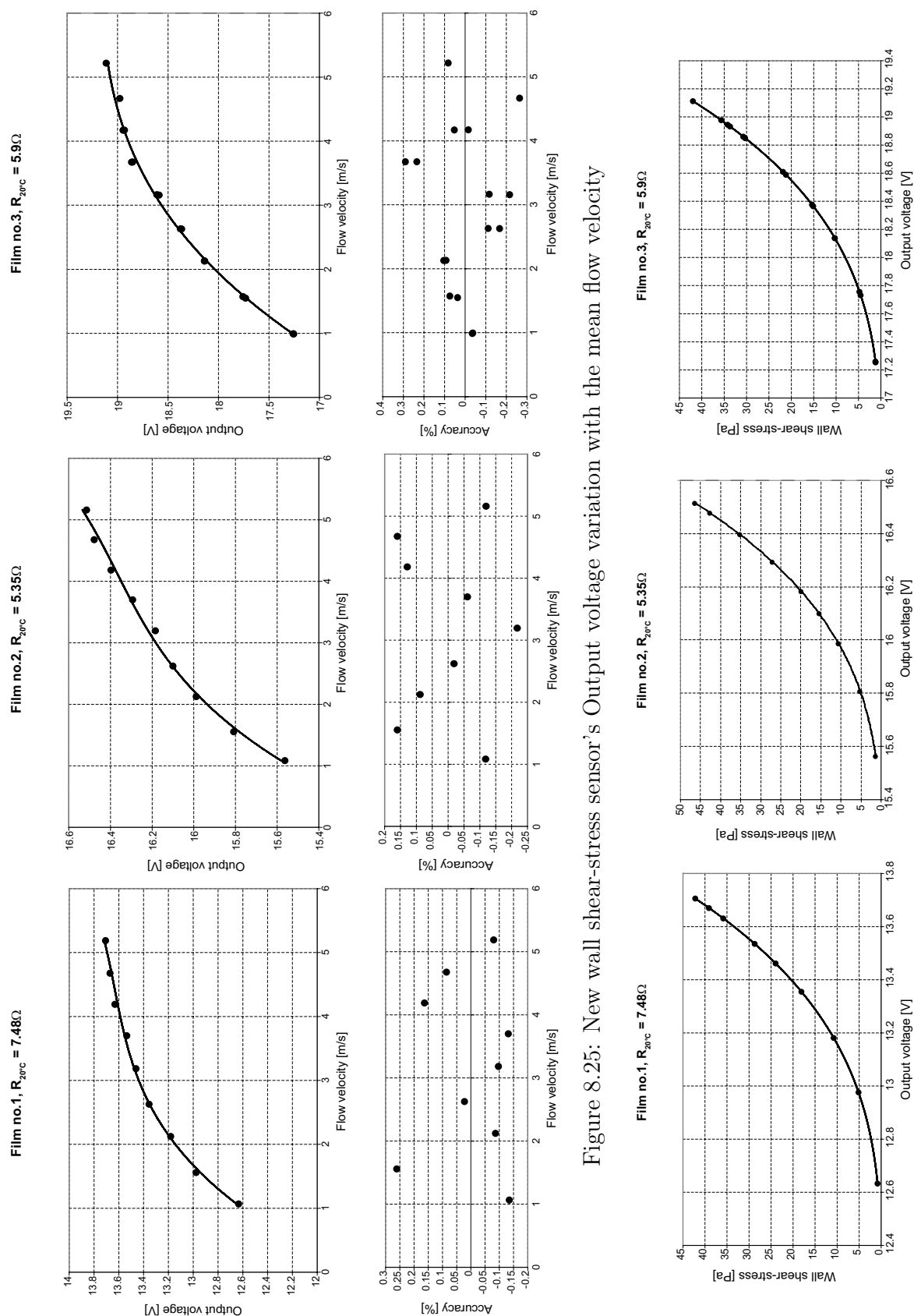


Figure 8.25: New wall shear-stress sensor's Output voltage variation with the mean flow velocity

Figure 8.26: Hot-films calibrations curves for a new wall shear-stress sensor

A comparison between the commercial hot-film probe with the new shear-stress sensor, used together with the miniCTA and DISA system is performed, see figure 8.27.

The comparisons showed a very good behavior of the new shear-stress sensor when using the DISA system, while using the miniCTA an inconvenient was noticed, namely the new anemometer, at high flow velocity, is no more capable to keep the film temperature constant.

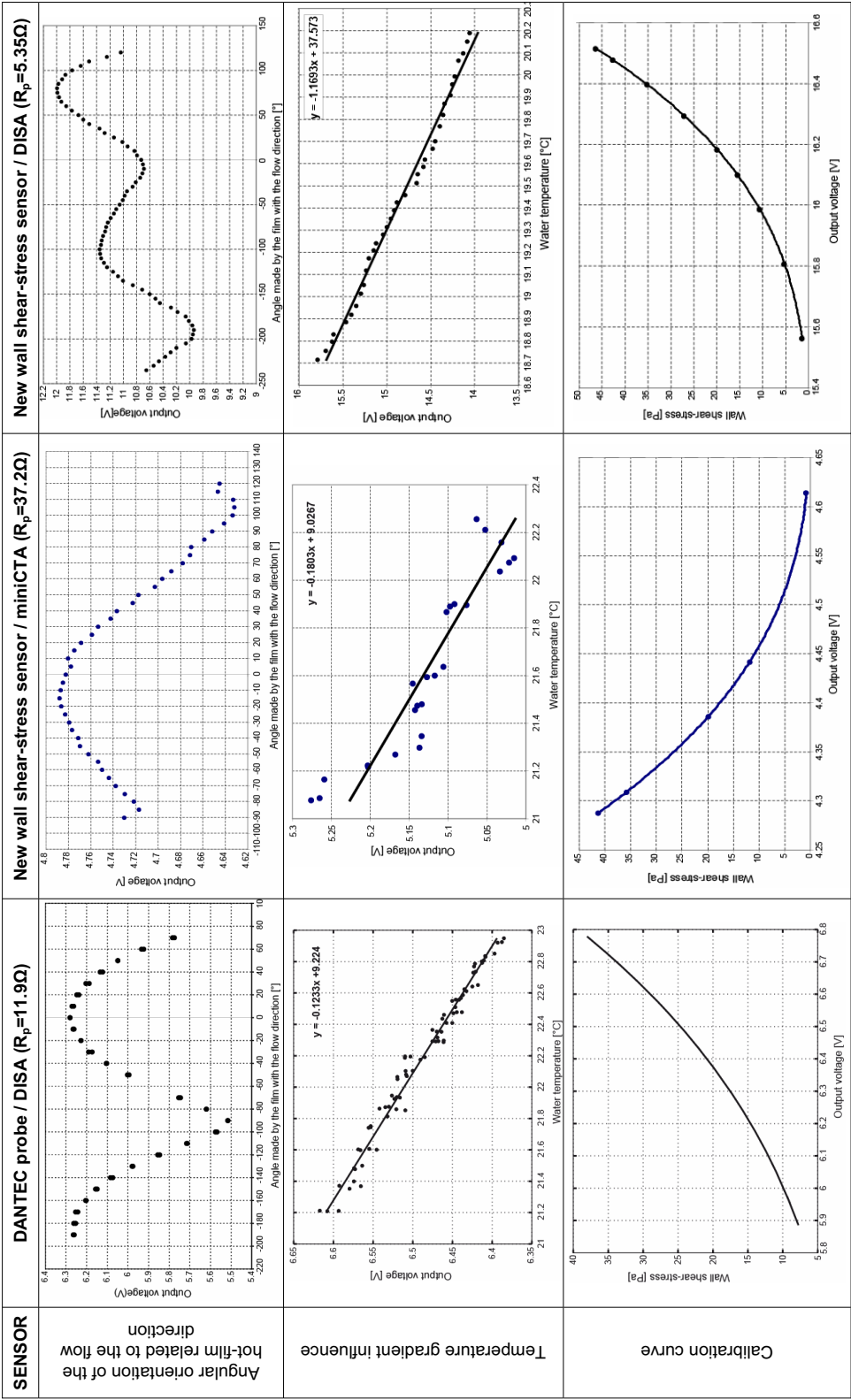


Figure 8.27: Calibration curve and sensitivity parameters comparisons for the DANTEC probe and new wall shear-stress sensor



# Chapter 9

## CONCLUSIONS

A first goal of the thesis was the wall shear-stress measurements in the cone of a Francis turbine, both at the inlet and at the outlet sections, for a better understanding of the complex phenomena in this part of a Francis turbine, by means of a complex acquisition system based on a classical flush-mounted hot-film probe which is calibrated in a hydrodynamic water tunnel, together with a constant temperature thermal anemometer.

The hot-film probes calibration is a very complex operation. The calibration curve is obtained starting from the theoretical relation between the wall shear-stress and the velocity distribution in the boundary layer and taking into account the influence of several parameters over the measurements: water temperature, orientation of the hot-film probe in the flow, contamination of the probe. The resulting calibration is a nonlinear relationship between voltage and shear stress. The relative calibration accuracy was found to be within 2% of the measured shear stress for a flush-mounted hot-film sensor and constant temperature anemometer.

Following the hot-film probe calibration, wall shear-stress measurements are performed in a Francis turbine's cone, for 4 near BEP operating points and 1 operating point at part load for 2 different  $\sigma$  values, corresponding to 9 positions at the inlet and 7 positions at the outlet of the hot-film probe. In this part of the project to eliminate the contamination parameter's influence, a drift correction procedure was developed.

The main purpose of the wall shear-stress measurements was the study of the boundary layer separation in the cone from 2 different points of view, steady and unsteady. The steady analysis was carried out, by studying the mean values of the wall shear-stress. Moreover, as the steady analysis results evidenced high fluctuations, the wall shear-stress unsteady aspect should be also studied. The unsteady analysis was performed, by studying the fluctuating parts of the wall shear-stress for each angular position of the hot-film probe in the cone and for each operating point.

The steady analysis offered informations about the boundary layer separation tendencies, while the unsteady analysis allowed the detection of the runner wake and the blade passage. For the near BEP operating points, the wall shear-stress decreases with the increasing of the flow rate, but no boundary layer separation took place. Meanwhile, at the cone outlet the bend influence is evidenced and the magnitude of the wall shear stress fluctuations decreases to 0. The wall shear stress values, corresponding to the partial load, are higher than for the standard operating points and the mean value is independent on the  $\sigma$  value. Moreover, 2 remarks can be made regarding the wall shear-stress synchronous with the rope passage: its magnitude is high related to the one obtained for the standard

operating points and it depends on the rope proximity to the wall. The global accuracy of the measurements was within 5% of the measured value.

A comparison with the CFD calculations results is performed and it doesn't show any difference, for the same probe angular position in the cone, in the studied operating points, evidencing that the wall law model used in this code should be reconsidered.

The boundary layer development was presented and it was also studied the validity of the universal logarithmic for the turbine flow conditions. Main investigations showed a strong 3D character of the boundary layer in the presence of an adverse pressure gradient in an unsteady sheared flow. There were also presented an adjustment using the composite power law, which offered a good description of the boundary layer.

As in turbulent flows, an increase in Reynolds number generates shorter timescales and, thus, smaller length scales, small and fast sensors are required for a acceptable resolution of the flow field. Nowadays, the wall shear-stress study, for water applications, is limited due to the availability of existing sensors to be implemented in a complex system and to study a 3D flow. From this point of view, MEMS offers opportunities for developing and manufacturing sensors with regard to these requirements: high accuracy and low cost.

The main goal of this thesis was the design, fabrication and testing of a new wall shear-stress sensor for 3D complex flows applications. The innovative aspect comes from the capability of this new device to detect the flow direction and to be implemented all over a turbomachine. It represents a bridge between 2 different discipline, micro-mechanical technology and fluid mechanics.

During this research, different developments, validations and accomplishments resulted and were highlighted. The main topics, achievements and contributions can be categorized into: design of a new wall shear-stress sensor, fabrication steps development, validation and improvements, numerical simulations of the thermal behavior of the heated-films, manufacturing of the new device, time response study, tests in hydrodynamic water tunnel and calibration sensitivity parameters study and calibration performance. Furthermore, there are summarized the results and contributions in each area.

For accomplishing the new device manufacturing, the flow and thermal microsensors state-of-the art was presented, by a general background and some examples. Another study deals with the wall shear-stress technics used nowadays and after considering all the advantages and disadvantages of the presented technics, for water applications, the most adapted for the present application was the hot film.

Moreover, to succeed in manufacturing a device adapted to our special requirements, a first study of the materials used for the substrate in microtechnology and available in CMI is presented. The initial choice was pyrex, as its thermal conductivity is low. Furthermore, as for this material the electrodischarge procedure needed in the electrical connections realization is a manually one, needing a precise tool handling for every hole, while the positioning relatively to the workpiece is not precise, the second choice was silicon.

Another important study was related to the heated elements. A first aspect was considered regarding to the metallic film size, and, more precisely, to its longitudinal length, for a high frequency response. The geometry of the heated film is another essential parameter in this development. 3 different designs are presented and tested. For flow direction detection, a 3 hot-films configuration in one shear-stress sensor is proposed positioned in triangle.

For a good understanding, all the microtechnology technics used for fabricating a new device were detailed. Meanwhile, another important step before the fabrication of the new sensor was the choice of the material for the heated element. A detailed study of the 4 materials usually used for heated elements because of their properties as well as for their availability in small dimensions was performed and presented.

The new multidirectional wall shear stress sensor is based on the heat transfer generated by a hot film with a general top-area of  $1.12 \times 0.1$  mm and a thickness of 110 nm. The film, in platinum, is maintain at a constant temperature, of  $65^{\circ}\text{C}$ , by a feed-back electronic.

The outcome of the new wall shear-stress sensor required 2 generation processing. Several optimizations and development procedures were needed to obtain a robust device. During the first generation fabrication, an optimization required for the holes diameter, corresponding to the future electrical connections, needed in the refilling process was performed. There were tested different diameters for holes, by forming a network of more than 400 holes, with a variable diameter between 250 and  $700\text{ }\mu\text{m}$ .

Moreover, the materials used in the fabrication process are optimized related to the suited application, constituting an determinant element for the measurement quality.

A first testing stage of the sensor was undertaken, using a new constant-temperature anemometer adapted to the films resistances values, for the first generation. The package of probes corresponding to this generation has been designed and realized. The results were poor due to a high thermal conduction in substrate, the detachment of the protecting  $\text{SiO}_2$  layer on the electrical connections and a very short life time in the water. By improving the design, a second generation of sensors was thought. Nevertheless, for eliminating the inconveniences observed on the first generation of sensors, new design was presented.

For optimum performances, 3 heated elements in platinum were deposited on an isolated cavity performed in a silicon substrate. For creating the insulating cavity, another important development was achieved, by silicon pillars performance and refilling, for thermal isolation applications. For this study 2 parameters were optimized: the thickness of the insulating cavity and the silicon pillars forms and dimensions.

To estimate the thickness of the thermal isolation needed for the substrate conduction reduction, there were carried out numerical computations of the device. There were investigated 2 cases: steady case without and with mean flow velocity. The working principle of the sensor is explained in detail, and simulations are carried out using finite element analysis software ANSYS. For the calculations, silicon pillars height was varied for 10, 20 and  $50\text{ }\mu\text{m}$ . For both cases, thermal numerical analysis shows that such thick silicon dioxide layers allow a very good thermal isolation between the heated structures and the surrounding neighbouring structures starting with a minimum distance of  $10\text{ }\mu\text{m}$ , due to the very reduced thermal conductivity of the thick  $\text{SiO}_2$ .

Another parameter, the designs of the silicon pillars used for fabricating very thick silicon dioxide layers for thermal isolation was studied. For finding the optimum dimensions and forms of the Si pillars, there are explored and presented more than 22 designs having different widths and the trench openings, between  $1.8 - 2.2\text{ }\mu\text{m}$ , as well as different forms.

It is used DRIE technique, for creating high-aspect-ratio silicon pillars, which are then oxidized and/or refilled with LPCVD oxide or nitride, to create oxide layers. For the same design of the silicon pillars and trenches, there were compared the method using the

deposition of nitride in parallel with the one of oxide. A major criteria for the trenches filling was the surface planarity at the end of the refill. Filling by oxidation and nitride deposition was the most adequate for the application.

Furthermore, tests on chemical-mechanical polishing were performed until a planar and uniform surface on the top of the sensor is obtained. The process flow included 5 masks fabrication and the sensor manufacturing was validated.

Wires welding were performed, while for the packaging there were developed and manufactured several different plastic and stainless steel components for testing and characterization of the probe in the hydrodynamic water tunnel in the LMH. Moreover, for the calibration procedure there was developed a rotating support adapted to the new probe, for observing the influence of the angle between the longitudinal direction of the films and the direction of the flow, on the measurements, corresponding to each of the hot-films.

Sensors were packaged and calibrated in the same conditions as the commercial one used previously for the wall shear-stress measurements in the Francis turbine's cone.

Although a relative limited tests number were performed due to the limitations in electronic devices, the high potential of the new wall shear-stress has been foreseen. The tests and calibrations performed evidenced that:

- the new wall shear-stress sensor behavior is coherent with the existing theory,
- the time response is satisfactory for the water applications,
- using the adequate electronic device, the sensor allows reproducible wall-shear stress measurements,
- a very good angular sensitivity to the flow direction of the new sensor.

For the thermal response, the wall shear stress sensor shows a maximum time constant response of 0.42 ms when the sensor is operated at constant temperature using a constant temperature anemometer, which by comparison with the theory is about 2 times bigger, due to the simplifying assumptions made for the calculation. Otherwise, a good frequency response for the new wall shear-stress sensor is obtained.

The parameters studied and the results obtained are satisfactory. It was demonstrated the design, fabrication and testing of new directional wall shear stress sensor. The sensor is robust, with a good sensitivity for water measurements. Main improvements which make the current device distinct are its design for an directional response and the insulating cavity for substantially heat losses reducing to the surrounding substrate. Moreover, the use of platinum as the sensor element contributes to a sensor with improved sensitivity and lower noise characteristics.



# Chapter 10

## PERSPECTIVES

As a great effort was devoted to the new device's fabrication, a lack of time was registered for the electronic device improvement or development.

For the turbomachines applications, an improvement constant-temperature anemometer must be conceived, as some requirements are needed:

- an adapted miniature anemometer for the water applications should be developed, by integrating the 3 CTA corresponding to the 3 films on one device;
- a compromise between the components and the size should be made, by simplifying the design, while remaining practicality.

Another perspective and continuation of this thesis can be the integration in the fabrication process and on the same substrate as the heated element, a part or the whole electronic device used together with the sensor. Actually, nowadays microfabrication procedures allow the integration on a large scale of electronically components.

From hydrodynamic point of view, a new support for the new miniature hot-film probe has to be developed to adapt the system to 2D foils and to all parts of a turbine. Moreover, the new probe should be implemented in all interesting parts, from flow point of view and unsteady phenomena, of a turbine, as well as for the boundary layer detection on a foil.



# ANNEXE



# Appendix A

## Measurement systems for wall hot-film probe calibration

### A.1 Measurement system for the velocity acquisition

A detailed description of the whole acquisition system used for the velocity measures, element by element is described. This arrangement is used to measure the mean flow velocity and the friction velocity in the region where it can be applied the wall log-law.

#### A.1.1 The Pitot tube

The Pitot tube, see figure A.1, is a device for measuring the mean flow velocity in the water tunnel. The total pressure is measured on the open end of the inner tube, see figure A.2. The end of the outer concentric tube is sealed and a series of orifices arranged perpendicular to the main flow, on the curved surface, give an accurate indication of the static pressure.

The choice of using it to measure flow velocity, by placing it in the calibration tunnel, was determined by its simplicity, by its low-cost and also by the fact that it is a long-lasting instrument.



Figure A.1: Pitot tube

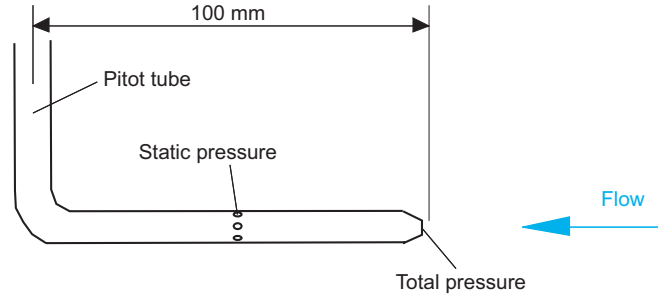


Figure A.2: Pitot tube - scheme

Therefore, there will be measured the pressure difference and, knowing the local value of the water density, which depends on the temperature, from Bernoulli's equation it is found the flow velocity value:

$$c = \sqrt{\frac{2 \cdot \Delta p}{\rho}}, \quad (\text{A.1})$$

where  $\Delta p$  is the difference between the total pressure and the static pressure of the fluid, meaning the dynamic pressure.

Observation The water density  $\rho$  [ $kg/m^3$ ] is relied by the temperature,  $\theta$  [ $^{\circ}C$ ] using an empirical relation, according to CEI code:

$$\rho = 1000.1800014 + 0.0084284 \cdot \theta - 0.0052857 \cdot \theta^2 \quad (\text{A.2})$$

The Pitot tube, see figure A.3, is installed at a distance equal with the half of the height of the test section (i.e. at  $137.5\text{ mm}$  from the interior side of the steel plate) and at an enough distance from the plexiglass wall of the tunnel, i.e.  $50.5\text{ mm}$ . Before any measurements performance, the calibration circuitry has to be drained and the voltage offset evaluated.

### A.1.2 The Preston tube

For the wall shear stress evaluation, corresponding to an operating point in the calibration tunnel, one must evaluate the velocity distribution in the boundary layer developed on the test section upper wall of the tunnel. For measuring the friction velocity, meaning the flow velocity in the boundary layer, it is used a Preston tube, see figure A.4. This tube uses the evolution of the pressure in the boundary layer, base on which one is able to find the friction velocity in the boundary layer.

The Preston tube, presented in the figure A.5, is able to measure pressure until  $0.05\text{ mm}$  from the wall and due to its end which is flattened it allows a spatial resolution of  $0.7\%$  from the measured value.

Taking into account the boundary layer measurements performed earlier, see Ritter and Schmidt [1981], on the test section upper wall, it was chosen as measurement section, the section M, see figure 4.3, for the hot-film probe calibration.

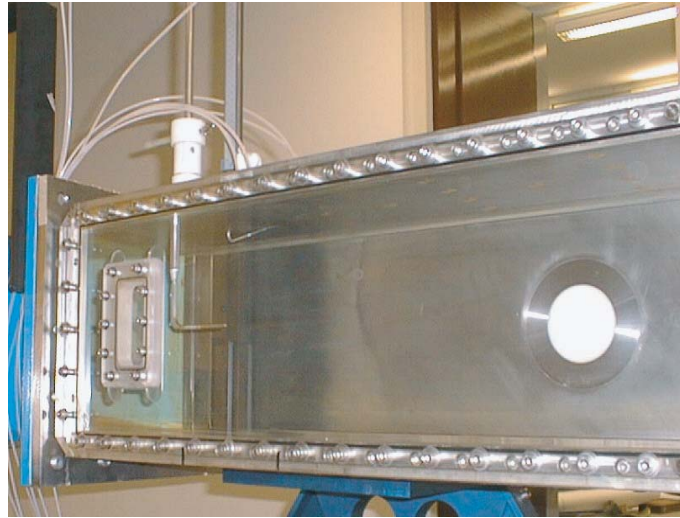
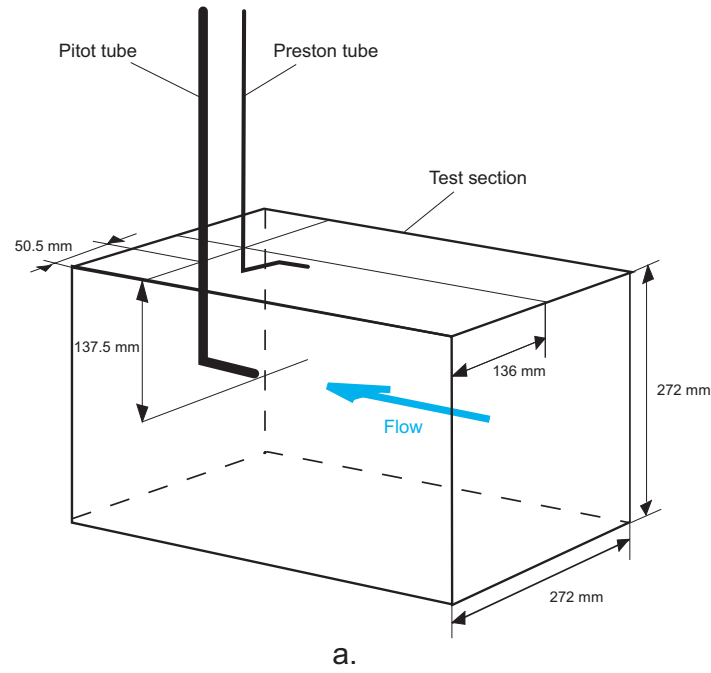


Figure A.3: Preston and Pitot tubes localization in the calibration tunnel  
a. schematic view; b. photo

In the turbulent boundary layer theory, the field of interest for the wall shear-stress estimation is placed at a distance from the wall at about 0.05 to 0.15 from the boundary layer thickness,  $\delta_\infty$ . For the present case, see Ritter and Schmidt [1981], this region has 2 mm height, at about 5 cm behind the measurement section M.

The Preston tube is placed at 136 mm from the plexiglas wall of the tunnel and the minimum distance from the its extremity to the upper wall is 0.05 mm, see figure A.6.



Figure A.4: Preston tube

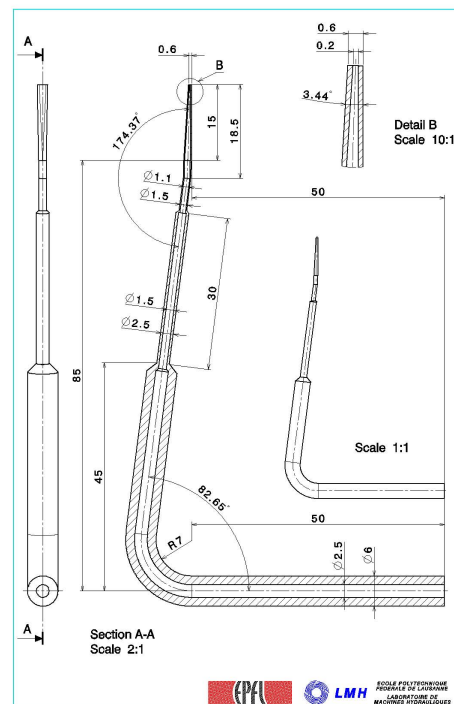


Figure A.5: Preston tube - scheme

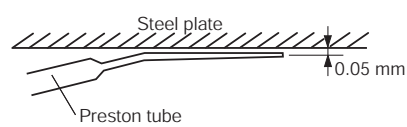


Figure A.6: Preston tube place related to the upper wall



### A.1.3 Instrumentation for flow pressure probe sensors

A specific instrumentation for flow pressure probe sensors together with an amplifier is used for the measurements with different probes and tubes.

The instrumentation for flow pressure probe sensors is made of 8 Keller sensors, which allow both the connection of a 5 holes stationary probe and of a Pitot tube. To acquire the flow velocity there will be used this specific configuration, Pitot and Preston tubes and an amplifier.

The main role of the instrumentation for flow pressure probe sensors, illustrated in figure A.7 is to ensure the drain of both the calibration circuit and the measure circuit used for the pressure sensors to ensure a good accuracy of the measurements.



Figure A.7: Differential pressure instrumentation system and amplifier for pressure probes

Flow in the hydrodynamic water tunnel is stationary with turbulent fluctuations. Pressure sensors can measure unsteady values, but the presence of the long tubes with different rigidities which link the measurement point to the sensor, leads to a deformation of the unsteady information making it irrelevant for the studied phenomenon. In the measurements, for the sensors survey, it is used only the stationary part of the amplifier.

### A.1.4 Oscilloscope

The oscilloscope is used only to monitor the hot film probe signal, as well as to verify the voltage value acquired. It is also used for the calibration of the anemometer.

### A.1.5 SC-2040

An acquisition module CA-1000 from the National Instruments is used for the data acquisition. Actually, the SC-2040, figure A.8 is an instrument which allows the acquisition, simultaneously, of 8 signals. There will be used the channels for acquiring the signals as it follows: 1<sup>st</sup> channel for the signal coming from hot-film probe, 2<sup>nd</sup> for the

signal coming from Pitot tube, 3<sup>rd</sup> for the signal coming from Preston tube and the 4<sup>th</sup> for the signal coming from the temperature sonde. The input range of tension goes from  $-10V$  to  $+10V$ . The maximum sampling frequency is  $100kHz$  divided by the number of acquired channels.

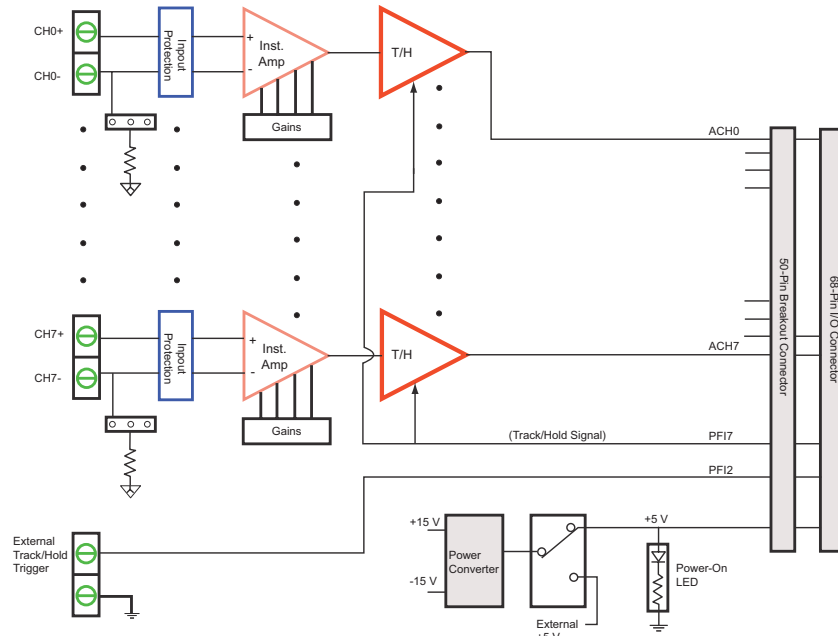


Figure A.8: SC-2040

This eight-channel simultaneously sampling differential amplifier is only for the use of the National Instruments MIO-16E Series DAQ boards. It consists of 8 channels, each one having an amplifier with DIP switch-programmable gains of 1, 10, 100, 200, 300, 500, 600, 700 or 800, and a track-and-hold amplifier (the DAQ board will switch the SC-2040 between hold and track mode).

The first part of this amplifier is the analog circuitry that is made up by 8 channels with DIP-switch-programmable instrumentation amplifiers followed by buffered track-and-hold amplifiers.

For protecting each input against voltages is used the input protection, which is the second block of the SC-2040, a  $1\text{ k}\Omega$  resistor in series with each input line and followed by low-leakage diodes). It is used for protection against voltages up to  $\pm 15V$  powered off and  $\pm 30V$  powered on.

The third part contains the instrumentation amplifiers, which allow the conversion of the differential input signals into single-ended signals and, then, the amplification of these signals.

Then the signals coming out of the instrumentation amplifiers enter the track-and-hold amplifiers that work as buffers in track mode while they freeze the outputs into hold mode.

After that, the signal is passed to the DAQ board through the output connection. In this part, the output of every channel is connected to the 68-pin rear signal connector (which brings and carries out the signal to the DAQ board and provides  $+5\text{ V}$  power) and the 50-pin supplemental I/O connector.

### A.1.6 Workstation

The signals coming from the Pitot and Preston tubes and taken by the SC-2040 are recorded through an AT-MIO-16E Series Data Acquisition Card and they are digitalized and then visualized on the screen of a computer. The software used for the data acquisition is written using LabVIEW 6 under the Windows NT environment.

In the calibration procedure, the flow is steady and only the mean value of the signal is considered. It is taken the average of the signal for the calibration of the sensors. To obtain this average, it is used a sampling frequency of 10kHz and acquired samples of 1'000'000 data and this will lead to an acquisition time of 10 seconds for every measurement.

## A.2 Measurement system for the hot-film probe

The acquisition system and the measurement procedure for the hot-film probes are detailed in this part of the thesis.

Hot-film sensors flush mounted in the water tunnel are used to measure steady wall shear-stress magnitudes in experiments.

The signal coming from the hot-film probe, see figure 4.4, right arm, is transformed into a voltage using a constant temperature anemometer, after what it can be visualized on an oscilloscope; then, using the same system SC-2040 as for the velocity acquisition the signal is acquired and observed on the screen of the PC.

### A.2.1 The hot-film probes

The hot film is a device for providing velocity data. Its microscopic size offers it both high spatial resolution and high frequency response, as well as a high sensitivity.

The use of this type of probe is explained by its facility of mounting in a interface on the wall, confining the flow to be investigated and measured with a sensor flush with wall surface. The small dimensions of the probe permit measurements in locations that are not readily accessible, without any modifications concerning the hydraulic geometry, and without any flow perturbation.

### A.2.2 The Constant-Temperature Anemometer (CTA)

An anemometer is an instrument for measuring fluid velocity using a probe made of thin tungsten/platinum wire or a thin metallic film.

One of the most often used anemometry is the hot-wire anemometry, a thermal anemometer, which is an indirect technique allowing to measure the flow velocity through measurements of heat losses from the hot probe located inside the studied flow.

The heat losses of hot film depend on many factors, like:

- The temperature difference between sensor and fluid;
- The flow velocity by direction, magnitude;
- The geometry of the sensor;
- The properties of sensor material and fluid.

The heat transfer from the hot-film probe, essentially, consists of 2 main components: the heat flux that is convected directly from the heated sensor into the surrounding fluid and the heat flux that is, first, conducted to the film supports and then to the fluid.

A typical set-up for operation of a hot-wire anemometer sensor is the constant-temperature system. This type of system is widely used, because it allows measurement of the very fast velocity fluctuations without the use of complex compensation circuitry. It involves automatic control of the current supplying the sensor so that the temperature of the hot-film probes should be maintain at a constant level, no matter the outer conditions for heat transfer, throughout the measurements. The sensor current is, mainly, a function of the flow velocity, but not only. Its continuous voltage output is suited to digital sampling, and this provides time series that can form the basis for statistical evaluation of the flow structure. The major advantage of the constant-temperature anemometer is the temporal resolution.

For calibration and measurements, it is used a DISA 55M System, produced by DANTEC Measurement Technology. It consists of a Wheatstone bridge and a servo amplifier, systematized in figure A.9. The active bridge arm of the Wheatstone bridge consists of the probe,  $R_{var}$ , and one of the 2 top resistances,  $R_1$ , while the passive arm consists of the other top resistance,  $R_{int}$ , and the comparison resistor,  $R$ , as well as, a few compensating networks for eliminating the influences of the cable parameters,  $R_c$ .

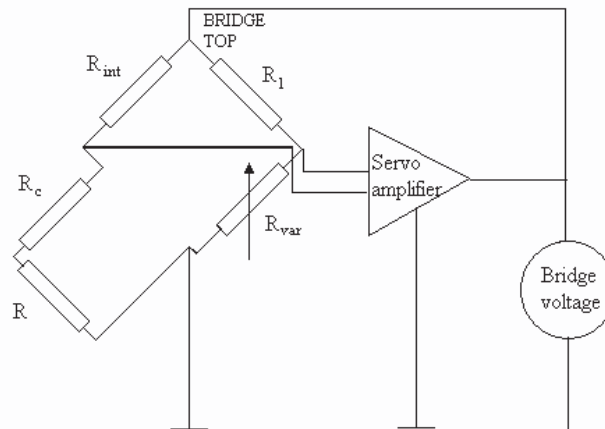


Figure A.9: Constant temperature anemometer

Operating mode When the bridge is in balance, there is no voltage difference between the ends of the horizontal bridge diagonal. As said before, the velocity of the flow is measured by its cooling effect on a heated sensor. A feedback loop keeps the sensor temperature constant under all flow conditions.

Any change in the flow will have an impact over the probe, located in the flow, and this will determine the change of its temperature. The resultant resistance change of the bridge leads to a voltage difference at the horizontal diagonal, which is feed to the inputs of the servo amplifier.

The output voltage of the servo amplifier is applied to the bridge unit in such a way that by increasing or decreasing the bridge operating voltage there will be restored the original temperature. The voltage drop across the sensor thus becomes a direct measure of the power dissipated by the sensor.

To use this constant-temperature anemometer, its calibration is needed, for every specified hot-film probe.

## Appendix B

### Constant Temperature Anemometer calibration

Total resistance measured at the anemometer's output, for the water temperature value  $T = 23.8^\circ C$  is:

$$R_{measured} = 13.47\Omega \quad (B.1)$$

Meanwhile, the specific resistance for a temperature value,  $T$ , is evaluated by relationship B.2, where  $\alpha$  represents the temperature coefficient of the hot-film's resistance.

$$R = R_{20^\circ C}[1 + \alpha_{20^\circ C}(T - 20)] \quad (B.2)$$

For  $T = 23.8^\circ C$ , and taking into account the hot-film probe's properties, the resistance is obtained.

$$R_{23.8^\circ C} = 11.9[1 + 0.0047 \cdot (23.8 - 20)] = 12.113\Omega \quad (B.3)$$

It is known that the total resistance measured with the anemometer contains the specific resistance at the temperature of  $23.8^\circ C$  and the resistance of the additional elements, support, cable, see relationship B.4.

$$R_{total} = R_T + R_{add} \quad (B.4)$$

Thus, for this specific case, the resistance of the additional elements can be evaluated, see relation B.5.

$$R_{add} = R_{measured} - R_T = 1.357\Omega \quad (B.5)$$

To avoid the risk of damaging the hot-film probe it is chosen an overheating rate value of  $H = 1.1$ , usually used for water. The anemometer is adjusted for a water temperature of  $23.8^\circ C$ , for which the difference of the temperature between the water and the film is define by relationship B.6:

$$\Delta T = \frac{H - 1}{\alpha_{23.8^\circ C}}, \quad (B.6)$$

where  $\alpha$ , at a temperature  $T$ , is defined corresponding to B.7.

$$\alpha = \frac{\alpha_{20}}{1 + \alpha_{20}(T - 20)} \quad (\text{B.7})$$

In this way, the  $\alpha_{23.8^\circ C}$  is obtained, see relation B.8.

$$\alpha_{23.8} = \frac{0.0047}{1 + 0.0047(23.8 - 20)} = 0.462\% \quad (\text{B.8})$$

Moreover, the overheating rate can be written as the ratio between the resistance that has to be adjusted at the anemometer and the specific resistance at temperature  $T$ , see relationship B.9.

$$H = \frac{R}{1 + R_{23.8}} \quad (\text{B.9})$$

Thus, the resistance value to add to the total resistance measured at the anemometer is obtained.

$$R - R_{23.8} = HR_{23.8} - R_{23.8} = 0.1R_{23.8} = 1.21\Omega \quad (\text{B.10})$$

The final adjustments for the anemometer are:

- Resistance:  $R = 14.38\Omega$ ;
- HF Filter: 2;
- Gain: 5.

# Appendix C

## Fabrication technologies

In this section, rather than going into any detail of technological matters of the MEMS, it is given some background of the technology that has enabled the development of new microsensor, which is the main subject of this thesis and which has served for the manufacturing the new device.

MEMS have its roots in silicon-based devices from semiconductor fabrication. Silicon planar technology is the principal method used for most silicon integrated circuits and devices manufacturing. Silicon is mainly used due to its well-known electrical and mechanical properties. In addition to silicon, alternative substrates such as metal, glass/quartz, plastic, ceramics are gaining in popularity. The MEMS toolbox consists of a set of processes based on silicon micro-fabrication techniques. The key process steps are lithography, bulk micromachining, thin film deposition, surface micromachining, lift-off and chemical mechanical polishing. The new device is fabricated using combination of these techniques.

### C.1 Photolithography

Many steps in the semiconductor fabrication process should only affect specific areas of the wafer. To define the desired areas on the wafer and to block the remaining areas, *masking layers* are used. Lithography is a method by which geometrical pattern transfer can be achieved from a master pattern to the substrate. Lithography, in some form, is typically the first step in most processes and, as a result, is probably the most important, influencing the accuracy of the final product. Photolithography is the most common form of lithography technology used; moreover for keeping up with the demanding resolution needs of the semiconductor industry, technologies such as X-ray lithography, electron beam lithography, and ion beam lithography have been developed.

The basic steps for photolithography using positive and negative resists are shown in figure C.1.

Photolithography is typically the transfer of a specific pattern to a photosensitive material, on a surface of the wafer, by selective exposure to light. Photolithography has become the dominant technique in microelectronic industry where very precise definition of fine line patterns is a major requirement. This technology is useful because it can transfer the pattern to the wafer surface very quickly.

The first step of the photolithography is the coating of the wafer's surface with a photoresist layer. The mask is placed over the wafer's surface and exposed to the UV light.

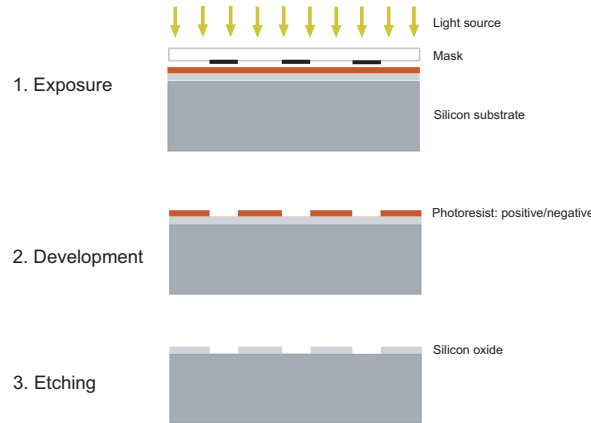


Figure C.1: Photolithography process

Afterwards, the photoresist is developed. Finally, etching techniques will uncover the pattern desired to be transferred. Successive process steps will affect only the uncovered areas where there is no photoresist.

Photoresist is a light-sensitive material which can be processed into a specific pattern after being exposed to light energy in the shape of the desired pattern. There are 3 major exposure methods related to the way the photoresist is illuminated, see figure C.2. One way is to have a mask which is more or less pressed against the photoresist-layer, so called **contact**; another set-up supposes the mask close to the substrate, so called **proximity**, while in the third method the mask is placed in a projection system to have a projection of the mask on the photoresist-layer, so called **projection**.

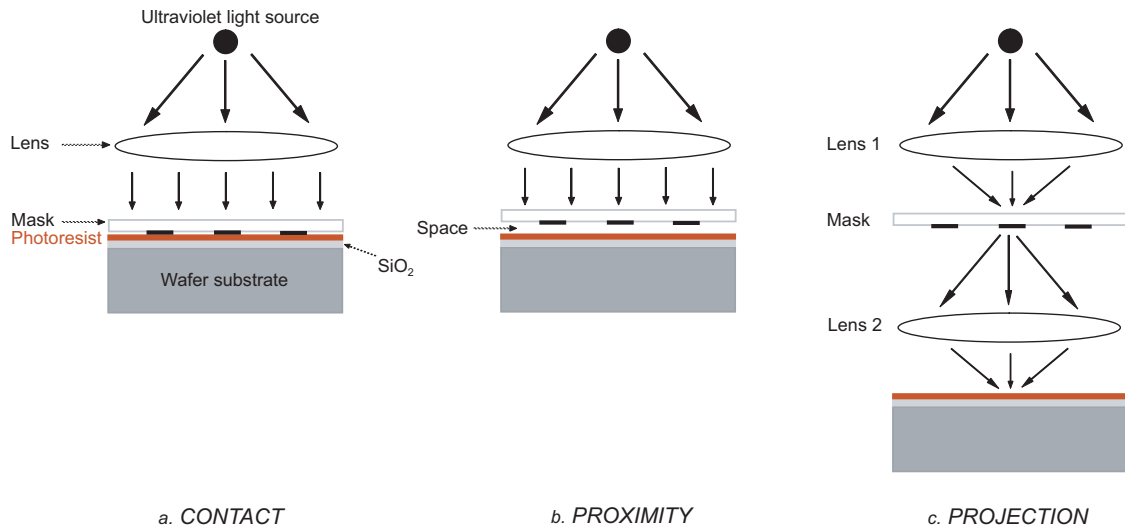


Figure C.2: Writing techniques in photolithography

The photolithography technique allows the transfer of different shapes created using CAD software onto the surface of the wafer with sub-micron resolution.

For the new development, this technique was used several times, for films, electrical tracks and backside connections design on wafers.



## C.2 Film deposition technique

The addition of material on the top of the wafer requires a process step, generally, referred to as deposition. Several different techniques are employed for deposition, the process being, generally, defined as a uniform sprinkling of material on the surface of the wafer, either over the entire surface or throughout a masking layer for deposition, on selective areas.

Different materials can be deposited, mainly, insulators, conductors and semiconductor materials. Main deposition materials are explored and presented further. Native oxides are only available when native material is still on the surface. Thus, once a wafer has been covered with other materials, like metal, a native oxide can no longer be grown. Besides, after some materials deposition on the wafer, the wafer can no longer be subjected to high temperatures, which are required to grow native oxides but can melt other materials used in semiconductor fabrication. Thermal oxides are also limited to thin layers,  $\delta < 1\mu m$ . For these 3 reasons, it has to be used deposited dielectrics, to cover the wafer and form insulation layers. Deposited dielectrics offer a wide variety of insulating materials including  $SiO_2$  and  $SiN$ ; they can be deposited on top of any material including metal, and they can be deposited in thick layers  $\delta \sim 1 - 2\mu m$ , to reduce the capacitance between interconnect layers.

Polysilicon is a granular silicon material and is not single-crystal like the substrate wafer. It is generally doped to act as a conductor and is used as an interconnect layer or as a high-resistance layer to form integrated resistors. Although metal is a better conductor, lower resistance, the main advantages of polysilicon over the others conductors are: it can withstand subsequent high temperature steps, a native thermal oxide can be grown on top of polysilicon, and it has similar material properties to Si and  $SiO_2$ .

Many types of basic metal, like aluminum, gold, copper, nickel, titanium, metal alloys, and other metal compounds, are used to form interconnection layers in semiconductor fabrication. Metals are generally deposited by evaporation or sputtering to cover the entire wafer before being patterned, to form all interconnects in one process step. Although most metals have a low melting temperature and must therefore be deposited after all high temperature steps, like diffusion, oxidation, they are very conductive and provide low resistance interconnections even in very thin layers,  $\delta < 1\mu m$ . Depositing metal interconnect layers are typically the last steps performed in the semiconductor fabrication process. The individual layers are insulated from each other by deposited dielectric layers with vertical openings that connect layers at the required points.

Deposition technologies can be divided into two common groups: Chemical Vapor Deposition, CVD, which vaporizes chemically the material to be deposited, illustrated in figure C.3, and Physical Vapor Deposition, PVD, processes, often called thin film processes, which constitutes atomistic deposition processes where the material is vaporized from a solid or liquid source, under the form of atoms or molecules. The vaporized material then floats down, transported in a low pressure or plasma environment, to the wafer surface where it solidifies, forming thin layers of films.

CVD systems are characterized by good uniformity and high throughput, requiring, meanwhile, a frequent cleaning.

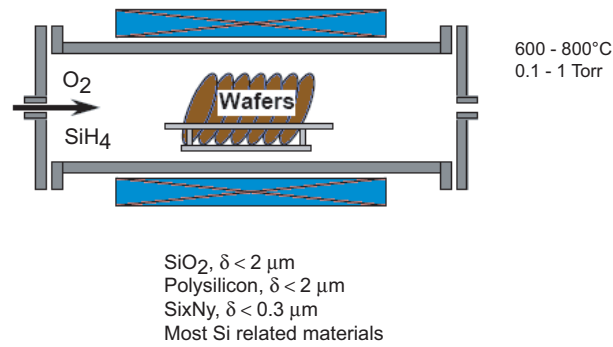


Figure C.3: Chemical Vapor Deposition technology

PVD can be used to deposit films of elements, alloys as well as compounds, using reactive deposition processes. Its most eloquent advantage is the low deposition temperature. The main categories of PVD processing are arc vacuum evaporation, sputter deposition and ion plating. Each process has its own advantages, disadvantages and applications.

In the *evaporation deposition technique*, vapors are produced from a source by increasing its temperature by different methods; the material vapors condense on the desired substrate. It has the advantage, related to the sputtering deposition, that it is a limited contamination due to the vacuum level obtained, about  $5 \cdot 10^{-7}$  mbar. The alloy deposition by evaporation is a complex processus and the deposited layer composition is difficult to control.

There are 2 different techniques for the evaporation deposition, see figure C.4:

- resistance heated evaporation, Joule effect;
- e-beam evaporation.

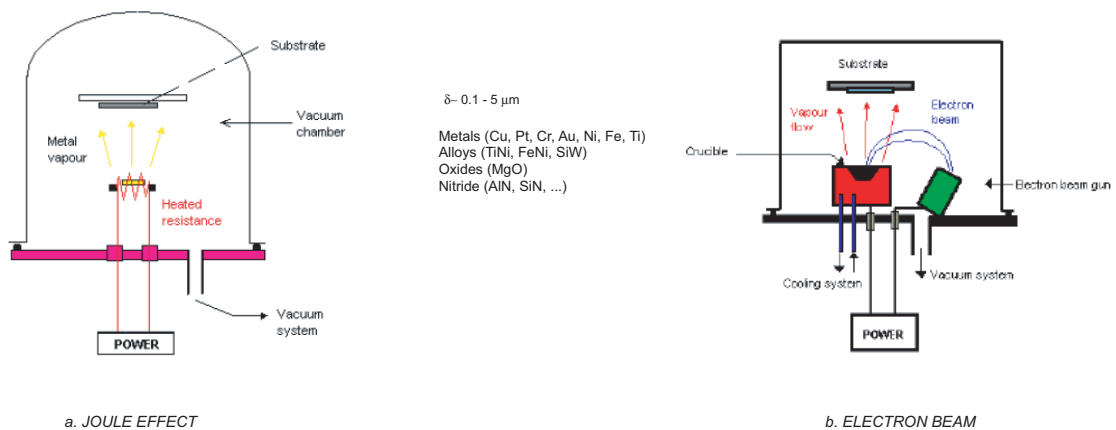


Figure C.4: Deposition by evaporation technology

The deposition by Joule effect evaporation is the most simple. This technique consists in depositing initially grains, shots or small ends of wire of the material to be evaporated

in a nacelle from tungsten, tantalum, molybdenum or carbon. The nacelle is then heated by Joule effect. The grains melt and the metal evaporates.

The disadvantages related to this technique are:

- the impossibility of evaporating metals at high melting point,
- the limited thickness of the layer deposited, due to the small quantity of metal which can be deposited in the nacelle;
- the potential contamination of the nacelle in itself.

The deposit technique by evaporation using electron beam consists in initially depositing a pastille, grains, shots or small ends of wire in a crucible. An electron beam with high energy is directed on the material. The electrons' kinetic energy is converted into heat at the impact point. The electron beam can melt and evaporate any type of material when the calorific contribution is higher than the losses. The beam is concentrated on the material surface, so that material in fusion can be placed in a cooled container. Actually, only the material surface is in fusion. The material in contact with the walls of the crucible is solid. This eliminates the problems of contamination by the crucible and makes it possible to deposit layers of high purity, constituting the main advantage of this technique.

The main disadvantages related to this technique are:

- the emission of x-rays, which can damage the substrates surfaces,
- the ejection of droplets out of the crucible which can deposit on the substrates when using too high power.

**Sputter deposition technique** means the deposition of particles vaporized from a surface, called "target", following a collision with particles with high energy, see figure C.5. It is a non thermal vaporization process, where surface atoms are physically ejected from a target, from an atomic sized energetic bombarding particle which is usually a gaseous ion accelerated from plasma. The sputtering target has a long lived vaporization source that can be mounted to vaporize in any direction. This process is a line of such processes, the film thickness drops down when surfaces do not face targets directly. The material deposited can be pure metals - Al, Ti, Pt -, an alloy or a dielectric material -  $SiO_2$ , Si. The deposit of nitride or oxide coatings can be carried out with a metal target in the presence of oxygen. These deposits are known as reactive sputtering.

Sputter deposition is widely used to deposit thin films on semiconductor materials, coatings on architectural glass, reflective/antireflective optical coatings, magnetic films, dry film lubricants and decorative coatings.

The advantages of the sputtering deposition related to the evaporation are:

- good uniformity in thickness of the material deposited on the wafers,
- better control of alloys composition, than by the evaporation,
- substrates surface can be cleaned by vacuum before deposition.

The main disadvantages related to this type of deposition are:

- some materials, organic materials, do not support the ionic bombardment;
- low deposition rate for certain materials like  $SiO_2$ , Si;
- the vacuum level is lower in the equipment for sputtering deposition, which increases the risk of impurities insertion in the layers deposited.

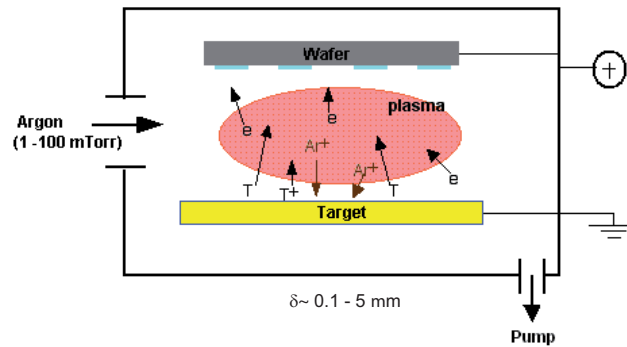


Figure C.5: Sputter deposition technique

For the new sensor development and manufacturing, by evaporation there were deposited the electrical tracks on the structure, while by sputtering there were deposited the heated elements structures and the protecting  $\text{SiO}_2$  layer on the sensor surface.

### C.3 Etching

Silicon etching is an essential process step for the fabrication of micro-electro-mechanical systems. To form functional structures on a substrate, the etching process is needed for thin films previously deposited on/in substrate itself. Bulk micromachining is the technology by which structures are made in the silicon substrate and not on top of it, by selectively removing material. The purpose of this technology is to make structures that are released or undercut. Etching processes are needed to pattern deposited layers and form contact opening in dielectric layers. Etch rate is defined as the vertical etch depth divided by the etching time.

Generally, the substrate is silicon, which can be machined using a diversity of physical and chemical etching techniques. Chemical etching processes will attack some materials more quickly than others, while mechanical etching will etch all material equally. Both processes require a masking layer, generally either photoresist or oxide, to block regions where etching is not desired. Some of these techniques allow etching through the substrate, to use the entire substrate thickness. In addition, the crystalline nature of silicon can be particularly advantageous when using certain wet etches. Etching methods can also be distinguished on the etch-profiles they produce:

- *isotropic*: etch-speed equal in all directions leading to rounded structures, see figure C.6,
- *anisotropic*: etching speed highly dependent on the crystallographic directions leading to sharp edges and corners, see figure C.7,
- *directional*, mostly due to geometrical effects of dry etching.

Supplementary chemical species may be added to assist in etching or passivation. Etching mechanisms can vary from physical removal due to bombardment to chemical reactions followed by removal of volatile reaction products. By combination of both

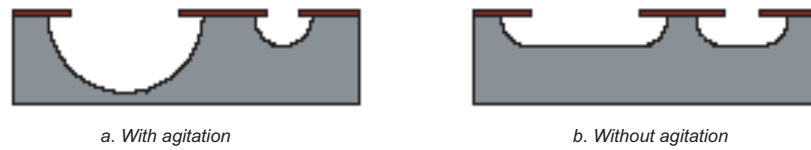


Figure C.6: Cross-section showing isotropic etching

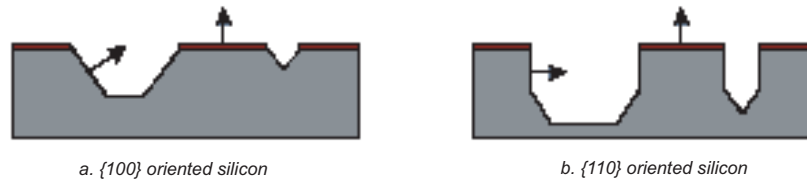


Figure C.7: Cross-section showing anisotropic etching for 2 wafer orientations

effects, tailoring their mutual influence, it is possible to obtain etching processes that vary between isotropic and almost perfectly directional.

*Chemical Etching.* Most materials can be selectively removed by chemical processes. This allows the etching process to stop once the desired material has been removed rather than continuing all the way through the wafer. The primary disadvantage of chemical etching is that it is isotropic, it etches in all directions -not just vertically, and will undercut the masking layer which is undesirable in many cases.

*Chemical-Mechanical Etching.* Reactive ion etching (RIE) is the main technique of chemical-mechanical etching, in which ions in plasma bombard the surface and etch away material. The plasma can be chosen to selectively etch one material more than another. RIE is a very common process in modern semiconductor fabrication and is typically used for contact openings through dielectrics.

*Mechanical Etching.* Purely mechanical etching processes such as Ion Milling, are not material selective; they bombard the wafer surface and remove any material they strike. However, a thick high-strength mask material can be used to block the etching process from the surface, so that only specific areas on the wafer are etched. Because there is no chemical undercutting, mechanical etching creates a straight vertical etching profile.

Generally, another classification of etching processes divides them in wet and dry etching. **Wet etching**, see figure C.8, involves the exposure of the wafer to chemical solvents, to lead to the conversion of the unprotected material into soluble compounds, which can be dissolved by chemical etchants. Traditional wet etch recipes include a hydrofluoric, nitric, and acetic acid mix, KOH, EDP, ethylenediamine-pyrocatechol-water, and TMAH, tetramethylammoniumhydroxide; they are mostly used for carrying out channels or creating membranes in silicon. Isotropic wet-chemical etching is obtained using solutions containing, for example, fluoride and can be customized using doping or voltage or light assisted etching.

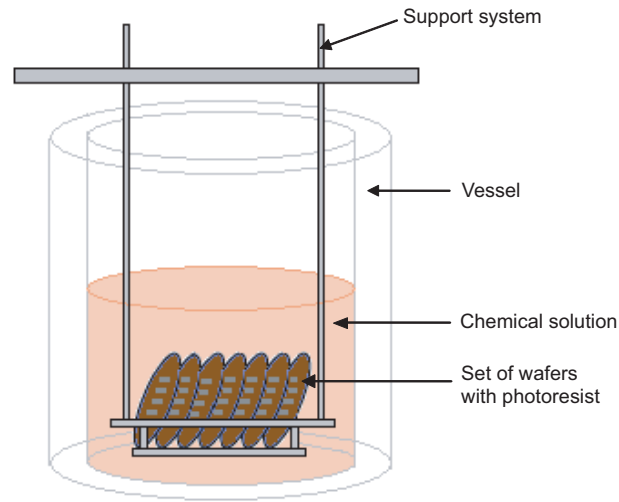


Figure C.8: Wet etching process

In *dry etching*, see figure C.9, the material is sputtered or dissolved using reactive ions or a vapor phase etchant. Dry etching has a great diversity of implementations which share some similarities:

- they take place in a vessel which can be brought at a certain vacuum, about  $10^{-5}$ – $0.5$  Torr,
- they use accelerated, so called reactive particles, meaning ions, atoms for etching.

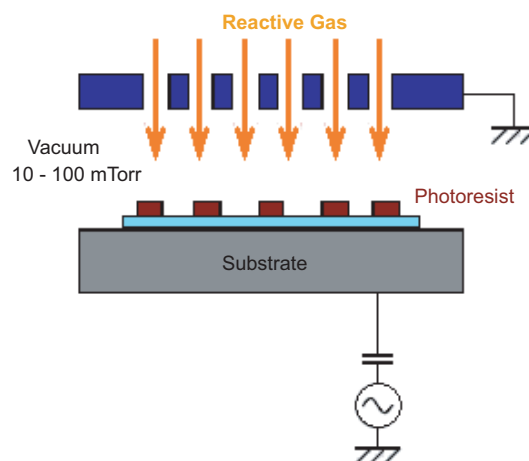


Figure C.9: Dry etching technique

Dry etching techniques such as plasma and gas phase etching are extensively used, while newer techniques, such as deep reactive ion etching (DRIE), allows the fabrication of complex in-plane geometry and high aspect ratios structures. Dry etching allows etching almost straight down without undercutting, providing much higher resolution.

Even so, bulk micromachining is not suitable to create all desired geometries. Devices requiring complex, multi-layer or multi-depth structures are frequently difficult or not possible by bulk micromachining alone. The etching methods mentioned above share the fact that they generally result in moderate etching speeds.

In the new sensor the etching technique was used for creating the backside electrical connections, as well as for the creation of the insulating methods used for heat transfer reduction.

## C.4 Surface micromachining

Surface micromachining is the technique used to create complex planar structures. Surface micromachining is the process of creating movable structures by placing the structures on initially rigid platforms, then removing the platforms, usually by etching the material away.

The fabrication process, illustrated in figure C.10, starts with a silicon wafer or other substrate and grows layers on top. These layers are selectively etched by photolithography and a wet or a dry etch. There can be involved as many layers as needed with different mask on each layer.

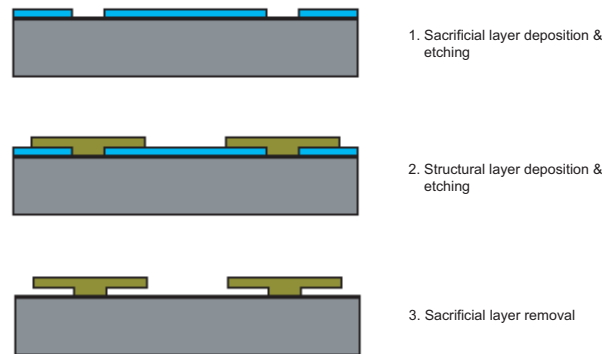


Figure C.10: Surface micromachining process

Unlike bulk micromachining, the substrate may or may not be structurally significant in the final device and is often used only as a mechanical support for building structural layers. As the structures are built on top of the substrate and not inside it, the substrate's properties are not important, and the expensive silicon wafers can be replaced by cheaper substrates, such as glass or plastic.

Any material, which can be deposited, can be used as a structural layer. A variety of sacrificial layers is available, like phosphosilicate glass, polysilicon, photoresist, polyimide, and metals.

Using surface micromachining, it is possible to build freestanding, released, and interlocking structures with any geometry; some examples include electrostatic micromotors, out-of-plane hinged structures, and springs. However, from stress and other mechanical considerations, only thin layers,  $\delta \leq 1\mu m$ , of materials can be deposited. Thus, the overall thickness of devices created by surface micromachining is relatively thin.

Summarizing, the surface micromachining properties are:

1. Single-sided wafer processing;
2. Small device size;
3. Compatibility with CMOS processing.

## C.5 Chemical Mechanical Polishing

Chemical-mechanical polishing, commonly abbreviated CMP, is the technique used in semiconductor fabrication for planarizing the top surface of an in-process semiconductor wafer or other substrate, see figure C.11.

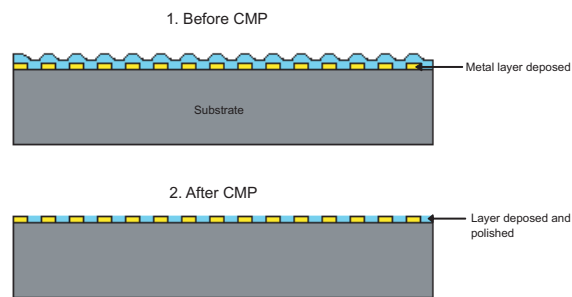


Figure C.11: Chemical mechanical polishing process

The CMP uses an abrasive and corrosive chemical slurry together with a polishing pad and retaining ring, typically with a greater diameter than the wafer, see figure C.12. The pad and wafer are pressed together by a dynamic polishing head and held in place by a plastic retaining ring. The dynamic polishing head is rotated at different rates. A slightly slurry containing nanometer-sized silica particles is added. The combined action of wear and etching yields the smooth surfaces. The planarization, for example, may be needed to bring the entire surface within the depth of field of a photolithography system, or to selectively remove material based on its position.

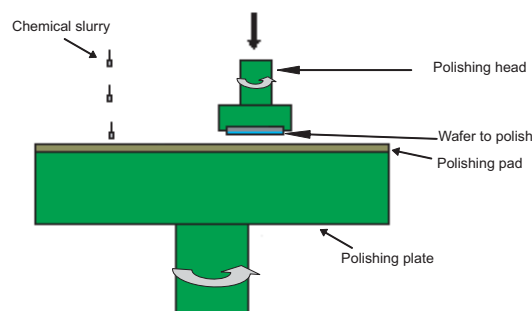


Figure C.12: Chemical mechanical polishing machine



The process of material removal is an iterative and manual. The chemicals in the slurry also react with and/or weaken the material to be removed. The abrasive accelerates this weakening process and the polishing pad helps to wipe the reacted materials from the surface.

Chemical-mechanical polishing can also be applied to materials like silicon nitride, silicon oxide and polysilicon.

## C.6 Lift-off

Some materials, like gold, platinum cannot be etched by acids, but using a technique called "lift off".

Lift off is a simple, easy technique used to pattern noble metal films. Actually, it is a combination of photolithography and vacuum deposition. A film, usually metallic, is blanket-deposited all over the substrate, covering the photoresist and areas, where the photoresist has been cleared.

The main steps of a lift-off process are presented in figure C.13. During the lift-off, the photoresist under the film is removed with solvent, usually acetone, taking the film with it, and leaving only the film which was deposited directly on the substrate.

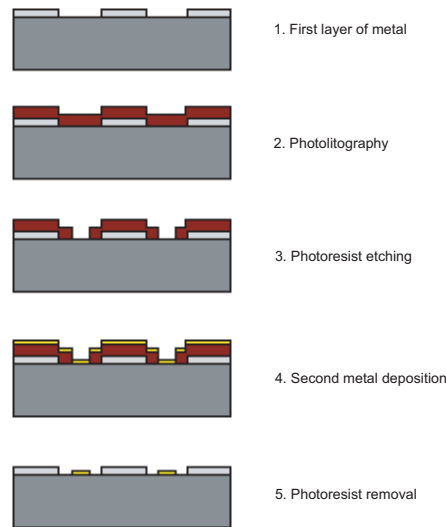


Figure C.13: Lift-off technique

There are three basic ways in which lift-off can be performed:

1. Standard photoresist processing;
2. LOL 2000 processing;
3. Surface-modified photoresist processing.

The method chosen depends on the process requirements. Patterns can be defined with high fidelity and for very fine geometries, depending on the type of lift-off process used.

When using noble metals, it is advantageous to deposit, in the first place, a thin layer of a more active metal, to ensure good adhesion of the noble metal.

## C.7 Electroplating

Electroplating is an electrochemical process by which metal is deposited on a substrate by passing an electric current through an electrolytic bath.

Usually there are: *an anode*, positively charged electrode, the source of the material to be deposited; *electrochemistry* representing the medium through which metal ions are exchanged and transferred to the substrate to be coated; and *a cathode* which is the substrate, the negatively charged electrode, to be coated. Plating is done in a bath which is usually a non-metallic tank. The tank is filled with electrolyte which has the metal, to be plated, in ionic form, see figure C.14.

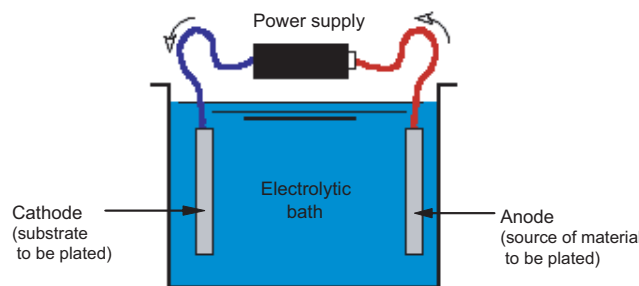


Figure C.14: Schematic view of the electroplating process

Actually, it means the deposition of a metallic coating on an object by putting a negative charge onto the object and immersing it into a solution containing a salt of the metal to be deposited. The metallic ions of the salt are charged with positive charge and attracted to the part. When they reach it, the negatively charged part provides the electrons to reduce the positively charged ions to metallic form.

The anode is connected to the positive terminal of the power supply. The anode is usually the metal to be plated, supposing that the metal will corrode in the electrolyte. The cathode is the substrate to be plated. This is connected to the negative terminal of the power supply. The power supply is regulated to minimize ripples as well to deliver a steady predictable current. For materials such as gold, the anode is not sacrificial, but it is made out of material that does not dissolve in the electrolyte, such as titanium.

Metal layers with thickness greater than  $1\mu\text{m}$  can be achieved. The apparatus required is relatively simple, but control is difficult and imprecise. The quality of the surface is usually poor. Electroplating can be combined with the photolithography process. If a thick layer or deep feature is required, the resist layer must be equally thick.

The electroplating technique served for copper deposition used in electrical connections.

## C.8 Wafer dicing

In the manufacturing of micro devices, die cutting or dicing is the process of reducing a wafer containing multiple identical integrated circuits to dice each containing one of those circuits.

During this process, a wafer with up to thousands of circuits is cut into individual pieces, called a die. In between the functional parts of the circuits, a thin non-functional spacing is foreseen where a saw can safely cut the wafer without damaging the circuit. This spacing is called the scribe. A very thin and accurate saw is therefore needed to cut the wafer into pieces. The most common dicing method - abrasive sawing - has limitations when confronted with the new requirements of the semiconductor industry. The increasing use of brittle materials and the reduction of wafer thickness are difficult trends for diamond saws, generating chipping and cracking in thin compound wafers.

Material processing with lasers takes advantage of all the characteristics of laser light. The high energy density and directionality achieved with lasers allows strong localized heat- or photo-treatment of materials with spatial resolution below one micrometer. The pulsed and monochromatic light allows the control of depth of heat treatment or selective excitation. The laser beam can be moved to process large areas, being a sterile tool and no subject to wear and tear.

Laser processing is applied to manufacture laterally structured electrodes for solar cells which improve the built-in electric field of thin film solar cells and give rise to light trapping. An other application is the photo chemical processing of DFB gratings for InP and GaN laser. Laser beam induced lift-off of GaN from sapphire substrates is applied to generate free standing thin film GaN substrates, LEDs or other electronic devices .

In conventional laser cutting, the laser is focused on the work piece that has to be cut. The beam has a conical shape before and after the focal point. Therefore, the working distance is short.

For drilling, cutting and welding micromechanical components for modern sensors applications, in industrial field, pulsed Nd-YAG lasers with moderate power are used, see figure C.15.

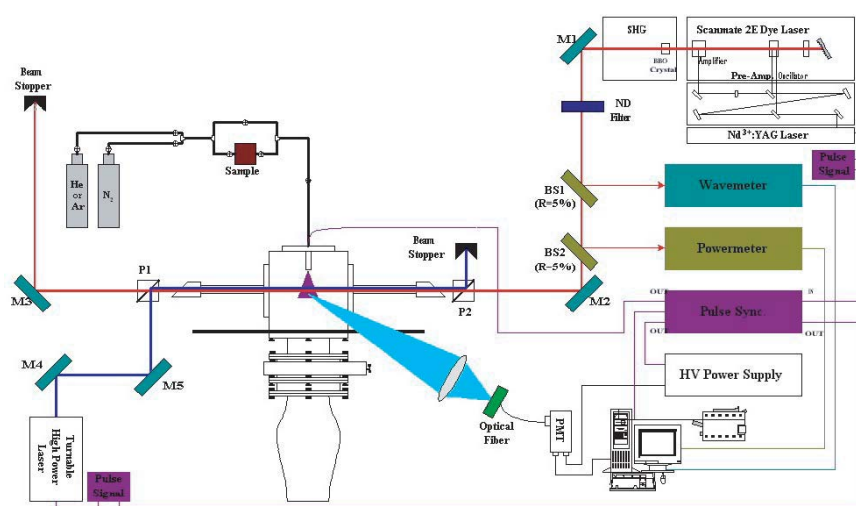


Figure C.15: Schematic view of laser induced fluorescence with molecular beams

With an advanced Nd-YAG zig-zag-slab laser, pulse energy up to 300mJ within time duration of  $200\mu s$  can be obtained. The laser beam intensity profile is Gaussian, for achieving a best focusing and the least critical focus depth. The resulting laser beam has

a very high brightness. The mean output power of this laser allows cutting at speeds as high as 1mm/s. In material processing with longer pulses, the laser-material interaction is different and, in particular, higher material ablation rates are performed. Moreover, the green light material processing allows a better focus and a higher absorption for most materials.

Meanwhile, laser micro-cutting applications performed with a high power zig-zag slab laser have a wide potential, mainly for research and prototyping applications. Most materials, like metallic, ceramic, glass with thickness up to 1mm can be processed with a minimum kerf width, depending on sheet thickness and material properties.

The zigzag slab lasers are mainly used for non-linear processes, because of its high beam quality and inherently linear polarization of the beam. The maximum optical power and therefore the productivity of the green laser material processing is basically limited by the damage threshold in the non-linear materials.

# Bibliography

- \*\*\*\* (1993). Model acceptance tests to determinate the hydraulic performance of hydraulic turbines, storage pumps and pump-turbines. International Standard I.C.E.
- Alfredsson, P., Johansson, A., Haritonidis, J., and Eckelmann, H. (1987). The fluctuation wall-shear stress and the velocity field in the viscous sublayer. *Phys. Fluids*, 31:1026–1033.
- Arpe, J. (2003). *Experimental Investigation of Unsteady Pressure and Velocity Field in a draft tube of Francis Turbine*. PhD thesis, Ecole Polytechnique Federale de Lausanne, Lausanne, Switzerland.
- Barenblatt, G., Chorin, A., Hald, O., and Prostokishin, V. (1997a). Structure of the zero-pressure-gradient turbulent boundary layer. In *Proc. Natl. Acad. Sci. USA, Applied Mathematics*, volume 94, pages 7817–7819.
- Barenblatt, G., Chorin, A., and Prostokishin, V. (1997b). Scaling laws for fully developed turbulent flow in pipes. In *Appl. Mech. Rev.*, pages 413–429.
- Barenblatt, G., Chorin, A., and Prostokishin, V. (2002). A model of a turbulent boundary layer with a nonzero pressure gradient. In *Proc. Natl. Acad. Sci. USA Applied Mathematics*, volume 99, pages 5772–5776.
- Bechert, D. (1995). On the calibration of preston tubes. *AIAA J.*, 34:205–206.
- Bechert, D., Hoppe, G., and Reif, W.-E. (1985). On the drag reduction of the shark skin. *AIAA Paper 85-0546*.
- Bechert, D., Hoppe, G., van der Hoeven, J., and Makris, R. (1992). The berlin oil channel for drag reduction research. *Exp. Fluids*, 12:251–260.
- Béguin, C., Hibert, C., Baer, W., and Berca, E. (2002). Réalisation de contacts électriques traversant un substrat silicium. Technical report, LMH-EPFL, Lausanne, Switzerland.
- Bellhouse, B. and Schultz, D. (1967). The determination of fluctuating velocity in air with heated thin-film gauges. *J. Fluid Mech.*, 29:289–295.
- Berca, E., Avellan, F., Cannehan, F., and Langlet, P. (2004a). Silicon pillars development for thermal isolation applications. In *The 4th International Workshop on Microfactories, IWMMF'04*, Shanghai, China.
- Berca, E. and Ciocan, G. (2002). Delivery 2-3.5. Technical report, Laboratory for Hydraulic Machines, Lausanne, Switzerland.

- Berca, E., Ciocan, G., and Avellan, F. (2004b). Wall friction and boundary layer development in the cone of a francis turbine scale model. In *22nd IAHR Symposium on Hydraulic Machinery and Systems*.
- Boillat, M., van der Wiel, A., Hoogerwerf, A., and de Rooij, N. (1995). A differential pressure liquid flow sensor for flow regulation and dosing systems. In *Proc., IEEE Micro Electro Mechanical Systems*, pages 350–352.
- Bradbury, L. and Castro, I. (1971). A pulsed-wire technique for velocity measurements in highly turbulent flow. *J. Fluid Mech.*, 22:679–687.
- Bradshaw, P. and Gregory, N. (1959). The determination of local turbulent skin friction from observations in the viscous sub-layer,. Technical report, Reports and Memoranda 3202, ARC, London.
- Chow, J., Zilliac, G., and Bradshaw, P. (1997). Mean and turbulence measurements in the near field of a wingtip vortex. *AIAA J.*
- Ciocan, G. (1998). *Contribution à l'analyse des écoulements 3D complexes en turbomachines*. PhD thesis, l'Institut National Polytechnique de Grenoble, France, Grenoble, France.
- Ciocan, G., Avellan, F., and Berca, E. (2002). *Wall friction measurements: application in a Francis turbine cone*. In *ASME - European Fluids Engineering Summer Conference*, number FEDSM2002-31333.
- Ciocan, G., Avellan, F., and Kueny, J. (2000). Optical measurement techniques for experimental analysis of hydraulic turbines rotor-stator interaction. In *ASME Fluids Engineering Conference*, number FEDSM2000-11056.
- Ciocan, G., Mauri, S., Arpe, J., and Kueny, J. (2001). The experimental and numerical study of the non stationary velocity field at the exit of a turbine runner. In *La Houille Blanche*, volume 56, pages 46–59.
- Clauser, F. (1954). Turbulent boundary layers in adverse pressure gradients. In *Aero. Sci.*, volume 21, pages 91–108.
- Coles, D. (1956). The law of the wake in the turbulent boundary layer. In *Journal of Fluid Mechanics*, volume 1, pages 91–108.
- Cousteix, J. (1989). *Aérodynamique :turbulence et couche limite*. Cepadues Editions, Toulouse, France.
- de Bree, H., Jansen, H., Lammerink, T., Krijnen, G., and Elwenspoek, M. (1999). Bi directional fast flow sensor with a large dynamic range. *J. Micromech. Microeng.*, 9(2):186–189.
- Dengel, P. and Fernholz, H. (1989). Generation of and measurements in a turbulent boundary layer with zero skin friction. In ed H. H. Fernholz and Fiedler, H. E., editors, *Advances in Turbulence*, volume 2, pages 432–437. Berlin: Springer.

- Dengel, P. and Fernholz, H. (1990). An experimental investigation of an incompressible turbulent boundary layer in the vicinity of separation. *J. Fluid Mech*, 212:615–636.
- Dengel, P., Fernholz, H., and Hess, M. (1987). Skin-friction measurements in two- and three-dimensional highly turbulent flows with separation. In ed G Compte-Bellot and Mathieu, J., editors, *Advances in Turbulence*, volume 40, pages 470–479. Berlin: Springer.
- Dickinson, J. (1965). *The determination of turbulent skin friction*. PhD thesis, Laval University Québec.
- Ebefors, T., Kalvesten, E., and Stemme, G. (1998). Three dimensional silicon triple-hot-wire anemometer based on polyimide joints. In *Proc. Eleventh Annual Int. Workshop on Micro Electro Mechanical Systems. An Investigation of Micro Structures, Sensors, Actuators, Machines and Systems*, pages 93–98.
- Enoksson, P., Stemme, G., and Stemme, E. (1996). A coriolis mass flow sensor structure in silicon. In *Proc., 9th Annual Int. Workshop on Micro Electro Mechanical Systems. An Investigation of Micro Structures, Sensors, Actuators, Machines and Systems*, pages 156–161.
- Fernholz, H. and Finley, P. (1977). An initial compilation of compressible turbulent boundary layer data. *Advisory Group Aerospace Research and Development*, AGARDograph 223.
- Fernholz, H. and Finley, P. (1981). A further compilation of compressible turbulent boundary layer data with a survey of turbulence data. *Advisory Group Aerospace Research and Development*, AGARDograph 263.
- Fernholz, H., Janke, G., Schober, M., Wagner, P., and Warnack, D. (1996). New developments and applications of skin-friction measuring techniques. *Meas. Sci. Technol.*, 7:1396–1409.
- Finley, P. and Gaudet, L. (1995). The preston tube in adiabatic compressible flow. *Exp. Fluids*, 19:133–141.
- Gasser, D. (1992). Experimentelle untersuchung stark verzogelter turbulenter grenzschichten. Master’s thesis, ETH Zurich.
- Gasser, D., Thomann, H., and Dengel, P. (1993). Comparison of four methods to measure the wall shear stress in a turbulent boundary layer with separation. *Exp. Fluids*, 15:27–32.
- Ginder, R. and Bradbury, L. (1973). Preliminary investigation for skin friction measurements in highly turbulent flows,. Technical report, ARC Report.
- Goldberg, H., Breuer, K., and Schmidt, M. (1994). A silicon wafer-bonding technology for microfabricated shear-stress sensors with backside contacts. In *Solid-state Sensor and Actuator Workshop*, Technical Digest, pages 111–115.

- Goldstein, R. et al. (1983). *Fluid Mechanics Measurements*. Hemisphere Publishing Corporation, Berlin, 2nd edition.
- Hakkinen, R. (1991). Survey of skin friction measurements techniques. *AIAA Minisymposium*.
- Hanratty, T. and Campbell, J. (1996). Measurement of wall shear stress. In Goldstein, R. J., editor, *Fluid Mechanics Measurements*, volume Second edn, pages 575–648.
- Haritonidis, J. (1989). The measurements of wall-shear stress. *Advances in Fluid Mechanics Measurements*, pages 229–261.
- Head, M. and Rechenberg, I. (1962). The preston tube as a means of measuring skin friction. *J. Fluid Mech.*, 14:1–17.
- Head, M. and Vasanta Ram, V. (1971). Simplified presentation of the preston tube calibration. *Aeronautical Quarterly*, XXII:295–300.
- Hirt, F. and Thomann, H. (1986). Measurements of wall shear stress in turbulent boundary layers subject to strong pressure gradients. *J. Fluid Mech.*, 171:547–562.
- Ho, C. and Tai, Y. (1996). Mems and its applications for flow control. *J. Fluids Eng.*, 118:437–447.
- Ho, C. and Tai, Y. (1998). Micro-electro-mechanical systems (mems) and fluid flows. *Annu. Rev. Fluid Mech.*, 30:579–612.
- Huang, A., Ho, C., Jiang, F., and Tai, Y. (2000). Mems transducers for aerodynamics - a paradigm shift. *AIAA*.
- Iliescu, M., Ciocan, G., and Avellan, F. (2002). *3D PIV and LDV Measurements at the runner outlet of a Francis Turbine*. In *ASME - European Fluids Engineering Conference*, number FEDSM2002-31332.
- Jandard, A. (2000). Study and development of an experimental method for measuring the wall friction in a turbine. Technical Report IMHEFDI/2000J, LMH/EPFL, Lausanne, Switzerland.
- Janke, G. (1987). Hot wire in wall proximity. In ed G Compte-Bellot and Mathieu, J., editors, *Advances in Turbulence*, pages 488–498. Berlin: Springer.
- Janke, G. (1993). *Über die Grundlagen und einige Anwendungen der Öl-Film-Interferometrie zur Messung von Wandreibungsfeldern in Luftströmungen*. Master's thesis, Technische Universität Berlin.
- Jiang, F., Tai, T., Ho, C., Rainer, K., and Garstenauer, M. (1994a). Theoretical and experimental studies of micromachined hot-wire anemometer. In *Digest IEEE Int. Electron Devices Meetings (IEDM)*, pages 139–142.
- Jiang, F., Tai, Y., Gupta, B., Goodman, R., Tung, S., Huang, J., and Ho, C. (1996). A surface micromachined shear stress imager. In *Proc. IEEE Microelectromechanical Systems (MEMS'96)*, number 110–115, New York.



- Jiang, F., Tai, Y., Ho, C., and Li, W. (1994b). A micromachined polysilicon hot-wire anemometer. In *Solid-state Sensor and Actuator Workshop*, Technical Digest, pages 264–267, Hilton Head Island.
- Kalvesten, E. (1995). *Pressure and wall shear stress sensors for turbulence measurements*. PhD thesis, Royal Institute of Technology, Stockholm, Sweden.
- Kalvesten, E., Vieider, C., Lofdahl, L., and Stemme, G. (1996). An integrated pressure-flow sensor for correlation measurements in turbulent gas flows. *Sens. Actuators A*, A52(1-3):51–58.
- Kempf, G. (1929). Neue ergebnisse der widerstandsforschung. *Werft, Reederei, Hafen*, II:234–239.
- Kälvesten, E., Lofdahl, L., and Stemme, G. (1996). An integrated silicon based wall pressure-shear stress sensor for measurement in turbulent flows. *Sensors and Actuators*.
- Konstantinov, N. and Dragnysh, G. (1960). *The measurement of friction stress on a surface*. English translation, DSIR RTS 1499.
- Kucherenko, S. and Leaver, K. (2000). Modelling effects of surface tension on surface topology in spin coatings for integrated optics and micromechanics. *J. Micromech. Microeng.*, 10:299–308.
- Lehmann, V. (1996). Porous silicon-a new material for mems. In *MEMS 96*, pages 1–6.
- Löfdahl, L. and Gad-el Hak, M. (1999). MemS-based pressure and shear stress sensors for turbulent flows. *Meas. Sci. Technol.*, 10:665–685.
- Liu, C., Tai, Y., Huang, J., and Ho, C. (1994). Surface micromachined thermal shear stress sensor. In *The ASME Symposium on Application of microfabrication to Fluid Mechanics*, volume Winter Annual Meeting, Chicago.
- Liu, Y., Cui, T., Sunkam, R., Coane, P., Vasile, M., and Geoertter, J. (2003). Novel approach to form and pattern sol-gel polymethylsilsesquioxane-based spin-on glass thin and thick films. *Sensors and Actuators*, 88:75–79.
- Lofdahl, L., Kalvesten, E., Hadzianagnostakis, T., and Stemme, G. (1996). An integrated silicon based wall pressure-shear stress sensor for measurements in turbulent flows. In *Proc., 1996 Int. Mechanical Engineering Congress and Exposition*, pages 245–251.
- Lofdahl, L., Stemme, G., and Johansson, B. (1992). Silicon based flow sensors used for mean velocity and turbulence measurements. *Exp. Fluids*, 12:270–276.
- Lui, C., Tai, Y.-C., Huang, J.-B., and Ho, C.-M. (1994). Surface micromachined thermal shear stress sensor. In et al., E. B., editor, *Application of Microfabrication to Fluid Mechanics*, volume ASME FED 197.
- Mauri, S. (2002). *Numerical simulation and flow analysis of the elbow diffuser*. PhD thesis, Ecole Polytechnique Federale de Lausanne, Switzerland, Lausanne, Switzerland.

- Mofat, R. (1985). Using uncertainty analysis in planning of an experiment. In *Journal of Fluid Engineering*, volume 107, pages 173–178.
- Nagano, Y., Tsuji, T., and Houra, T. (1998). Structure of turbulent boundary layer subjected to adverse pressure gradient. In *International Journal of Heat and Fluid Flow*, volume 19, pages 563–572.
- Nam, C. and Kwon, Y. (1996). Selective oxidized porous silicon (sops) substrate for microwave power chip-packaging. In *IEEE EP*, pages 202–204.
- Ng, K.-Y. (1990). A liquid shear-stress sensor using wafer-bonding technology. Master's thesis, Massachusetts Institute of Technology.
- Ou, H., Yang, Q., Lei, H., Wang, H., Wang, Q., and Hu, X. (1999). Thick  $\text{SiO}_2$  layer produced by anodisation. *Electronics Lett.*, 35:1950–1951.
- Oudheusden, B. and Huijsing, J. (1988). Integrated flow friction sensor. *Sensors and Actuators*, 15:135–144.
- Padmanabhan, Goldberg, H., Breuer, K., and Schmidt, M. (1996). A wafer-bonded floating-element shear stress microsensor with optical position sensing by photodiodes. *Journal of Microelectromechanical Systems*, 5(4):307–315.
- Pan, T., Hyman, D., Mehregany, M., Reshotko, E., and Williams, B. (1995). Characterization of microfabricated shear stress sensors. In *Proceedings of 16th International Congress on Instrumentation in Aerospace Simulation Facilities*, WPAFB, OH.
- Patel, V. (1965). Calibration of the preston tube and limitations on its use in pressure gradients. *J. Fluid Mech.*, 23:185–208.
- Prandtl, L. (1932). Zur turbulenten stromung in rohren und laengs platten. In *Ergeb. Aerodyn. Versuch.*, 4, pages 18–29, Goettingen.
- Ritter, B. and Schmidt, M. (1981). Qualification du tunnel a eau du laboratoire de mecanique des fluides. Technical Report IMHEFDI/81R, LMH/EPFL, Lausanne, Switzerland.
- Ruderich, R. and Fernholz, H. (1986). An experimental investigation of the structure of a turbulent shear flow with separation, reverse flow, and re-attachment. *J. Fluid Mech.*, 163:283–322.
- Ryhming, I. L. (1985). *Dynamique des fluides*. Presses Polytechniques Romandes, Lausanne, Switzerland, 1st edition.
- Schlichting, H. (1979). *Boundary-Layer Theory*. McGraw-Hill Series in Mechanical Engineering. McGraw-Hill, New-York, United States of America, 7th edition.
- Schmidt, M., Howe, R., Senturia, S., and Haritonidis, J. (1988). Design and calibration of a microfabricated floating-element shear-stress sensor. In *IEEE Transactions on Electron Devices*, volume Vol. ED-35, pages 750–757.

- Susan-Resiga, R., Ciocan, G., Anton, I., and Avellan, F. (2006). Analysis of the swirling flow downstream a francis turbine runner. *Journal of Fluids Engineering*, 128(1):177–189.
- Svedin, N., Kalvesten, E., Stemme, E., and Stemme, G. (1998). A new silicon gas-flow sensor based on lift force. *J. Microelectromech. Syst.*, 7(3):303–308.
- Svedin, N., Stemme, E., and Stemme, G. (2001). A static turbine flow meter with a micromachined silicon torque sensor. In *Technical Digest, MEMS 2001, 14th IEEE Int. Conf. on Micro Electro Mechanical Systems*, pages 208–211, Interlaken, Switzerland.
- Tanner, L. and Blows, L. (1986). A study on the motion of oil films on surfaces in air flow, with application to the measurement of skin friction. *J. Phys. E. Sci. Instrum.*, 9:194–202.
- Tardu, S., Pham, C., and Binder, G. (1991). Effects of longitudinal diffusion in the fluid and of heat conduction to the substrate on the response of wall hot-film gauges. In ed A V Johansson and Alfredsson, P. H., editors, *Advances in Turbulence*, volume 3, pages 506–513. Berlin: Springer.
- Vagt, J. and Fernholz, H. (1973). Use of surface fences to measure wall shear stress in three-dimensional boundary layers. *Aeronautical Quarterly*, XXIV:87–91.
- van Baar, J., Wiegerink, R., Lammerink, T., Krijnen, G., and Elwenspoek, M. (2001). Micromachined structures for thermal measurements of fluid and flow parameters. *J. Micromech. Microeng.*, 11(4):311–318.
- van der Wiel, A., Boillat, M., and de Rooij, N. (1995). A bi-directional silicon orifice flow sensor characterized for fluid temperature and pressure. In *Proc., 8th Int. Conf. on Solid-State Sensors and Actuators and Eurosensors IX*, volume 2, pages 420–423.
- van der Wiel, A., Linder, C., de Rooij, N., and Bezing, A. (1993). A liquid velocity sensor based on the hot-wire principle. *Sens. Actuators A*, 693:37–38.
- van Honschoten, J., Krijnen, G., Svetovoy, V., de Bree, H., and Elwenspoek, M. (2001). Optimization of a two wire thermal sensor for flow and sound measurements. In *Proc., 14th Int. Conf. Micro Electro Mechanical Systems (MEMS 2001)*, pages 523–526.
- von Kármán, T. (1930). Mechanische ähnlichkeit und turbulenz. In eds. C.W.Oseen and W.Weibull, editors, *Proc. 3rd International Congress for Applied Mechanics*, volume 1, pages 85–93, Stockholm. AB Sveriges Litografiska Tryckerier.
- Wagner, P. (1991). The use of near-wall hot-wire probes for time-resolved skin-friction measurements. In ed A V Johansson and Alfredsson, P. H., editors, *Advances in Turbulence*, volume 3, pages 524–529. Berlin: Springer.
- Warnack, D. (1996). Eine experimentelle untersuchung beschleunigter turbulenter wandgrenzschichten. Master's thesis, Technische Universität Berlin.
- White, F. (1991). *Viscous Fluid Flow*. McGraw-Hill Series in Mechanical Engineering. McGraw-Hill, New-York, United States of America, 2nd edition.

- Winter, K. (1977). An outline of the techniques available for the measurement of skin friction in turbulent boundary layers. *Progr. Aerosp. Sci.*, 18:1–55.
- Xu, Y., Jiang, F., Lin, Q., Clendenen, J., Tung, S., and Tai, Y.-C. (2002). Under water shear stress sensor. In *Proc., 15th IEEE Int. Conf. on Micro Electro Mechanical Systems (MEMS 02)*.
- Zhang, C. and Najafi, K. (2002). Fabrication of thick silicon dioxide layers using drie, oxidation and trench refill. In *MEMS 02*, pages 160–163.
- Zhang, C. and Najafi, K. (2004). Fabrication of thick silicon dioxide layers for thermal isolation. In *J. Micromech. Microeng.*, volume 14, pages 769–774.
- Zurfluh, U. (1984). Experimentelle bestimmung der wandschubspannung in turbulenten grenzsichten. Master’s thesis, ETH Zurich.

# List of Figures

1.1	Comparison of computed (left) and measured (right) wall shear stress on a wingtip, Chow et al. [1997] . . . . .	2
1.2	Wall shear stress distribution on a typical propeller driven fighter . . .	3
3.1	Boundary layer illustration . . . . .	8
3.2	Boundary layer on a flat plate . . . . .	9
3.3	The three zones of the boundary layer on a flat plate . . . . .	11
3.4	Shear stress distribution in turbulent boundary layer, with the wall distance: near the wall and total . . . . .	13
3.5	Comparison between a laminar and a turbulent velocity profile . . . . .	13
3.6	The distribution $c^+(y^+)$ in the turbulent boundary layer . . . . .	15
3.7	Temperature distribution in the boundary layer, on a heated flat plate .	16
3.8	Floating element technique . . . . .	21
3.9	Oil-film interferometry technique . . . . .	21
3.10	Preston tube technique . . . . .	22
3.11	Surface fence technique . . . . .	23
3.12	Wall pulsed wire technique . . . . .	23
3.13	Wall hot-wire technique . . . . .	24
3.14	Wall hot-film technique . . . . .	25
4.1	Test section area in the calibration tunnel . . . . .	28
4.2	L.M.H. calibration tunnel . . . . .	29
4.3	Tunnel upper wall design and the measurement instruments places . . .	30
4.4	Measurement flow chart . . . . .	30
4.5	Flow velocity variation with the rotating speed of the tunnel's pump . .	31
4.6	Main heat transfer components on a heated element . . . . .	32
4.7	Wall shear stress evolution with the anemometer's output voltage . . .	36
4.8	The adjustment of a logarithmic tendency in the turbulent boundary layer zone with flow of constant momentum . . . . .	38
4.9	Velocity distribution in the boundary layer . . . . .	38
4.10	Flow velocity distribution with the velocity in the boundary layer and the measurements accuracy . . . . .	39
4.11	Calibration procedure systematized . . . . .	41
4.12	Uni-directional hot-film probe mounting in the calibration tunnel . . . .	41
5.1	Area evolution in FLINDT draft tube . . . . .	44
5.2	Operating points characterization for wall shear-stress measurements . .	44
5.3	Flush mounted hot-film probe - detailed view . . . . .	45

5.4	Flush mounted hot-film probe - front view . . . . .	45
5.5	Rotating support and hot-film probe . . . . .	46
5.6	Rotating support for hot-film probe, mechanical design . . . . .	46
5.7	Hot-film probe orientation . . . . .	47
5.8	Output voltage variation with the mean flow velocity . . . . .	47
5.9	Calibration coefficients, $A$ and $B$ , determination . . . . .	49
5.10	Hot-film probe calibration curve . . . . .	50
5.11	Method used to adjust the voltage drift due to the water temperature changes . . . . .	51
5.12	Hot-film probe output voltage evolution with the water temperature . .	52
5.13	Angular variation of the voltage given by the sensor . . . . .	53
5.14	Angular variation of the wall shear-stress . . . . .	54
5.15	Coefficients calculation of the 2 calibration curves . . . . .	54
5.16	Probe contamination influence on the calibration curves . . . . .	55
5.17	FLINDT Francis turbine scale model . . . . .	56
5.18	Draft tube pressure recovery . . . . .	56
5.19	Wall shear stress measurement sections . . . . .	57
5.20	Wall shear stress sensors locations . . . . .	57
5.21	Variation of the output voltage of the hot-film probe with the water temperature in the cone . . . . .	58
5.22	Temperature curves comparison obtained in the cone and in the calibration curve . . . . .	59
5.23	Angle made by the longitudinal direction of the hot film with the flow direction . . . . .	59
5.24	Influence of the hot-film probe orientation on the wall shear-stress . . .	60
5.25	Drift correction scheme . . . . .	60
5.26	Method for correction the measurements . . . . .	61
5.27	Measurements correction procedure . . . . .	61
5.28	The spatial positions of the wall shear-stress probe in the measurement section at the runner outlet . . . . .	62
5.29	Steady wall shear-stress distributions at a distance of $0.25\phi_{\text{runner}}$ from the runner outlet . . . . .	63
5.30	Mean pressure distribution with the operating point and the pressure sensor spatial position . . . . .	63
5.31	Wall shear stress distribution with the operating point and the hot-film probe spatial position . . . . .	63
5.32	Tangential velocity components at the runner outlet . . . . .	64
5.33	Comparison with the numerical approaches . . . . .	64
5.34	Phase average scheme . . . . .	65
5.35	Spectral analysis of the wall shear-stress for operating point A . . . . .	66
5.36	Spectral analysis of the wall shear-stress for operating point B . . . . .	66
5.37	Spectral analysis of the wall shear-stress for operating point C . . . . .	67
5.38	Spectral analysis of the wall shear-stress for operating point D . . . . .	67
5.39	Wall shear stress phase average with runner rotation, operating point A	68
5.40	Wall shear stress phase average with runner rotation, operating point B	68
5.41	Wall shear stress phase average with runner rotation, operating point C	68

5.42	Wall shear stress phase average with runner rotation, operating point D	69
5.43	The signals in phase corresponding to all standard operating points . . .	69
5.44	The signal shifted evidenced for all standard operating points . . . . .	70
5.45	Wall shear stress phase average with the blade passage . . . . .	71
5.46	Steady wall shear-stress distributions at the cone's inlet, for both the near BEP and partial load operating points . . . . .	71
5.47	Spectral analysis for partial load operating points, corresponding to an- gular position $12^\circ$ . . . . .	73
5.48	Wall shear stress phase average with the vortex frequency for angular position $12^\circ$ . . . . .	73
5.49	Spectral analysis for partial load operating points, corresponding to an- gular position $45^\circ$ . . . . .	74
5.50	Wall shear stress phase average with the vortex frequency for angular position $45^\circ$ . . . . .	74
5.51	Spectral analysis for partial load operating points, corresponding to an- gular position $78^\circ$ . . . . .	75
5.52	Wall shear stress phase average with the vortex frequency for angular position $78^\circ$ . . . . .	75
5.53	Spectral analysis for partial load operating points, corresponding to an- gular position $102^\circ$ . . . . .	76
5.54	Wall shear stress phase average with the vortex frequency for angular position $102^\circ$ . . . . .	76
5.55	Spectral analysis for partial load operating points, corresponding to an- gular position $180^\circ$ . . . . .	77
5.56	Wall shear stress phase average with the vortex frequency for angular position $180^\circ$ . . . . .	77
5.57	Spectral analysis for partial load operating points, corresponding to an- gular position $225^\circ$ . . . . .	78
5.58	Wall shear stress phase average with the vortex frequency for angular position $225^\circ$ . . . . .	78
5.59	Spectral analysis for partial load operating points, corresponding to an- gular position $270^\circ$ . . . . .	79
5.60	Wall shear stress phase average with the vortex frequency for angular position $270^\circ$ . . . . .	79
5.61	Spectral analysis for partial load operating points, corresponding to an- gular position $315^\circ$ . . . . .	80
5.62	Wall shear stress phase average with the vortex frequency for angular position $315^\circ$ . . . . .	80
5.63	Spectral analysis for partial load operating points, corresponding to an- gular position $348^\circ$ . . . . .	81
5.64	Wall shear stress phase average with the vortex frequency for angular position $348^\circ$ . . . . .	81
5.65	The spatial positions of the wall shear-stress probe in the measurement section at the cone outlet . . . . .	82
5.66	Steady wall shear-stress distributions at the Francis cone outlet . . . .	82
5.67	Mean pressure distribution at the cone outlet with the operating point .	83

5.68	Steady wall shear-stress distributions at the cone inlet and outlet . . . .	83
5.69	Wall shear stress distribution with the operating point and the spatial position, at the cone outlet . . . . .	84
5.70	Wall shear stress distribution with the operating point for the same spatial positions, at the cone inlet and outlet . . . . .	84
5.71	Spectral analysis of the wall shear-stress corresponding to the 12° angular position of the hot-film probe . . . . .	85
5.72	Spectral analysis of the wall shear-stress corresponding to the 78° angular position of the hot-film probe . . . . .	85
5.73	Spectral analysis of the wall shear-stress corresponding to the 102° angular position of the hot-film probe . . . . .	86
5.74	Spectral analysis of the wall shear-stress corresponding to the 192° angular position of the hot-film probe . . . . .	86
5.75	Spectral analysis of the wall shear-stress corresponding to the 258° angular position of the hot-film probe . . . . .	87
5.76	Spectral analysis of the wall shear-stress corresponding to the 282° angular position of the hot-film probe . . . . .	87
5.77	Spectral analysis of the wall shear-stress corresponding to the 348° angular position of the hot-film probe . . . . .	88
5.78	Steady wall shear-stress distribution for the part load operating point with vapor phase . . . . .	89
5.79	Steady wall shear-stress distribution for the part load operating point without vapor phase . . . . .	89
5.80	Wall shear stress distribution with the operating point and the spatial position, both at the cone inlet and outlet . . . . .	89
5.81	Spectral analysis, at the cone outlet, for partial load operating points, corresponding to angular position 12° . . . . .	90
5.82	Wall shear stress phase average with the rope frequency for angular position 12° . . . . .	90
5.83	Spectral analysis, at the cone outlet, for partial load operating points, corresponding to angular position 78° . . . . .	91
5.84	Wall shear stress phase average with the rope frequency for angular position 78° . . . . .	91
5.85	Spectral analysis, at the cone outlet, for partial load operating points, corresponding to angular position 102° . . . . .	92
5.86	Wall shear stress phase average with the rope frequency for angular position 102° . . . . .	92
5.87	Spectral analysis, at the cone outlet, for partial load operating points, corresponding to angular position 192° . . . . .	93
5.88	Wall shear stress phase average with the rope frequency for angular position 192° . . . . .	93
5.89	Spectral analysis, at the cone outlet, for partial load operating points, corresponding to angular position 258° . . . . .	94
5.90	Wall shear stress phase average with the rope frequency for angular position 258° . . . . .	94



5.91	Spectral analysis, at the cone outlet, for partial load operating points, corresponding to angular position $292^\circ$ . . . . .	95
5.92	Wall shear stress phase average with the rope frequency for angular position $292^\circ$ . . . . .	95
5.93	Spectral analysis, at the cone outlet, for partial load operating points, corresponding to angular position $348^\circ$ . . . . .	96
5.94	Wall shear stress phase average with the rope frequency for angular position $348^\circ$ . . . . .	96
6.1	LDV measurement location in the measurements sections related to the wall shear-stress locations . . . . .	98
6.2	Near wall LDV measurements . . . . .	99
6.3	Velocity distribution in the cone near wall region . . . . .	99
6.4	Near wall velocity measurements for near BEP operating points at the runner and cone outlet . . . . .	99
6.5	Near wall velocity measurements for near BEP and 2 off-design operating points at the runner and cone outlet . . . . .	100
6.6	Velocity profile distribution, in boundary layer inner variables, for the near BEP operating points . . . . .	100
6.7	Velocity profile distribution, in boundary layer inner variables, for the near BEP and 2 off-design operating points . . . . .	101
6.8	The intermediate region of wall-bounded shear flow . . . . .	101
6.9	Velocity profiles using inner-variables, White [1991] . . . . .	103
6.10	Velocity profile distribution, in boundary layer inner variables, for the near BEP and 2 off-design operating points . . . . .	104
6.11	Local system attached to the hot-film probe, $x'$ and $z'$ . . . . .	105
6.12	Boundary layer flow angle distribution, for the near BEP operating points . . . . .	105
6.13	Boundary layer flow angle distribution, for the near BEP and 2 off-design operating points . . . . .	105
6.14	Comparison between the shear-stress angle and flow angle distribution in the boundary layer, for all operating points studied . . . . .	106
6.15	Velocity distribution by 2 different scaling laws . . . . .	106
6.16	Boundary layer's "chevron" in the cone, both at the outlet and at the inlet, for all operating points studied . . . . .	108
7.1	Schematic presentation of the floating element balance, Padmanabhan et al. [1996] . . . . .	113
7.2	MEMS flush-mounted wall shear-stress sensor, Kalvesten [1995] . . . . .	116
7.3	MEMS shear-stress sensor developed by Jiang et al. [1996] . . . . .	117
7.4	Different designs proposed for the hot film . . . . .	119
7.5	Main fabrication steps for the initial configuration of the new hot-film sensor . . . . .	123
7.6	Top view of the new sensor, corresponding to different designs for the hot-film probe . . . . .	124
7.7	Top schematic view and cross-section in the new sensor . . . . .	125
7.8	The 3 masks used for first generation sensors fabrication . . . . .	126
7.9	Wafer design used for laser dicing . . . . .	126

7.10	Wetox reducing on the front side of the device . . . . .	127
7.11	First photolithography illustration . . . . .	127
7.12	Heated elements deposition . . . . .	128
7.13	Heated elements pattern . . . . .	128
7.14	Second metallically layer used for increasing electrical tracks . . . . .	129
7.15	Protection $SiO_2$ layer and photoresist deposition . . . . .	129
7.16	Protection $SiO_2$ layer and photoresist deposition for holes refilling . . .	130
7.17	Electrical connections refilling, schematic view . . . . .	130
7.18	Schematic view of the holes refilling purpose . . . . .	131
7.19	Schematic view of the mask used for metal filling validation by electrodeposition . . . . .	131
7.20	Views in a hole, after the silicon and wetox layers etching, showing a complete removal of the $SiO_2$ layer . . . . .	132
7.21	Cross-sections showing the $SiO_2$ layer thickness deposited on the lateral walls of a hole, on the left side, and general view of the $SiO_2$ layer deposition in a hole, both on the bottom and on the lateral walls . . . . .	132
7.22	Cross-section through a hole, before - left side - and after - right side -, $SiO_2$ dry etching on the bottom . . . . .	133
7.23	Lateral walls observation, showing a sufficient oxide layer thickness . . .	133
7.24	Cross-section through a hole refilled with Cu . . . . .	134
7.25	Detailed view of the silicon- $SiO_2$ -copper interface, from the left to the right side) . . . . .	134
7.26	First generation of the new hot-film sensors . . . . .	135
7.27	CTA development for preliminary tests . . . . .	135
7.28	Detailed view of the packaging system . . . . .	136
7.29	Temperature coefficient of resistance determination . . . . .	137
7.30	Power variation, at the wall shear-stress sensor, with the mean flow velocity, in the hydrodynamic tunnel . . . . .	137
7.31	Detailed view on a first generation sensor, after tests in the water tunnel	138
7.32	Cross-section for the new generation of hot-film sensors . . . . .	139
7.33	Numerical simulation of the heat transfer in the device, improved with an insulating surface . . . . .	141
7.34	Cross-section in the device, illustrating the heat transfer . . . . .	141
7.35	Computational domain presentation . . . . .	142
7.36	Heat transfer calculation results for the steady case, with flow velocity .	144
7.37	Detailed view over the heated element, illustrating the conduction heat transfer . . . . .	144
7.38	Pillars design and trenches dimensions studied . . . . .	145
7.39	Pillars design and trenches dimensions studied . . . . .	146
7.40	SEM photos showing the trenches filling depending on the Si pillars design: a) square design,b) circle design, c) cross design . . . . .	146
7.41	Schematic view of the trench filling by oxidation and LTO deposition .	147
7.42	SEM photos showing the trenches filling by this method depending on the Si pillars design: a) square design, b) and c) cross design . . . . .	147
7.43	Schematic view of the trench filling by oxidation, polysilicon deposition and oxidation . . . . .	147

7.44	New designs for the silicon pillars . . . . .	148
7.45	SEM photos showing the trenches filling by oxidation only in the new designs configuration . . . . .	148
7.46	SEM photos showing the trenches filling by the complex method corresponding to the new designs . . . . .	149
7.47	Schematic view of the trench filling by oxidation and nitride deposition	150
7.48	SEM photos showing the trenches filling by oxidation and nitride deposition . . . . .	150
7.49	SEM photos showing the trenches filling by oxidation and LTO deposition	151
7.50	Chemical mechanical polishing results on a wafer surface . . . . .	151
7.51	Mask no.1 used for creating the insulating surface in the substrate . . .	152
7.52	Mask no.2 for the heated film and a first layer corresponding to the electrical track deposition . . . . .	152
7.53	Mask no.3 corresponding to the second layer of the electrical tracks . .	152
7.54	Mask no.4 for the holes realization, corresponding to the electrical connections . . . . .	152
7.55	Main fabrication steps for the second generation of the new hot-film sensor	153
7.56	New multidirectional hot-film sensor . . . . .	153
7.57	A processed wafer . . . . .	154
7.58	Wires welding on the sensor's backside . . . . .	154
7.59	New wall shear-stress sensor's encapsulation . . . . .	154
7.60	New rotating system design . . . . .	155
7.61	The whole encapsulating system used for the new wall shear-stress calibration . . . . .	155
8.1	Temperature coefficient of resistance evaluation for air . . . . .	158
8.2	Temperature coefficient of resistance evaluation for water . . . . .	158
8.3	First electronical device developed . . . . .	159
8.4	Model of non-cylindrical hot film . . . . .	160
8.5	Principle of the constant temperature anemometer . . . . .	161
8.6	Equivalent substrate assumption . . . . .	162
8.7	Constant-current anemometer . . . . .	164
8.8	Constant-current anemometer preliminary test for a film resistance of $R = 71.5\Omega$ . . . . .	167
8.9	Constant-current anemometer's output from step input current . . . . .	168
8.10	MiniCTA . . . . .	170
8.11	Film no.1, $R = 37.2\Omega$ , output voltage evolution with the water temperature . . . . .	171
8.12	Film no.2, $R = 29.5\Omega$ , output voltage evolution with the water temperature . . . . .	171
8.13	Film no.3, $R = 33.1\Omega$ , output voltage evolution with the water temperature . . . . .	172
8.14	Angular variation of the output voltage given by the film no.1, $R = 37.2\Omega$ . . . . .	173
8.15	Angular variation of the output voltage given by the film no.2, $R = 29.5\Omega$ . . . . .	173

8.16	Angular variation of the output voltage given by the film no.3, $R = 33.1 \Omega$ . . . . .	173
8.17	Output voltage variation with mean flow velocity, film no.1, $R = 37.2 \Omega$	174
8.18	Output voltage variation with mean flow velocity, film no.2, $R = 29.5 \Omega$	174
8.19	Output voltage variation with mean flow velocity, film no.3, $R = 33.1 \Omega$	174
8.20	Calibration curve corresponding to film no.1, $R = 37.2 \Omega$ . . . . .	175
8.21	Calibration curve corresponding to film no.2, $R = 29.5 \Omega$ . . . . .	175
8.22	Calibration curve corresponding to film no.3, $R = 33.1 \Omega$ . . . . .	175
8.23	New wall shear-stress sensor's output voltage evolution with the water temperature . . . . .	176
8.24	Angular variation of the voltage given by the new wall shear-stress sensor	176
8.25	New wall shear-stress sensor's Output voltage variation with the mean flow velocity . . . . .	177
8.26	Hot-films calibrations curves for a new wall shear-stress sensor . . . . .	177
8.27	Calibration curve and sensitivity parameters comparisons for the DAN-TEC probe and new wall shear-stress sensor . . . . .	179
A.1	Pitot tube . . . . .	189
A.2	Pitot tube - scheme . . . . .	190
A.3	Preston and Pitot tubes localization in the calibration tunnel . . . . .	191
A.4	Preston tube . . . . .	192
A.5	Preston tube - scheme . . . . .	192
A.6	Preston tube place related to the upper wall . . . . .	192
A.7	Differential pressure instrumentation system and amplifier for pressure probes . . . . .	193
A.8	SC-2040 . . . . .	194
A.9	Constant temperature anemometer . . . . .	196
C.1	Photolithography process . . . . .	200
C.2	Writing techniques in photolithography . . . . .	200
C.3	Chemical Vapor Deposition technology . . . . .	202
C.4	Deposition by evaporation technology . . . . .	202
C.5	Sputter deposition technique . . . . .	204
C.6	Cross-section showing isotropic etching . . . . .	205
C.7	Cross-section showing anisotropic etching for 2 wafer orientations . . .	205
C.8	Wet etching process . . . . .	206
C.9	Dry etching technique . . . . .	206
C.10	Surface micromachining process . . . . .	207
C.11	Chemical mechanical polishing process . . . . .	208
C.12	Chemical mechanical polishing machine . . . . .	208
C.13	Lift-off technique . . . . .	209
C.14	Schematic view of the electroplating process . . . . .	210
C.15	Schematic view of laser induced fluorescence with molecular beams . . .	211

# List of Tables

3.1	Wall shear-stress technologies and their applications . . . . .	19
5.1	Technical data for the 55R46 flush mounted hot-film probe . . . . .	45
5.2	Calibration curves coefficients . . . . .	54
5.3	Studied operating points characterization . . . . .	56
6.1	Main optical probe characteristics . . . . .	98
6.2	The power scaling law constants . . . . .	109
7.1	Progress in micromachined shear-stress sensor technology . . . . .	115
7.2	Main thermal properties for the available substrate materials . . . . .	118
7.3	Main thermal properties for the available heated element materials . . .	121
7.4	Detailed calculation domain . . . . .	143
8.1	Wall shear-stress sensor's thermal time constant calculation without considering conduction losses . . . . .	165
8.2	Wall shear-stress sensor's thermal time constant calculation with considering conduction losses . . . . .	165
8.3	Time responses measurements for 1 new wall shear-stress sensors with medium resistance values . . . . .	169
8.4	Time responses measurements for another new wall shear-stress sensors with high resistance values . . . . .	169



Elena-Lavinia BERCA  
Rue Jean-Prouvé 45  
1762 Givisiez (FR)

22 May 1978  
Single  
Romanian

Tel. private: 026/4651990  
Mobile : 078 /7204475  
Prof. : 021/6932577

laviberca@yahoo.com



## **EDUCATION**

- Studies**
- from 2001 to 2007, PhD thesis in Laboratory for Hydraulic Machines, École Polytechnique Fédéral de Lausanne, Switzerland
  - from 1<sup>st</sup> of April to 31 of July 2001, Diploma project in Laboratory for Hydraulic Machines, École Polytechnique Fédéral de Lausanne, Switzerland
  - from 1996 to 2001, The Power Engineering Faculty, Hydraulic Machinery Department, “Politehnica” University of Bucharest, Romania
  - from 1992 to 1996, The Economical High School Ploiesti, Romania, computer specialization with intense program of learning English
- Certificates**
- 2007, PhD Degree in Hydraulic Machines, Laboratory for Hydraulic Machines, EPFL, Switzerland
  - 2001, Engineer Degree in Hydraulic Machines, Hydraulic Machinery Department, “Politehnica” University of Bucharest, Romania
  - 1996, High school diploma, The Economical High School Ploiesti, Romania
  - 1996, Certificate as assistant-operator in computers, The Economical High School Ploiesti, Romania

## **PROFESSIONAL EXPERIENCE**

- 2003-2006      **EPFL, Lausanne**  
**Mechanical Engineer Assistant** in Laboratory for Hydraulic Machines – participation in International Project Hydrodyna (Harnessing: The Dynamic Behaviour of Hydro Turbines, Storage Pumps and Pump-Turbines) – Eureka no. 3246
- My main responsibilities have been:
- The design, using AUTOCAD and L-Edit, of a new miniature hot-film probe capable to measure wall friction inside a turbomachine;
  - Numerical simulations of the probe’s behaviour using ANSYS and CFX software;
  - The new hot-film probe manufacturing in the clean room, using microtechnology techniques:
    - Development of a new technique for creating silicon pillars for thermal isolation applications
    - Masks design and fabrication using Direct Laser Writer system;
    - Positive resist coating and developing, alignment by proximity/contact double side mask;
    - Deposition by sputtering and evaporation
    - Lift-off, dry etching using a fluorine chemistry high density plasma etcher, electroplating
  - The qualification of this new probe both in steady and dynamic conditions:
    - Development of the calibration instrumentation and procedure for the new hot-film probe;
    - Calibration performance for several miniature probes.

- 2001-2003      **EPFL, Lausanne**  
**Mechanical Engineer Assistant** in Laboratory for Hydraulic Machines – participation in International Project FLINDT (FLow Investigation in Draft Tube) – Eureka no. 1625  
My main responsibilities have been:
- Development of the calibration procedure for a commercial hot-film probe;
  - Calibration performance for 3 hot-film probes;
  - Wall friction measurements for 4 “standard” and 2 off-design operating points, using the commercial hot-film probe for 2 sections: at the runner outlet and at the cone outlet, of a Francis turbine;
  - The steady and unsteady analysis performance for the 2 sections and each operating point of the turbine;
  - Boundary layer development analysis in the cone of a Francis turbine.
- 2000-2001      Collaboration with the department of Hydraulics and Hydraulic Machinery from “Politehnica” University of Bucharest concerning several different national projects, studies of hydropower plant implementation, dams calculations, etc.
- 2000              Industrial stage at the “Portile de Fier I” hydropower plant, Romania, during the refurbishment of the six turbines

## **SCIENTIFIC ACTIVITIES**

- 2002-2004      2 international refereed conference paper in hydraulic and 1 in microtechnology field:
- Berca E.L., Avellan F., Cannehan F. and Langlet Ph.: “Silicon Pillars Development for Thermal Isolation Applications”, the 4<sup>th</sup> International Workshop on Microfactories, IWMF’04, Shanghai, China, Oct. 15-17, 2004
- Berca E.L., Ciocan G.D. and Avellan F.: “Wall Friction and Boundary Layer Development in the Cone of a Francis Turbine Scale Model”, Proceedings of the 22<sup>nd</sup> IAHR Symposium on Hydraulic Machinery and Systems, Stockholm, Sweden, June 29- July 2, 2004
- Ciocan G.D., Avellan F., Berca E.L. “Wall Friction Measurements: Application in A Francis Turbine Cone”, *FEDSM2002-31333, Joint US ASME – European Fluids Engineering Conference*, Montreal, Canada, 14-18 July 2002
- 1998-2001      Participation in Scientific Sessions for Students. In the Hydropower and Hydraulic Machines section I obtained 1<sup>st</sup> and the 3<sup>rd</sup> prices.
- 1990-1995      Many participations in scientific contests at province level: 2<sup>nd</sup> price in English (1995), special mention in Geography (1992), 3<sup>rd</sup> price in Physics (1991), special mention in Mathematics (1990)

## **LANGUAGES**

- French            : Advanced level  
English          : Advanced level  
German          : Beginner level  
Romanian        : Mother tongue

## **COMPUTER ABILITIES**

- AutoCAD, Labview, L-edit, Ansys, CFX, Matlab, , Microsoft Office (Word, Excel, PowerPoint), Adobe Photoshop, Adobe Illustrator

## **LEISURE ACTIVITIES, OTHERS**

- Sports:            Gymnastics, Fitness, Swimming (intensively practiced during 8 years)
- Hobby:           Travel, Literature, Music